THE UNIVERSITY OF CHICAGO

MATERIALS AND DEVICES FOR ELECTROCEUTICALS

A DISSERTATION SUBMITTED TO

THE FACULTY OF THE DIVISION OF THE PHYSICAL SCIENCES

IN CANDIDACY FOR THE DEGREE OF

DOCTOR OF PHILOSOPHY

DEPARTMENT OF CHEMISTRY

BY

ALEKSANDER PROMIŃSKI

CHICAGO, ILLINOIS

JUNE 2022

Table of Contents

List of Figures

List of Tables

Acknowledgments

The six years I spent at the University of Chicago that led to the completion of this thesis have been an inspiring journey for me, both academically and personally. I believe that the challenges I faced made me a stronger person and a better scientist, and I can understand more about the world. In my graduate study, I was surrounded by many people whose support has been invaluable during this time, and I would like to acknowledge their contribution to my research and personal development.

First, I want to thank my research advisor, Professor Bozhi Tian. This thesis would not be completed if not for his enormous support. Over the years, we had many critical discussions over multiple research projects and our work together has generated many exciting scientific studies, only some of which are described in this thesis. I want to sincerely thank him for his ongoing support for my research and personal development. I also want to acknowledge my first advisor at the University of Chicago, Professor Yossi Weizmann, as I believe that his guidance in the first few years was invaluable, and everything I learned during that time has helped me grow as a scientist.

I want to thank all my collaborators and co-authors as the research presented in this thesis could not happen without you. I want to especially thank Dr. Menahem Rotenberg and Dr. Jiping Yue for their guidance and aid in animal experiments and everything I learned about cell biology, anatomy, and physiology. I want to thank all the members of the Tian Lab for the great atmosphere that resulted in the vast amount of collaboration and scientific contributions. Especially, Lingyuan Meng, Dr. Yiliang Lin, Jiuyun Shi, Dr. Chuanwang Yang, Pengju Li, Dr. Jihun Park, Dr. Yin Fang, Dr. Hector Acaron Ledesma, Dr. Erik Schaumann, and Dr. Vishnu Nair. I would like to thank all the students that I had an opportunity to mentor in the classroom and research. I want to give

special thanks to Matthew Seebald, Bernadette Miao, Eleonor Ostroff, Kavita Parekh and Jacob Phillips. Working with them has been a great opportunity for me, and I hope that they learned as much as I did during that time. I would also like to acknowledge the support of all staff members of the shared facilities. In particular, Dr. Justin Jureller from MRSEC Materials Preparation and Measurement Laboratory, Dr. Gerard Olack from Department of Geophysical Sciences, and Dr. Peter Duda from Pritzker Nanofabrication Facility. Their technical expertise was critical for the success of the studies presented in this thesis.

Finally, I would like to thank all my family and friends for their ongoing indispensable support for my academic endeavors. I want to thank my mother, Iwona, for her encouragement to follow my dreams, and my closest friends Wiktor Brzęczkowski, Tomasz Ślężak, Michał Sawczyk, and Kelly O'Leary, who were there for me and offered their support in the most challenging times.

Abstract

Pharmacology, or the use of chemical drugs for disease treatment, has been one of the driving forces for the development of human civilization since the time of the industrial revolution. However, biological structures respond to many other stimuli, one of which is the electrical field. At the dawn of the silicon age and thanks to the proliferation of microelectronics, we are beginning to build our understanding of electrical signaling in cells and tissue, and we can start developing electroceuticals which are devices capable of directly interrogating biological electric fields for health disorders treatment. These methods and devices find numerous therapeutic applications, for example, in treating heart defects, chronic pain management, epilepsy, and Parkinson's diseases, while not building dangerous drug dependency. Studying new materials and methods to make these treatments safe and affordable is critical.

This thesis will describe the discovery, analysis, and proof of concept applications of inorganic materials for bioelectronics and future electroceutical therapies. It will discuss biointerfaces and materials design fundamentals, followed by the original research studies. In particular, nanostructured materials will be at the center of the thesis. Detailed studies of electrochemical mesoporous carbon-based material and photoelectrochemical nanoporous silicon-based material will be presented. The applicability of such materials to electroceutical therapies will be investigated using clinically relevant animal models. Finally, it will describe new concepts for integrating information technology and artificial intelligence into bioelectronics studies. The presented technologies show translational potential and can become a basis of clinical therapies in the future.

Preface

I have dedicated the last nine years of my life to the pursuit of knowledge. Every day, I have been filled with wonder and gratitude for the opportunity to work at the bleeding edge of our understanding of physical and natural phenomena. As a culmination of my graduate education, this dissertation will describe my major research projects in the fields of materials science and bioelectronics. During my academic journey, I had an opportunity to touch on many research fields, from organic and physical chemistry, nanotechnology and materials science, to bioelectronics and bioengineering. The research projects I engaged in were highly interdisciplinary, which has taught me to think of them in the bigger picture and study it as a broad landscape of materials, methods, applications, and their future implications for societal benefits.

Electroceuticals, or bioelectronic therapies, which are a central topic of this thesis, represent the future frontier of medical therapies. Precise control over electrical signals in biological structures promises innovative treatments that can correct abnormal activity of tissues and organs with the timescale and precision not available to common pharmaceuticals. The current developments, some of which are described in this thesis, bring us closer to the translation of such technologies into medical therapies and, as some would hope, into our daily lives. While the prospect of science-fiction-like cybernetics is still decades away, the first electroceutical treatments hope to improve the quality of life for people struggling with chronic pain and other nervous system disorders. To realize such therapies, we need a solid foundation and understanding of the principles of materials design and interactions at the biointerfaces, which has been my motivation for pursuing the research described herein.

Chapter 1

Introduction

1.1 Motivations[1]

Designing efficient strategies for interfacing biological structures with artificial materials is a formidable challenge. Such biointerfaces are of critical importance to fundamental studies of biophysical interactions between cellular components and their environment and are a basis for recording and stimulation applications that are significant in biomedical fields, especially neuroscience research[1] with many promising avenues for translation. Specifically, nanotechnology-driven materials research for biological modulation has presented a number of advantages over approaches utilizing classical bulk materials and devices. Primary benefits of reducing the size of a device's active components include increased resolution with which stimulation or recording can be performed. Interacting with biological matter on the cellular and subcellular level allows for a high degree of specificity and fidelity in the biointerface, which is especially important for neural interfaces, such as retina implants for vision restoration[2]. Additionally, nanomaterials can be part of larger assemblies, where single nanostructures can act as separate transducers enabling high-throughput parallel communication[3], e.g., for the realization of efficient brain-machine interfaces. Another advantage of nanostructured materials is their improved mechanical compliance with biological tissue. Due to small dimensions and reduced bending stiffness, nanostructures elicit minimal immune responses in *in vivo* applications, creating

[1] Adapted from: Prominski, A., Li, P., Miao, B. A., & Tian, B. Nanoenabled Bioelectrical Modulation. *Accounts of Materials Research* **2021** *2* (10), 895-906.

stable interfaces suited for chronic implantation. Matching of mechanics and size allows cells to adapt freely to and seamlessly contact with nanostructured interfaces[4]. Furthermore, when nanodevices are sufficiently small, they can be internalized by certain cell types, resulting in intracellularly integrated systems[5]. Overall, nanostructures enable efficient and biocompatible means of biological modulation critical for future translational applications of such technologies.

Although bioelectrical interfaces are primarily concerned with recording and eliciting action potentials in electrically excitable cells[6], investigation of the effects of electric fields on growth, development, and migration of non-excitable cells is a growing direction as well[7]. Nanostructured materials have applications in classic bioelectronics as an electrode material, where surface area nanoengineering has greatly improved recording and stimulation performance[8,9], and single nanostructures have been used to record subcellular electronic signals[10]. Another side of bioelectronics is the synthesis and application of free-standing bioelectronic devices. Such devices can stimulate cells using light-induced phenomena, such as photovoltaic, photoelectrochemical, or photothermal effects[11]. Stimulation with free-standing nanostructures benefits from the remote signal transduction mechanism, i.e., there is no need to connect the electrode to the current or voltage source. Application of photoresponsive nanostructures that can stimulate native cells presents an important alternative to optogenetics[12]. While more work is required to improve the stability and efficiency of free-standing nanostructures for photomodulation and convenient delivery methods have to be devised, and without doubt this category of bioelectrical devices can achieve translational importance in the near future.

Taken together these considerations, I have pursed a study of nanotechnology-based materials systems and their proof of concept applications for electroceutical therapies, which I will describe in detail in this thesis.

1.2 Thesis Overview

In this thesis, I will present my basic studies on the materials and devices for electroceutical therapies. The work will focus on the synthesis, fabrication, and proof of concept applications of porous inorganic materials for the electrical stimulation of cells, tissues, and organs, forming a basis for future electroceutical therapies. Additionally, I will discuss the preliminary data on my concepts for machine intelligence-enabled electronic bioengineering.

In Chapter 2, I will discuss the principles of bioelectronic interfaces. I will analyze the size and time scales of bioelectronics, signal transduction mechanisms, and considerations of reactivity and biocompatibility for the design of stable, efficient, and safe electroceuticals. Then, I will introduce the concept of biomimetic design and how we can apply it to design materials with even more desirable properties.

In Chapter 3, I will describe the synthesis and fabrication of mesoporous carbon membranes. Thanks to the porous but monolithic design, these carbon membranes show excellent electrical properties, such as charge injection capacity, allowing efficient electrical signals delivery while achieving good stability and biocompatibility. I will describe materials design and its structural characterization and show how applying specific microfabrication strategies allows creating flexible micro-supercapacitor-like devices.

In Chapter 4, I will present proof of concept applications of the aforementioned micro-supercapacitor-like devices for bioelectronic interventions into the physiology of cells, tissues, and organs. I will first describe the stimulation of cells *in vitro*, followed by stimulations of retina and heart tissues *ex vivo*. Finally, I will demonstrate how the micro-super-capacitor-like device can stimulate sciatic nerves *in vivo* with short pulses and low currents, making it a suitable candidate

for the development of electroceutical therapies for pain management in the peripheral nervous system.

In Chapter 5, I will describe the development of the stain etching wet processing of pure silicon crystals for the synthesis of photojunctions that enable efficient photoelectrochemical stimulation of tissues and organs. I will describe how different materials processing conditions affect the generation of photoelectrochemical currents and characterize the electrochemistry of the materials.

In Chapter 6, I will show how thin single crystal silicon membranes with porous heterojunctions can be used for efficient nongenetic optical stimulation of isolated hearts *ex vivo* and sciatic nerves *in vivo* in a rat model. I will show how porous membranes can be used for single- and dual-chamber pacing of the heart and how we can map action potential evoked in the myocardium. I will also demonstrate stimulation of the sciatic nerve bundle and selective activation of muscles in the hindlimb.

In Chapter 7, I will describe the concept and preliminary results from machine vision-enabled bioelectronic training of cardiomyocytes. I will introduce the concepts of autonomous bioelectronic experimentation and my motivations for pursuing this direction. I will describe the software and hardware system coupled with cell culture devices I designed to demonstrate proof of concept of subthreshold stimulation for directing cellular development. I will discuss the developed methods, limitations, future challenges, and promises for such studies.

Finally, in Chapter 8, I will conclude the studies on the porous materials for electrical stimulation and their importance in developing electroceutical therapies. I will also present my outlook for future developments in the approaches to materials design in bioelectronics.

1.3 Bibliography

1 Vazquez-Guardado, A., Yang, Y., Bandodkar, A. J. & Rogers, J. A. Recent advances in neurotechnologies with broad potential for neuroscience research. *Nat Neurosci* **23**, 1522-1536, doi:10.1038/s41593-020-00739-8 (2020).

2 Tang, J. *et al.* Nanowire arrays restore vision in blind mice. *Nat Commun* **9**, 786, doi:10.1038/s41467-018-03212-0 (2018).

3 Obaid, A. *et al.* Massively parallel microwire arrays integrated with CMOS chips for neural recording. *Sci Adv* **6**, eaay2789, doi:10.1126/sciadv.aay2789 (2020).

4 Parameswaran, R. *et al.* Photoelectrochemical modulation of neuronal activity with free-standing coaxial silicon nanowires. *Nat Nanotechnol* **13**, 260-266, doi:10.1038/s41565-017-0041-7 (2018).

5 Rotenberg, M. Y. *et al.* Living myofibroblast-silicon composites for probing electrical coupling in cardiac systems. *Proc Natl Acad Sci U S A* **116**, 22531-22539, doi:10.1073/pnas.1913651116 (2019).

6 Fang, Y. *et al.* Recent advances in bioelectronics chemistry. *Chem Soc Rev* **49**, 7978-8035, doi:10.1039/d0cs00333f (2020).

7 Dawson, J., Lee, P. S., van Rienen, U. & Appali, R. A General Theoretical Framework to Study the Influence of Electrical Fields on Mesenchymal Stem Cells. *Front Bioeng Biotechnol* **8**, 557447, doi:10.3389/fbioe.2020.557447 (2020).

8 Rastogi, S. K. *et al.* Three-dimensional fuzzy graphene ultra-microelectrodes for subcellular electrical recordings. *Nano Research* **13**, 1444-1452, doi:10.1007/s12274-020-2695-y (2020).

9 Fang, Y. *et al.* Micelle-enabled self-assembly of porous and monolithic carbon membranes for bioelectronic interfaces. *Nat Nanotechnol* **16**, 206-213, doi:10.1038/s41565-020-00805-z (2021).

10 Zhao, Y. *et al.* Scalable ultrasmall three-dimensional nanowire transistor probes for intracellular recording. *Nat Nanotechnol* **14**, 783-790, doi:10.1038/s41565-019-0478-y (2019).

11 Jiang, Y. & Tian, B. Inorganic semiconductor biointerfaces. *Nat Rev Mater* **3**, 473-490, doi:10.1038/s41578-018-0062-3 (2018).

12 Delbeke, J., Hoffman, L., Mols, K., Braeken, D. & Prodanov, D. And Then There Was Light: Perspectives of Optogenetics for Deep Brain Stimulation and Neuromodulation. *Front Neurosci* **11**, 663, doi:10.3389/fnins.2017.00663 (2017).

Chapter 2

Bioelectronic Interfaces

This chapter was adapted from Fang, Y., Meng, L., Prominski, A., Schaumann, E. N., Seebald, M., & Tian, B. Recent advances in bioelectronics chemistry. Chemical Society Reviews, 49(22), 7978-8035, (2020) and Prominski, A., & Tian, B. Bridging the gap — biomimetic design of bioelectronic interfaces, Current Opinion in Biotechnology, 72, 69-75, (2021).

2.1 Introduction

In this chapter, I will discuss the fundamental principles of interacting with biological structures through various physical and chemical phenomena. Such junctions between artificial and biological structures, referred to as biointerfaces, are essential interactions that must be leveraged to design successful electroceutical therapies. I will begin by discussing the size and time scale of the formation of interfaces and how they affect our choice of materials, and the following section will discuss basic biophysical principles behind the transduction of bioelectronic signals. Subsequently, I will introduce concepts of mechanical matching at the biointerfaces and how to manage material reactivity to achieve stable and biocompatible interfaces. Finally, I will discuss the idea of biomimetic design and how we can take inspiration from nature to design novel materials and devices.

2.2 Size Scales of Bioelectronics

Biointerfaces can be formed at different length scales depending on the relevant biological question and application, ranging from large-area non-specific modulation to subcellular sensing (**Fig. 2.1a**). The following discussion provides not only a description of biointerface design but also a historical perspective on the field of bioelectronics. Relatively large, noninvasive electrodes were developed first and remain widely used today. For recording, those applications are mainly electroencephalography (EEG) for recording brain activity through the scalp, electrocardiography (ECG) for recoding of cardiac activity, and electromyography (EMG) for investigation of skeletal muscles. Similarly, large-area stimulations are routinely used in emergency cardiac arrest defibrillation, in physical therapy for electrical muscle stimulations, and to effectively treat some mental illnesses through electroconvulsive therapy[1]. By definition, large-area techniques have limited resolution and suboptimal efficiency due to making indirect contact and being placed far from the tissue of interest. The bioelectrical effects are averaged over a large area and it is therefore difficult to disentangle the variety of chemical interactions at this scale.

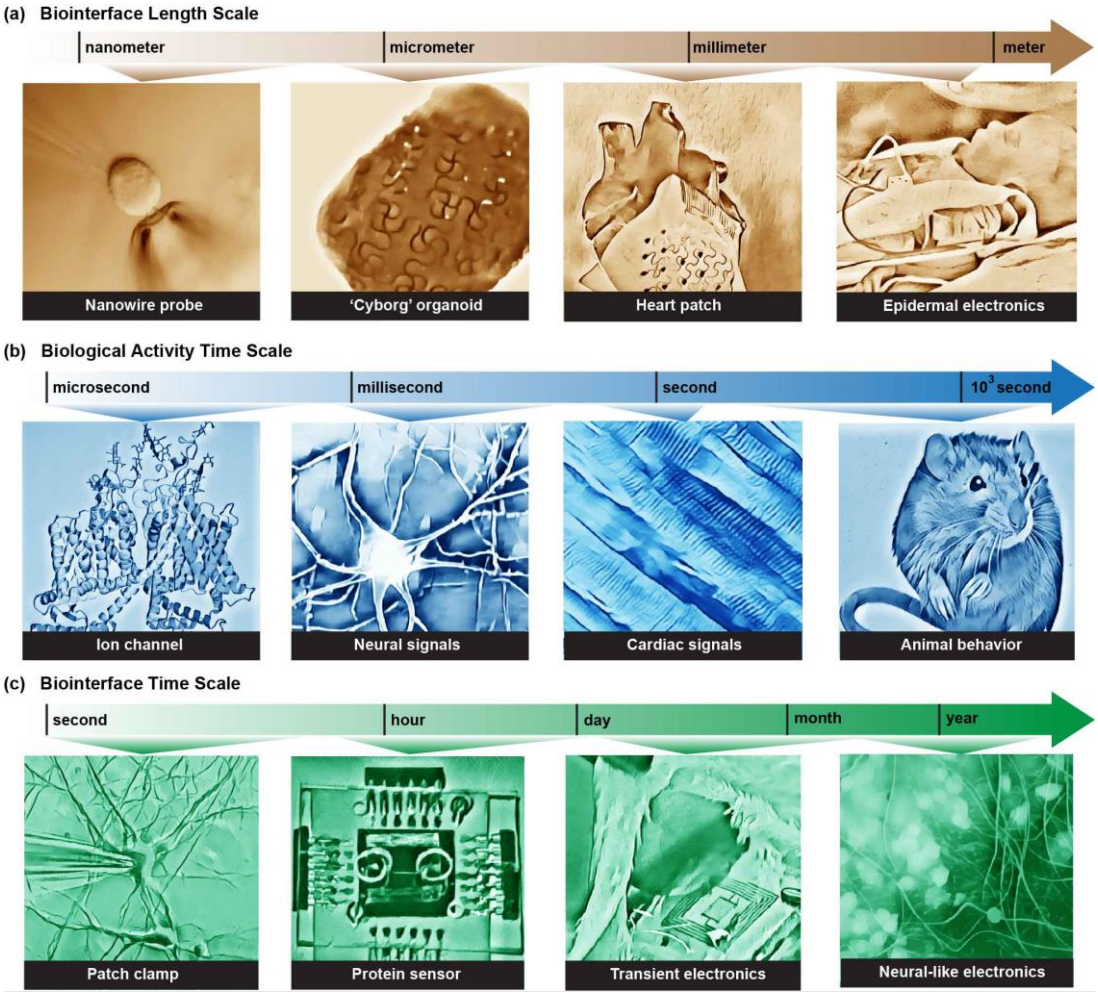

Figure 2.1 Bioelectronics and bioelectrical studies span a range of length and time scales. Awareness of chemistry and physics at all applicable levels is necessary to devise appropriate synthetic and analytical methods for the study of biointerfaces.

Progress in materials research brought the possibility of the creation of probes with higher resolution placed closer to the active cells, which facilitated the development of smaller and less invasive devices. The first step was the development of direct biointerfaces with a single organ. These efforts brought us artificial pacemakers, cochlear implants, and deep-brain stimulation probes, which improved survival and quality of life for millions of people. However, the realization

of challenging goals such as visual prosthetics or brain-machine communication requires single-cell resolution. Traditional electronics face certain key limitations in such applications. Namely, they possess undesirable mechanical properties, limited biocompatibility, and low interface resolution.

The advent of modern micro- and nanotechnology opened the next frontier in bioelectronics[2-14]. Probes became smaller and more adaptable, improving the biocompatibility of devices. Micron-sized devices allowed for measurement of local electric potentials deep inside tissues and interfacing with small groups of cells, bringing a whole new insight into the study of cell physiology. On this scale, substantial chemical interactions between the materials and the tissues, such as adhesive forces, have to be taken into account. Current state-of-the-art devices are capable of forming exact single-cell extracellular[15] and intracellular[16,17] interfaces. Hopefully, further development in the field will produce methods for single organelle modulation or even studies on specific cell structures such as microfilaments or ion channels. Such measurements will become highly local and allow the study of heterogeneity[18] and non-equilibrium processes in living cells. On the lowest scale, chemical and mechanical energy terms become approximately equal in magnitude,[19] which will without doubt reveal the presence of new fundamental processes.

With increased spatial resolution comes decreased signal throughput through the biointerface. While large-area recordings give only average readings of electrical activity, such recordings are generally more useful for practical applications. Signals from single cells are usually not representative of the entire tissue and can carry significant noise. Therefore, another challenge that comes with utilizing microscale biointerfaces is achieving high parallelization of modulation and recording. For this purpose, massive amounts of bioelectronic components have to be fabricated or assembled. Recently, significant effort has been put into clinical translation of

machine-brain interface technologies by Neuralink. Recent reports demonstrate simultaneous recording from 1020 electrodes[20]. While this number is ten-fold higher than those of classic microelectrode arrays (*e.g.*, Utah or Michigan probes)[21-26], it is still far from that achieved by biological interfaces. For example, human auditory nerves are made of some 30,000 myelinated neuron fibers[27] and optical nerves of more than a million[28]. The number of neuronal connections necessary to establish a high-fidelity computer-brain interface is still a matter of debate. However, with the first devices entering clinical trials[29,30], we should expect a better quantitative assessment of these technologies over the next few decades. It can be envisioned that new materials in a form of massively self-assembled neuro-mimetic fibrils will one day match the parallelization of information transfer observed in nature. A recent report showing bundles of microwires used for neuronal recording represents a promising early step in this direction[31]. It is therefore important to study nanoscale self-assembly processes, dynamic combinatorial libraries and other types of parallel chemistries for the synthesis of future bioelectronic devices.

2.3 Time Scales of Bioelectronics

The relevant time scales in the bioelectronics can be seen from two orthogonal perspectives. One describes the time scale over which biological signals are generated (**Fig. 2.1b**), and the other is the duration of the biointerface, that is, the time that the device and the biological system spend in contact. (**Fig. 2.1c**). The timing of recording and stimulation with respect to the biological events will be discussed first. For interfacing with highly active cells such as neurons or cardiac muscles, which can fire an action potential on the timescale of milliseconds, a high frequency response is required from the device. For investigations of even more transient biological events such as the action of molecular motors or activity of single ion channels, even higher temporal resolution on

the timescale of nano- to microseconds is required. The timing of the target process therefore determines the required kinetics of the recording or stimulation. For example, for studies of transient states, using diffusion-limited processes would be unwise. Conversely, devices meant to sense or stimulate slower physiological processes such as bone regeneration[32] require less temporal resolution but carry with them a different set of considerations. In this case, interfacial chemistry plays an important role as interactions such as adhesion have a significant effect on the stability of an interface as well as any immune response it can elicit. Likewise, devices that can potentially impact mechanotransduction or chemical transduction must consider the time scale of these processes, where signals are delivered and processed with significant delay, on the order of minutes to hours. Understanding the required stimulation or response frequency is thus a critical factor in matching the design of devices with their specific applications.

The other independent time scale is the period over which we expect our biointerface to be active. The interfacing time scale can range from extremely transient experiments to permanent implantation for clinical applications. Biointerfaces used in studies of individual physiological processes can be relatively short-lived. They are used to study single physiological interactions and disposed of soon after. As such, these types of experiments do not require extensive studies of stability and biocompatibility. Maintaining stable biointerfaces becomes a concern for experiments with tissues or cell cultures. In this case, devices need to maintain their integrity and it becomes important to evaluate additional interactions in the biointerface beyond the designated purpose of the device. If for example, the products of the device decomposition lead to uncontrolled proliferation of cells or increased cytotoxicity, such interactions cannot be ignored. It is therefore critical to take into account the chemical composition of such devices as well as the reactivity of their constituents. For applications requiring implantations of the device into an organism, not only

does device stability have to be higher, but additional considerations have to account for the immune system response to the presence of a foreign body. The origin and methods of mitigation of immune response to the biointerface will be discussed in the following section. Excellent stability and biocompatibility are required for a long-term integration of bioelectronics with a host body. An important example of an application that requires long-term integration is the formation of chronic brain interfaces. The delicate nature of brain tissue makes it not only more sensitive to invasive probes, but due to the brain's limited regeneration ability, replacement of used bioelectronics devices with new ones is not a feasible solution. Each removal and insertion of probes causes irreversible trauma that can lead to fatal accumulation of damages. Therefore, clinical applications of the machine-brain interface demand stable, long-term biointerfaces.

For long-term integration of bioelectronics, additional attention has to be paid to all the secondary electronics necessary for their operation. Bench-top controllers, transducers, and power sources can be used in short-term laboratory experiments without concern. The case is significantly different for implantable bioelectronics, where electrodes tethered to extensive external instrumentation limits the mobility of host organisms and makes such a solution impractical. Hence, lightweight and, ideally, remote-controlled recording and modulation devices represent an important design principle that requires significant thought. The essential issue is the integration of bioelectronic devices with proper microscale power supplies. Recent developments point to devices to which power can be delivered remotely, *e.g.*, through magnetic resonant coupling[33]. Another front is led by the freestanding devices that lack traditional electric circuits, but can locally stimulate tissues through magnetothermal[11,34], chemomagnetic[35], photoelectrochemical[36,37], photothermal[38-41], and photoacoustic[8,42] effects that are initiated with remotely delivered physical stimuli. Future research in applied bioelectronics will no doubt veer towards the development of

integrated, wireless devices for the ultimate goal of seamless, inconvenience-free bionic integration.

2.4 Signal Transductions

Biological systems fundamentally differ from standard electronics by their mechanisms of signal generation and transmission. In conventional conductors such as metals, the majority of electric charge is carried directly by electrons. In biological systems, rich in water, ions, and organic matter, electric current is carried mostly by ionic fluxes. These two modes of conduction are, in principle, very dissimilar, which requires a specific interface in which signals can be transduced (**Fig. 2.2**).

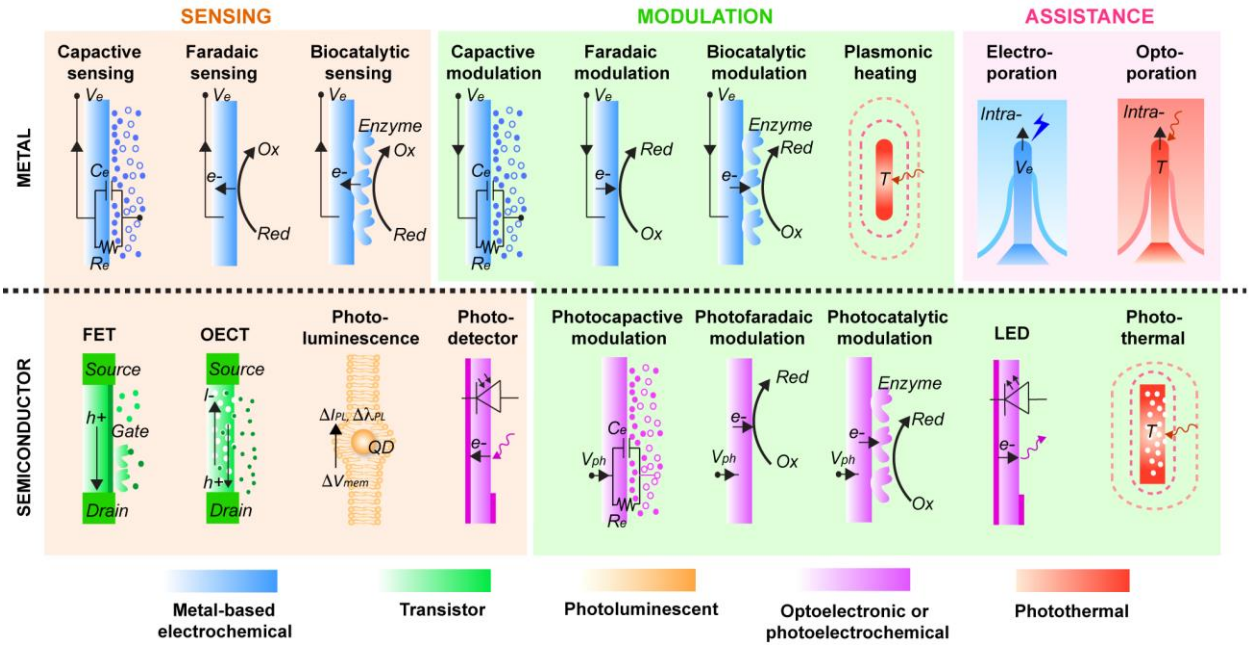

Figure 2.2 Signal transduction mechanisms in bioelectrical interfaces can vary depending on the material design and chemistry.

Top: Metal-based electrodes can be used for recording or injection of capacitive, faradaic, and biocatalytic currents. Free-standing metallic nanostructures allow used for plasmonic heating. Additionally, metallic structures can be used to facilitate interface interrogation penetrating cellular membranes using electroporation and optoporation. **Bottom:** Highly sensitive recording of bioelectric signals using field-effect transistor (FET) and organic electrochemical transistors (OECT). Readout of optical signals using photoluminescent materials and photodetectors. Free-standing nanoscale semiconductors allow for wireless injection of currents through photocapacitive, photofaradaic and photocatalytic effects. Micro light-emitting diodes (LED) can be used to deliver optical signals. Semiconductors without electric and radiative energy decay pathways can generate photothermal heating.

2.4.1 Bioelectricity in Cells and Tissues

Electrically active cells communicate via spikes of ion fluxes caused by a sudden release of ions, known better as action potentials. The potential difference between insides of cells and their extracellular environment (usually negative) is maintained by active transport and imbalance in the concentration of ions, typically K^+ and Na^+. The resting transmembrane potential existing due to this imbalance is classically described using the Goldman-Hodgkin-Katz (GHK) equation:

$$V_{rest} = \frac{RT}{F} \ln \frac{\sum_i^N P_{M_i^+} [M_i^+]_{out} + \sum_j^M P_{A_j^-} \left[A_j^-\right]_{in}}{\sum_i^N P_{M_i^+} [M_i^+]_{in} + \sum_j^M P_{A_j^-} \left[A_j^-\right]_{out}} \qquad Equation\ (2.1)$$

where V_{rest} is the resting membrane potential, R is the ideal gas constant, T is the absolute temperature, and F is the Faraday constant. The sums account for permeabilities P and concentrations [M] of monovalent ions on the inside and outside of the membrane[43]. The resting membrane potential is the mechanism by which cells store energy used for signaling. When stimulation occurs, passive ion channels open and ions freely flow in and out of the membrane. This ion flux generates electric currents which can create a local potential change in the tissue, effectively meaning this cell is interacting with neighboring cells to cause further signal transduction. A potential generated at point (x,y,z) by moving ions can be derived from Ohm's law and, treating the ions as pure monopoles, takes the form of:

$$V(x,y,z) = \sum_{i=1}^{n} \frac{I_i}{4\pi\sigma r_i} \qquad Equation\ (2.2)$$

where I_i is the current from the *i*th monopole, σ is the conductivity of the medium, and r_i is the distance from the monopole to the point (x,y,z)[43].

The aforementioned model averages molecular interactions and approximates properties of the media and the surrounding tissues. In reality, the environment of biological fluids is highly crowded, and in dense structures, *e.g.*, brain tissue, electrodiffusion is affected by heterogeneities at a molecular level[44]. Hence deviations from this classic interpretation can be observed on a subcellular length scale. Such heterogeneities can arise from the extracellular environment and interactions with large proteins and charged species, as well as from uneven spatial distribution of ion channels in the membrane. Therefore, it is paramount that the progress in nanodevices' research comes together with the development and validation of new theoretical models[44].

2.4.2 Electrochemical Sensing or Modulation Processes

The most straightforward electrode-tissue interface utilizes capacitive currents (**Fig. 2.2**). A chemically inert electrode can only inject current due to building capacitive charge on its surface due to applied potential. Ions with complementary charges will migrate towards the electrode, creating charge currents, and start building up a layer on the electrode surface called an electrical double layer (EDL). Ionic currents will flow only until the electrode is fully charged. The time constant for EDL formation can be described as:

$$\tau_{EDL} = R_e C_e \qquad Equation\ (2.3)$$

where R_e and C_e are the leakage resistance and capacitance of the electrode, respectively. This simple relation is an essential operational specification of the electrode. It describes its operational limits as well as its bandwidth – the maximum frequency at which signals can be delivered or received. The electrical interaction between the electrode and the membrane can be estimated with a highly simplified model of an equivalent circuit, in which the cell and electrode are treated as

potential sources, an interface is modelled as a parallel capacitor and a resistor, and an additional term is added for internal electrode resistance[45]. Using this equivalent circuit and *Equation 2.2*, we can derive the relation between cell and electrode potentials:

$$V_e = \frac{1}{4\pi\sigma r}\left[\left(\frac{1}{R_e} + sC_e\right)^{-1} + R_{int}\right]V_{cell} \qquad Equation(2.4)$$

where V_e is the electrode potential, V_{cell} is the potential at the cell surface, R_{int} is electrode's internal resistance, and s is the complex frequency of interacting waveforms. The above equation can be used to qualitatively describe both stimulation and recording. For stimulation, we choose to control electrode potential V_e and interact with the cell. For recording, the cell is firing its active potential $V_{cell,}$ and we measure readings received on the electrode.

By analyzing *Equation 2.4*, fundamental qualities of electrode-cell biointerfaces can be derived. First, electrical interaction, as parameterized by the potential, is inversely proportional to the distance r between the electrode and cell membrane. Hence the closer the distance between the electrode and the membrane, the stronger the interaction. Also, for strong interactions, it is recommended to keep leakage resistance (R_e) low and electrode capacitance (C_e) high. Resistance of interconnections plays a role in determining the signal-to-noise ratio (SNR) of the biointerface. For higher currents, R_{int} has to be kept low, but for good SNR, it has to be kept high. For designs in which the electrode is bifunctional and used for recording and stimulation, a compromise has to be made.

Purely capacitive electrodes rely only on EDL and have a limited range of operation. Stimulation with higher potentials can be accomplished using electrodes injecting Faradaic currents (Fig. 3). Such an electrode is chemically active and introduces new ions due to electrochemical reduction or oxidation occurring on its surface. It has been shown that highly

catalytic electrodes are capable of stimulating with strong potentials[46]. The drawback of using a chemically active electrode is its degradation over time. One possible way to prevent extensive damage to an electrode injecting Faradaic current is the application of principles used for the fabrication of supercapacitors[47]. These principles include the application of nearly completely reversible electrochemical reactions or precise structuring of the electrode on the atomic level, which permit increasing its capacity beyond the limit of traditional materials. Another possible development in this field might be the application of bioelectrocatalysis (**Fig. 2.3**), which uses electrode-bound enzymes to generate active species *in situ* for selective stimulation or process metabolites present in the system to be used for their detection[48,49]. Additionally, although redox signaling is paramount in biological systems[50,51], it was not thoroughly explored with respect to bioelectronic modulation.

2.4.3 Optoelectronic or Photoelectrochemical Sensing or Modulation Processes

Semiconductor-based optoelectronics or photoelectrochemical devices can be used to deliver (*e.g.*, using a light emitting diode [LED] or a photovoltaic device) or read out (*e.g.*, using an *in vivo* photometer) stimulation signals at the biointerface, when matched with electrical circuits or wireless microcontrollers (**Fig. 2.2**)[52,53]. To perform single cell studies, we can either use semiconductor structures/devices that are microns or nanometres in size, or use highly localized initial stimuli (*e.g.*, a laser spot) over macroscopic structures/devices.

Many of the devices for such studies are based on diode junctions. In particular, for photoelectrochemical stimulation applications, a photovoltaic mechanism is often adopted[36]. A diode device is typically created when hole-rich (p-type) and electron-rich (n-type) semiconductors are placed in contact, causing a shift in their valence and conduction bands near the p-n junction,

within a region called the depletion zone. Photoexcitation can promote an electron from the valence to the conduction band, creating an electron-hole pair[8]. The electrons and holes then diffuse away from the depletion zone in accordance with their charge, creating a potential difference on different parts of the device that can be used to stimulate cells and tissues similarly to wired electrodes described above.

Depending on the material, photoexcitation can inject capacitive current, Faradaic current, or a combination thereof into the biointerface (**Fig. 2.2**). These processes in freestanding structures can be understood within a framework analogous to that of the wired electrode. However, semiconductors are highly sensitive to their environment through the alteration of their surfaces' electronic structure. Photostimulation and other physical behaviors at the interfaces can be predicted both qualitatively and quantitatively using the concept of band bending. Band bending in semiconductor describes the alteration in native electronic structure due to the material environment, surface modification[54], or the material size and dimensionality[55]. Semiconductor physics and electronic processes underlaying their photoactivity require a more thorough discussion, better described in a literature specific to semiconductors[8,9].

2.4.4 Photothermal Modulation Processes

The photothermal effect arises from radiationless energy transfers in photoexcited materials. That is, the emitted energy translates into the kinetic energy of the material or its surroundings, and the temperature increases. In practice, this means that the best candidates for photothermal modulation primary respond to excitation with the generation of phonons or plasmons. In crystalline materials, nonradiative recombination can produce quantized oscillations in the bulk material, known as phonons, which are responsible for photothermal heating in those structures[56]. For certain metallic

nanomaterials, such as noble metal nanoparticles and carbon nanostructures, light absorption results in oscillations of associated free electrons on the material surface. These oscillations are referred to as surface plasmons, and their production can convert almost all incoming light energy to heat[57,58]. Continuous-wave irradiation of plasmonic materials can therefore create strong temperature gradients (**Fig. 2.2**)[38].

Transduction of thermal signals is another vital aspect of biophysics, yet it has not been studied as extensively as electrical signals. Cell physiology, especially the catabolic process responsible for energy generation, generates multiple intracellular and extracellular thermal gradients[59]. Such signals can trigger proliferation and affect other cellular metabolic pathways. It can be deduced from the GHK equation (**Eq. 2.1)** that temperature affects membrane potential, and its increase will make it more sensitive to stimulations. Additionally, multiple ion channels have been discovered to be especially receptive to temperature gradients such as thermosensitive potassium channel TREK-1[38]. For thermal sensing, purely resistive microelectromechanical devices as well as a range of nanostructures have proven effective. Quantum dots, upconverting nanoparticles, and metal cluster were all applied to create remote luminescent thermometers[60].

A closely related phenomenon can be observed when instead of steady irradiation, high-power pulsed lasers are used to illuminate plasmonic nanostructures. A sudden release of energy causes evaporation of solvents around the material surface, forming gas nanocavities which, upon collapsing, release ultrasonic waves traveling through the medium. This phenomenon is referred to in the literature as a photoacoustic effect[39,42,61]. Although the mechanism of the generation of photoacoustic waves is not fully understood it allowed the development of a variety of imaging and stimulation methods[62,63]. Recently, the photoacoustic effect was used to facilitate entry of recording electrodes into the cells through the local optoporation mechanism in a similar manner

to the classical electroporation (**Fig. 2.2**), but providing superior process control and cell viability[64]. However, potential applications of the photoacoustic effect in bioelectronics remain largely unexplored.

2.4.5 Transistor-based Sensing Processes

Transistors are some of the most important elements in nearly all modern electronics and bioelectronics. In particular, field-effect transistors (FETs, **Fig. 2.2**) are widely used as they have been extensively studied due to their importance in the operation of integrated circuits. In the regular planar configuration, a semiconductor substrate is connected to a source (S), drain (D), and gate (G) electrodes. The gate electrode is separated from the substrate using a dielectric insulator. When a voltage potential is applied between the source and drain electrodes, the current will flow through the semiconductor channel. The current through the semiconductor will be proportional to the potential applied to the gate. Depending on the doping of the semiconductor substrate, a transistor can operate in enhancement or depletion mode. For an ideal transistor in enhancement mode, no current flow will occur at gate potential below the specific threshold and beyond the threshold potential, current will rise linearly until saturation current is reached. The behavior is reversed in a depletion mode transistor. The ratio of current change to the applied potential in a transistor is defined as transconductance g_m and can be a direct measure of its sensitivity.

The external connection to the gate is typically omitted for bioelectronic sensing applications, as the gate potential variation is generated directly by the dynamic processes from charged species or cells. Notably, for FET-based detection of binding of unbinding of charged species (such as protein marker), the sensitivity is limited to the characteristic Debye screening length:

$$\lambda_D = \frac{1}{\sqrt{4\pi l_B \sum_i \rho_i z_i^2}} \qquad Equation\ (2.5)$$

Where l_b is the Bjerrum length, Σ_i is the sum of present ion species with concentrations ρ_i and valence z_i. The Debye screening length can be used to approximate sensitivity range and is on the order of <1 nm in concentrated electrolytes[8]. Specificity and sensitivity of FETs in bioelectronic situations can be improved by using surface modifications with biomolecules capable of molecular recognition[65]. The advantage of FET devices over metal-based capacitive and faradaic electrodes is that device current flows in a closed-circuit, so that the potential issues with the electrode impedance, electrode corrosion or biological invasiveness can be minimized. This also allows FET devices to achieve faster response times[66] and lower SNR[67] when compared to single terminal electrodes.

The second type of transistor – electrolyte gated transistor – has gained increased popularity in bioelectronics over the recent years due to its high transconductance, biocompatibility, and processing versatility. In this configuration, the semiconducting substrate and gate are replaced with porous structures which can be interpenetrated by ions increasing or decreasing current flow through the channel. The most popular materials for gating channels are made of organic conductors and semiconductors forming a class of organic electrochemical transistors (OECTs, **Fig. 2.2**). Transconductance in OECTs can be described using Bernards model[68,69] and the equation:

$$g_m = \left(\frac{W}{L}\right) d\mu C^*(V_{th} - V_G) \qquad Equation\ (2.6)$$

which accounts for channel geometry: width W, length L, and thickness d; charge carrier mobility μ; capacitance per unit volume of a channel C^*; gate voltage V_G and specific threshold voltage V_{th}.

Capacitance in organic materials can be widely tuned; therefore, characteristic of OECTs is their exceptionally high transconductance[70]. OECTs can be used for ion-selective sensing with the introduction of proper membranes[71]. A closely related topic to OECTs is a class of hydrogel-based devices called organic electronic ion pumps (OEIPs) which can be used for ion delivery[72-74] and as drug delivery platforms[69,75,76]. Detailed discussion on OECTs and OEIPs are available in the recent reviews focusing on these subjects[77,78].

2.4.6 Stimulation with Molecular and Optical Signals

Biological systems utilize a range of small molecules and peptides for intracellular or organism-wide signaling. Bioelectronic devices can be used to deliver signaling molecules and pharmaceuticals directly into tissue, increasing their availability and potency[79]. Microfluidic channels present one promising approach to this application. The drawback of this approach is that it requires the integration of secondary elements, such as pressure sources, to function properly. Although some micropumps with low power consumption have been devised[80,81], there is still much progress to be made in this area. An alternative approach is to design materials that can dispense drugs from inside their structure on-demand such as the aforementioned OEIPs. However, volumetric materials have limited cargo capacity, and molecules are usually delivered through diffusion and positive pressure, which lowers delivery speed and efficiency.

Apart from some small organisms, most cells and tissues cannot be directly stimulated using light. Two approaches exist to make ordinary cells susceptible to optical signals: optogenetics and optopharmacology. Optogenetics relies on genetic modification of target cells to display specially engineered optically responsive ion channels[82], while optopharmacology relies on delivery of photoresponsive drugs which, while inactive in their native form, can be distributed

evenly among cells and will become active only upon illumination[83]. Delivery of light to the stimulation location can be accomplished using waveguides or microlight sources such as upconverting materials, or micro-LEDs[84]. Efficiency of light delivery can be calculated using the equation:

$$I = P_S \cdot \eta_{coupling} \cdot \eta_{scattering} \cdot \Phi_{geometry} \qquad Equation\ (2.7)$$

where P_s is the output power of the source, η factors are coupling and scattering efficiency, and Φ is the geometric factor of the light interface[85]. The design of materials that can be used as waveguides focuses on maximizing coupling and scattering efficiency. Furthermore, for microlight sources, increasing the light power output without excess resistive heating is a challenge. Additionally, geometric factors can be taken to account, and directional light sources can be devised that focus their emission on the limited angular range and allow for efficient and highly localized stimulation. Because those optical systems require genetic modification or drug delivery for their functioning it is common to integrate them into single optofluidic system[86].

2.4.7 Transduction of Mechanical Signals

Nearly all biological systems have been observed to be sensitive to mechanical stimulation. Mechanical stimuli can be transduced through surface receptors and mechanosensitive ion channels or else directly detected by the cytoskeleton[87]. Mechanotransduction is an important mechanism that can be used for bioelectronics since it can greatly influence cell functions and their ultimate fate[88]. For example, mechanical obstacles or stimulation can significantly impair growth and myelination of oligodendrocytes[89]. Historically, studies have focused on the impact of bulk mechanical properties of extracellular matrix, namely its stiffness. More recently, the effects of

the presence of static curvature[90] have also drawn interest. Materials with gradients of mechanostatic interactions, tuneable stiffness, and active curvature actuation on the nanoscale are highly sought after.

2.5 Mechanical Match and Mismatch

Biology sets several constraints on the design of bioelectronics, which makes integrating biological and artificial systems especially challenging. One of the most important considerations is the mechanical matching across the interface. The most widely used metric of stiffness is the Young's modulus, which relates the stress and strain of a linearly elastic material. While cells themselves are in fact viscoelastic, and thus excluded from this definition, the most useful devices for biointerfaces with soft biological tissues have Young's moduli in the range of 0.1 – 50 kPa, with neural tissue and skeletal muscle targets on the lower and upper end, respectively[91]. In contrast, most of the substrates used in traditional electronic devices have Young's moduli in the range of 100 MPa to 10 GPa. It has been shown that mechanical mismatch can lead to rejection of the interface by causing an inflammatory response in tissues[92,93] or merely being a nuisance for an organism and limiting its motoric activities[94]. Other reports show that material stiffness affects the complex behavior of surrounding cells such as differentiation and adhesion[91]. As has been discussed in recent specialized reviews on this issue[92,95], this knowledge is of critical importance to the realization of neural interfaces for computer-brain communication[96] and deep brain stimulation for the restoration of motor functions[97]. The brain is highly reactive, and even slight insertion trauma caused by stiffness mismatch between the tissue and the probe can cause activation of microglia and macrophages[92]. In effect, this acute inflammation can turn into chronic inflammation, which will cause degradation of the interface or the device itself. Rejection of the

implant or loss of its integrity renders the device inoperative and would require extraction, treatment of damages, and reinsertion of new probes, complicating the treatment and significantly increasing side-effects. It is therefore critical to achieve mechanical matching in order to form stable biointerfaces.

Multiple solutions for improving mechanical matching have been devised with the most straightforward solution being reduction of dimensionality of materials and reduction of the size of their constituents to the microscale and nanoscale[98]. This approach allows for a lower bending stiffness and to realize flexible and stretchable biointerfaces with classic electronic materials such as silicon (Si) and gold (Au)[99]. While mechanical properties are improved, such materials are still far more rigid than biological tissues and may compromise the stability of a biointerface. The search for materials with intrinsically matching mechanical properties has arrived at organic conductors and semiconductors as suitable candidates, with the highest promise coming from their hydrogel formulations thanks to their high water content, which allows for transfer of ions and dissolved gases. However, significant efforts are still needed to improve the electronic and optoelectronic functions in these organic materials.

Another critical aspect of mechanical matching is planning for the geometry of the interface. Biological materials generally have rough surfaces which leave a gap when put against flat materials, such as thin inorganic layers. Intrinsically rough materials such as nanostructures and carbon-based materials tend to perform better in this area[100]. When possible, biocompatible adhesives could be employed to fill the gap[101].

An alternative approach is to use hard-soft composites, which may ultimately solve the compromise between the electronic/optoelectronic functions and the mechanical properties needed for future biointerfaces. The hard-soft composites contain hard materials, which bear some useful

functionality, and soft matrix materials that can act both to improve the mechanical match and to potentially offer some biological functionality themselves. This allows for a wide variety of hard materials, which include materials such as Si and noble metals that are already ubiquitous in electronics, to be incorporated into biological tissues while attenuating the immune response. By carefully tailoring soft carrier materials to desired applications, hard-soft composites can be employed to *in vitro* cultures, on the skin of test subjects, or even implanted into organisms.

2.6 Reactivity of the Materials

Biointerfaces are formed in environments that inherently can be volatile and difficult to design and control for. Cells and tissues present on the materials possess a wide range of pH values, varying concentration of ions, and a spectrum of molecules and biomolecules – most of them chemically active. For achieving chemically stable and electrically functional devices over a desired time frame, it is important to keep in mind the chemical processes that it undergoes during its operation. Depending on the application, this can be undesired or desired. Careful investigation of chemical properties of the material allows for proper tuning of its stability.

2.6.1 Reactivity of the Components

Bioelectronic components might be either unintentionally or intentionally reactive. Unintentional reactivity leads mostly to deterioration of the materials causing it to lose performance over time due to mechanical damage, chemical disintegration, or loss of electrical or electrochemical properties. Constituents released into the environment might also in turn react with biological structures. Unintentional reactivity can be minimized with the use of materials that are inert to

their environment or chemical passivation of their surfaces. Some materials, such as faradaic electrodes, require chemical reactions to perform their functions. Such materials will unavoidably interact chemically with the environment. This must be taken into account when designing the system. In this case, utilizing reversible redox reactions can substantially increase the lifetime of the interface. Other intentionally reactive materials are ones that undergo controlled disintegration and can be used for the applications in transient electronics – devices which do not require extraction as they safely decompose in biological conditions. Finally, reactive materials can be used to adapt to their environment or have self-healing properties. Achieving these properties requires careful study of chemistries present in the environment and the device alike.

2.6.2 Consequences of Reactivity

Reactive components will inevitably interact with their environment. Almost all devices undergo some deterioration and releases in a small number of their constituents, but for some transient applications in modulation or sensing, *e.g.*, intermediate heart pacing or drug delivery, long term stability might be undesired. An ideal device could be implanted and, after fulfilling its duty, decompose and be safely metabolized by an organism[102]. This approach would make a follow-up surgical extraction of the device unnecessary. For both cases it is important to ensure that the release of the material or its constituents into the system will not impair the development of cells and tissues or alter the cellular process in a harmful way[103,104].

Important classes of reactive materials are those capable of self-repair and self-healing. Inspired by biological systems, these materials are able to self-regenerate from mechanical and chemical damages and regain their original properties[90]. Self-healing properties arise from the insightful engineering of the chemical interactions present in the structure of materials. They can

be realized using either reversible reactions or through the implementation of mechanisms or catalysts that can be activated by damages to help the material recover its integrity[13]. In turn, these can be engineered using independent chemistries or processes working in concert with the biological environment. Self-healing properties are essential for conductive materials, which require constant electrical continuity for their uninterrupted operation. It is expected that the long-term integration of bioelectronics will require some type of regeneration ability in such materials.

2.7 Biomimetic Design in Bioelectronics

The biological systems evolved over millions of years to specialize in their respective functions, and while our understanding of such processes constantly improves, it does not seem that we would be able to alter or replace biological structures to make them fit our needs in the near future. On the other hand, we can actively strive to make our electronics more nature-like by intentionally introducing biomimetic structures and design paradigms. Our ultimate goal is to achieve minimally invasive integration through the application of Nature-inspired blueprints and materials. The more similar the structures and less mismatch between their properties - the more biocompatible they become and are less prone to rejection by the biological structure[105]. Proper structural and functional matching would maximize the efficiency of interactions and allow new bioelectronic devices to achieve viability levels that can enable the more delicate and precise study of the physiological process, and which will be adapted to future therapeutical applications as well.

To begin thinking about biomimetic design, we have to consider the specific lessons we can take from Nature on designing and building complex structures. (**Fig. 2.3**) The most important lesson is that biological systems are defined up to an atomic level. Almost every biological structure derives its function from the specific arrangement on the molecular scale. From nucleic

acids, through ribosomes, to proteins and protein complexes – a single change can often be introduced that would completely disturb the system. It is, of course, the principle of evolution that the accumulation of changes can enable new functions, but this observation only strengthens the importance of the relationship between the structure and function[106]. Even for the large structures with mineral deposits, such as bone tissue, the material's distribution is precisely controlled, enabling the properties difficult to achieve using heterogeneous materials. Such properties are enabled by the second principle of biological design, which is the formation of complex three-dimensional assemblies. Structures such as the brain cortex or renal pyramids in kidneys can only perform their function thanks to integrating multiple different cells and forming the appropriate spatial arrangement. Further, observing the lower dimensional biological structures, such as nerve bundles, will reveal the next biomimetic design principle – high-density packing and parallelization. For example, research-grade neural recording and stimulation electronics currently enable hundreds of channels[107,108], and translational efforts utilizing multiple shanks can bring the total number of interfacing electrodes to thousands[20], they remain outmatched by the human optical nerves, which are made of more than a million neuron fibers[109]. Therefore, to enable high-throughput and fidelity in biomimetic electronic applications, we must learn to form and scale-up our designs.

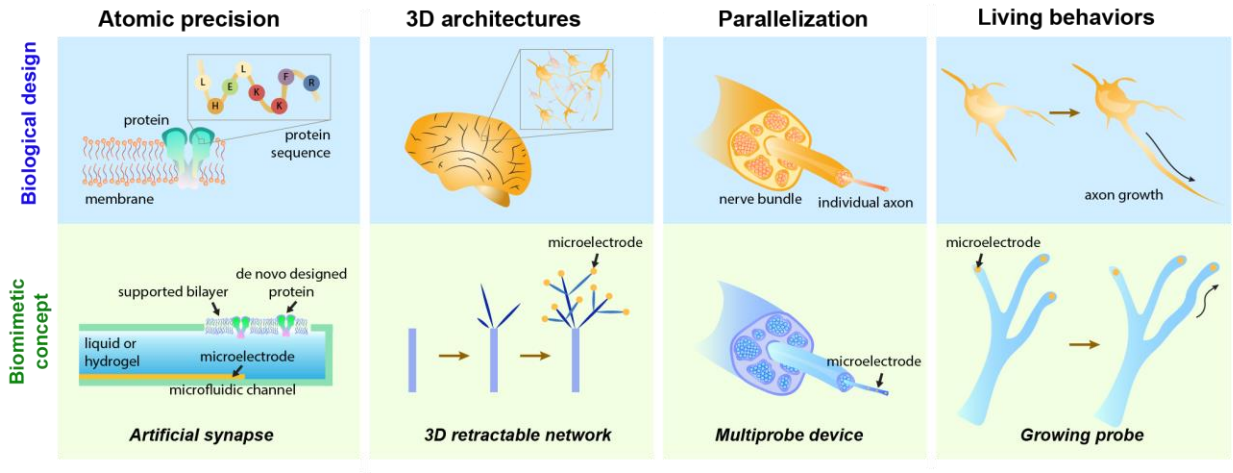

Figure 2.3 Characteristics of biological design.

Atomic-level definition of functions is a primary concept in natural systems. Precise structural definition later translates on to the organization at higher levels of hierarchy. The biological structures are, in general, three-dimensional and highly paralleled for increased efficiency. The final indispensable recognition is that biological systems demonstrate 'living behaviors,' which creates developmental, functional, and adaptational advantages over inanimate materials and systems. Bottom row shows concepts of artificial biomimetic structures and devices.

For the complete picture of the biological systems, we cannot forget about the plethora of living behaviors that they display. Growth, replication, motility, regeneration, and self-destruction are all processes that can be replicated in the biomimetic design. Many living behaviors are possible thanks to energy transfer mechanisms, e.g., adenosine triphosphate (ATP) dissociation can drive organelles' movement within the cell or rotation of flagellum for the entire cell propulsion. Driving such processes requires precise control over progressing chemical reactions both in time and space. In our biomimetic designs, we are yet to master the creation of structures operating in this far from equilibrium energy landscape.

Applying biomimetic design concepts can make our materials and electronic systems life-like and improve their compatibility with natural structures. The following sections will summarize current approaches and directions in electronics research inspired by the biological design paradigms.

2.7.1 Approaching the Biomimetic Design

Bioelectronics devices can take inspiration from biological structures in their physical properties, form, function, formation mechanism. (**Fig 2.4**) The most trivial biomimetic devices aim to approach biological structures' properties, especially their mechanical and (bio)chemical behavior. Biological structures show many desirable properties such as high tensile strength with low stiffness compared to classical man-made materials, but they also prefer to form interactions with materials showing such similarity. Mechanical matching and biochemical affinity between tissues and probes have decreased immune response and stabilized their interaction[110]. Additionally, synergy in both the spatial and temporal scales between the devices and the biological targets can improve stimulation and recording performance[111-114]. While progress in materials science closes to create perfectly matched materials, the gap can be further bridged when devices take the form of biological structures. On this front, matching the size and shape helps in the device integration.

Another aspect of biomimicry is the functional operation of the devices. While electronic signals are transferred mainly by the movement of electrons, the bioelectronic cues are delivered using ions and small molecules. Additionally, in biological systems, the information is rarely processed with binary logic and linear functions. Especially, the electrical activity of neurons is characterized by a high degree of nonlinearity and complex activation behaviors which can be

mimicked with nature-like circuits[115]. It can be expected that in the future, our bioelectronic devices will intrinsically adapt to the cellular forms of communication instead of relying heavily on digital signal processing and delivery, and achieve so through a closed loop system. Finally, we can take inspiration from the way natural structures are formed. For example, synthesis and assembly of biological structures are initially encoded in the cell genetic material. The biological morphogenesis is usually driven by self-assembly or directed by other endogenous fields (such as electrical or mechanical cues), which gives rise to order on all scales of the structural hierarchy[116]. The ideal goal of bioelectronics research efforts should be to bring together the advantages of all four corners of the biomimetic design. (**Fig. 2.4**) This would ultimately establish a seamless biointerfaces, as the biomimetic principles are applied to the materials or devices down to the subcellular or even molecular levels; the boundary between biology and electronics are blurred at this length scale.

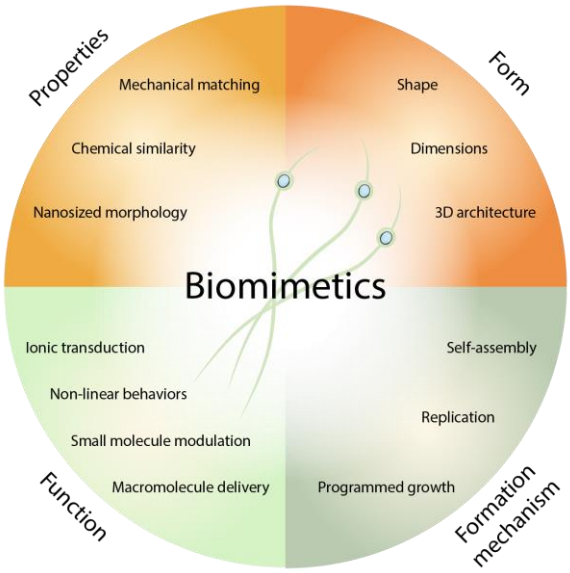

Figure 2.4 Principles of biomimetic design.

The systematic approach helps to identify promising biomimetic approaches. The four corners of biomimetic design: properties, form, function, and formation mechanism allow for planning which aspects of biomimicry can be employed in the system.

The assembly of the biomimetic devices requires fabrication methods that allow to define the structures with unprecedented precision. Advances in photolithographic fabrication allow to shape materials on the nanoscale and enable fabrication of biomimetic structures, but efforts are still primarily focused on 2D thin-film processes developed for silicon electronics, with limited strategies enabling 3D structures[117]. Recent progress in stereolithography is promising for the fabrication of volumetric biomimetic structures. However, cost and limited scalability remain a challenge. 3D printing methods, especially those enabling printing with multiple functional materials at the same time[118], have the potential to drive forward the effort in the fabrication of biomimetic structures[119]. 3D printing has an important advantage over lithography in such it streamlines the process from design to fabrication, which is advantageous when multiple iterations

can be used to evolve initial blueprints. Another technique for large-scale synthesis of thin and flexible electronics is the thermal drawing of multi-material fibers[120]. Assemblies of such fibers that resemble nerve bundles would allow highly multiplexed stimulation and recording while keeping the device's cross-sectional profile small. Finally, the programming of synthesis and assembly of bioelectronic devices in the form of genetic material or other methods would be a culmination of the biomimetic design. While our understanding of developmental biology is still limited and reprogramming the growth and function of organisms remains elusive, the first fundamental demonstrations of in vivo assembly of electronic material suggest the considerable potential of this research direction[121].

2.7.2 Biomimetic Design in the Current Literature

One of the first demonstrations of biomimetic electronics came in the form of materials mimicking extracellular matrix. The cells were grown onto nanoelectronic scaffolds in such approaches, creating systems with similar three-dimensional connectivity and mechanical properties as native tissues[122]. Biomimetic properties were achieved through the integration of nanostructured electronics and flexible polymers. Recently, the nanoelectronics scaffolds enabled complex extracellular recordings from cardiac spheroid organoids[123]. Further investigation into flexible biomimetic electronics allowed the creation of syringe-injectable electronics, expanding to the large volume and filling in internal cavities in an adaptable manner[124,125]. Eventually, the flexible electronics took upon the form of biological structures, and probes with neuron-like shapes were used for recording and stimulation[126]. Thanks to the matching of shape, size, and mechanical properties of subcellular features, unprecedented compatibility with biological structures was

achieved with minimal inflammation and loss in recording quality over the curse of 3 months, demonstrating the advantages of biomimicry in terms of form and properties.

In another recent study, the concept of morphing electronics was introduced to enable the compatibility of devices with growing tissues and organisms[127]. Stimulation electrodes were made from viscoplastic materials enabling adaptation of electrode shape to the growing sciatic nerve. The morphing electrode significantly improved integration and had a less negative impact on the nerve growth compared with the stiff cuff electrodes. While bioelectronics devices cannot genuinely grow just yet, this research shows how beneficial is the development of adaptable bioelectronic circuits and the incorporation of living-like behaviors.

An interesting concept in recent research is the creation of living bioelectronics, a subtype of living materials[128], which relies on augmenting normal cells and tissues with classically bioelectronics materials. It was shown that when cells internalize photoresponsive nanodevices[129], the optical stimulation can be used to perform nongenetic electrical interrogation of cells and cellular assemblies with subcellular resolution[130]. In one such study, the cells were merged with semiconductor nanowires forming hybrid composite cells that allowed probing of coupling between myofibroblasts and cardiomyocytes[131]. Living bioelectronic systems have the advantage of being part of a cell body that can grow and form junctions with native tissues allowing biocompatible implantation and integration. While *in vivo* demonstrations are yet to be shown, there is a vast potential for studying such hybrid systems, especially if in situ synthesis of bioelectric materials and replication living bioelectronics was achieved.

Genetically targeted assembly of bioelectronics is one of the most intriguing demonstrations shown in recent years[121]. In this work, the neurons were transfected to express ascorbate peroxidase Apex2 catalytic enzyme, which allowed to deposit electrically conductive

polyaniline directly onto cell membranes. With the application of additional additives, this approach allowed activation or inhibition of specific neuronal cells in vivo and altering motor functions of *Caenorhabditis elegans.* Encoding synthesis of bioelectronic materials directly into the genetic code may allow the highest level of biointegration, as well as enable other living behaviors (e.g., growth) and enable access to the final corner of biomimicry – formation mechanism.

2.8 Summary

Understanding fundamental principles of bioelectronic interfaces, situated at the intersection of physics, chemistry, and biology, allows us to draw general directions in which we can pursue material discovery and device designs for their application in future electroceutical therapies. Moreover, the inclusion of biomimetic design principles can enable the creation of electroceuticals that form seamless interfaces with cells and tissues. It is my belief that bioelectronics will develop into a significant branch of medical and information technologies in a not-so-distant future, once chronic machine-brain interfaces become safe and commonplace.

2.9 Bibliography

1 Moffa, A. H. *et al.* Efficacy and acceptability of transcranial direct current stimulation (tDCS) for major depressive disorder: An individual patient data meta-analysis. *Progress in Neuro-Psychopharmacology and Biological Psychiatry* **99**, doi:10.1016/j.pnpbp.2019.109836 (2020).

2 Dai, X. C., Hong, G. S., Gao, T. & Lieber, C. M. Mesh Nanoelectronics: Seamless Integration of Electronics with Tissues. *Accounts of Chemical Research* **51**, 309-318, doi:10.1021/acs.accounts.7b00547 (2018).

3 Fu, T. M., Hong, G. S., Viveros, R. D., Zhou, T. & Lieber, C. M. Highly scalable multichannel mesh electronics for stable chronic brain electrophysiology. *Proceedings of the National Academy of Sciences of the United States of America* **114**, E10046-E10055, doi:10.1073/pnas.1717695114 (2017).

4 Fu, T. M. *et al.* Stable long-term chronic brain mapping at the single-neuron level. *Nature Methods* **13**, 875-+, doi:10.1038/nmeth.3969 (2016).

5 Hong, G. S. *et al.* Syringe Injectable Electronics: Precise Targeted Delivery with Quantitative Input/Output Connectivity. *Nano Letters* **15**, 6979-6984, doi:10.1021/acs.nanolett.5b02987 (2015).

6 Hong, G. S. *et al.* A method for single-neuron chronic recording from the retina in awake mice. *Science* **360**, 1447-+, doi:10.1126/science.aas9160 (2018).

7 Hong, G. S. & Lieber, C. M. Novel electrode technologies for neural recordings. *Nature Reviews Neuroscience* **20**, 330-345, doi:10.1038/s41583-019-0140-6 (2019).

8 Jiang, Y. *et al.* Rational design of silicon structures for optically controlled multiscale biointerfaces. *Nature Biomedical Engineering* **2**, 508-521, doi:10.1038/s41551-018-0230-1 (2018).

9 Ray, T. R. *et al.* Bio-Integrated Wearable Systems: A Comprehensive Review. *Chem Rev* **119**, 5461-5533, doi:10.1021/acs.chemrev.8b00573 (2019).

10 Won, S. M. *et al.* Recent Advances in Materials, Devices, and Systems for Neural Interfaces. *Adv Mater* **30**, e1800534, doi:10.1002/adma.201800534 (2018).

11 Chen, R., Canales, A. & Anikeeva, P. Neural recording and modulation technologies. *Nature Reviews Materials* **2**, 1-16, doi:10.1038/natrevmats.2016.93 (2017).

12 Chortos, A., Liu, J. & Bao, Z. Pursuing prosthetic electronic skin. *Nature Materials* **15**, 937-950, doi:10.1038/nmat4671 (2016).

13 Someya, T., Bao, Z. & Malliaras, G. G. The rise of plastic bioelectronics. *Nature* **540**, 379-385, doi:10.1038/nature21004 (2016).

14 Li, Q. *et al.* Cyborg Organoids: Implantation of Nanoelectronics via Organogenesis for Tissue-Wide Electrophysiology. *Nano Letters* **19**, 5781-5789, doi:10.1021/acs.nanolett.9b02512 (2019).

15 Cohen-Karni, T., Timko, B. P., Weiss, L. E. & Lieber, C. M. Flexible electrical recording from cells using nanowire transistor arrays. *Proceedings of the National Academy of Sciences of the United States of America* **106**, 7309-7313, doi:10.1073/pnas.0902752106 (2009).

16 Duan, X. *et al.* Intracellular recordings of action potentials by an extracellular nanoscale field-effect transistor. *Nature Nanotechnology* **7**, 174-179, doi:10.1038/nnano.2011.223 (2012).

17 Tian, B. *et al.* Three-dimensional, flexible nanoscale field-effect transistors as localized bioprobes. *Science* **329**, 830-834, doi:10.1126/science.1192033 (2010).

18 Xiang, L., Chen, K., Yan, R., Li, W. & Xu, K. Single-molecule displacement mapping unveils nanoscale heterogeneities in intracellular diffusivity. *Nature Methods*, doi:10.1038/s41592-020-0793-0 (2020).

19 Phillips, R. & Quake, S. R. The Biological Frontier of Physics. *Physics Today* **59**, 38-43, doi:10.1063/1.2216960 (2006).

20 Musk, E. An Integrated Brain-Machine Interface Platform With Thousands of Channels. *Journal of Medical Internet Research* **21**, e16194-e16194, doi:10.2196/16194 (2019).

21 Drake, K. L., Wise, K. D., Farraye, J., Anderson, D. J. & BeMent, S. L. Performance of Planar Multisite Microprobes in Recording Extracellular Single-Unit Intracortical Activity. *IEEE Transactions on Biomedical Engineering* **35**, 719-732, doi:10.1109/10.7273 (1988).

22 Jones, K. E., Campbell, P. K. & Normann, R. A. A glass/silicon composite intracortical electrode array. *Annals of Biomedical Engineering* **20**, 423-437, doi:10.1007/BF02368134 (1992).

23 Maynard, E. M., Nordhausen, C. T. & Normann, R. A. The Utah Intracortical Electrode Array: A recording structure for potential brain-computer interfaces. *Electroencephalography and Clinical Neurophysiology* **102**, 228-239, doi:https://doi.org/10.1016/S0013-4694(96)95176-0 (1997).

24 Vetter, R. J., Williams, J. C., Hetke, J. F., Nunamaker, E. A. & Kipke, D. R. Chronic neural recording using silicon-substrate microelectrode arrays implanted in cerebral cortex. *IEEE Transactions on Biomedical Engineering* **51**, 896-904, doi:10.1109/TBME.2004.826680 (2004).

25 Wise, K. D. Silicon microsystems for neuroscience and neural prostheses. *IEEE Engineering in Medicine and Biology Magazine* **24**, 22-29, doi:10.1109/MEMB.2005.1511497 (2005).

26 Campbell, P. K., Jones, K. E., Huber, R. J., Horch, K. W. & Normann, R. A. A silicon-based, three-dimensional neural interface: manufacturing processes for an intracortical electrode array. *IEEE Transactions on Biomedical Engineering* **38**, 758-768, doi:10.1109/10.83588 (1991).

27 Spoendlin, H. & Schrott, A. Analysis of the human auditory nerve. *Hearing Research* **43**, 25-38, doi:10.1016/0378-5955(89)90056-7 (1989).

28 Jonas, J. B., Schmidt, A. M., Muller-Bergh, J. A., Schlotzer-Schrehardt, U. M. & Naumann, G. O. H. Human optic nerve fiber count and optic disc size. *Investigative Ophthalmology and Visual Science* **33**, 2012-2018 (1992).

29 Willett, F. R. *et al.* Hand Knob Area of Premotor Cortex Represents the Whole Body in a Compositional Way. *Cell* **181**, 396-409.e326, doi:https://doi.org/10.1016/j.cell.2020.02.043 (2020).

30 Eichenlaub, J.-B. *et al.* Replay of Learned Neural Firing Sequences during Rest in Human Motor Cortex. *Cell Reports* **31**, 107581, doi:https://doi.org/10.1016/j.celrep.2020.107581 (2020).

31 Obaid, A. *et al.* Massively parallel microwire arrays integrated with CMOS chips for neural recording. *Science Advances* **6**, eaay2789, doi:10.1126/sciadv.aay2789 (2020).

32 Zhang, Y. *et al.* Using an Engineered Galvanic Redox System to Generate Positive Surface Potentials that Promote Osteogenic Functions. *ACS Applied Materials & Interfaces* **10**, 15449-15460, doi:10.1021/acsami.8b02798 (2018).

33 Zhang, Y. *et al.* Battery-free, fully implantable optofluidic cuff system for wireless optogenetic and pharmacological neuromodulation of peripheral nerves. *Science Advances* **5**, 1-12, doi:10.1126/sciadv.aaw5296 (2019).

34 Chen, R., Romero, G., Christiansen, M. G., Mohr, A. & Anikeeva, P. Wireless magnetothermal deep brain stimulation. *Science* **347**, 1477-1480, doi:10.1126/science.1261821 (2015).

35 Rao, S. Y. *et al.* Remotely controlled chemomagnetic modulation of targeted neural circuits. *Nature Nanotechnology* **14**, 967-+, doi:10.1038/s41565-019-0521-z (2019).

36 Jiang, Y. *et al.* Nongenetic optical neuromodulation with silicon-based materials. *Nature Protocols* **14**, 1339-1376, doi:10.1038/s41596-019-0135-9 (2019).

37 Parameswaran, R. *et al.* Optical stimulation of cardiac cells with a polymer-supported silicon nanowire matrix. *Proc Natl Acad Sci USA* **116**, 413-421, doi:10.1073/pnas.1816428115 (2019).

38 Yoo, S., Hong, S., Choi, Y., Park, J. H. & Nam, Y. Photothermal inhibition of neural activity with near-infrared-sensitive nanotransducers. *ACS Nano* **8**, 8040-8049, doi:10.1021/nn5020775 (2014).

39 Carvalho-de-Souza, J. L., Pinto, B. I., Pepperberg, D. R. & Bezanilla, F. Optocapacitive Generation of Action Potentials by Microsecond Laser Pulses of Nanojoule Energy. *Biophysical Journal* **114**, 283-288, doi:10.1016/j.bpj.2017.11.018 (2018).

40 Carvalho-de-Souza, J. L. *et al.* Photosensitivity of neurons enabled by cell-targeted gold nanoparticles. *Neuron* **86**, 207-217, doi:10.1016/j.neuron.2015.02.033 (2015).

41 Jiang, Y. *et al.* Heterogeneous silicon mesostructures for lipid-supported bioelectric interfaces. *Nature Materials* **15**, 1023-1030, doi:10.1038/nmat4673 (2016).

42 Kubanek, J., Shukla, P., Das, A., Baccus, S. A. & Goodman, M. B. Ultrasound elicits behavioral responses through mechanical effects on neurons and ion channels in a simple nervous system. *Journal of Neuroscience* **38**, 3081-3091, doi:10.1523/JNEUROSCI.1458-17.2018 (2018).

43 Plonsey, R. & Barr, R. C. *Bioelectricity: a quantitative approach*. (Springer Science & Business Media, 2007).

44 Savtchenko, L. P., Poo, M. M. & Rusakov, D. A. Electrodiffusion phenomena in neuroscience: A neglected companion. *Nature Reviews Neuroscience* **18**, 598-612, doi:10.1038/nrn.2017.101 (2017).

45 Yuk, H., Lu, B. & Zhao, X. Hydrogel bioelectronics. *Chemical Society Reviews* **48**, 1642-1667, doi:10.1039/c8cs00595h (2019).

46 Sanjuan-Alberte, P., Alexander, M. R., Hague, R. J. M. & Rawson, F. J. Electrochemically stimulating developments in bioelectronic medicine. *Bioelectronic Medicine* **4**, 1-7, doi:10.1186/s42234-018-0001-z (2018).

47 Choi, C. *et al.* Achieving high energy density and high power density with pseudocapacitive materials. *Nature Reviews Materials* **5**, 5-19, doi:10.1038/s41578-019-0142-z (2020).

48 Ruff, A., Conzuelo, F. & Schuhmann, W. Bioelectrocatalysis as the basis for the design of enzyme-based biofuel cells and semi-artificial biophotoelectrodes. *Nature Catalysis* **3**, 214-224, doi:10.1038/s41929-019-0381-9 (2020).

49 Chen, H., Dong, F. & Minteer, S. D. The progress and outlook of bioelectrocatalysis for the production of chemicals, fuels and materials. *Nature Catalysis* **3**, 225-244, doi:10.1038/s41929-019-0408-2 (2020).

50 Rudolph, T. K. & Freeman, B. A. Transduction of Redox Signaling by Electrophile-Protein Reactions. *Science Signaling* **2**, re7-re7, doi:10.1126/scisignal.290re7 (2009).

51 Dickinson, B. C. & Chang, C. J. Chemistry and biology of reactive oxygen species in signaling or stress responses. *Nature Chemical Biology* **7**, 504-511, doi:10.1038/nchembio.607 (2011).

52 Burton, A. *et al.* Wireless, battery-free subdermally implantable photometry systems for chronic recording of neural dynamics. *Proc Natl Acad Sci U S A* **117**, 2835-2845, doi:10.1073/pnas.1920073117 (2020).

53 Lu, L. *et al.* Wireless optoelectronic photometers for monitoring neuronal dynamics in the deep brain. *Proc Natl Acad Sci U S A* **115**, E1374-E1383, doi:10.1073/pnas.1718721115 (2018).

54 Zhang, Z. & Yates, J. T. Band bending in semiconductors: Chemical and physical consequences at surfaces and interfaces. *Chemical Reviews* **112**, 5520-5551, doi:10.1021/cr3000626 (2012).

55 Vilan, A. & Cahen, D. Chemical Modification of Semiconductor Surfaces for Molecular Electronics. *Chemical Reviews* **117**, 4624-4666, doi:10.1021/acs.chemrev.6b00746 (2017).

56 Pankove, J. I. *Optical processes in semiconductors*. (Prentice-Hall, 1971).

57 Mayer, K. M. & Hafner, J. H. Localized surface plasmon resonance sensors. *Chem Rev* **111**, 3828-3857, doi:10.1021/cr100313v (2011).

58 Jauffred, L., Samadi, A., Klingberg, H., Bendix, P. M. & Oddershede, L. B. Plasmonic Heating of Nanostructures. *Chem Rev* **119**, 8087-8130, doi:10.1021/acs.chemrev.8b00738 (2019).

59 Donner, J. S., Thompson, S. A., Kreuzer, M. P., Baffou, G. & Quidant, R. Mapping intracellular temperature using green fluorescent protein. *Nano Lett* **12**, 2107-2111, doi:10.1021/nl300389y (2012).

60 Bai, T. & Gu, N. Micro/Nanoscale Thermometry for Cellular Thermal Sensing. *Small* **12**, 4590-4610, doi:10.1002/smll.201600665 (2016).

61 Dalby, M. J. *et al.* Nanomechanotransduction and interphase nuclear organization influence on genomic control. *Journal of Cellular Biochemistry* **102**, 1234-1244, doi:10.1002/jcb.21354 (2007).

62 Beard, P. Biomedical photoacoustic imaging. *Interface Focus* **1**, 602-631, doi:10.1098/rsfs.2011.0028 (2011).

63 Park, S., Frank, J. A. & Anikeeva, P. Silicon biointerfaces for all scales. *Nature Biomedical Engineering* **2**, 471-472, doi:10.1038/s41551-018-0268-0 (2018).

64 Dipalo, M. *et al.* Plasmonic meta-electrodes allow intracellular recordings at network level on high-density CMOS-multi-electrode arrays. *Nat Nanotechnol* **13**, 965-971, doi:10.1038/s41565-018-0222-z (2018).

65 Li, Q., Lu, N., Wang, L. & Fan, C. Advances in Nanowire Transistor-Based Biosensors. *Small Methods* **2**, 1700263, doi:10.1002/smtd.201700263 (2018).

66 Schöning, M. J. & Poghossian, A. Recent advances in biologically sensitive field-effect transistors (BioFETs). *Analyst* **127**, 1137-1151, doi:10.1039/B204444G (2002).

67 Fromherz, P., Offenhausser, A., Vetter, T. & Weis, J. A neuron-silicon junction: a Retzius cell of the leech on an insulated-gate field-effect transistor. *Science* **252**, 1290, doi:10.1126/science.1925540 (1991).

68 Bernards, D. A. & Malliaras, G. G. Steady-state and transient behavior of organic electrochemical transistors. *Advanced Functional Materials* **17**, 3538-3544, doi:10.1002/adfm.200601239 (2007).

69 Rivnay, J. *et al.* Organic electrochemical transistors. *Nature Reviews Materials* **3**, doi:10.1038/natrevmats.2017.86 (2018).

70 Khodagholy, D. *et al.* High transconductance organic electrochemical transistors. *Nature Communications* **4**, 1-6, doi:10.1038/ncomms3133 (2013).

71 Ghittorelli, M. *et al.* High-sensitivity ion detection at low voltages with current-driven organic electrochemical transistors. *Nature Communications* **9**, 1441, doi:10.1038/s41467-018-03932-3 (2018).

72 Jakešová, M. *et al.* Wireless organic electronic ion pumps driven by photovoltaics. *npj Flexible Electronics* **3**, doi:10.1038/s41528-019-0060-6 (2019).

73 Isaksson, J. *et al.* Electronic control of Ca2+ signalling in neuronal cells using an organic electronic ion pump. *Nature Materials* **6**, 673-679, doi:10.1038/nmat1963 (2007).

74 Williamson, A. *et al.* Controlling Epileptiform Activity with Organic Electronic Ion Pumps. *Advanced Materials* **27**, 3138-3144, doi:10.1002/adma.201500482 (2015).

75 Seitanidou, M., Blomgran, R., Pushpamithran, G., Berggren, M. & Simon, D. T. Modulating Inflammation in Monocytes Using Capillary Fiber Organic Electronic Ion Pumps. *Advanced Healthcare Materials* **8**, 1900813, doi:10.1002/adhm.201900813 (2019).

76 Jonsson, A. *et al.* Bioelectronic neural pixel: Chemical stimulation and electrical sensing at the same site. *Proceedings of the National Academy of Sciences* **113**, 9440, doi:10.1073/pnas.1604231113 (2016).

77 Berggren, M. *et al.* Ion Electron–Coupled Functionality in Materials and Devices Based on Conjugated Polymers. *Advanced Materials* **31**, 1805813, doi:10.1002/adma.201805813 (2019).

78 Arbring Sjöström, T. *et al.* A Decade of Iontronic Delivery Devices. *Advanced Materials Technologies* **3**, 1700360, doi:10.1002/admt.201700360 (2018).

79 Jonsson, A. *et al.* Therapy using implanted organic bioelectronics. *Science Advances* **1**, 1-6, doi:10.1126/sciadv.1500039 (2015).

80 Cobo, A., Sheybani, R. & Meng, E. MEMS: Enabled Drug Delivery Systems. *Advanced Healthcare Materials* **4**, 969-982, doi:10.1002/adhm.201400772 (2015).

81 Meng, E. & Hoang, T. MEMS-enabled implantable drug infusion pumps for laboratory animal research, preclinical, and clinical applications. *Advanced Drug Delivery Reviews* **64**, 1628-1638, doi:10.1016/j.addr.2012.08.006 (2012).

82 Boyden, E. S., Zhang, F., Bamberg, E., Nagel, G. & Deisseroth, K. Millisecond-timescale, genetically targeted optical control of neural activity. *Nature Neuroscience* **8**, 1263-1268, doi:10.1038/nn1525 (2005).

83 Levitz, J. *et al.* Dual optical control and mechanistic insights into photoswitchable group II and III metabotropic glutamate receptors. *Proceedings of the National Academy of Sciences of the United States of America* **114**, E3546-E3554, doi:10.1073/pnas.1619652114 (2017).

84 Delbeke, J., Hoffman, L., Mols, K., Braeken, D. & Prodanov, D. And then there was light: Perspectives of optogenetics for deep brain stimulation and neuromodulation. *Frontiers in Neuroscience* **11**, 1-20, doi:10.3389/fnins.2017.00663 (2017).

85 Seymour, J. P., Wu, F., Wise, K. D. & Yoon, E. State-of-the-art mems and microsystem tools for brain research. *Microsystems and Nanoengineering* **3**, 1-16, doi:10.1038/micronano.2016.66 (2017).

86 Qazi, R. *et al.* Wireless optofluidic brain probes for chronic neuropharmacology and photostimulation. *Nature Biomedical Engineering* **3**, 655-669, doi:10.1038/s41551-019-0432-1 (2019).

87 Wang, N. Review of cellular mechanotransduction. *Journal of Physics D: Applied Physics* **50**, doi:10.1088/1361-6463/aa6e18 (2017).

88 Li, Y., Xiao, Y. & Liu, C. The Horizon of Materiobiology: A Perspective on Material-Guided Cell Behaviors and Tissue Engineering. *Chemical Reviews* **117**, 4376-4421, doi:10.1021/acs.chemrev.6b00654 (2017).

89 Hernandez, M. *et al.* Mechanostimulation promotes nuclear and epigenetic changes in oligodendrocytes. *Journal of Neuroscience* **36**, 806-813, doi:10.1523/JNEUROSCI.2873-15.2016 (2016).

90 Zhao, W. *et al.* Nanoscale manipulation of membrane curvature for probing endocytosis in live cells. *Nature Nanotechnology* **12**, 750-756, doi:10.1038/nnano.2017.98 (2017).

91 Guimarães, C. F., Gasperini, L., Marques, A. P. & Reis, R. L. The stiffness of living tissues and its implications for tissue engineering. *Nature Reviews Materials*, 1-20, doi:10.1038/s41578-019-0169-1 (2020).

92 Lacour, S. P., Courtine, G. & Guck, J. Materials and technologies for soft implantable neuroprostheses. *Nature Reviews Materials* **1**, doi:10.1038/natrevmats.2016.63 (2016).

93 Salatino, J. W., Ludwig, K. A., Kozai, T. D. Y. & Purcell, E. K. Glial responses to implanted electrodes in the brain. *Nature Biomedical Engineering* **1**, 862-877, doi:10.1038/s41551-017-0154-1 (2017).

94 Copits, B. A., Pullen, M. Y. & Gereau, R. W. Spotlight on pain. *PAIN* **157**, 2424-2433, doi:10.1097/j.pain.0000000000000620 (2016).

95 Acarón Ledesma, H. *et al.* An atlas of nano-enabled neural interfaces. *Nature nanotechnology* **14**, 645-657, doi:10.1038/s41565-019-0487-x (2019).

96 McFarland, D. J. & Wolpaw, J. R. Brain-computer interfaces for communication and control. *Communications of the ACM* **54**, 60-66, doi:10.1145/1941487.1941506 (2011).

97 Micera, S., Caleo, M., Chisari, C., Hummel, F. C. & Pedrocchi, A. Advanced Neurotechnologies for the Restoration of Motor Function. *Neuron* **105**, 604-620, doi:10.1016/j.neuron.2020.01.039 (2020).

98 Rogers, J. A., Someya, T. & Huang, Y. Materials and mechanics for stretchable electronics. *Science* **327**, 1603-1607, doi:10.1126/science.1182383 (2010).

99 Xue, Z., Song, H., Rogers, J. A., Zhang, Y. & Huang, Y. Mechanically-Guided Structural Designs in Stretchable Inorganic Electronics. *Advanced Materials* **1902254**, 1-32, doi:10.1002/adma.201902254 (2019).

100 Zhu, C., Du, D. & Lin, Y. Graphene-like 2D nanomaterial-based biointerfaces for biosensing applications. *Biosensors and Bioelectronics* **89**, 43-55, doi:10.1016/j.bios.2016.06.045 (2017).

101 Taboada, G. M. *et al.* Overcoming the translational barriers of tissue adhesives. *Nature Reviews Materials*, doi:10.1038/s41578-019-0171-7 (2020).

102 Koo, J. *et al.* Wireless bioresorbable electronic system enables sustained nonpharmacological neuroregenerative therapy. *Nature Medicine* **24**, 1830-1836, doi:10.1038/s41591-018-0196-2 (2018).

103 Irimia-Vladu, M. "Green" electronics: biodegradable and biocompatible materials and devices for sustainable future. *Chem. Soc. Rev.* **43**, 588-610, doi:10.1039/C3CS60235D (2014).

104 Hoppe, A., Güldal, N. S. & Boccaccini, A. R. A review of the biological response to ionic dissolution products from bioactive glasses and glass-ceramics. *Biomaterials* **32**, 2757-2774, doi:10.1016/j.biomaterials.2011.01.004 (2011).

105 Guimarães, C. F., Gasperini, L., Marques, A. P. & Reis, R. L. The stiffness of living tissues and its implications for tissue engineering. *Nature Reviews Materials* **5**, 351-370, doi:10.1038/s41578-019-0169-1 (2020).

106 Thornton, J. M., Todd, A. E., Milburn, D., Borkakoti, N. & Orengo, C. A. From structure to function: Approaches and limitations. *Nature Structural Biology* **7**, 991-994, doi:10.1038/80784 (2000).

107 Zhang, M., Tang, Z., Liu, X. & Van der Spiegel, J. Electronic neural interfaces. *Nature Electronics* **3**, 191-200, doi:10.1038/s41928-020-0390-3 (2020).

108 Vazquez-Guardado, A., Yang, Y., Bandodkar, A. J. & Rogers, J. A. Recent advances in neurotechnologies with broad potential for neuroscience research. *Nat Neurosci* **23**, 1522-1536, doi:10.1038/s41593-020-00739-8 (2020).

109 Jonas, J. B., Schmidt, A. M., Muller-Bergh, J. A., Schlotzer-Schrehardt, U. M. & Naumann, G. O. Human optic nerve fiber count and optic disc size. *Invest Ophthalmol Vis Sci* **33**, 2012-2018 (1992).

110 Zhang, E. N. *et al.* Mechanically Matched Silicone Brain Implants Reduce Brain Foreign Body Response. *Advanced Materials Technologies* **6**, doi:ARTN 2000909 10.1002/admt.202000909 (2021).

111 Rastogi, S. K. *et al.* Three-dimensional fuzzy graphene ultra-microelectrodes for subcellular electrical recordings. *Nano Research* **13**, 1444-1452, doi:10.1007/s12274-020-2695-y (2020).

112 Wang, L. *et al.* Functionalized helical fibre bundles of carbon nanotubes as electrochemical sensors for long-term in vivo monitoring of multiple disease biomarkers. *Nat Biomed Eng* **4**, 159-171, doi:10.1038/s41551-019-0462-8 (2020).

113 Tang, J. *et al.* Nanowire arrays restore vision in blind mice. *Nat Commun* **9**, 786, doi:10.1038/s41467-018-03212-0 (2018).

114 Fang, Y. *et al.* Recent advances in bioelectronics chemistry. *Chemical Society Reviews*, doi:10.1039/d0cs00333f (2020).

115 Abu-Hassan, K. *et al.* Optimal solid state neurons. *Nat Commun* **10**, 5309, doi:10.1038/s41467-019-13177-3 (2019).

116 Rivnay, J., Wang, H., Fenno, L., Deisseroth, K. & Malliaras, G. G. Next-generation probes, particles, and proteins for neural interfacing. *Sci Adv* **3**, e1601649, doi:10.1126/sciadv.1601649 (2017).

117 Park, Y., Chung, T. S. & Rogers, J. A. Three dimensional bioelectronic interfaces to small-scale biological systems. *Current Opinion in Biotechnology* **72**, 1-7, doi:https://doi.org/10.1016/j.copbio.2021.07.023 (2021).

118 Skylar-Scott, M. A., Mueller, J., Visser, C. W. & Lewis, J. A. Voxelated soft matter via multimaterial multinozzle 3D printing. *Nature* **575**, 330-335, doi:10.1038/s41586-019-1736-8 (2019).

119 Zhu, Z., Ng, D. W. H., Park, H. S. & McAlpine, M. C. 3D-printed multifunctional materials enabled by artificial-intelligence-assisted fabrication technologies. *Nature Reviews Materials*, doi:10.1038/s41578-020-00235-2 (2020).

120 Canales, A., Park, S., Kilias, A. & Anikeeva, P. Multifunctional Fibers as Tools for Neuroscience and Neuroengineering. *Acc Chem Res* **51**, 829-838, doi:10.1021/acs.accounts.7b00558 (2018).

121 Liu, J. *et al.* Genetically targeted chemical assembly of functional materials in living cells, tissues, and animals. *Science* **367**, 1372-1376, doi:10.1126/science.aay4866 (2020).

122 Tian, B. *et al.* Macroporous nanowire nanoelectronic scaffolds for synthetic tissues. *Nat Mater* **11**, 986-994, doi:10.1038/nmat3404 (2012).

123 Kalmykov, A. *et al.* Organ-on-e-chip: Three-dimensional self-rolled biosensor array for electrical interrogations of human electrogenic spheroids. *Sci Adv* **5**, eaax0729, doi:10.1126/sciadv.aax0729 (2019).

124 Jia, L. *et al.* Syringe Injectable Electronics. *Nature Nanotechnology* **10**, 629-636, doi:10.1038/nnano.2015.115.Syringe (2015).

125 Lee, J. M. *et al.* Nanoenabled Direct Contact Interfacing of Syringe-Injectable Mesh Electronics. *Nano Lett* **19**, 5818-5826, doi:10.1021/acs.nanolett.9b03019 (2019).

126 Yang, X. *et al.* Bioinspired neuron-like electronics. *Nat Mater* **18**, 510-517, doi:10.1038/s41563-019-0292-9 (2019).

127 Liu, Y. *et al.* Morphing electronics enable neuromodulation in growing tissue. *Nat Biotechnol* **38**, 1031-1036, doi:10.1038/s41587-020-0495-2 (2020).

128 Nguyen, P. Q., Courchesne, N. D., Duraj-Thatte, A., Praveschotinunt, P. & Joshi, N. S. Engineered Living Materials: Prospects and Challenges for Using Biological Systems to Direct the Assembly of Smart Materials. *Adv Mater* **30**, e1704847, doi:10.1002/adma.201704847 (2018).

129 Zimmerman, J. F. *et al.* Cellular uptake and dynamics of unlabeled freestanding silicon nanowires. *Sci Adv* **2**, e1601039, doi:10.1126/sciadv.1601039 (2016).

130 Rotenberg, M. Y. *et al.* Silicon Nanowires for Intracellular Optical Interrogation with Subcellular Resolution. *Nano Lett* **20**, 1226-1232, doi:10.1021/acs.nanolett.9b04624 (2020).

131 Rotenberg, M. Y. *et al.* Living myofibroblast-silicon composites for probing electrical coupling in cardiac systems. *Proc Natl Acad Sci U S A* **116**, 22531-22539, doi:10.1073/pnas.1913651116 (2019).

Chapter 3

Hierarchical Porous Carbon Membranes: Synthesis, Characterization, and Device Microfabrication

This chapter was adapted from Fang, Y., Prominski, A., Rotenberg, M.Y. et al. "Micelle-enabled self-assembly of porous and monolithic carbon membranes for bioelectronic interfaces." Nature Nanotechnology, 16, 206–213 (2021).

3.1 Introduction

Multi-scale, nanostructured bioelectronics has been extensively studied for their application in bioelectronics[1-4]. Especially, electrical stimulation devices find numerous therapeutic applications for treating health disorders such as epilepsy and Parkinson's disease. To successfully translate future electroceutical therapies, we must understand the principles necessary to design and synthesize materials that can achieve mechanical and electrochemical compliance with living cells and tissues. It is essential to study soft and flexible materials that do not release toxic reactive species and form stable interfaces during permanent implantation[5].

Nanostructuring of many classic electrode materials has been shown to increase their softness and electrical performance[6]. Recently, carbon nanostructures have been explored as an electrode material for bioelectronics as an alternative to conductive polymers, such as poly(3,4,-ethylenedioxythiophee) polystyrene sulfonate (PEDOT:PSS), which provides excellent electrochemical and mechanical properties[6,7], but suffers from significant degradation during long-term operation. Many forms of carbon nanostructures, such as graphene and carbon nanotubes,

have been explored to reduce impedance and enhance the performance of electrodes in bioelectronic applications[8-10]. However, the methods presented so far utilize polymer adhesives to bind nanostructures to the support electrode materials. This approach has significant drawbacks such as reducing material porosity due to filling the pores with the binder, limitations in the binder conductivity, and possible dissociation of free-standing nanostructures from the composite, which might result in cytotoxicity *in vivo*[11,12]. Therefore, there is a need to develop nanostructured materials that are monolithic in their design that would provide high electrochemical performance while being resistant to degradation and achieving mechanical and chemical compliance in the persistent biointerfaces.

In this chapter, I will show how nanomaterial building blocks enable bottom-up construction of monolithic (*i.e.*, binder-free) carbon membranes and engineer their surface and internal porosity creating biointerface-forming electrode material with high mechanical and biological compliance. I will describe how micelle-enabled self-assembly was used to prepare a binder-free carbon-based material. I will then demonstrate how applying an 'upside-down' fabrication strategy makes such material compatible with standard photolithography processing and enables the creation of a super-capacitor-like flexible stimulation device. The electrochemical performance and stability of such a device have been thoroughly evaluated, and promising results make it a suitable candidate for application in electroceutical stimulation of cells, tissues, and organs.

3.2 Carbon Membrane Synthesis and Characterization

We adopted a bottom-up approach for the direct preparation of monolithic (*i.e.*, binder-free) and hierarchical carbon membranes. Nanoscale micelles were prepared through biphasic interaction between triblock copolymer Pluronic F127 (the primary organic template) and resin (the primary carbon precursor) in ethanol. The micelle solution was spin-coated onto the thermal oxide silicon wafer. Following solvent evaporation-induced self-assembly (**Fig. 3.1a(i))**, the packed micelles were carbonized completely into mesoporous carbon membranes. The carbonization process leads to the crosslinking of carbon precursors and the formation of monolithic membrane structures. The process yields highly ordered mesostructures with a uniform pore size of 7 nm, as shown in transmission electron microscopy (TEM) images (**Figs. 3.1b, 3.2**). Nitrogen adsorption/desorption measurements further confirmed a narrow pore size distribution (**Fig. 3.3**).

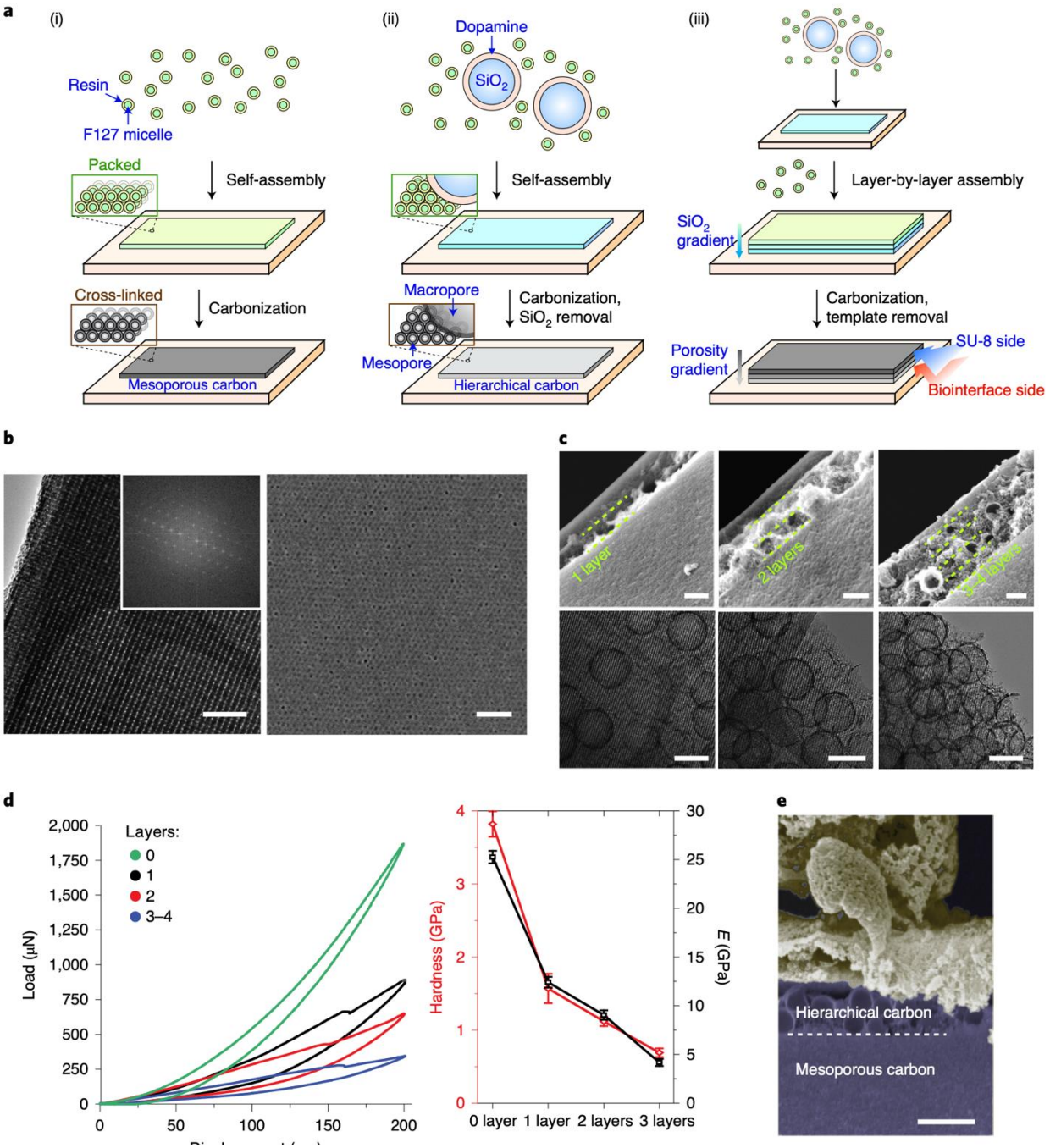

Figure 3.1 Hierarchical porous carbon synthesis and characterization.

(**a**) Illustration of the preparation of hierarchical porous carbon. (i) Synthesis of mesoporous carbon; (ii) synthesis of hierarchical carbon containing both mesopores and macropores; (iii) layer-by-layer assembly of carbon layers creating porosity gradient. The bottom layer of the carbon

membranes will become the side for biointerface formation after the device fabrication is completed (Fig. 3.6, and Fig. S6). (**b**) Transmission electron microscopy (TEM; left; scale bar, 100 nm), corresponding fast Fourier transform (FFT) diffraction pattern (left inset) and scanning electron microscopy (SEM) images (right; scale bar, 100 nm) of mesoporous materials showing the highly ordered mesostructures. (**c**) Cross-sectional view (upper panels) and associated top view (lower panels) of the hierarchical porous material. The hierarchical structures display two components: a bottom layer constructed from ordered mesoporous structure and layers of porous vesicles assembled into multiple layers. Scale bar, 200 nm. (**d**) Left: representative load versus displacement plots of the hierarchical porous thin film measured with a nano-indenter with various numbers of vesicle layers. The experiment was repeated four times. Right: Hardness and Young's modulus calculated from the load versus displacement plots (mean ± s.e.m., n = 4 independent measurements at various locations on each kind of sample). As the number of layers increases, the Young's modulus and hardness decrease, indicating that the film becomes softer. (**e**) Cross-sectional (false colour) SEM image of cardiomyocytes (CMs) cultured on the hierarchical porous film, implying that soft-hard hybrid interfaces can form between the film and cells. Scale bar, 500 nm. Results in **b**, **c**, and **e** are representative of five independent repeats.

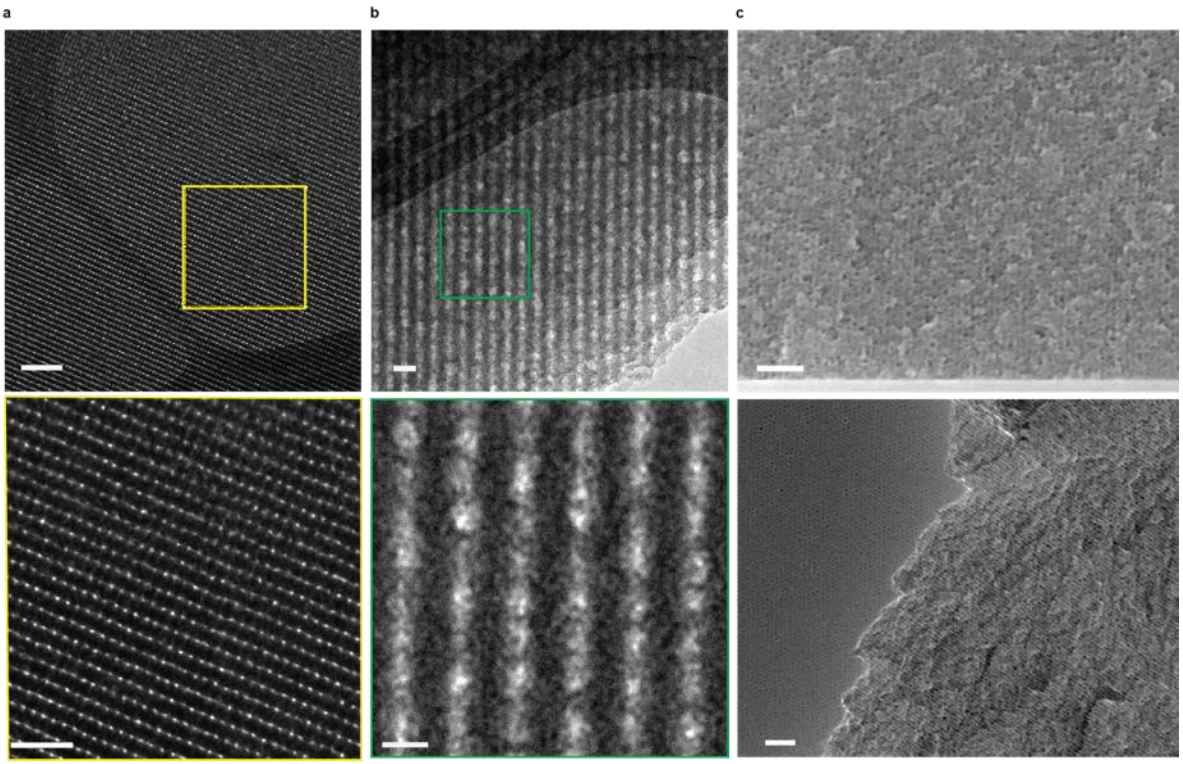

Figure 3.2 The mesoporous carbon membranes are highly ordered.

(**a**) TEM images (top; scale bar, 100 nm) with a close-up view of the region marked in yellow (bottom; scale bar, 50 nm), (**b**) High-resolution TEM images (top; scale bar, 20 nm) with a close-up view of the region marked in green (bottom; scale bar, 10 nm). (**c**) SEM images of pure mesoporous films (scale bar, 100 nm), showing the highly ordered mesostructures. The bottom image shows the edge and the sidewall of porous carbon membrane that was prepared by manual fracturing, showing an extension of ordered structures into the membrane interior. These images are representative of more than twenty fabricated mesoporous carbon membranes.

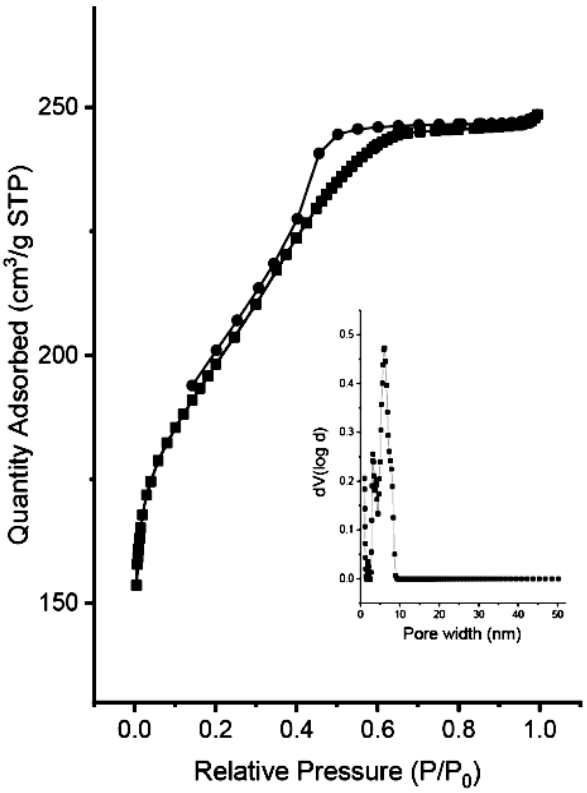

Figure 3.3 The mesoporous carbon has narrow pore size distribution.

Nitrogen adsorption and desorption curves of a mesoporous carbon film with corresponding pore size distribution (inset).

To reduce the stiffness of carbon films for improved compliance with soft biological interfaces, we introduced an inorganic template for the creation of a macroporous layer. Addition of ~200-300 nm-sized silica (SiO_2) spheres coated with dopamine into the Pluronic F127 and resin mixture during the membrane preparation (**Fig. 3.1a(ii)**) introduced macroporous (*i.e.*, with pore size >50 nm) structures (**Fig. 3.1c; Figs. 3.4 and 3.5**). The role of dopamine here is to stabilize dispersion of SiO_2 spheres in the micelle solution and to provide an additional carbon source. The hierarchical porous carbon preparation scheme permitted layer-by-layer assembly (**Fig. 1a(iii)**) of mesoporous

carbon by spin coating, where the thickness and porosity of individual layers can be controlled. Subsequent buffered hydrogen fluoride (HF) treatment removes the SiO_2 templates and releases the membrane (**Figs. 3.5a**). While the mesoporous film had a Young's modulus and hardness of 25.30 GPa and 3.82 GPa respectively, an addition of ~700 nm of the macroporous layer reduced these values to 4.20 GPa and 0.69 GPa (**Fig. 3.1d**). We hypothesized that electrochemical devices made from highly porous layers may deliver efficient capacitive currents that may be useful for biological modulation when biointerfaces are formed (**Fig. 3.1e**)[13].

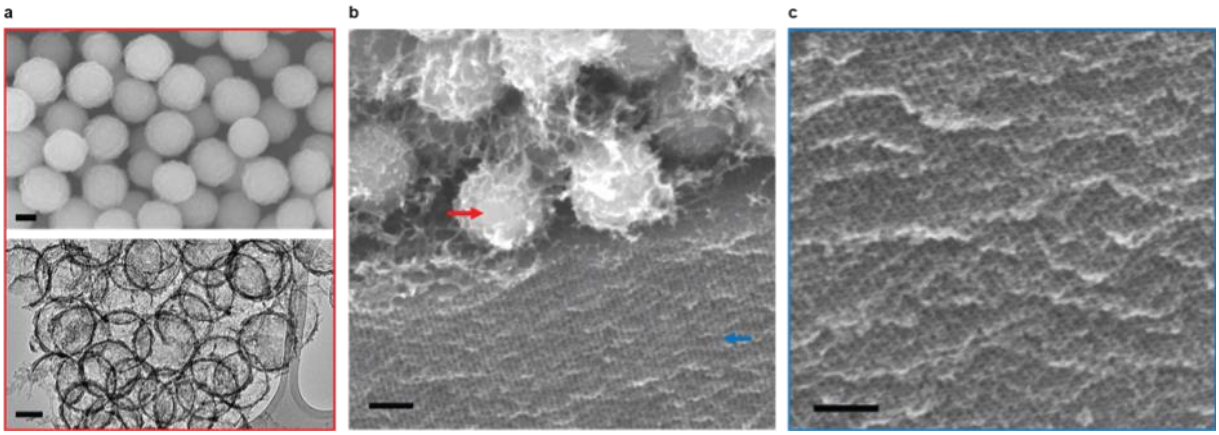

Figure 3.4 SiO_2 nanospheres can yield hierarchical carbon membranes.

(**a**) SEM images (upper panel) of the nanosphere building blocks used to construct the hierarchical porous film. SiO_2-C nanospheres (prepared by carbonization of SiO_2-dopamine core-shell structures) show diameters around 200-300 nm and are uniform. TEM images (lower panel) show the hollow spherical structures after the SiO_2 is etched. Scale bar, 100 nm. (**b**) SEM images showing the junction parts of the hierarchical porous film, in which a two-layer structure is found. The SiO_2 nanospheres were not etched in this SEM imaging. The nanosphere building blocks are indicated by the red arrow, and ordered mesoporous structures are indicated by the blue arrow. Scale bar, 100 nm. (**c**) SEM images of the mesostructures in the hierarchical porous film in (**b**).

Scale bar, 100 nm. SEM characterizations were independently repeated five times with similar results.

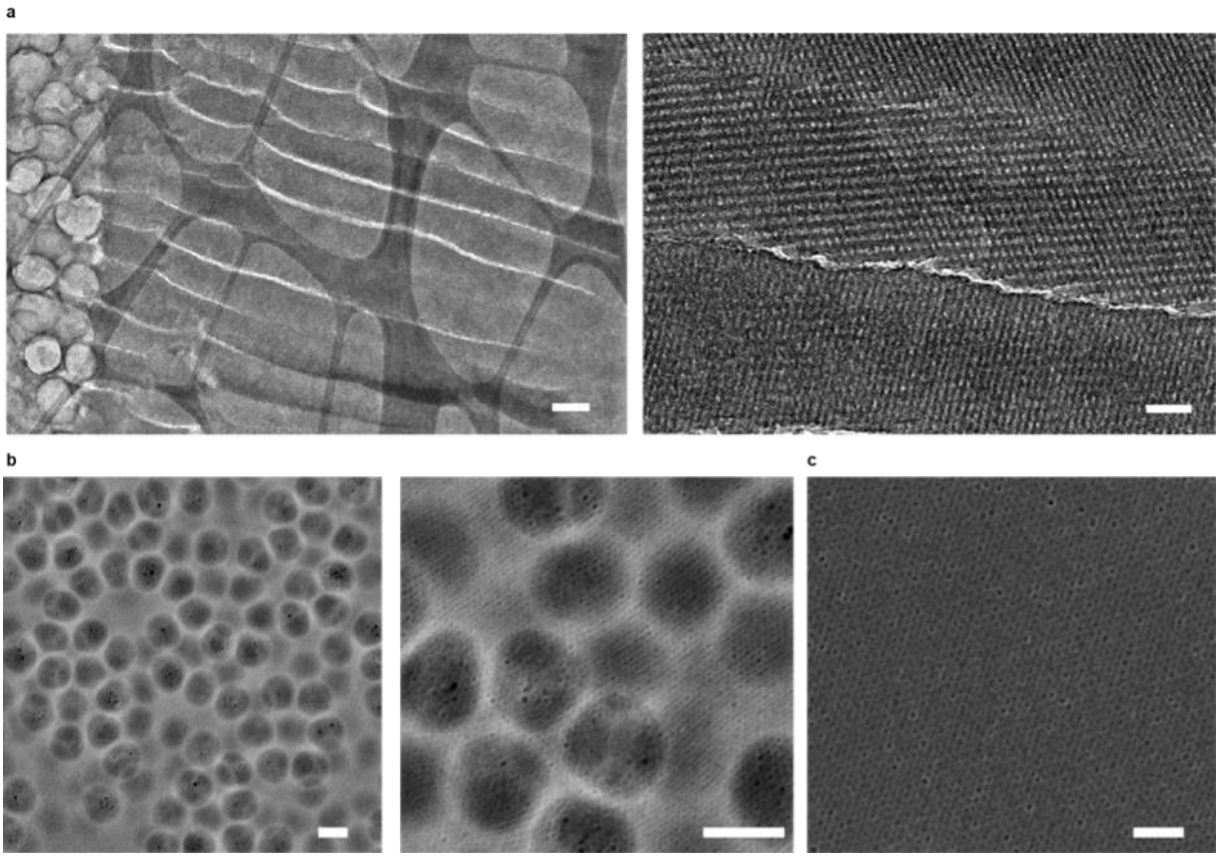

Figure 3.5 Hierarchical carbon membranes have sharp interfaces.

(**a**) TEM images of the cross-sectional view for the porous carbon film, showing a sharp interface between the hierarchical porous domain (*i.e.*, a domain containing both macroporous and mesoporous structures) and the purely mesoporous domain. The right image shows a Zoom-in view of the mesoporous domain. The cracks in both images are due to the microtome process. Scale bars, 200 nm (left) and 50 nm (right). (**b**) SEM images of the thin film from the macroporous side, showing that the ordered mesoporous structures are preserved. The darker areas reflect the macropores. Scale bar, 200 nm. (**c**) SEM image of the thin film from the mesoporous side, showing

a continuous mesoporous surface. Scale bar, 100 nm. **(a) – (c)** are representative field of views from more than three independent characterizations.

3.3 Device Fabrication and Characterization

We fabricated the device in a micro-supercapacitor-like design and over an SU-8 substrate. The SU-8 think film is chosen (**Figs. 3.6b, 3.7 and 3.8**) because it is photo-patternable, mechanically flexible, and chemically stable, and it has been commonly applied as a substrate or encapsulation material in flexible electronics[14,15]. Since SU-8 is incompatible with the carbonization conditions under high temperature, all photolithography processes have to be performed on the fully carbonized membrane. To avoid difficult substrate transfer steps, we followed an 'upside-down' fabrication method (**Figs. 2a, 3.8**), where the last step releases the device from the substrate and exposes the side for potential biointerfaces (*i.e.*, the original interface between the thermal oxide and the carbon, **Fig. 3.1a (iii)**). This fabrication technique requires that the softer layer (*i.e.*, the layer that forms direct biointerfaces) be on the bottom of the as-made membrane, hence the layer-by-layer assembly has to start from the layer that yields macropores. We used patterned metals layer as the mask for carbon etching as well as the electrical conductor to the carbon-based porous biointerfaces. By shrinking the pad size for interdigitated patterns, we were able to produce multichannel micro-supercapacitor-like devices (**Fig. 3.7b-c**). Raman spectra mapping showed carbon peaks at 1330 and 1590 cm^{-1} only in the patterned region, confirming the presence of carbon membrane (**Fig. 3.6c**).

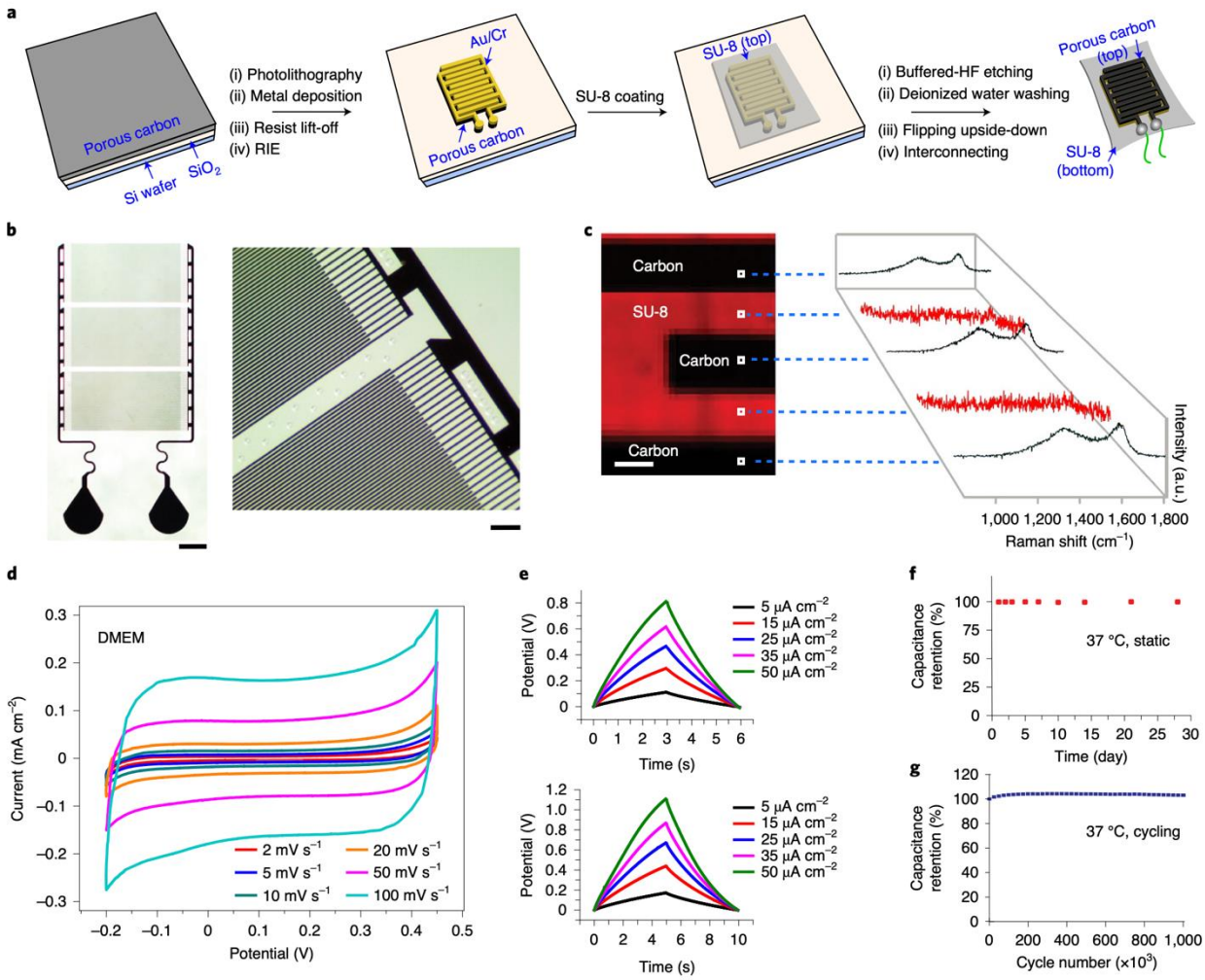

Figure 3.6 Device fabrication and characterization.

(**a**) Overview of a flexible device fabrication workflow. (**b**) An optical image (left; scale bar, 1 mm) and a close-up view of the hierarchical porous carbon micro-supercapacitor device (right; scale bar, 200 μm). Photographs are representative of more than twenty devices that were fabricated. (**c**) Raman spectra for the micro-supercapacitor device at the indicated locations (left; scale bar, 10 μm). The spectra showing typical carbon peaks at around 1330 cm^{-1} and 1590 cm^{-1} are only found in the designed pattern region (right). (**d**) CV profiles for the micro-supercapacitor at different scan rates in cell culture medium DMEM. (**e**) Charge-discharge curves in DMEM medium of the micro-supercapacitor device at different current densities for the time window of 6

s (top) and 10 s (bottom). (**f**) Electrochemical stability of the device during storage at 37°C in a buffer solution (PBS) over a 1-month period. (**g**) Electrochemical stability over 1,000,000 CV cycles in the range -0.1 to 0.1 V at the frequency of 4 Hz at 37°C in a buffer solution (PBS).

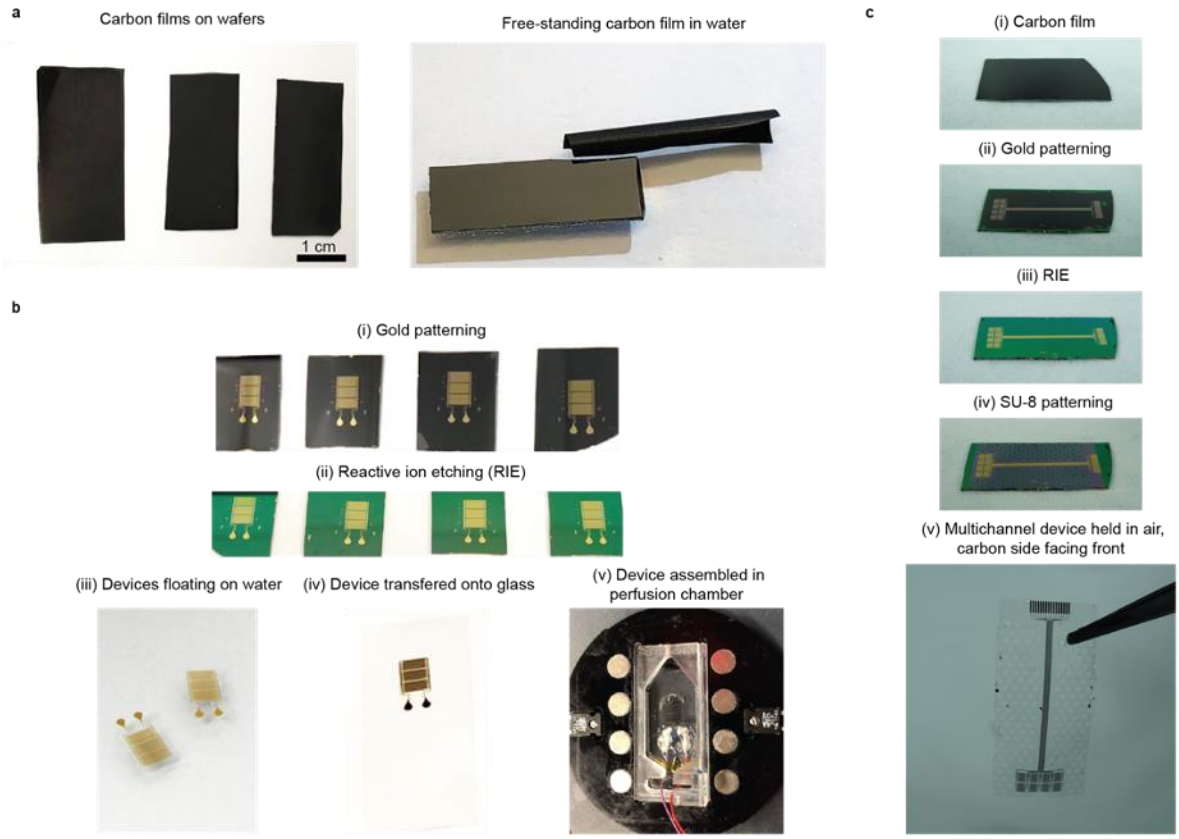

Figure 3.7 The porous carbon-based materials and devices are freestanding and can be manipulated.

(**a**) Photographs showing the as-synthesized carbon film on silicon wafers and the freestanding carbon film after its release using buffered HF. (**b**) Representative photographs of interdigitated devices during fabrication processes. The devices floating on water (iii) have the gold/SU-8 side facing up, while the device transferred onto glass (iv) shows the carbon side up. A device can be

assembled in perfusion chamber for the retinal slice experiments (v). (**c**) Representative photographs of a multichannel interdigitated device fabrication.

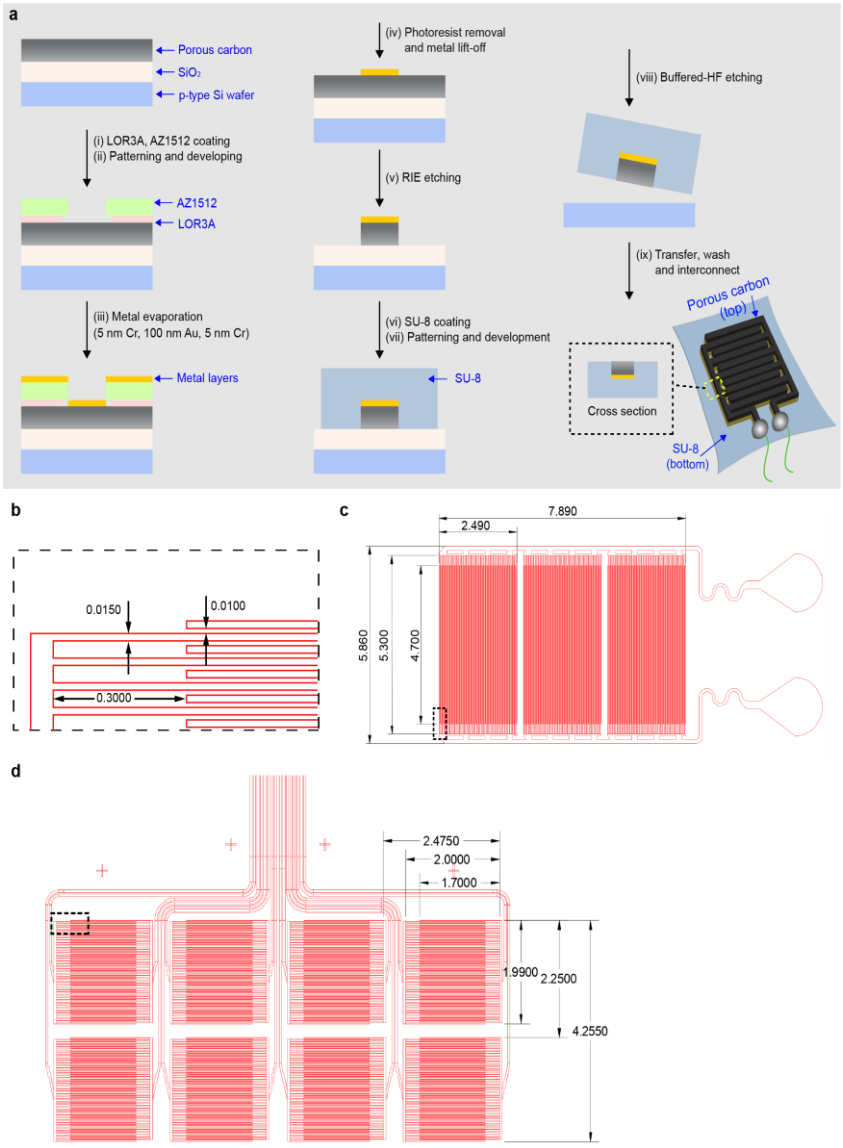

Figure 3.8 The device fabrication and design are scalable and generalizable.

(**a**) Cross-sectional schematics of the flexible micro-supercapacitor device fabrication. (**b**) Geometry of a representative interdigitated electrode pattern used in the flexible devices. (**c**) CAD design of the large area device. (**d**) CAD design of 8-site multichannel recording/stimulation

device. Interconnects and FFC header not shown. Dashed rectangles in (**c**) and (**d**) show sample position of features displayed in (**b**). All measurements are in millimetres.

Mechanical simulations for puncture deformation showed that compared to the uniformly covered multilayered device, the interdigitated pattern can reduce the maximum von Mises stress present in both the carbon and metal layers, suggesting a mechanical justification of the micro-supercapacitor-like device (**Fig. 3.9**). We also performed electrostatics simulations to model the electric potential at the surface of the device and between the interdigitated electrodes (**Fig. 3.10**). Comparing a 2-prong and a 10-prong electrode model with the same total electrode area, the 10-prong electrode geometry yields a more confined electrical potential distribution at the cross-section (**Fig. 3.10c**). This is reminiscent of the local return electrode designs for the photovoltaic devices used for retinal implants[16]. We speculate that this confined z-axis electrical potential may be beneficial for stimulation of cell monolayers *in vitro* or tissues with multilayered circuit organization (*e.g.*, retina).

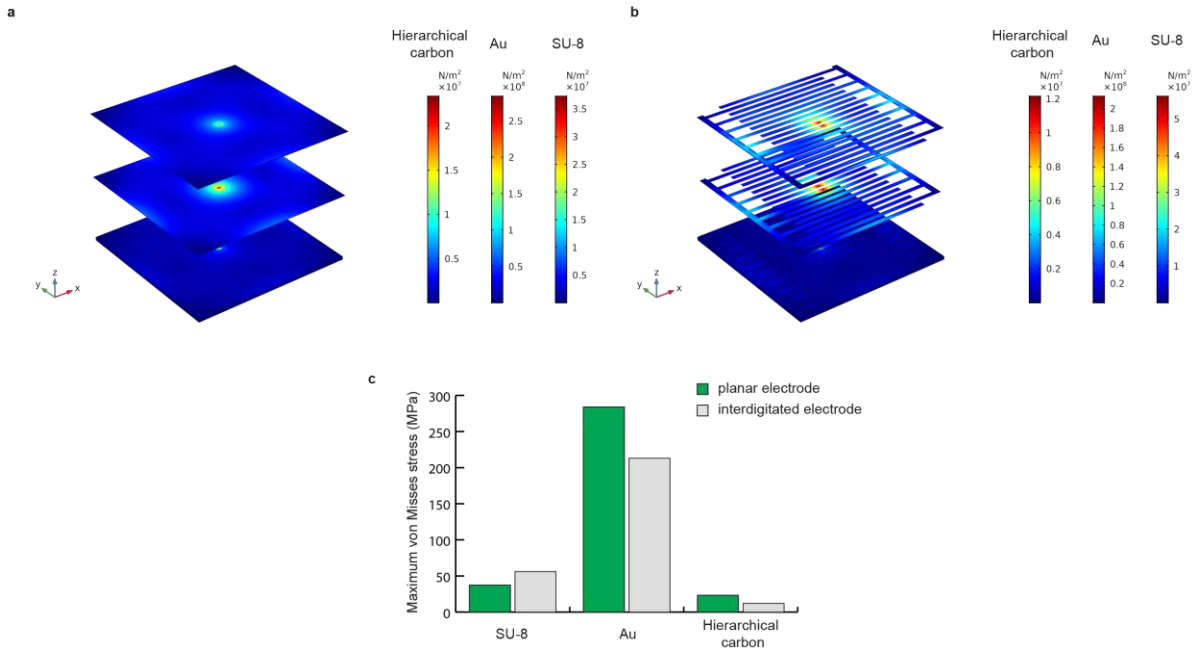

Figure 3.9 COMSOL simulations of puncture resistance in the carbon/Au/SU-8 composite suggest that the interdigitated design can mitigate the stress.

(**a**) von Mises stress distribution in a 0.5 mm x 0.5 mm square material composite; exploded view. (**b**) von Mises stress distribution in 10-prong interdigitated pattern of carbon/Au on a 0.5 mm x 0.5 mm SU-8. (**c**) Comparison of maximum stress present in the material layers. Interdigitated design can reduce the maximum stress in the critical material layers, *i.e.*, Au and porous carbon. For simulation, we have considered the hierarchical carbon membrane (*i.e.*, containing the macroporous carbon structures).

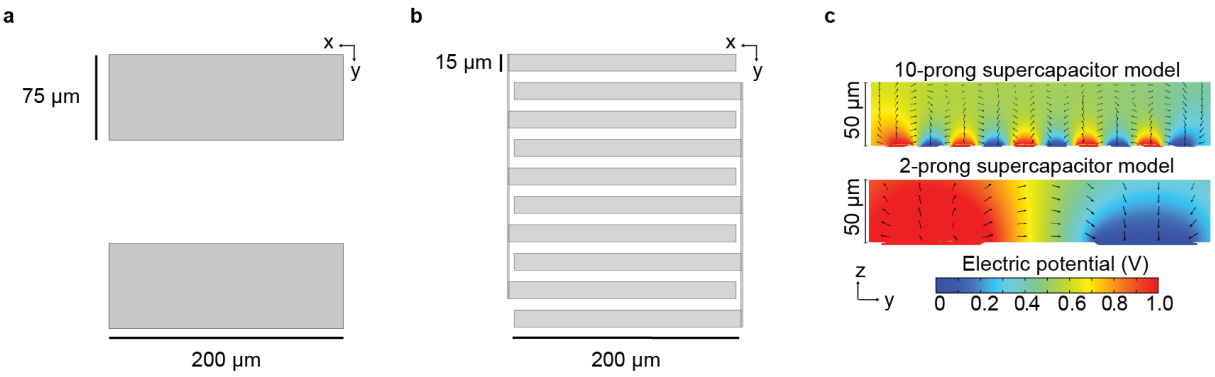

Figure 3.10 COMSOL simulation of electric potentials suggests that the interdigitated design has more confined electric potential distribution.

(**a**) 2D geometry of a 2-prong large electrode device. (**b**) 2D geometry of a 10-prong electrode device. (**c**) Simulated electrolyte potentials between the two electrodes with a relative voltage of 1 V. Comparison of the cross-sectional electric potential distributions between a ten-prong micro-supercapacitor and a two-electrode system of the same area show differences in the electric potential penetration depth. Arrows indicate the electric field direction and strength.

Next, we conducted electrochemical tests using several physiological electrolytes. The electrochemical performance of the porous carbon membranes was analysed by cyclic voltammetry (CV) and galvanostatic charge/discharge techniques (**Figs. 3.6d-e, 3.11-3.14)** In Na_2SO_4 electrolyte solution, the device showed near-rectangular CV profiles up to a scan rate of 100 mV/s (**Fig. 3.11a-b**), confirming that the device acted as an electrostatic double-layer capacitor. Notably, the devices also showed a near-rectangular CV profile in Dulbecco's Modified Eagle Medium (DMEM) up to a scan rate of 100 mV/s, demonstrating that the capacitor behaviour was maintained even in cell culture media (**Fig. 3.6d**). Areal specific capacitances calculated from the CV profiles (**Fig. 3.11c**) were comparable to those of other supercapacitors or micro-supercapacitors[17-19] (**Table 3.1**). Electrochemical impedance spectroscopy tests revealed low

equivalent resistances of ~ 680 Ω and 715 Ω of the device in phosphate-buffered saline (PBS) and DMEM solutions, respectively (**Fig. 3.15**), suggesting good charge transport properties. Without optimization, the charge injection limit of the device is estimated to be at least ~ 120 μC/cm^2 (**Fig. 3.16**), which is comparable to Pt and Pt/Ir alloy electrodes used in tissue stimulations (**Table 3.2**). Additionally, the electrode preserved a near-rectangular CV profile with a scan rates up to 4 V/s (**Fig. 3.17a**).

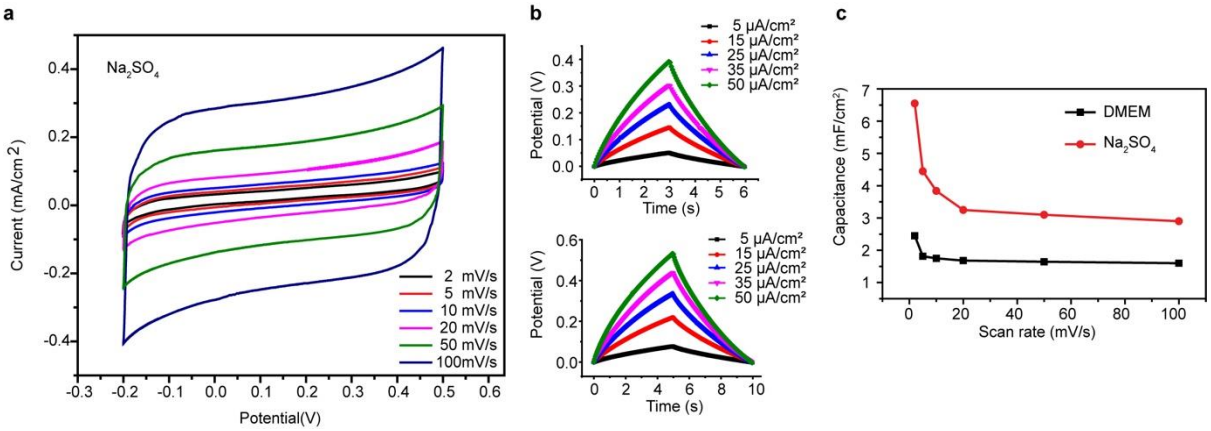

Figure 3.11 The device electrochemical performance was characterized in Na_2SO_4 solution. (**a**) CV profiles for the micro-supercapacitor device at different scan rates in Na_2SO_4 solution. (**b**) Charge-discharge curves for the micro-supercapacitor device at different current densities for the same time windows (6 s and 10 s). (**c**) The specific capacitance with DMEM and Na_2SO_4 electrolytes of hierarchical porous carbon micro-supercapacitor as a function of scan rate.

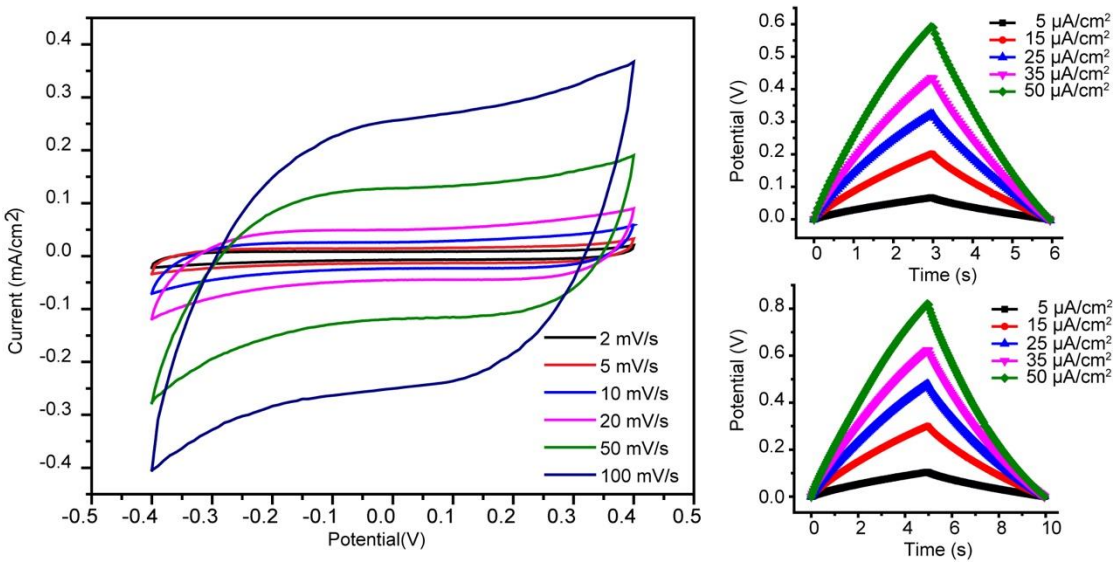

Figure 3.12 The device electrochemical performance was characterized in PBS solution.

CV profiles for the micro-supercapacitor device at different scan rates in PBS solution (left) and charge-discharge curves of the micro-supercapacitor device at different current densities for the same time windows (right, 6 s and 10 s).

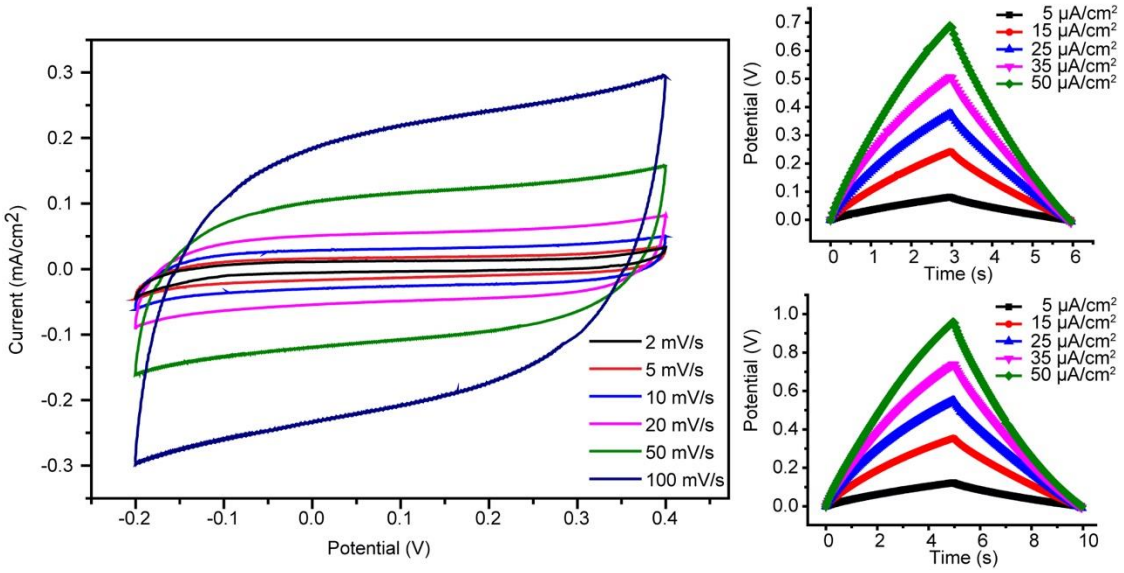

Figure 3.13 The device electrochemical performance was characterized in ACSF solution.

CV profiles for the micro-supercapacitor device at different scan rates in culture medium ACSF solution (left) and charge-discharge curves for the micro-supercapacitor device at different current densities for the same time windows (right, 6 s and 10 s).

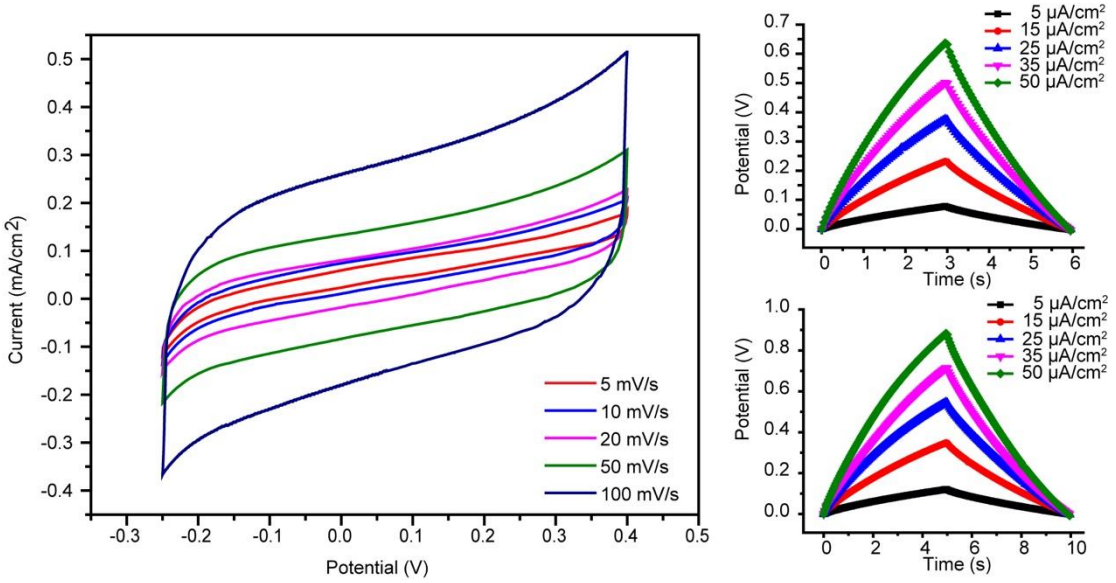

Figure 3.14 The device electrochemical performance was characterized in HEPES-buffered Tyrode's solution.

CV profiles for the micro-supercapacitor device at different scan rates in HEPES-buffered Tyrode's solution (left) and charge-discharge curves for the micro-supercapacitor device at different current densities for the same time windows (right, 6 s and 10 s).

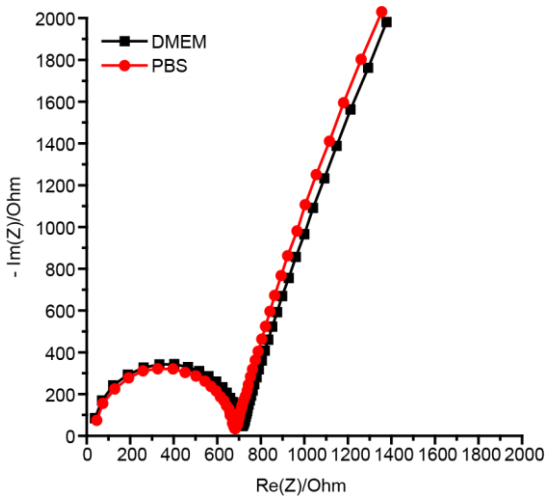

Figure 3.15 Device impedance characterization suggests good interfacial charge transport. Impedance measurements of the micro-supercapacitor device in DMEM culture medium (black) and PBS (red).

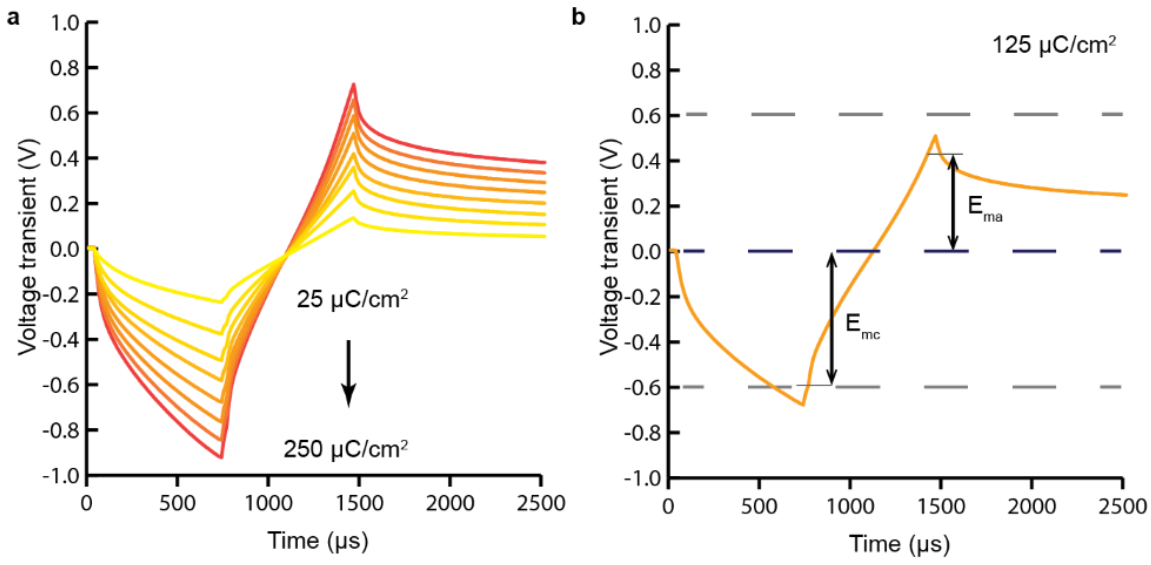

Figure 3.16 The measurement of voltage transients yields the charge injection limit of the device.

(**a**) Comparison of voltage transients of mesoporous carbon electrodes at the charge injection from 25 µC/cm² to 250 µC/cm² with 25 µC/cm² intervals. (**b**) The voltage transient for 125 µC/cm² charge per pulse with identified maximum negative (E_{mc}) and maximum positive (E_{ma}) potentials.

Table 3.1 Specific capacitance for different types of supercapacitors and micro-supercapacitors.

The values shown below were acquired at different scan rates.

Material	**Specific capacitance (mF/cm^2)**	**Reference**
Porous carbon	0.8	10.1016/j.carbon.2014.11.017
Graphene	3	10.1038/ncomms6714
rGo-CNT	2.8	10.1002/adfm.201201292
PEDOT	1.0	10.1039/C6EE00615A
Onion-like carbon	1.1	10.1016/j.elecom.2013.09.003
Activated carbon	0.9	10.1038/nnano.2010.162
Photoresist-derived carbon	0.5	10.1039/C4TA00570H
This material	**~ 1-3** at 100 mV/s in different saline solutions	

Table 3.2 Charge injection capacity for different types of electrodes used for biointerfaces.

Material	**Charge injection limit (mC/cm^2)**	**Reference**
Pt and PtIr alloys	0.05 - 0.15	10.1146/annurev.bioeng.10.061807.160518
Roughened Pt	1.0	10.1021/la504876n
CNT array	1-1.6	10.1021/nl061241t
PEDOT:PSS	2.71	10.1002/adfm.201703019
TiN	~ 1	10.1146/annurev.bioeng.10.061807.160518
IrOx	1 - 5	10.1146/annurev.bioeng.10.061807.160518
This material	**> 0.12**	

Lastly, the intrinsic device stability in physiological solution was tested by submerging the device in 37 °C PBS solution for one month, during which no obvious change in capacitance rate was observed (**Fig. 3.6f**). The device showed electrochemical and mechanical stabilities over the course of at least 1,000,000 cycles (**Fig. 3.6g; 3.17 and 3.18**). Together, these results demonstrate that the device is promising for bioelectronic interfaces.

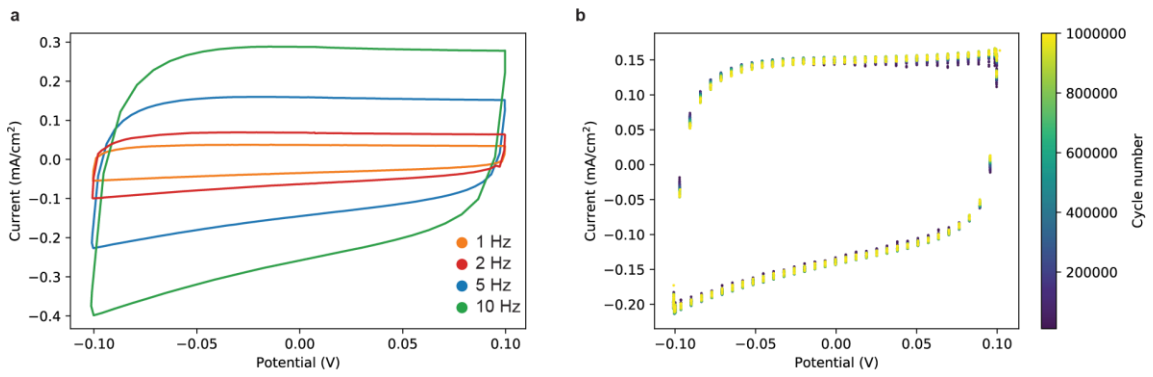

Figure 3.17 The micro-supercapacitor-like device is stable and can operate at high frequency.

(**a**) CV profiles for high frequency sweep in PBS at 25°C. (1 Hz – 0.4 V/s, 2 Hz - 0.8 V/s, 5 Hz – 2 V/s, 10 Hz – 4 V/s) (**b**) Representative CV profiles during 1 million cycles at 4 Hz (sweep rate 1.6 V/s) in PBS at 37 °C.

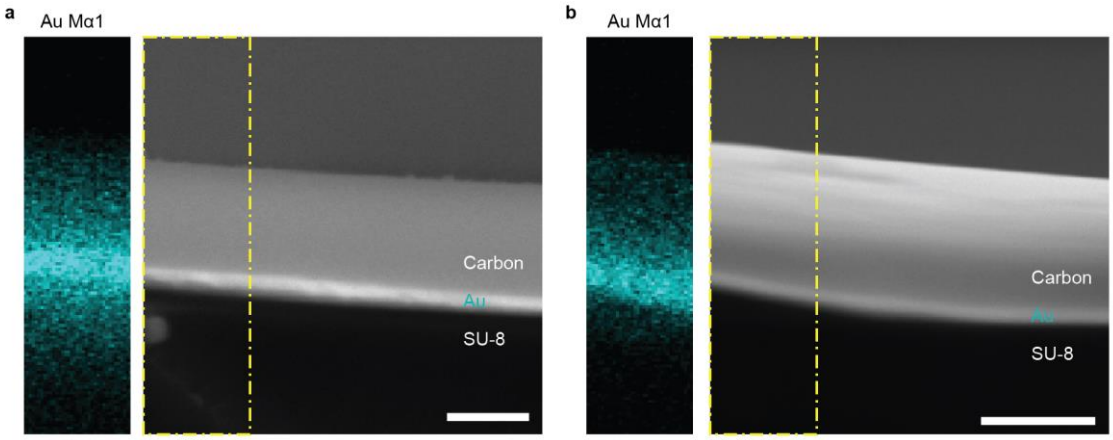

Figure 3.18 SEM reveals no interface lamination after 1 million of electrochemical cycles.

SEM images of carbon interface before (**a**) and after (**b**) 1 million CV cycles. Section shows Au EDX mapping at the boundaries with mesoporous carbon and SU-8 layers. Scale bar, left: 0.5 µm; right: 1 µm. The experiment was reproduced twice with similar results over the entire imaged sample.

3.4 Summary

This chapter described the development of a hierarchical carbon-based with a monolithic structure. The microscopic structure and mechanical performance of the material and its electrochemical properties have been assessed. The 'upside-down' fabrication strategy has yielded flexible micro-supercapacitor-like devices with interdigitated electrode arrays. Due to their promising performance, mechanical compliance, and stability, such devices are suitable for their applications to bioelectronic investigations and can become possible materials for future electroceutical therapies. Proof of concept demonstrations of bioelectronic applications in in vitro, ex vivo, and in vivo systems will be described in a subsequent chapter.

3.5 Methods

Hierarchical porous carbon film preparation

Resol was prepared by crosslinking of phenol and formaldehyde, using methods from the literature[20]. Pluronic block copolymer F127 (template) and phenolic resol (carbon source) were mixed at ratio of 1:2 into an ethanol solution. The precursor solution was stirred for 1 hour before use. Vesicle structures were constructed using silica nanosphere templates. 200 nm-diameter silica nanospheres (NanoComposix, 10 mg/ml) were surface modified with a dopamine layer, according to a literature method[21]. The modified nanospheres were then added into precursor solution and mixed until a homogeneous mixture formed. Silicon wafer (Nova Electronic Materials, p-type, 600 nm thermal oxide SiO_2) was cut into small pieces with suitable sizes (e.g. 2 cm × 4 cm) and cleaned by O_2 plasma (Plasma Etcher, PE100) at 100 W for 2 minutes. The precursor solution with silica nanospheres was spin-coated (Laurell, WS-650 spin coater) onto the surface-cleaned silicon at 1500 rpm for 45 s. Multiple layers were formed by leaving the silicon wafer at room temperature

for 10 minutes and then repeating the spin-coating. Then pure precursor solution was spin-coated onto the substrate at 3000 rpm for 45 s. The wafers were kept immobile for 4-6 h at 25 °C, then baked in an oven for 24 h at 100°C. After baking, the wafers were transferred into an inert argon atmosphere and heated at 700°C (temperature rise rate at 5°C/min) for 30 min. The thin film was etched off the silicon wafer and nanospheres were etched by submerging the wafers in buffered hydrofluoric acid (HF) for 8 h. The thin film was rinsed with deionized (DI) water 6 times and dried prior to further characterizations.

Device design

CAD was performed in AutoCAD software and schematics of comb-like devices are shown in **Figure 3.8**. The pattern of interdigitated electrodes was consistent in each of the fabricated devices (**Fig. 3.8b**). Electrodes had a width of 15 µm with 10 µm spacing between them and 300 µm distance to the edge of the comb. The single channel device (**Fig. 3.8c**) was comprised of 150 pairs of electrodes connected to 2 large pads, allowing for manual connection to jumper wires. The multichannel electrode (**Fig. 3.8d**) had 8 sites arranged in 4 columns and 2 rows, and each site had 40 pairs of electrodes. Traces coming from the electrode sites were connected to 16 pads (2.25 mm length, 0.3 mm width, 0.5 mm pitch) matching a ZIF connector (FH12A-16S-0.5SH(55), Hirose Electric Co Ltd.). SU-8 patterns were designed with perforations in the area outside of the electrodes to increase the surface area available to buffered HF and to reduce the time required for SiO_2 etching. However, we did not notice significant difference in fabrication and performance of devices with and without perforations.

Device fabrication

A hierarchical porous carbon film obtained on p-type wet thermal oxide silicon wafer was used as a substrate for fabrication. A standard photolithography procedure was applied to make the desired pattern on the substrate. A schematic of the microfabrication protocol is shown in Figure S6a. Metal layers act as a hard mask for reactive-ion etching, and as a conductive and mechanical support for the carbon films. Chromium was used to improve adhesion between material layers. 5 nm Cr, 100 nm Au and 5 nm Cr layers were evaporated on the patterned surface using an e-beam evaporator (EvoVac, Angstrom Engineering), and extra carbon was removed by reactive-ion etching (Oxford Instruments PlasmaPro, NGP80). The supporting SU-8 layer had a thickness of approximately 10 μm. Patterns were exposed using a direct writer (MLA150, Heidelberg). The pattern on the SU-8 layer was etched from the substrate with buffered HF and transferred into DI water, afterwards washing the device with DI water 6 times. For free standing devices, electrodes were transferred onto polyimide film and allowed to dry. For single site devices, jumper wires were connected to the pads using conducting silver paste (Ted Pella) and after 24 h of drying, the connections and excess of connecting traces were insulated using silicon glue (Kwik-Sil, World Precision Instruments). For multisite devices, excess of traces was partially insulated using silicon glue. The connector header was strengthened with polyimide tape, cut to appropriate dimensions, and inserted into the ZIF connector. For cell and tissue culture, the devices were directly transferred onto glass microscope slides or into glass-bottom culture dishes. After ensuring even placement, the devices were allowed to dry and partially adhere to the glass. Next, jumper wires were connected using silver paste and left to dry for 24 h, after which the device was fixed to the dish and connections insulated with silicon glue. Devices were sterilized by oxygen plasma (100 W for 1 min) and ultraviolet light irradiation before cell or tissue culture.

Raman spectroscopy

Raman spectra were recorded using a LabRAM HR evolution system (Horiba, Japan), and the mapping was done in the ultralow frequency module using a 532 nm laser.

Electrochemical measurements

Cyclic voltammetry (CV) was performed over a wide range of scan rates at room temperature or 37 °C in various electrolytes. A potentiostat (SP-200, BioLogic) controlled with EC-Lab software with the three-electrode cell was used. A platinum wire was used as the counter electrode, a Ag/AgCl electrode (1M KCl) as the reference electrode, and a micro-supercapacitor device as the working electrode. Areal cell capacitance (C) was calculated from the cathodic phase of CV by $C = (\int I\, dv)/(sVA)$, where I is the current, s is the scan rate, V is the potential window, and A is area of the electrode. Galvanic charge/discharge measurements were tested using two symmetric devices in a two-electrode configuration using source meter (Keithley 2636A, Tektronix, Inc.) controlled by a LabVIEW program (National Instruments). The voltage shown was the potential between the two symmetric devices.

Voltage transients

Voltage transients were measured using a potentiostat (SP-200, BioLogic) controlled with EC-Lab Express. A platinum wire was used as a counter electrode and a Ag/AgCl (1 M) electrode was used as a reference. For the measurement, the carbon electrode was stabilized at 0 V versus Ag/AgCl for 1 ms in PBS at room temperature. 700 µs long cathodic and anodic current pulses were delivered to the electrode with the interpulse delay of 28 µs. The most negative (E_{mc}) and positive (E_{ac}) polarization potentials were assigned 28 µs after the maximum of a respective peak to account

for access voltage and instrument delay. The charge injection limit was taken as a maximum charge injected without exceeding the -0.6 – 0.6 V potential window.

Electron microscopy

Transmission electron microscopy (TEM, Tecnai F30, FEI) and scanning electron microscopy (SEM, Carl Zeiss, Merlin) were used to characterize the hierarchical porous materials and material/cell interfaces. CMs on the materials were fixed in 5% glutaraldehyde PBS solution for 30 min, washed in DI water, and then dehydrated with an increasing ethanol gradient from 30% to 98%. The samples were dried in a critical point dryer (Leica EM CPD300) and observed on the same SEM after coating with an 8 nm Pt/Pd metal layer on a sputter coater (Ted Pella, Inc.). The SEM was operated at a 2-kV accelerating voltage. Images were analysed using ImageJ.

Mechanical test

Indentation modulus and hardness were measured by performing nanoindentation using a Hysitron 950 TriboIndenter in ambient conditions with a Berkovich indenter (three-sided pyramid-shaped diamond tip, tip radius ~100 nm). All measurements were kept at a constant displacement of 200 nm. The data were analysed using standard Oliver and Pharr (1) analysis to extract the reduced modulus (E_r) and hardness by selecting upper fit at 95% and lower fit at 20%. The Young's modulus E of the samples was extracted based on Eq. (3.1)[22], a general relation that applies to any axisymmetric indenter. The diamond tip has a Young's modulus E_i = 1141 GPa and a Poisson's ratio ν_i = 0.07[23]. Here, we assume the Poisson's ratio of the samples ν = 0.25, which has been widely used for amorphous carbon[24].

$$\frac{1}{E_r} = \frac{1-\nu^2}{E} + \frac{1-\nu_i^2}{E_i} \qquad (3.1)$$

Finite element simulations

Finite element analysis was performed using COMSOL Multiphysics software.

Finite element analysis of the electric potential distribution

The finite element analysis of the 3D electric potential distribution at the cross-section of the micro-supercapacitor-like device was performed using the AC/DC module of COMSOL Multiphysics software. The electric scalar potential, *V*, satisfies Poisson's equation,$-\nabla \cdot (\varepsilon_0 \varepsilon_r \nabla V) = \rho$, where ε_0 is the permittivity of free space, ε_r is the relative permittivity, and ρ is the space charge density. The electric fields are obtained from the gradient of *V*: $\boldsymbol{E} = -\nabla V$, and the displacement is defined as $\boldsymbol{D} = \varepsilon_0 \varepsilon_r \mathbf{E}$**.** To simplify the simulation (versus the actual device with three hundred prongs), a pair of five-prong comb-like electrode model was built with a gap of 10 μm and prongs of 200 μm length and 15μm width. Prong width and gap width were consistent with the experimental setup. A relative voltage of 1 V was applied between left- and right-side set of electrodes. The medium was modelled as conductor with conductivity of 1.4 S/m and relative permittivity of 80, which correspond to approximate values for DMEM cell culture media.[25] For comparison, the electric potential distribution of two planar electrodes with the same area was also calculated. The area of each electrode was equal to the total area of a single comb, and the gap width between the two planar electrodes was equal to the summation of the gaps in each comb-like electrode; as such, each electrode was of 75 μm width and 200 μm length with a gap of 50 μm between the two.

Finite element analysis of von Mises stress

The finite element analysis of the von Mises stress was performed using the Structural Mechanics and Shell modules of COMSOL Multiphysics software. The geometry of the device was simplified

as a block of SU-8 with dimensions of 0.5 mm × 0.5 mm × 0.01 mm and as 2 shells of either complete planar layers of gold (0.0001 mm) and carbon (0.0006 mm) or the shells in the comb-like shapes with electrode width of 0.015 mm and spacing of 0.010 mm. All materials were modelled as linearly elastic. Density, Young's modulus and Poisson's ratio were used to model material deformation and stress. Gold was modelled using COMSOL library values, SU-8 was modelled using literature values[26] and the carbon layer was modelled using Young's modulus measured using nanoindentation, (E_i = 4.2 GPa) and approximate values of Poisson's ratio[24] (ν_i = 0.25) and density (d = 1600 kg/m^3, graphite density excluding pore volume). For the simulation, edge boundaries of the SU-8 block were constrained and point pressure of 0.001 N was applied at the centre of top boundary down the z-axis.

3.6 Bibliography

1 Xie, Z., Avila, R., Huang, Y. & Rogers, J. A. Flexible and Stretchable Antennas for Biointegrated Electronics. *Advanced Materials* **32**, 1902767, doi:10.1002/adma.201902767 (2019).

2 Wang, L. *et al.* Functionalized helical fibre bundles of carbon nanotubes as electrochemical sensors for long-term in vivo monitoring of multiple disease biomarkers. *Nature Biomedical Engineering* **4**, 159-171, doi:10.1038/s41551-019-0462-8 (2019).

3 Someya, T., Bao, Z. & Malliaras, G. G. The rise of plastic bioelectronics. *Nature* **540**, 379-385, doi:10.1038/nature21004 (2016).

4 Huang, Z. *et al.* Three-dimensional integrated stretchable electronics. *Nature Electronics* **1**, 473-480, doi:10.1038/s41928-018-0116-y (2018).

5 Chen, R., Canales, A. & Anikeeva, P. Neural recording and modulation technologies. *Nature Reviews Materials* **2**, 16093, doi:10.1038/natrevmats.2016.93 (2017).

6 Pan, L. *et al.* Hierarchical nanostructured conducting polymer hydrogel with high electrochemical activity. *Proceedings of the National Academy of Sciences of the United States of America* **109**, 9287-9292, doi:10.1073/pnas.1202636109 (2012).

7 Lee, Y. *et al.* Stretchable organic optoelectronic sensorimotor synapse. *Science advances* **4**, eaat7387-eaat7387, doi:10.1126/sciadv.aat7387 (2018).

8 Rastogi, S. K., Kalmykov, A., Johnson, N. & Cohen-Karni, T. Bioelectronics with nanocarbons. *Journal of Materials Chemistry B* **6**, 7159-7178, doi:10.1039/c8tb01600c (2018).

9 Yang, W., Thordarson, P., Gooding, J. J., Ringer, S. P. & Braet, F. Carbon nanotubes for biological and biomedical applications. *Nanotechnology* **18**, 412001, doi:10.1088/0957-4484/18/41/412001 (2007).

10 Chen, N. *et al.* Neural interfaces engineered via micro- and nanostructured coatings. *Nano Today* **14**, 59-83, doi:10.1016/j.nantod.2017.04.007 (2017).

11 Hansen, S. F. & Lennquist, A. Carbon nanotubes added to the SIN List as a nanomaterial of Very High Concern. *Nature Nanotechnology* **15**, 3-4, doi:10.1038/s41565-019-0613-9 (2020).

12 Zhu, W. *et al.* Nanomechanical mechanism for lipid bilayer damage induced by carbon nanotubes confined in intracellular vesicles. *Proceedings of the National Academy of Sciences of the United States of America* **113**, 12374-12379, doi:10.1073/pnas.1605030113 (2016).

13 Abbott, J. *et al.* A nanoelectrode array for obtaining intracellular recordings from thousands of connected neurons. *Nature biomedical engineering* **4**, 232-241, doi:10.1038/s41551-019-0455-7 (2020).

14 Tian, B. *et al.* Macroporous nanowire nanoelectronic scaffolds for synthetic tissues. *Nat Mater* **11**, 986-994, doi:10.1038/nmat3404 (2012).

15 Jia, L. *et al.* Syringe Injectable Electronics. *Nature Nanotechnology* **10**, 629-636, doi:10.1038/nnano.2015.115.Syringe (2015).

16 Flores, T., Goetz, G., Lei, X. & Palanker, D. Optimization of return electrodes in neurostimulating arrays. *Journal of neural engineering* **13**, 036010-036010, doi:10.1088/1741-2560/13/3/036010 (2016).

17 Song, B. *et al.* in *2015 IEEE 65th Electronic Components and Technology Conference (ECTC)* (IEEE, 2015).

18 Lee, G. *et al.* High-performance all-solid-state flexible micro-supercapacitor arrays with layer-by-layer assembled MWNT/MnOxnanocomposite electrodes. *Nanoscale* **6**, 9655-9664, doi:10.1039/c4nr02035a (2014).

19 Pech, D. *et al.* Ultrahigh-power micrometre-sized supercapacitors based on onion-like carbon. *Nature Nanotechnology* **5**, 651-654, doi:10.1038/nnano.2010.162 (2010).

20 Meng, Y. *et al.* Ordered Mesoporous Polymers and Homologous Carbon Frameworks: Amphiphilic Surfactant Templating and Direct Transformation. *Angewandte Chemie International Edition* **44**, 7053-7059, doi:10.1002/anie.200501561 (2005).

21 Liu, R. *et al.* Dopamine as a Carbon Source: The Controlled Synthesis of Hollow Carbon Spheres and Yolk-Structured Carbon Nanocomposites. *Angewandte Chemie International Edition* **50**, 6799-6802, doi:10.1002/anie.201102070 (2011).

22 Oliver, W. C. & Pharr, G. M. Measurement of hardness and elastic modulus by instrumented indentation: Advances in understanding and refinements to methodology. *Journal of Materials Research* **19**, 3-20, doi:10.1557/jmr.2004.19.1.3 (2004).

23 Li, X. & Bhushan, B. A review of nanoindentation continuous stiffness measurement technique and its applications. *Materials Characterization* **48**, 11-36, doi:10.1016/s1044-5803(02)00192-4 (2002).

24 Suk, J. W., Murali, S., An, J. & Ruoff, R. S. Mechanical measurements of ultra-thin amorphous carbon membranes using scanning atomic force microscopy. *Carbon* **50**, 2220-2225, doi:10.1016/j.carbon.2012.01.037 (2012).

25 Chen, M.-T., Jiang, C., Vernier, P. T., Wu, Y.-H. & Gundersen, M. A. Two-dimensional nanosecond electric field mapping based on cell electropermeabilization. *PMC Biophys* **2**, 9-9, doi:10.1186/1757-5036-2-9 (2009).

26 Al-Halhouli, A. T., Kampen, I., Krah, T. & Büttgenbach, S. Nanoindentation testing of SU-8 photoresist mechanical properties. *Microelectronic Engineering* **85**, 942-944, doi:10.1016/j.mee.2008.01.033 (2008).

Chapter 4

Application of Supercapacitor-like Device for Stimulation and Physiology Recording

This chapter was adapted from Fang, Y., Prominski, A., Rotenberg, M.Y. et al. "Micelle-enabled self-assembly of porous and monolithic carbon membranes for bioelectronic interfaces." Nature Nanotechnology, 16, 206–213 (2021).

4.1 Introduction

The micro-supercapacitor-like device represents an interesting system for applications in biomodulation. Its ability to present shallow electric-field to the cells and tissue allows achieving regulation and stimulation with safe, biocompatible, and energy-efficient overpotential. Moreover, its flexible form enables the formation of tight contact with curved tissues such as hearts and nerves, providing means for efficient stimulation.

In this chapter, I show the in vitro and in vivo biocompatibility studies of monolithic carbon-based membranes. Then, I will describe how the super-capacitor-like device can be used to stimulate and train cardiomyocyte cell cultures. Subsequently, I will demonstrate modulation of neural circuits in the retina model and application of shallow electric field to selective neuron activation. Finally, I will present the application of flexible devices to the pacing of isolated hearts and sciatic nerves in a rat model. I will also show a proof of concept multichannel array electrode for recording heart physiology.

4.2 Biological Training *In Vitro*

We first confirmed the viability of CMs and primary rat cardiac fibroblasts (RCFs) cultured over the device. Live-dead assays showed that ~100% of CMs were still alive after a 3-day culture (**Fig. 4.1**). RCFs nuclear staining on the device showed healthy nucleus morphology, and no obvious nuclear changes due to cell death or apoptosis were observed (**Fig. 4.2a**). To have a more sensitive evaluation of the device *in vitro* biocompatibility, we conducted the lactate dehydrogenase (LDH) cytotoxicity assay using RCFs (**Fig. 4.2b**). The LDH cytotoxicity percentages in SU-8 group on day 1 (mean value, 3.91%) and day 2 (mean value, 2.97%) indicate that SU-8 alone caused a very mild cytotoxicity *in vitro*, although SU-8 is widely recognized as a biocompatible material[1,2]. When all the device materials are present (*i.e.*, SU-8, porous carbon and metals), the LDH percentages are 8.77 % (mean) and 4.93 % (mean) for day 1 and day 2, respectively. However, the LDH levels in both the SU-8 and the device groups decreased on day 2 versus on day 1, suggesting that the cellular tolerance for these synthetic materials increased over time.

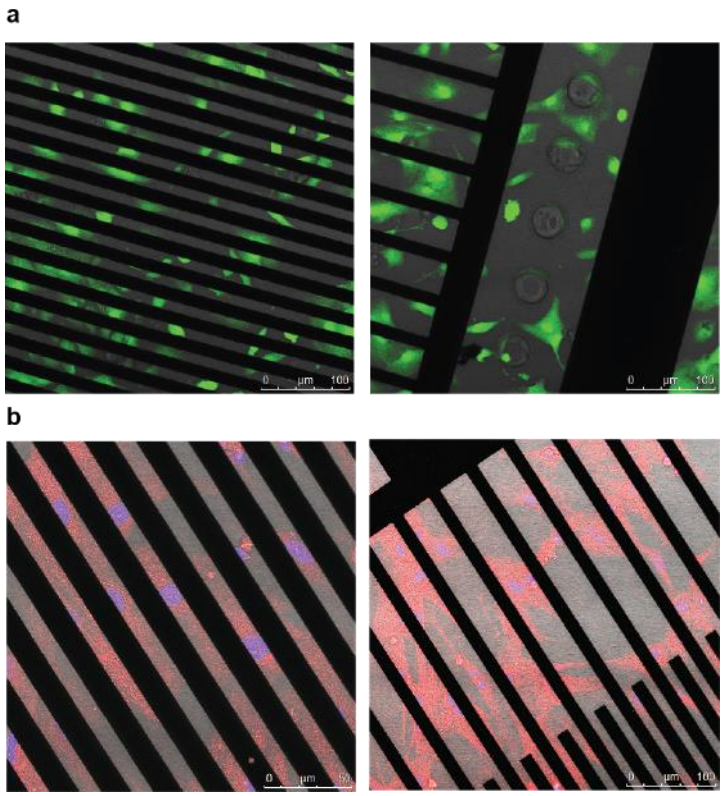

Figure 4.1 The LIVE/DEAD assay suggests good *in vitro* compatibility.

Cells were cultured on device for 3 days before being stained with calcein-AM (green, live cells), ethidium homodimer-1 (red, dead cells), and DAPI (blue, nuclei). (**a**) After being cultured on a device for 3 days, almost all CMs survived, demonstrating good biocompatibility of the device. Scale bar, 100 μm. (**b**) In a positive control experiment, the cells were treated with 100% EtOH for 20 minutes before staining. All CMs were dead afterwards. The experiment was reproduced twice with similar results.

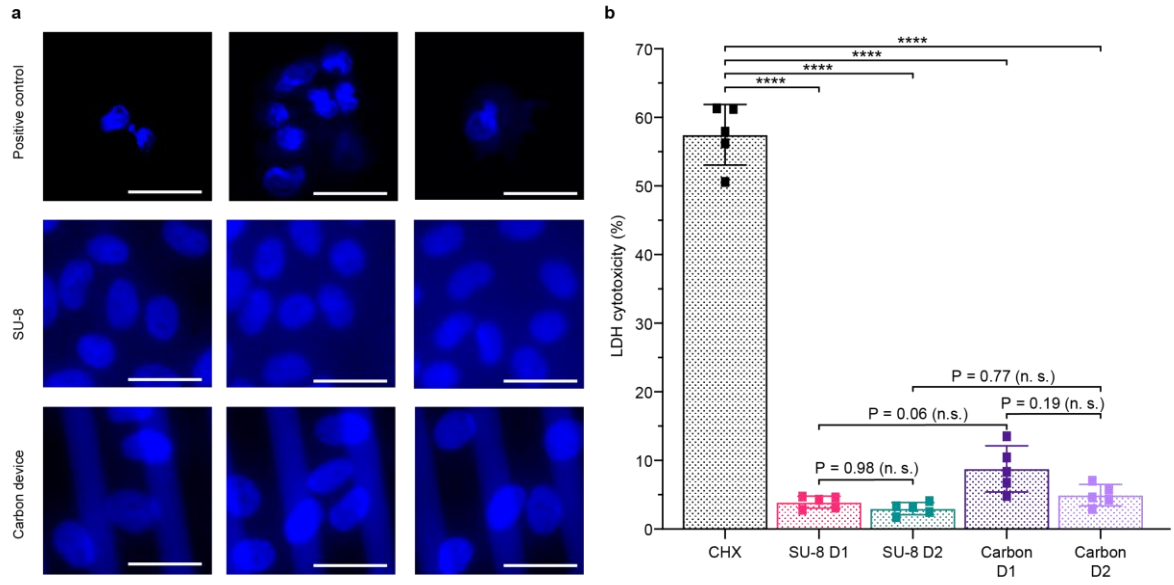

Figure 4.2 Nuclear staining and LDH assays suggest reasonable *in vitro* biocompatibility.

(**a**) Representative images of fibroblast nuclear staining. Scale bar, 25 µm. Positive control samples were prepared by treating fibroblasts with 1 mM hydrogen peroxide to induce apoptosis. On SU-8 and carbon device, the staining showed healthy nucleus morphology. Ten images were taken at random spots across the cell culture area on each sample, and the experiments were independently repeated three times with similar results. (**b**) LDH cytotoxicity percentage from the fibroblasts seeded on SU-8 and carbon devices. Data are presented as mean ± SD. Treatment with 10 µg/mL cycloheximide (CHX) for 24 hours was used to induce cell death as a positive control. LDH cytotoxicity percentage from the fibroblasts on carbon micro-supercapacitor was around 8.77% on day 1 (D1) and 4.93% on day 2 (D2) in comparison to 3.91% on D1 and 2.97 % on D2 in the SU-8 groups. N = 5 independent measurements over five parallel experimental repeats. P values were determined by one-way ANOVA with Tukey's test; n.s., not significant or $P > 0.05$, and ****$P < 0.0001$.

Haematoxylin and eosin stain of mice skin tissues surrounding the implanted devices showed that subcutaneous implantation caused some mild histological changes in week 1 and 4 (**Fig. 4.3a**). No significant inflammation reactions and tissue damage were observed. The histological appearance of the skin tissue above the implanted device (*i.e.*, the epidermis and the dermis) was normal in week 4, except for the mild thickening of subcutaneous connective tissue and mild recruitment of immune cells including macrophages and neutrophils. Additionally, we monitored mouse body weight and no weight loss was observed between control groups and device groups (**Fig. 4.3b**).

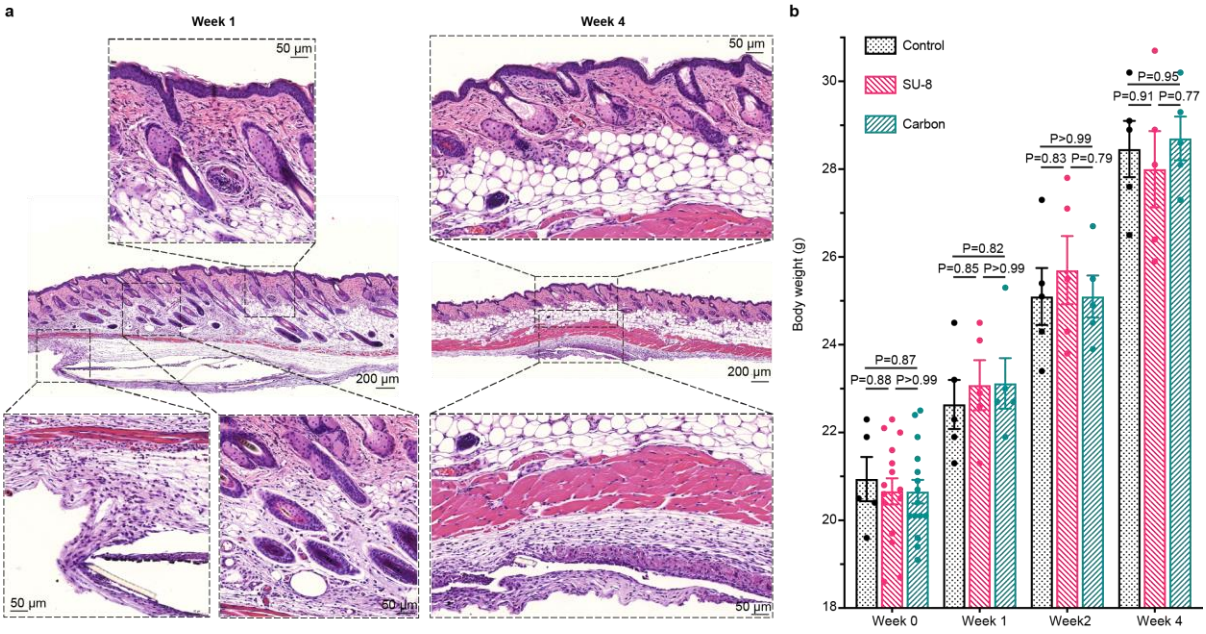

Figure 4.3 The porous carbon-based devices have reasonable *in vivo* biocompatibility.

(**a**) Representative H&E stainings indicated that sub-cutaneous implantation of carbon-based devices only caused mild histological changes at week 1 and week 4. At week 1, subcutaneous connective tissues were observed with mild thickening and mild recruitment of immune cells including macrophages and neutrophils. No major inflammation reactions and tissue damage were observed. Besides, two mild inflammation loci were observed in the skin tissue right above the

embedded device, which may be linked to the skin wound healing after the implantation surgery. Due to the geometry of the SU-8 membrane in the device, it created an artificial cavity in subcutaneous tissue during histological processing and staining. Later at week 4, the histological appearance of the skin tissue above the implanted device was normal, except for the mild subcutaneous thickening and mild recruitment of immune cells including macrophages and neutrophils. The experiment was repeated in five mice for each time point with similar results. (**b**) Body weights measured at four time points (week 0, week 1, week 2, and week 4) upon implantation (mean ± s.e.m.; n = 15 independent mice samples in both week 0 SU-8 and week 0 carbon groups; n = 5 mice in all other groups). Compared to the control group (with pseudo implantation) and the group with SU-8 implantations, no statistically significant weight loss was observed after implantations of carbon-based micro-supercapacitor-like devices in all measured time points. Two-way ANOVA (mixed-effects model with Geisser-Greenhouse correction) was performed for multiple comparisons. Comparisons within each time point were all found to be not significant ($P > 0.05$).

We analysed the formation of biointerface between the device and the cultured CMs by verification of expression of typical cardiac markers, such as cardiac troponin and connexin-43 (**Fig. 4.4**). We additionally confirmed that cells could spread out on the device surface and form subcellular interfaces (**Figs. 4.5** and **4.6**). To evaluate how the charging/discharging cycles from the micro-supercapacitor-like device affect the CMs electrophysiology, we applied the stimulation current to the CM-interfacing devices and performed simultaneous calcium imaging to monitor cellular electrical activity. Each side of the interdigitated electrodes acts as a lead and a square current waveform is applied between them (see Methods for details). Prior to stimulation, CMs

were synchronized with a baseline rate of ~0.67 Hz. Upon application of an input electric current waveform, overdrive pacing was achieved, and the contraction rate immediately synchronized to the pacing frequency (**Fig. 4.4,** large field of view **Fig. 4.7**). It is noteworthy that the pacing rate doubles that of the stimulation rate (*i.e.*, the applied current frequency) (0.5 Hz pacing rate in **Fig. 4.8**, 1 Hz pacing rate in **Fig. 3b** and **Fig. 4.7**). This is expected as both the anodic and the cathodic phases of the electrochemical stimulation (from the same finger electrode area) can depolarize the CMs, although the action potentials (APs) may be initiated at different subcellular locations. One advantage of the electrical stimulation from the interdigitated layout is that it can achieve direct cell modulation uniformly across the entire device area. Also, the confined electrical potential around the finger electrodes may help improve the efficiency of stimulation as CM cultures are typically monolayer or sub-monolayer, and it may be unnecessary to deliver an electric field far above the cell surface.

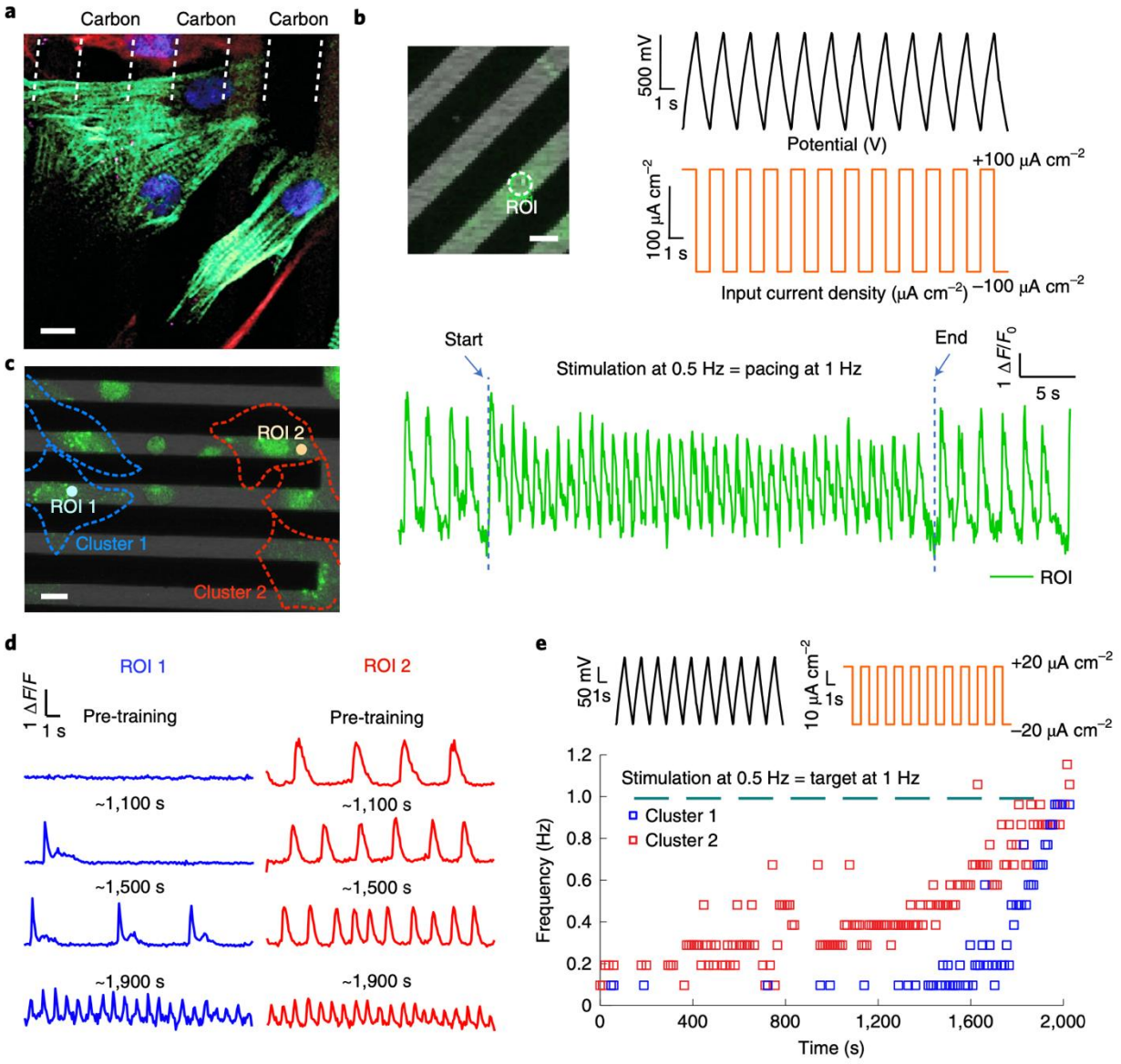

Figure 4.4 *In vitro* biological training.

(a) Representative immunohistochemistry images for cardiac cells cultured on the micro-supercapacitor device. Cells were stained for cardiac troponin (CMs, green), connexin-43 (magenta), vimentin (fibroblasts, red) and DAPI (nuclei, blue). Dash lines, the edges of the interdigitated carbon electrodes. Scale bar, 10 μm. The experiment was repeated twice with similar results. (**b**) Upper left: representative image of CMs loaded with calcium sensitive dye; transmitted light shows the micro-supercapacitor (appeared in black). Scale bar, 10 μm. Upper right: device

voltage (top) and input current density (bottom) during the stimulation. Bottom: cell contraction rate illustrated by plotting the intensity profile of the region of interest (ROI, highlighted in the image). Overdrive stimulation was reproduced with similar results in three independent experiments. (**c**) Representative image of CMs loaded with calcium sensitive dye recorded during subthreshold stimulation for 2000 s. Scale bar, 10 μm. Overlay shows approximate positions of CMs in the field of view and their cluster assignment was color-coded in blue (cluster 1) and red (cluster 2). (**d**) Representative traces of fluorescence intensities at the region of interest (ROI dots in panel **c**) at the beginning of experiment and at 1100, 1500 and 1900 s of stimulation. Microphotographs (c) and cell trainings (d) in subthreshold pacing are representative of three independent experiments. (**e**) Frequency analysis of cell contraction frequency during subthreshold training. Top panel shows the voltage (left) and the input current density (right) waveforms during the training process. Bottom: frequency analysis shows fluctuating but gradual increase in the contraction rate, which eventually reached the target training frequency of 1 Hz.

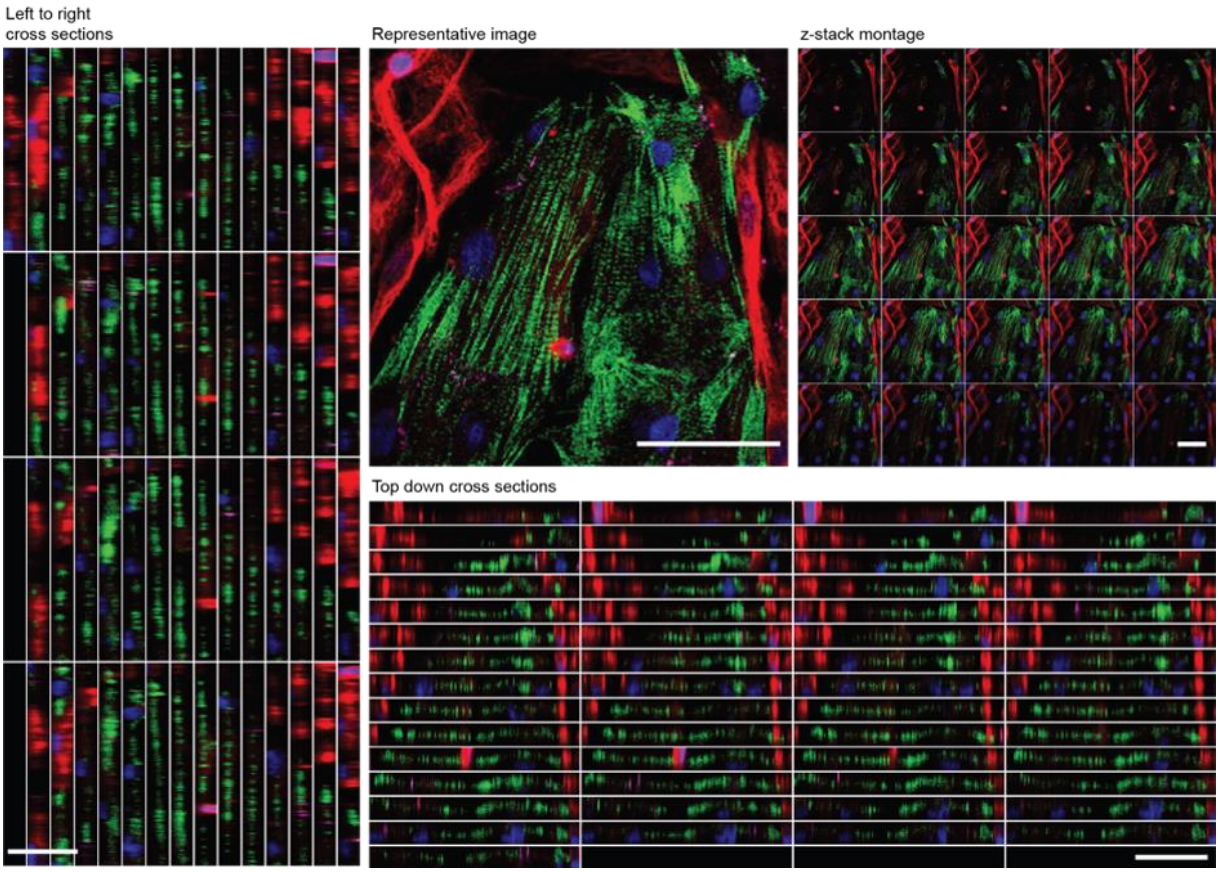

Figure 4.5 Immunohistochemistry images show both the cardiomyocytes and fibroblasts on a micro-supercapacitor-like device.

Cross sections (left to right and top down) and Z-stack montage views for images of the cardiac cells cultured on the device. Cells stained for cardiac troponin (CMs, green), connexin-43 (magenta), vimentin (fibroblasts, red) and DAPI (nuclei, blue). Scale bar, 50 μm. This experiment was repeated twice with similar results.

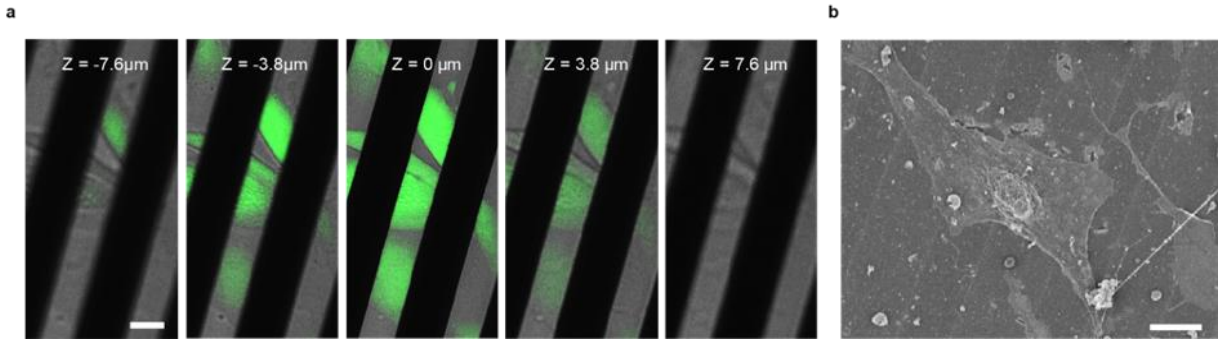

Figure 4.6 Representative confocal fluorescence and SEM images suggest that the interdigitated electrodes form subcellular interfaces with CMs.

(**a**) Representative Z-stack images of the cells loaded with fluo-4 dye adhered to the device. The electrodes are completely opaque, as represented by dark regions. Scale bar, 10 µm. The experiments were reproduced for more than five times with similar results. (**b**) Representative SEM image shows adhered cells on the device. Scale bar, 10 µm. The experiments were reproduced for more than five times with similar results. In all these images, the cells did not align with the device prong orientation. Therefore, there is a negligible topographical effect from the device substrate over the cell culture.

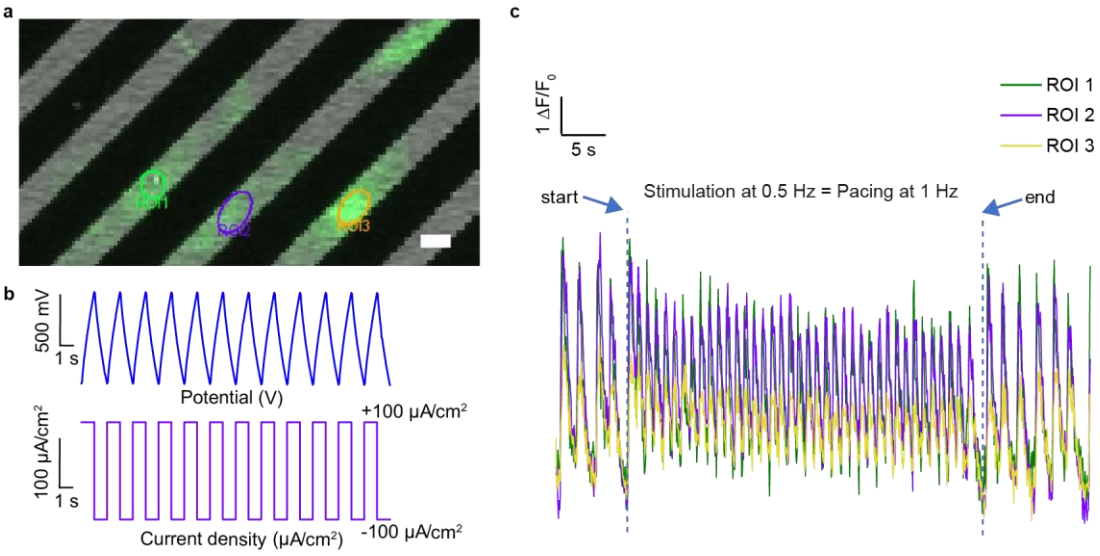

Figure 4.7 *In vitro* overdrive stimulation of cardiomyocytes shows immediate synchronization.

(a) Representative images of the cells recorded during stimulation at ROI regions (green, purple and yellow). Scale bar, 10 µm. (b) Typical input waveforms of the device during a stimulation process showing voltage (top) and current (bottom) applied to the cells. Input current frequency is 0.5 Hz, the stimulation time is ~40 s. (c) Intensity profiles of the marked ROIs during experiment. The intensity profile immediately synchronizes to 1 Hz. Overdrive stimulation was reproduced with similar results in three independent experiments.

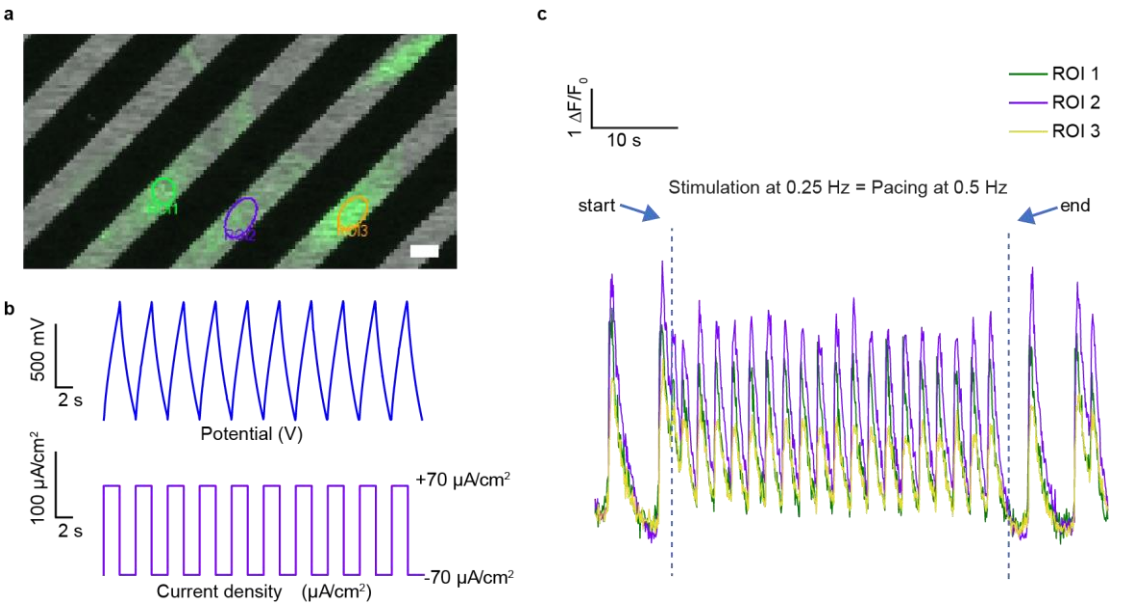

Figure 4.8 ***In vitro*** **overdrive stimulation of cardiomyocytes shows immediate synchronization**.

(**a**) Representative images of the cells recorded during stimulation at ROI regions (green, purple and yellow). Scale bar, 10 µm. (**b**) Typical input waveforms of the device during a stimulation process showing voltage (top) and current (bottom) applied to the cells. Input current frequency is 0.25 Hz, the stimulation time is ~40 s. (**c**) Intensity profiles of the marked ROIs during experiment. The intensity profile immediately synchronizes to 0.5 Hz. Overdrive stimulation was reproduced with similar results in three independent experiments.

Although this ability to perform overdrive pacing of CMs may have promising therapeutic applications, we also wanted to demonstrate the utility of the device for *in vitro* cellular manipulation that would allow for basic mechanistic investigations. To this end, we applied current stimulation with subthreshold amplitude, which did not elicit a direct overdrive pacing response. **Figure 4.4c** shows a field of view in which 5 CMs synchronized in 2 clusters were identified with

very low spontaneous activity (~0.2 Hz and 0 Hz). When a low amplitude current waveform was applied (5 times lower than for overdrive pacing), the CMs did not show an immediate response. However, when the stimulation was applied for a longer duration, a gradual increase in contraction was observed. After ~1900 s of stimulation, the cells were evidently 'upregulated' by the current stimulation and their contraction rate increased to the target stimulation rate of 1 Hz. **Figure 4.4d** shows representative calcium imaging traces from two regions of interest (ROI), before and during the training of the two cell clusters, and **Figure 4.4e** shows gradual increase in contraction frequency over time. These results resemble the gradual increase in the rate of electrical activity previously observed in CMs upon subthreshold optical stimulation[3]. While the cells within each cluster are synchronized throughout the training, the two clusters display negligible synchronization to each other before they reach the targeted frequency (**Fig. 4.9**). This fact suggests that the subthreshold training displays cellular level heterogeneity and the stochastic events may be involved in this process. Although a detailed understanding of the precise underlying mechanism here requires further rigorous investigation, we postulate that repetitive stimulation alters the resting membrane potential of the CMs to the point that they are sufficiently depolarized to elicit APs. Possible mechanism might relate to the 'memory effect', which refers to the way supra-threshold stimulation alters the excitability of cells and their resulting resting frequency[4]. Because the porous carbon-based devices operate via capacitive charge injection, we were able to pace or train the CMs in a biocompatible way without generating faradaic reactions which, also could cause electrode hydrolysis, increase the resistance over time, and in severe cases, cause device failure.

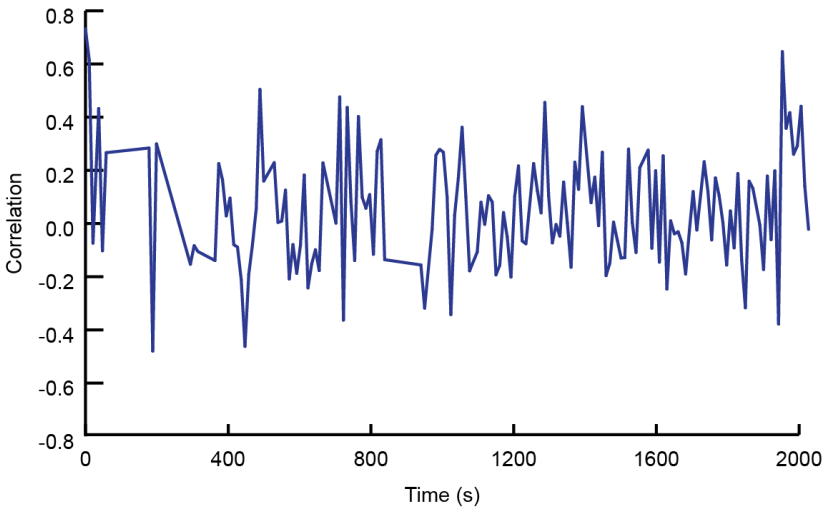

Figure 4.9 Correlation analysis between frequencies of cells in cluster 1 and cluster 2 suggests heterogeneity in sub-threshold training.

During entire experiment period no correlation or synchronization between cells was observed, which suggest that they are not electrically connected.

4.3 Biological Modulation at the Tissue and Organ Levels

Intact neural tissues represent highly crowded environments with non-neuronal factors, such as the extracellular matrix and glial interactions, that can influence neuronal activation. To determine whether the micro-supercapacitor-like device can modulate activity in intact neural circuits, we performed stimulation experiments on isolated mouse retinas. The laminated organization of the retina and its diverse neural circuit motifs make the retina an accessible model system to study brain circuit functions. Additionally, the use of retinal tissue allows us to stimulate physiologically relevant "input neurons," *i.e.,* the photoreceptors, and record activity from the "output neurons," *i.e.,* the retinal ganglion cells (RGCs) of a well-defined sensory circuit. In these experiments, we utilized retinas isolated from transgenic mice (*Slc17a6*$^{tm2(cre)Lowl}$*/Gt(ROSA)26Sor*$^{tm95.1(CAG-GCaMP6f)Hze}$) expressing the calcium indicator GCaMP6f in all RGCs[5,6]. This enabled simultaneous

monitoring of neural activity via multiple neurons. Micro-supercapacitor-like devices and interconnects were fixed on glass coverslips using glue and PDMS and used as bottoms for the retina perfusion chamber. Dissected retinas were then positioned with the photoreceptor layer facing the micro-supercapacitor-like device and the RGC layer facing upward **(Fig. 4.10a)**. Using two-photon laser scanning microscopy, we recorded calcium transients from RGCs while stimulating the photoreceptor layer with micro-supercapacitor modulation. We used square current waveforms applied across the interdigitated electrodes within the device to modulate the neural activity of the ganglion cell layer. Current flow direction was periodically switched by alternating between the anodic and cathodic phases every 3.5 s. Throughout the stimulation process, large periodic transients could be observed across several RGCs. During the anodic phase, RGCs exhibited large calcium transients, while during the cathodic phase, the calcium levels in RGCs returned to resting levels **(Fig. 4.10b)**. To corroborate that the micro-supercapacitor stimulation observed was due to activation of the glutamatergic pathway from photoreceptors to bipolar cells to RGCs, we applied a cocktail of glutamate receptor antagonists, including AP-5, L-AP4, and DNQX, to silence glutamate transmission in the retina. Upon glutamate receptor blockade, the large calcium transients could no longer be observed in RGCs during micro-supercapacitor stimulation (**Fig. 4c**). These results demonstrated that the charging and discharging stimulation at the supercapacitor-photoreceptor interface evoked changes in glutamate release from photoreceptor neurons and could therefore activate the retinal network.

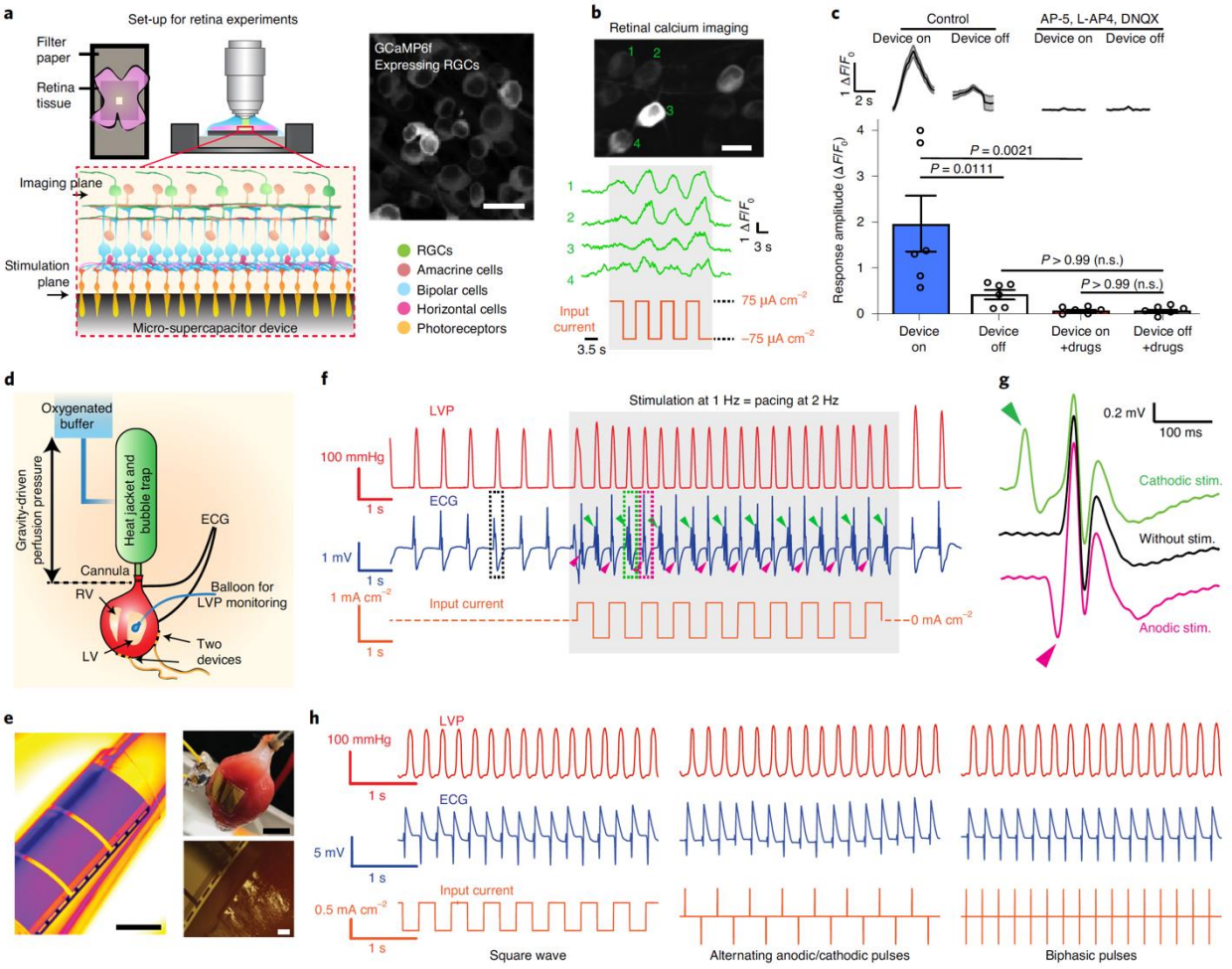

Figure 4.10 Biological modulation at the tissue and organ level.

(**a**) Left: schematic of the experimental setup for the retinal stimulation. Right: a max-intensity projection of RGCs expressing GCaMP6. Scale bar, 25 μm. (**b**) Top: a retinal calcium image showing activated RGCs upon the stimulation. Scale bar, 15 μm. Middle: representative calcium traces from individual RGCs (numbered in the upper image). Bottom: the input current density during the stimulation. Confocal images in **a** and **b** are representative field of views from four repeats. (**c**) Top: calcium transient traces represented as average ± standard error (s.e.m.) in both control and glutamate antagonist conditions. Bottom: the quantification of response amplitudes of calcium transients (mean ± s.e.m., n = 6 RGCs across various experimental conditions). Calcium transients from each RGC were averaged across five repeated measurements, and statistical

analyses were performed using pairwise one-way analysis of variance (ANOVA) with Bonferroni correction. Adjusted P values were indicated in the plot; n.s., not significant. (**d**) Schematic of the Langendorff perfusion system. ECG and LVP were monitored to show the effect of stimulation on the heart rate. (**e**) Images of a micro-supercapacitor-like device conforming around a cylindrical holder (left; scale bar, 2 mm) and around the curvilinear and contractile cardiac tissue (upper right; scale bar, 5 mm) with a close-up view (lower right; scale bar, 500 μm). Images in **e** are representative of more than ten independent experiments. (**f**) Representative LVP profiles and ECG recordings of the isolated heart stimulated at a frequency of 1 Hz. Input current density was synchronized to the corresponding stimulated portions of the LVP and ECG recordings. Dashed boxes and arrows are spontaneous APs (black) and APs that follow positive (green) and negative (pink) artifacts. (**g**) A closer look of the APs in the ECG recording with corresponding colours. (**h**) Representative LVP and ECG profiles of the isolated heart stimulated by 2 Hz square current waveform (left), 5 ms alternating pulses (middle), 1 ms biphasic pulses (right) to achieve pacing at 4 Hz. Presented results from the isolated heart stimulation are representative of three independent experiments using independent hearts and electrodes.

Next, we evaluated the bioelectronic stimulation in tissues and organs that required the traditional charge injection configuration. The rat heart contained a ~75 μm thick epicardium separating the CMs and the device[7]. Therefore, a single micro-supercapacitor-like device was not sufficient to accumulate the depolarizing charge. In these experiments, one porous carbon-based device (*i.e.*, working electrode) was placed on the left ventricular (LV) wall of a rat heart to apply different current waveforms, while the other device) was placed on the right ventricular (RV) wall (**Fig. 4.10d**). We found that the two porous-carbon device configuration is highly efficient as both

flexible devices form good contacts with the heart surface (**Fig. 4.10e**). We first applied anodic/cathodic current square waves with different frequencies as this can yield similar charging/discharging processes from a supercapacitor device (1 Hz, ± 0.5 mA/cm^2, **Fig. 4.10f**; 1.67 Hz, ± 0.4 mA/cm^2, **Fig. 4.11;** 2 Hz, ± 0.37 mA/cm^2, **Fig. 4.10h**; and 5 Hz, **Fig. 4.12**). Upon stimulation, the heart immediately contracted at double the stimulation rate (**Figs. 4.10f** and **4.10h**). This is similar to the observed *in vitro* pacing with a micro-supercapacitor device configuration, suggesting that both the anodic and cathodic stimulations from the working electrode can achieve a pacing effect. Due to the capacitive nature of our device and lack of faradaic charge injection, we hypothesize that the mechanism governing the electrical stimulation is similar to field coupling[8,9]. We observed positive/negative ECG artifacts during the stimulation (**Figs. 4.10f** and **4.10g**), while no artifact was associated with the spontaneous contraction. As the ECG was recorded from the aorta and the LV, the observed artifact may be attributed to the working electrode positioned on the LV. It should be noted that the artifact shapes and the positions are dependent on the device/ECG configurations, so they vary in different settings. As the elicited heart potentials were initiated near the onset of the anodic/cathodic phases of the square waves (**Fig 4.10h** left; **Fig. 4.13a**), we next shrank the duration for each phase while keeping the spacing of adjacent phases the same (*i.e.*, 250 ms). The results from the alternating anodic/cathodic pulses (5 ms, **Fig. 4.10h** middle; **Fig. 4.13b**) show effective overdrive pacing with 3.7 μC/cm^2 charge injection per phase/pulse. Finally, we attempted the electrical pacing with conventional charge-balanced biphasic pulses and achieved efficient overdrive pacing at 0.7 μC/cm^2 charge injection in 1 ms pulse width (**Fig. 4.10** right, **Fig. 4.13c**).

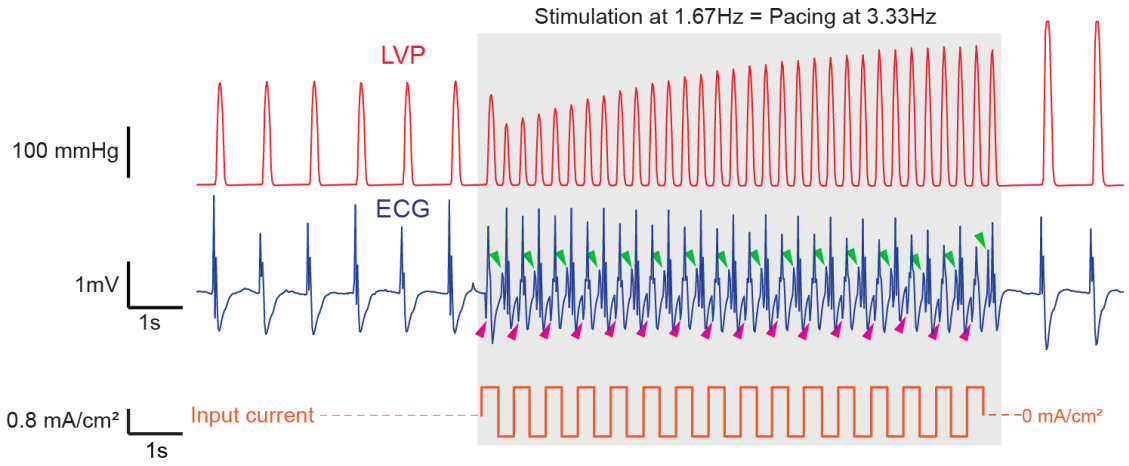

Figure 4.11 Representative LVP profiles and ECG recordings of the isolated heart stimulated at a frequency of 1.67 Hz show pacing at 3.33 Hz.

Arrows follow positive (green) and negative (pink) artifacts.

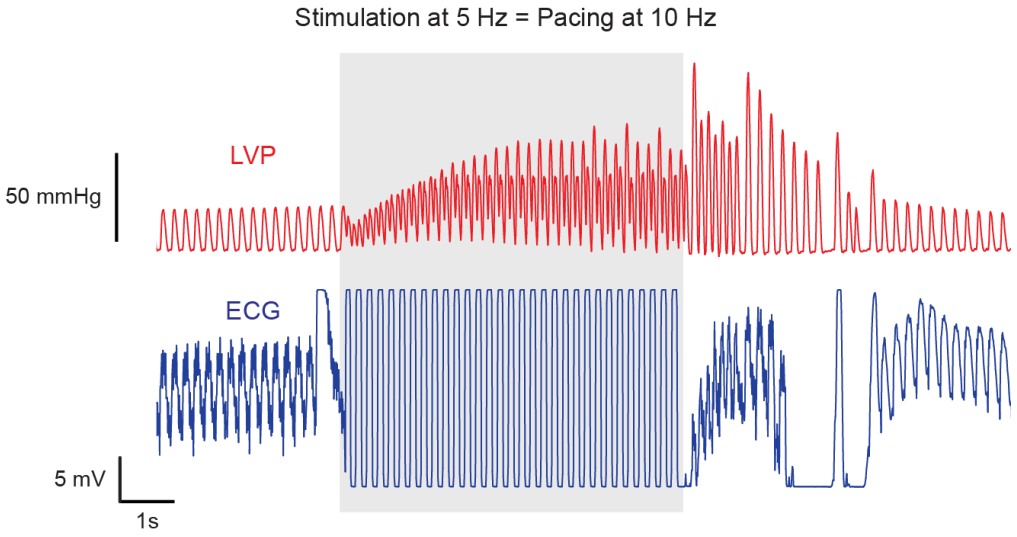

Figure 4.12 Representative LVP profiles and ECG recordings of the isolated heart show pacing at 10 Hz.

ECG signal is overtaken by the stimulation artifact and the pacing can be observed in LVP recording.

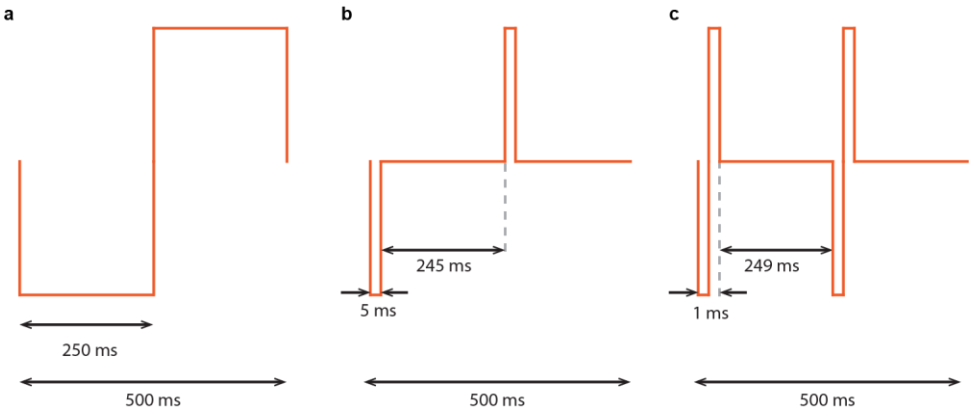

Figure 4.13 We used different input current waveforms in the isolated heart stimulations. Not to scale. (**a**) Continuous wave biphasic. Used in **Fig. 4h** (left). (**b**) Alternating pulses. Used in **Fig. 4h** (middle). (**c**) Biphasic pulses. Pulse is equally subdivided into 500 µs per phase. Used in **Fig. 4h** (right).

To demonstrate the utility of the porous carbon-based device for *in vivo* neuro-modulation applications, we interfaced it with sciatic nerves. We used an acute setting in which the device was interfaced with the exposed nerve. When one device was interfaced with the sciatic nerve and the other device was interfaced with the rat's body, we observed that the associated limb was clearly moving with every cathodic phase of the current injection. This was further validated by electromyography (EMG) recordings from the rat limb, which showed large potential spikes that were synchronized to the cathodic phase (**Figure 4.14**). Other functions of this micelle-based and self-assembled bioelectronics device may incorporate the flexible electrical sensing, as shown preliminarily in the ECG recording from isolated hearts (**Fig. 4.15**).

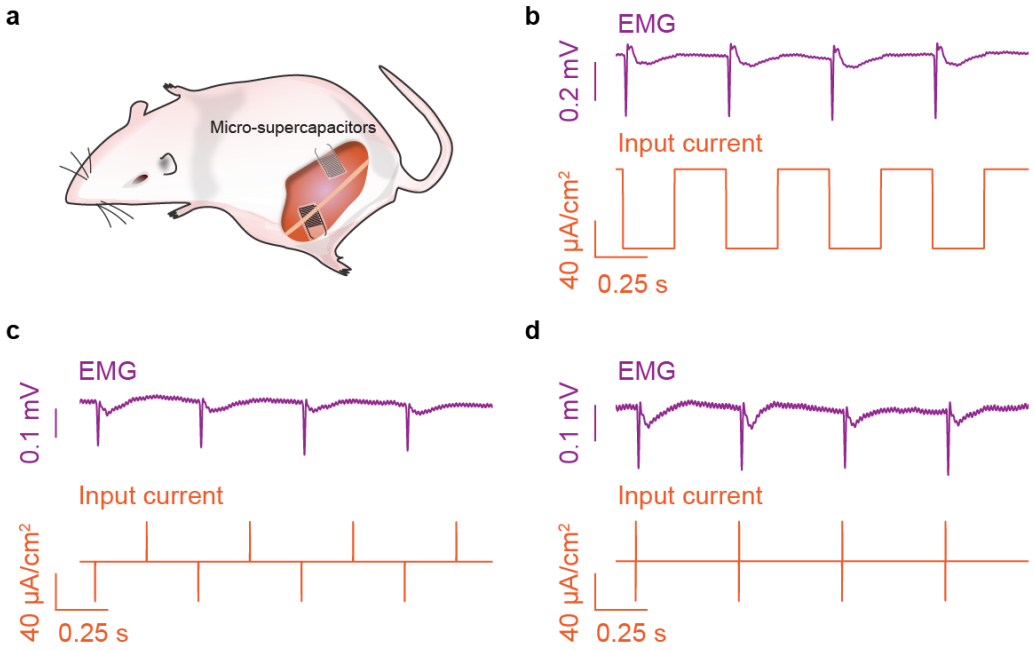

Figure 4.14 The porous carbon-based devices can be used for *in vivo* nerve stimulation.

(**a**) Schematic illustrating the *in vivo* experimental setup. The representative EMG recordings of the stimulated limb, and the corresponding input current for a 2 Hz stimulation using **(b)** continuous current wave, **(c)** 1 ms alternating pulses, and **(d)** 1 ms biphasic pulses. For alternating waveforms, it was apparent that only the cathodic phase could stimulate the sciatic nerve.

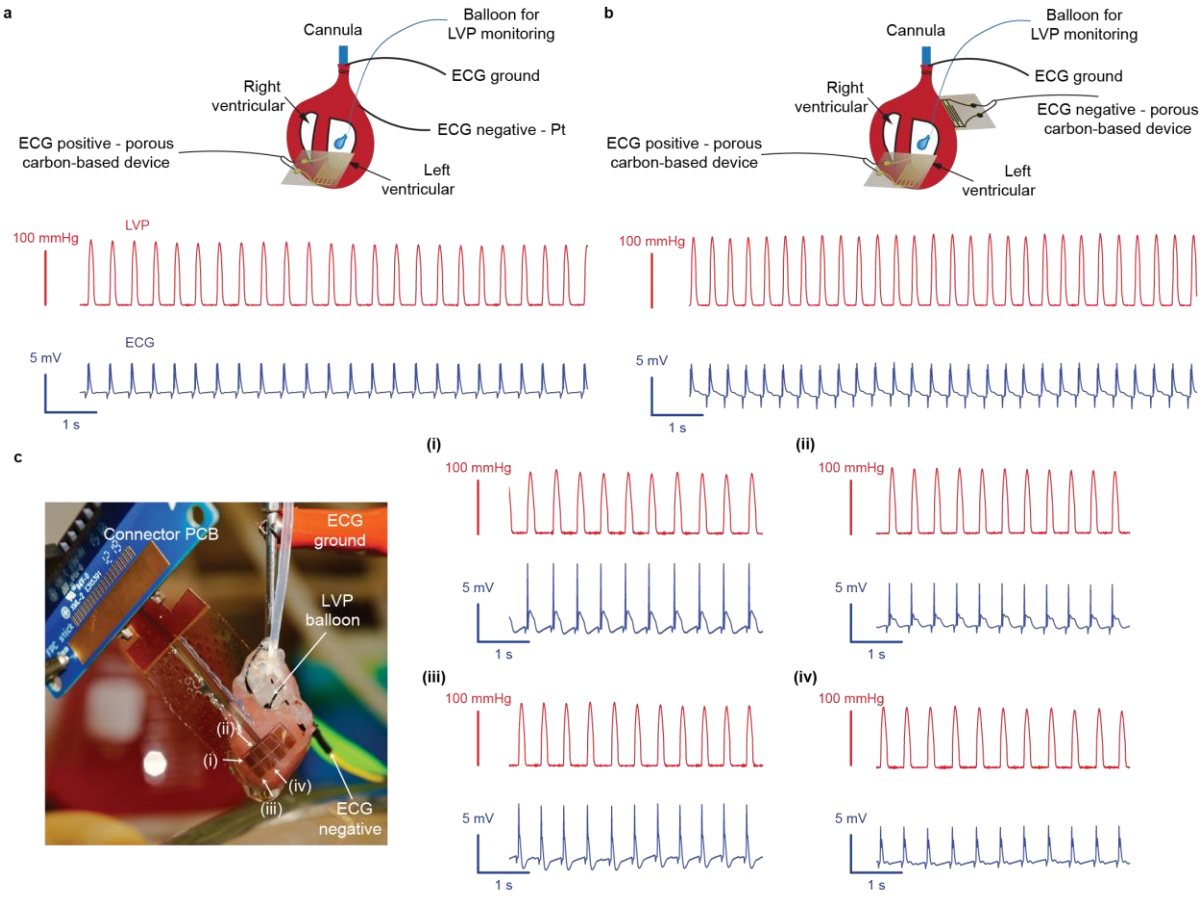

Figure 4.15 The porous carbon-based devices can be used for ECG recording of rat heart electrophysiology.

(**a**) Recording using large area carbon electrode as a positive lead. (**b**) Recording using large area carbon electrodes as positive and negative leads. (**c**) Photograph of multielectrode array positioned on rat heart (recording site approximately 4 mm^2) and (**i-iv**) recording from specific sites. Traces (**i-iv**) were recorded under at different time points, but without moving the electrode.

Finally, we showed that the porous carbon device can be used for bioelectrical recording. In the isolated heart model, we assembled ECG recording leads with positive lead at LV, negative at the aorta and ground at the cannula. We found that micro-supercapacitor-like device can successfully be used as a positive (**Fig. 4.15a**) or positive and negative leads (**Fig. 4.15b**) for ECG

recording. Additionally, we fabricated multichannel electrodes with reduced area per single recording site (4 mm^2 vs 40 mm^2 for large area device) (**Fig. 4.15c**), and demonstrated the recording from the individual site.

4.4 Summary

In this chapter, I have described the application of a carbon-based micro-supercapacitor-like device to biological modulation. The interdigitated electrode design allowed to control current flow through capacitive charging/discharging, demonstrating that alternative stimulation waveforms can be used for bioelectronic modulations in addition to the classical pulsed-based stimulation approaches. The device showed reasonable cytotoxicity *in vitro* and *in vivo,* and was successfully applied to stimulate cardiomyocytes and upregulate their contraction rate. The shallow electric field was applied to study neural circuits in a retina model. Finally, the material was used to successfully pace isolated hearts, stimulate sciatic nerves in a rat model, and record electrocardiography signals. Due to its low cost and biological compliance, this material represents a suitable candidate for use in devices for future electroceutical therapies.

4.5 Methods

Cell culture

Hearts were excised from P1-3 neonatal rats into ice cold HBSS (without Ca^{2+} or Mg^{2+}). The hearts were cut to small <1 mm piece, and then rinsed with HBSS to remove blood. A Pierce™ primary cardiomyocyte isolation kit (Thermo Fisher Scientific) was used for digesting the tissue according to manufacturer protocol. After isolation, the suspended cells were pre-plated for 2 h, allowing

fibroblasts to adhere to the tissue culture plate. Then the enriched CMs population was seeded onto the micro-supercapacitor device pre-treated with fibronectin (Sigma). The cells were allowed to sit in culture media (DMEM high glucose + 10% FBS, 1% Glutamax and 1% penicillin–streptomycin) for 24 h, then the media was changed to CM-specific media (DMEM high glucose + 10% FBS, 1% penicillin–streptomycin, and 0.1% growth supplement from isolation kit).

LIVE/DEAD Viability

CMs were cultured on the device for 3 days and then stained with green fluorescent calcein-AM (Life Technologies), red fluorescent ethidium homodimer-1 (Life Technologies) for 30 min. DAPI was included for nuclear counterstaining in dead cells. 100% EtOH treated cells for 20 min were included as a positive control. The as-stained cells were imaged using a Leica SP5 confocal microscope.

Nuclear staining assay

Primary rodent fibroblasts harvested from rat pup hearts (postnatal day 1-3) were seeded and cultured on top of sterilized carbon micro-supercapacitors with fibroblast culture medium (high glucose DMEM + 10% FBS) for 36 hours in an environment of 37°C and 5% CO_2. The seeded device was washed with PBS and then fixed with buffered 4% paraformaldehyde at room temperature. After permeabilization with 0.25% Triton X-100 in PBS, cells were counterstained with Hoechst 33342 (0.1 μg/ml) and imaged on Olympus inverted fluorescent microscope and Leica Confocal SP5 system. Positive control samples were prepared by treating fibroblasts with 1 mM hydrogen peroxide to induce apoptosis.

Lactate dehydrogenase (LDH)-cytotoxicity assay

Primary rodent fibroblasts harvested from rat pup hearts (P1-P3) were seeded and cultured on top of sterilized carbon micro-supercapacitors with fibroblast culture medium (high glucose DMEM + 10% FBS) in an environment of 37°C and 5% CO_2. The culture medium supernatant was harvested at 24 (day 1, D1) and 48 hours (day 2, D2). LDH activity in the medium supernatant was measured using Pierce LDH Cytotoxicity Assay Kit (Thermo, US). Five independent measurements were conducted in each condition. Cycloheximide (CHX) at the concentration of 10 μg/mL for 24 hours was used to induce cell death as a positive control for this assay. LDH cytotoxicity percentage was calculated by $(LDH_{sample} - LDH_{baseline})/(LDH_{max} - LDH_{baseline}) \times 100\%$,where$LDH_{sample}$ is the corresponding LDH release from the CHX-, device-, and SU-8-treated samples, $LDH_{baseline}$ is the spontaneous LDH release activity, and LDH_{max} is the maximum LDH activity detected in whole cell lysates.

Evaluation of *in vivo* biocompatibility in mice

A piece of carbon micro-supercapacitor (0.5 cm × 0.5 cm) was surgically implanted under the dorsal skin of 6 to 8-week-old C57BL/6J mice through incisions, which were later closed with sutures. Mouse body weights were recorded on a weekly basis. At 1 or 4 weeks, mice were euthanized, and skin tissue surrounding the implant site was excised and fixed with buffered formalin for histology. The excised tissues were processed and stained with hematoxylin and eosin (H&E) for histopathological evaluation at university human tissue resource centre.

Device connections for the bioelectrical stimulations

Devices were generally connected in a two-electrode (*i.e.*, working electrode and counter electrode) configuration, where the counter electrode was connected to the ground. Square current waveforms (**Figs. 4.4b, 4.4e, 4.10b**, **4.10f,** and **4.10h** (left); **Figs.4.11, 4.12a, and 4.14**) were delivered using a source meter (Keithley 2636A) controlled using a LabVIEW program. Current pulses (**Figs. 4h**, middle and right; **Figs. 4.13b-c**) were delivered using a potentiostat (SP-200, BioLogic) using EC-Lab Express software. The electric potential was reported as the potential between the two electrodes. In the *in vitro* cardiac training (**Figs. 4.10b-e**, **Figs. 4.7-4.9**), the square current waveforms were applied to the two interdigitated electrodes within the same carbon micro-supercapacitor-like device (*i.e.*, one interdigitated electrode as the working electrode and the other interdigitated electrode as the grounded counter electrode). In the *ex vivo* retinal experiments **(Fig. 4b)**, the stimulation of isolated hearts (**Figs. 4f.10** and **4.10h**; **Figs. 4.11** and **4.12**) and sciatic nerves (**Fig. 4.14**), we used two carbon micro-supercapacitor-like devices (*i.e.*, with one device as the working electrode, and the other device as the grounded counter electrode). For the traces reported in this article, the square current waveforms or the current pulses were applied *between* the two macroscopic devices.

Calcium imagin

CMs were treated with calcium sensitive dye (2 µM Fluo-4, AM, cell permeant, Thermo Fisher Scientific) for 30 min at 37 °C. Cells were rinsed and incubated for 30 min to allow complete de-esterification. The treated cells were then visualized with a Leica SP5, STED-CW Super-resolution Laser Scanning Confocal. Movies showing fluo-4 fluorescence in cells and colonies were segmented by hand in ImageJ, using the built-in ROI manager to generate a binary mask that was

true for every pixel that was within an oscillatory cell. Normalized change in fluorescence $\Delta F/F_0$ movies were produced using a freely available ImageJ plugin. The remainder of the analysis was conducted using a home-built routine written in Python 3.7. For a given cell at a given time point, the signal was calculated as the average $\Delta F/F_0$ pixel intensity within the cell. The full length of the signal was subdivided into sections of 100 frames duration, for frequency and correlation analysis. Changes in oscillation frequency for individual cells and groups thereof were characterized by plotting the magnitude of the Fourier transform of each section and observing the frequency with the highest power. Because some cells were not oscillatory for some of the time sections, we implemented a power threshold of 150 and only plotted frequencies exceeding this threshold.

Immunocytochemistry

Primary cardiac cells were cultured onto devices for 3 days and were fixed (4% paraformaldehyde), permeabilized (0.2% Triton-X), and then blocked (2% BSA solution) for an hour to prevent nonspecific binding. Cells were incubated overnight at 4 °C with rabbit anti-cardiac troponin I antibody (1:400 in 2% BSA), chicken anti-vimentin antibody (1:500 in 2% BSA), and mouse anti-Connexin 43 antibody (1:100 in 2% BSA). Cells were rinsed and subsequently stained for 1 h with Alexa Fluor 488 anti-rabbit, Alexa Fluor 594 anti-chicken, and Alexa Fluor 647 anti-mouse secondary antibodies (1:250). DAPI (Invitrogen, P36931) was used to label the nuclei. Stained cells were imaged using the Leica SP5 Confocal and analysed using ImageJ.

Retina slice

Vglut2-IRES-Cre mice (016963-*Slc17a6*$^{tm2(cre)Lowl}$*/J*) and floxed *Ai95(RCL-GCaMP6f)-D* mice (028865-*Gt(ROSA)26Sor*$^{tm95.1(CAG-GCaMP6f)Hze}$*/J*) were acquired from The Jackson Laboratory and

were crossed to each other in the laboratory of Dr. Wei to obtain hybrid *Vglut2-IRES-Cre/GCaMP6f* transgenic mice. Mice of both sexes (postnatal days 21-35) were used for retinal calcium imaging experiments. Mice were anesthetized with isoflurane and decapitated after dark adaptation. Under infrared illumination, retinas were isolated from the pigment epithelium in oxygenated Ames' medium (Sigma-Aldrich, A1420), cut into dorsal and ventral halves, and mounted on filter papers as described in the literature[10]. Retinas were kept in the dark at room temperature in Ames' medium bubbled with 95% O_2/5% CO_2 until use (0–7 h). Glass coverslips with adhered micro-supercapacitor devices were used as the bottoms of the imaging chamber. During imaging, retinas were placed on top of micro-supercapacitor devices and gently pressed against the surface using a platinum (Pt) wire weight and perfused with oxygenated Ames at 32–33°C. Cells were visualized with infrared light (>900 nm) and an IR-sensitive video camera (Watec). Calcium transients from GCaMP6f expressing retinal ganglion cells were recorded by a custom-built two-photon microscope (Bruker) equipped with a Ti:sapphire laser (Chameleon Ultra II; Coherent Technologies) tuned to 920 nm[11]. Data were acquired using PrairieView software from a 100 μm × 100 μm field of view with an acquisition rate of ~15 Hz. ROIs were manually drawn in ImageJ to enclose the soma of each GCaMP6f-expressing cell and a background region where there was no detectable GCaMP6s expression. Using custom MATLAB scripts, we calculated the average intensity over time for all ROIs and subtracted the background trace from light-responsive somatic traces to remove noise. The calcium traces were resampled to 75 Hz and smoothed using a moving average sliding window of 25 data points (~333 ms). For each stimulation protocol, the average dF/F_0 was calculated for every cell.

Isolated heart

An adult rat was heparinized (1,000 IU/kg IP) and anesthetized using open-drop exposure of isoflurane in a bell jar configuration. The heart was removed and placed in ice cold HBSS buffer, and the aorta was cannulated in preparation for use in a Langendorff setup. Oxygenated HEPES-buffered Tyrode's solution (containing, in mM, NaCl 126, KCl 5.4, Glucose 10, HEPES 10, $MgCl_2$ 1, $CaCl_2$ 2, $MgSO_4$ 1.2, NaH_2PO_4 0.39; bubbled with 99.5% O_2; pH 7.3) was perfused through the cannulated aorta. The perfusion was passed through a heating coil and bubble trap (Radnoti), and the heart was placed in a water-jacketed beaker (Fisher Scientific) to maintain a temperature of 37°C. The perfusion pressure was maintained at 80–100 mmHg by adjusting the height of the IV bag containing the perfusion buffer. The sinoatrial node along with the atria were removed, which resulted in a slow atrioventricular node pace (~1 Hz). The perfusion and left ventricular pressures (LVP) were monitored using a BP-100 probe (iWorx) connected to the perfusion line and a water filled balloon inserted to the LV, respectively. For ECG recordings, needle electrodes were positioned on the LV wall and aorta and connected to a C-ISO-256 preamplifier (iWorx). All signals (perfusion, LVP and ECG) were amplified using an IA-400D amplifier (iWorx) and interfaced with a PC using a DigiData 1550 digitizer with Clampex software (Molecular Devices). Two devices were placed on the heart; one below the heart's apex, and the other covering the LV wall. Recordings from supercapacitor devices (**Fig. 4.15**) were achieved with C-ISO-256 preamplifier (iWorx) as in a regular ECG setup, but with devices connected as input electrodes.

In vivo rat nerve stimulation

Adult rats were deeply anesthetized with isoflurane (3-4%). The fur was removed from the hindquarters using a surgical clippers and hair removal cream. A semi-circular incision across the midline was made in the skin, and the fascial plane was opened between the gluteus maximus and the anterior head of the biceps femoris, thereby exposing the sciatic nerve. In this setting, two devices were used. One device was placed under the sciatic nerve and the other under the rat's skin.

Animal subjects

Mice and rats were housed in the animal facility of the University of Chicago. The animal room was maintained at a humidity of 40-60 % and a temperature of 18-23 °C under a 12-h light/12-h dark cycle. The animals were allowed free access to food and water. All animal procedures were approved by the Institutional Animal Care and Use Committees (IACUC) of the University of Chicago.

General data processing

Analysis of numerical data was performed using Microsoft Excel, OriginPro or Python scripts. Statistical analyses were performed using GraphPad Prism. Plotting was performed using OriginPro, Adobe Illustrator or Python scripts using matplotlib library.

4.6 Bibliography

1 Tian, B. *et al.* Macroporous nanowire nanoelectronic scaffolds for synthetic tissues. *Nat Mater* **11**, 986-994, doi:10.1038/nmat3404 (2012).

2 Liu, J. *et al.* Syringe-injectable electronics. *Nature nanotechnology* **10**, 629-636, doi:10.1038/nnano.2015.115 (2015).

3 Parameswaran, R. *et al.* Optical stimulation of cardiac cells with a polymer-supported silicon nanowire matrix. *Proceedings of the National Academy of Sciences of the United States of America* **116**, 413-421, doi:10.1073/pnas.1816428115 (2019).

4 Hund, T. J. & Rudy, Y. Determinants of excitability in cardiac myocytes: mechanistic investigation of memory effect. *Biophysical journal* **79**, 3095-3104, doi:10.1016/S0006-3495(00)76544-1 (2000).

5 Martersteck, E. M. *et al.* Diverse Central Projection Patterns of Retinal Ganglion Cells. *Cell Rep* **18**, 2058-2072, doi:10.1016/j.celrep.2017.01.075 (2017).

6 Ellis, E. M., Gauvain, G., Sivyer, B. & Murphy, G. J. Shared and distinct retinal input to the mouse superior colliculus and dorsal lateral geniculate nucleus. *J Neurophysiol* **116**, 602-610, doi:10.1152/jn.00227.2016 (2016).

7 Jenkins, M. W. *et al.* Optical pacing of the adult rabbit heart. *Biomed Opt Express* **4**, 1626-1635, doi:10.1364/BOE.4.001626 (2013).

8 Copene, E. D. & Keener, J. P. Ephaptic coupling of cardiac cells through the junctional electric potential. *Journal of Mathematical Biology* **57**, 265-284, doi:10.1007/s00285-008-0157-3 (2008).

9 Sperelakis, N. & McConnell, K. Electric field interactions between closely abutting excitable cells. *IEEE Engineering in Medicine and Biology Magazine* **21**, 77-89, doi:10.1109/51.993199 (2002).

10 Wei, W., Elstrott, J. & Feller, M. B. Two-photon targeted recording of GFP-expressing neurons for light responses and live-cell imaging in the mouse retina. *Nature protocols* **5**, 1347-1352, doi:10.1038/nprot.2010.106 (2010).

11 Denk, W. & Detwiler, P. B. Optical recording of light-evoked calcium signals in the functionally intact retina. *Proceedings of the National Academy of Sciences of the United States of America* **96**, 7035-7040, doi:10.1073/pnas.96.12.7035 (1999).

Chapter 5

Development of Stain Etching for Synthesis of Nanostructured Photojunctions in Silicon Membranes

Research study presented in this chapter is expected for publication in Prominski, A., Shi, J., Li, P., Yue, J., Lin, Y., Park, J., Tian, B. & Rotenberg, M. Y. "Porosity-based heterojunctions enable leadless optoelectronic modulation of tissues." Nature Materials (2022).

5.1 Introduction

Advances in the synthesis and fabrication of flexible bioelectronic devices significantly minimized the biochemical mismatch between the artificial devices and biological tissue[1-3]. However, the leads of even the most flexible devices can still lead to the development of serious complications such as infection[4-6] and thrombosis[5,7]. We can resolve such limitations by applying leadless biomodulation techniques utilizing energy delivery through the electromagnetic [8-12]. Promising are applications of near-infrared light sources which can partially penetrate through tissues. The most studied approach to light-based stimulation involves the application of optogenetics[13-15]. However, this approach is limited to ultraviolet and visible wavelengths and requires the application of genetic modifications, which limits its potential for clinical translation.

An alternative approach to harvesting light for stimulation is applications of photoelectrochemical devices[10-12]. Most of such designs involve the fabrication of either p-n or p-i-n diode junctions through variation of doping in the successive layers of the semiconductor.

An alternative yet relatively unexplored strategy is the creation of nanoporous/non-porous semiconductor heterojunctions[16-18]. In such heterojunctions, band diagrams enable electron-hole separation and photocurrent generation similarly to classical heterojunctions (**Fig. 5.1**). Nanoporous/non-porous heterojunctions are a promising candidate as it yields a pure semiconductor interface and potentially more deformable surface due to the presence of nanoporosity[19,20].

In this chapter, I will describe the development of a fast and efficient method for obtaining pure-silicon porosity-based heterojunctions outperforming previously described gold-decorated p-i-n membranes. I have discovered that combining stain etching and high-power oxygen plasma treatment allows achieving strong photoelectrochemical currents without the need for dopant modulation. This method enables the creation of heterojunctions through simple wet etching without the need for expensive instrumentation. I will begin by exploring the material surface morphology and its internal structure. I will follow with the optimization of stain etching conditions through screening of stain etching conditions. The chapter will conclude with the investigation of the electrochemical performance of the material, identification of redox reactions present at the interface, origins of strong photovoltaic effects, material stability in a salt solution and possible methods of its improvement.

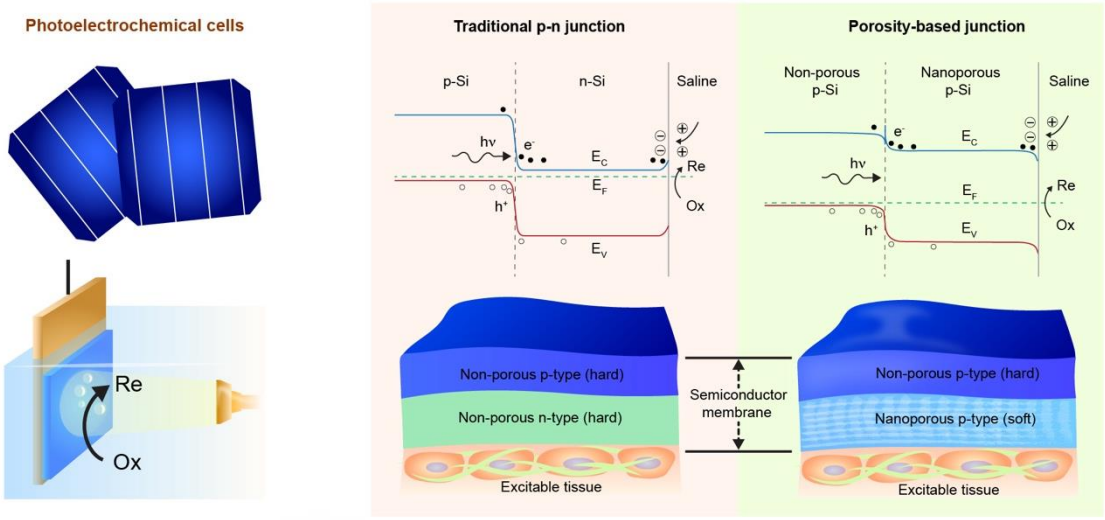

Figure 5.1 Nanoporous/non-porous silicon materials enable efficient photoelectrochemical effects and their soft surface structure makes them suitable for application in biointerfaces. Diodes are the key building blocks for solar cells and photoelectrochemical cells. The p-n junction creates built-in electrical field that separates the light-generated electrons and holes. In a photocathodic reaction, the electrons can reach the surface of an n-type silicon for reduction reactions. A difference in porosity can create a diode-like band alignment in a p-type silicon. This heterojunction demonstrates strong photoelectrochemical properties without the need for dopant modulation. Moreover, the porous surface yields a softer biointerface, that may further reduce the biomechanical mismatch.

5.2 Materials Synthesis and Structure Characterization

Stain etching is a type of electroless etching enabled by hole injection from strong oxidants in solution phase into the valence band of semiconductors[21]. Stain etching can produce different types of porous structures on the surface of silicon, and this porous silicon has been explored as coating layers in photovoltaics, photoluminescent agents in bioimaging, and active electrode components

in lithium batteries. Porous silicon has an enlarged bandgap compared with bulk silicon[16]; however, the photoelectrochemical performance of a nanoporous silicon/non-porous silicon heterojunction has not been leveraged for any bioelectronics applications. Instead, the focus of silicon nanostructuring was aimed for improving light absorbance and for reducing surface impedance[22]. Moreover, the field has been engulfed by efforts focused on metal-assisted chemical etching, which have produced many nanostructures from photolithography-defined metal masks[23]. However, while metal-assisted etching can be used to obtain a variety of morphologies, the semiconductor-metal junctions introduce additional complexity to the system. Thus, the benefits of metal-free self-limiting etching fabrications should not be overlooked, as the simplicity of process and purity of material can lead to improved biocompatibility and stability.

We used metal-free nitric acid/hydrofluoric acid-based etching to generate nanoporous/non-porous silicon heterojunctions directly in p-type crystalline silicon. Scanning electron microscopy (SEM) showed the formation of porous structures and micro-sized pillars on the surface of the silicon (**Fig. 5.2a**). The sponge-like pore morphology was independent of etching time (**Fig. 5.3**), but the pillars tended to grow and coalesce over time (**Fig. 5.4**). Pillar height was determined by atomic force microscopy to be in the range of hundreds of nanometers (**Fig. 5.2b**). We attribute the formation of micropillars to the coalescence of hydrogen bubbles (self-masking process), which results in hierarchical surface morphology (**Fig. 5.2c**). Cross-sectional microscopy showed that while the thickness of the nanoporous layer correlated poorly with etching time, the microstructured pillars grew continuously during etching (**Fig. 5.5**). The micropillars formed during etching may contribute to enhanced photoelectrochemical properties through increased surface light trapping[22].

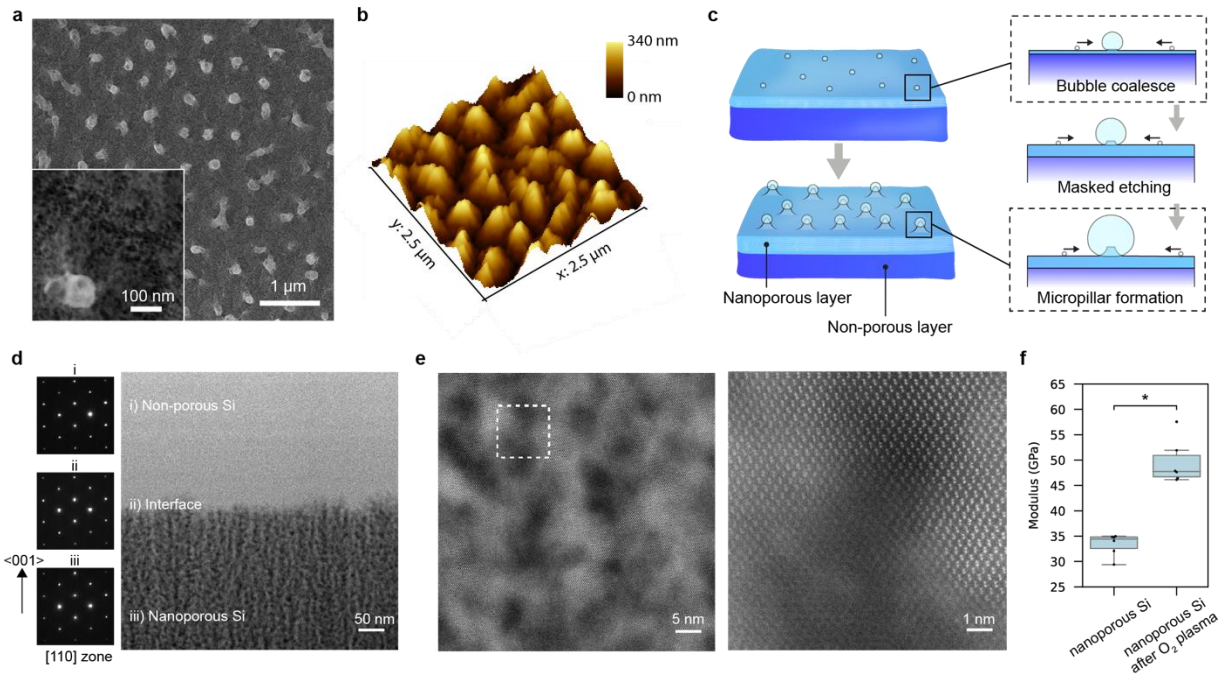

Figure 5.2 Microscopy analysis of the material structure.

(a) Scanning electron microscope image shows porosification of the material surface and formation of microscale pillars. Inset shows porous surface. (**b**) Three-dimensional reconstruction of the material surface from atomic force microscopy (AFM) scan shows that the height of the pillar-like structures is hundreds of nanometers. (**c**) Formation of micropillars can be attributed to the coalescence of hydrogen bubbles during wet etching. Schematic presents the proposed model of self-masking leading to pillar formation. (**d**) Scanning transmission electron microscopy (STEM) image shows the interface between the non-porous and nanoporous silicon in the material. Selected area electron diffraction patterns taken on different material domains show the same crystalline diffraction pattern and no signs of amorphization. (**e**) High-magnification STEM images show crystallinity in the nanoporous region. Characterisation was performed on samples etched for 1 min in 1% HNO_3 in HF (v/v). (**f**) Elastic modulus of nanoporous silicon samples. Boxes bind interquartile range (IQR) divided by the median; whiskers extend 1.5 ± IQR. All

datapoints are plotted. Statistics are calculated using Student's t-test. p-values for comparisons are shown: * $p < 0.001$. All datapoints are plotted.

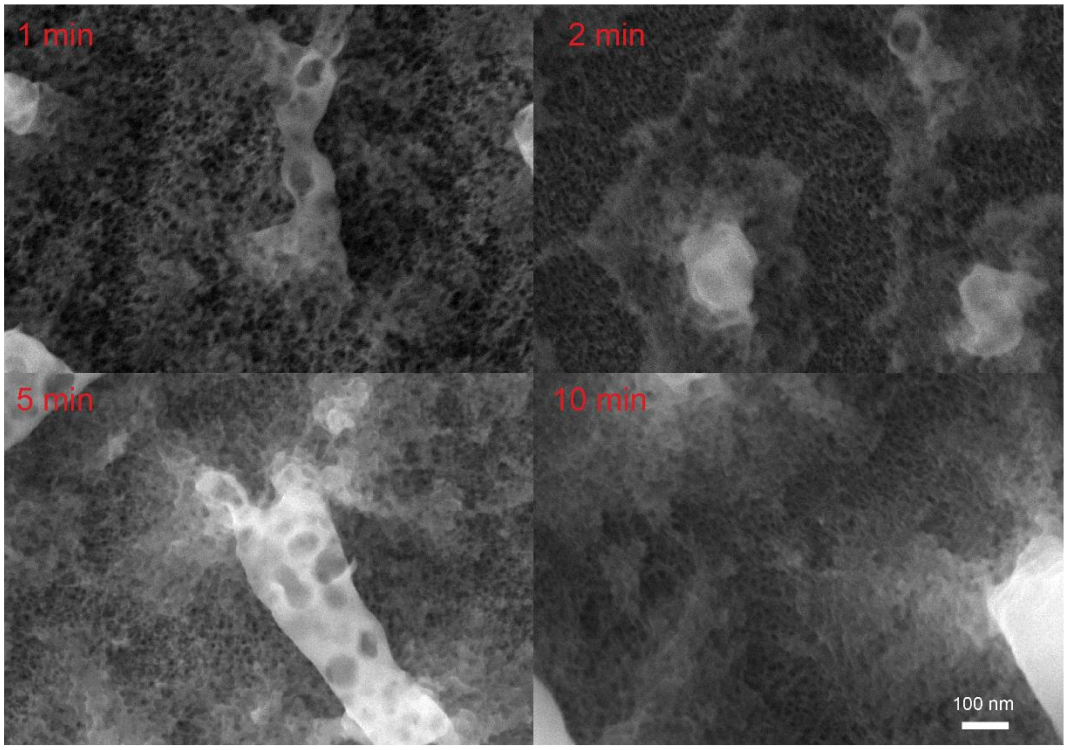

Figure 5.3 Scanning electron microscopy analysis of the wafer surface after etching with 1% nitric acid for a specified amount of time.

High magnification images show that the sponge-like morphology of the pore surface is not affected by the etching time.

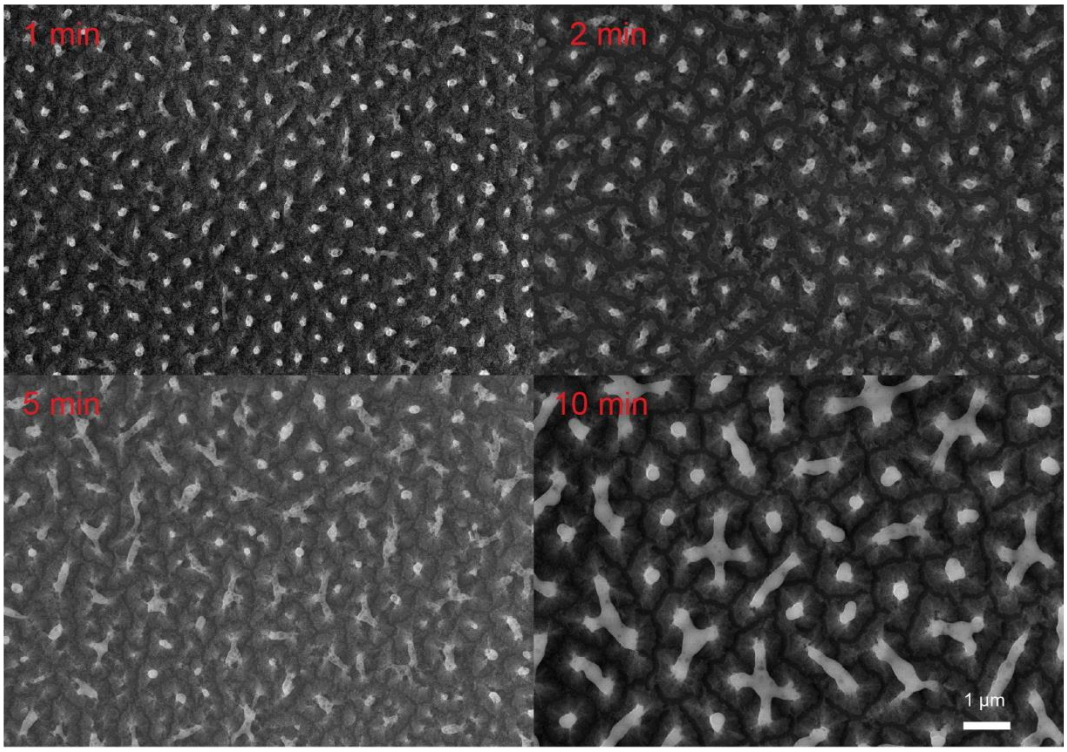

Figure 5.4 Scanning electron microscopy analysis of the wafer surface after etching with 1% nitric acid for a specified amount of time.

Low magnification images show growth and eventual coalescence of the microscale pillar-like structures.

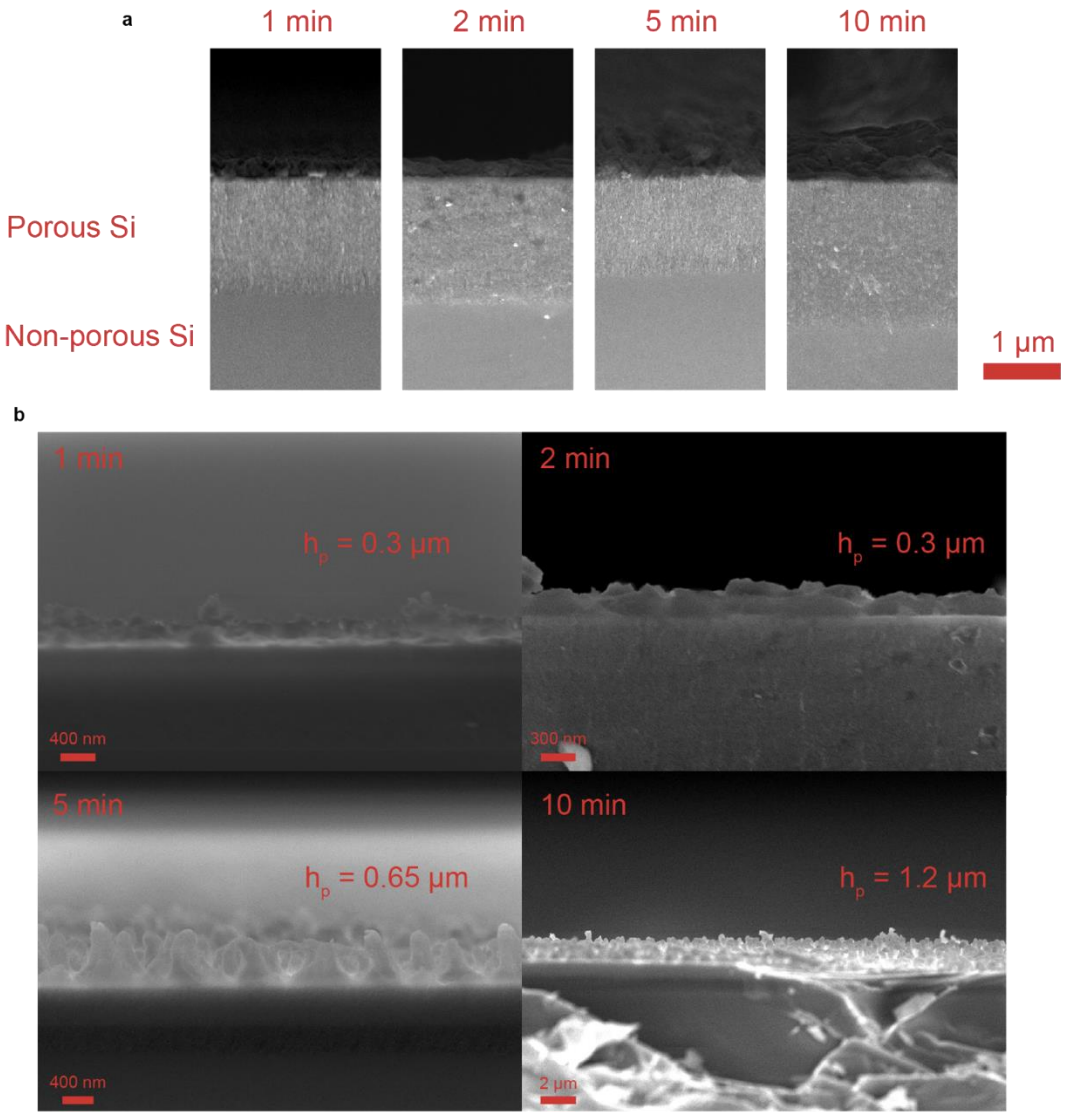

Figure 5.5 Cross sectional scanning electron microscopy images of stain etched silicon substrates using 1% nitric acid.

(**a**) High magnification images show formation of porous silicon layer in which its thickness does not increase with the etching time. (**b**) Low magnification images show growth of microscale pillar-like structures with the increased etching time. h_p – approximate height of the pillar-like structures.

Next, we used scanning transmission electron microscopy (STEM) to further understand the microscopic structure of the material. STEM images showed a sharp interface between nanoporous and non-porous domains in a pure silicon sample (**Fig. 5.2d**). Selected area electron diffraction patterns revealed that both domains and their interface were a coherent single crystal. High-magnification STEM images (**Fig. 5.2e**) further confirmed the crystalline lattice of the nanoporous silicon domain. A coherent single-crystal structure yields efficient charge transport due to the absence of amorphous regimes, while the nano-sized features in the nanoporous domain produce the band shift necessary to enable diode-like behaviour (**Fig. 5.1a**) through the quantum confinement effect.

We used indentation to study the mechanical properties of the nanoporous layer. We determined the elastic modulus of the nanoporous silicon layer to be 33 ± 2 GPa (**Fig. 5.2f, Fig. 5.6**), which is smaller than that of single crystalline silicon[24]. Oxygen plasma treatment increased the modulus to 50 ± 4 GPa (**Fig. 5.2f**), which suggests that oxidation of the nanoporous silicon may have mitigated the mechanical impact of the structural defects in silicon by introducing the atomic- or nanoscale oxide phase. Additionally, we used spectroscopic ellipsometry to determine the uniformity of the porous layer. The high homogeneity of elliptical properties can be found locally on a surface area of sub-millimetre scale in the material. However, when larger areas of over 1 mm were scanned, larger differences were observed, probably due to changes in the material roughness (**Fig. 5.7**). However, such difference does not seem to affect the photoelectrochemical properties of the material which were found to be rather uniform as described in the following sections.

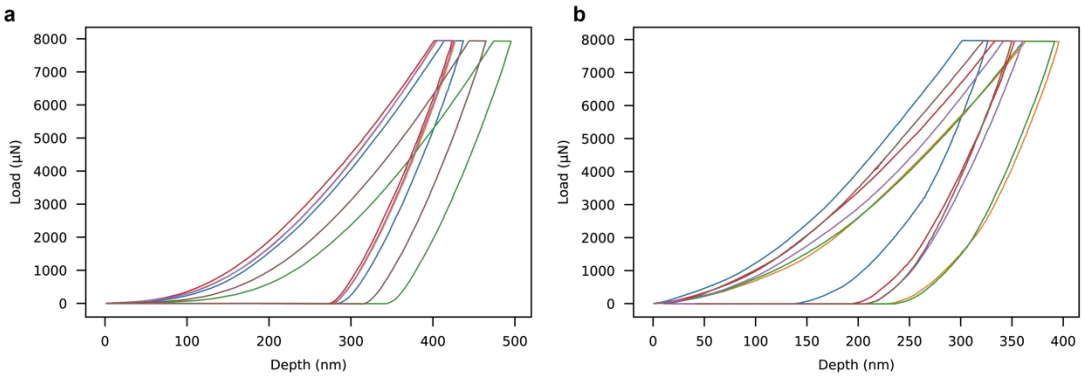

c

nanoporous Si		nanoporous Si + O_2 plasma	
Modulus (GPa)	Hardness (GPa)	Modulus (GPa)	Hardness (GPa)
34.08	2.12	57.56	3.77
34.85	2.25	47.63	2.41
29.39	1.60	46.43	2.51
34.99	2.31	47.87	3.34
34.77	2.27	46.13	3.20
32.08	1.84	51.93	3.27

Figure 5.6 Nanoindentation measurement.

Load-unload curves for **(a)** nanoporous Si, and **(b)** plasma-treated nanoporous Si. **(c)** Summary of calculated mechanical properties. For each group, 3 positions were measured on 2 samples for the total of 6 measurements.

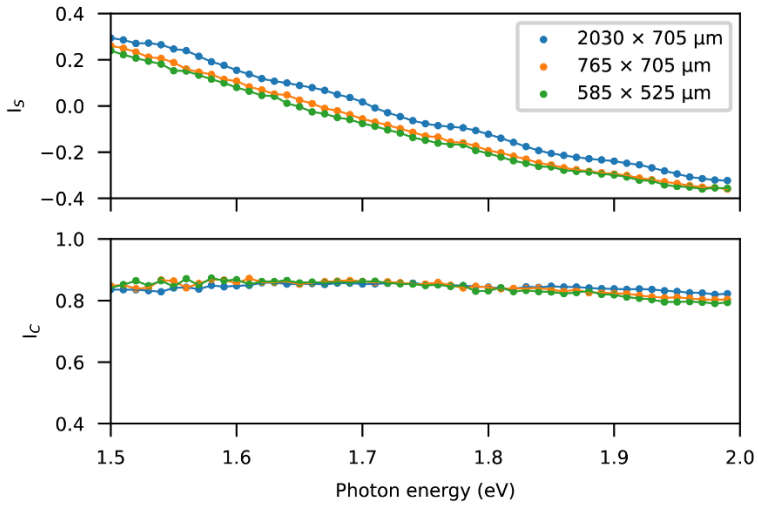

Figure 5.7 Spectroscopic ellipsometry measurement of porous silicon sample.

Polarization state components I_S and I_C were recorded using different spot sizes in the wavelength range of 1.5-2.0 eV. I_S and I_C are parameters directly measured by the spectroscopic ellipsometer that are often transformed into Ψ and Δ components for fitting into models of materials optical constants. Both parameters are sensitive to the local changes in the optical constants and recorded parameters are representative of the material volume irradiated by the selected spot size. The small difference between values measured using large and small spot sizes suggests good uniformity of the porous layer on the millimeter scale in the entire volume.

5.3 Stain Etching and Oxygen Plasma Treatment in the Photoelectrochemical Current Generation

To create a highly efficient photoelectrochemical silicon surface, we investigated different stain etching conditions and oxygen plasma treatment. We used our previously reported patch-clamp photoresponse measurement setup (**Fig. 5.8a**) to screen a large set of etching conditions on bulk silicon wafers and silicon membranes[25]. In our analysis, we focused on the total charge injection

over the illumination period, and the contributions coming from capacitive and faradaic currents (**Fig. 5.8b**) determined from the numerical analysis of recorded current transients. For each etching condition, we performed measurements before and after oxygen plasma treatment. **Figure 5.8c** shows photocurrents achieved using 1% (v/v) nitric acid in concentrated (50%) hydrofluoric acid. We have found that the majority of the injected charge originates from the capacitive effect and faradaic currents account only for 4% of the total charge and less if shorter light pulses are used. Oxygen plasma treatment enhanced the photocurrents for etching times between 1 and 20 min, with comparable saturation levels. The time-independence of the achieved photocurrents may be due to the self-limiting nature of the stain etching process; the valence band of the porous silicon becomes significantly low such that hole injection and over-etching are inhibited. We found that even 10 s of stain etching was sufficient to transform non-photoresponsive p-type silicon wafers into strong photoresponsive materials (**Fig. 5.8d**).

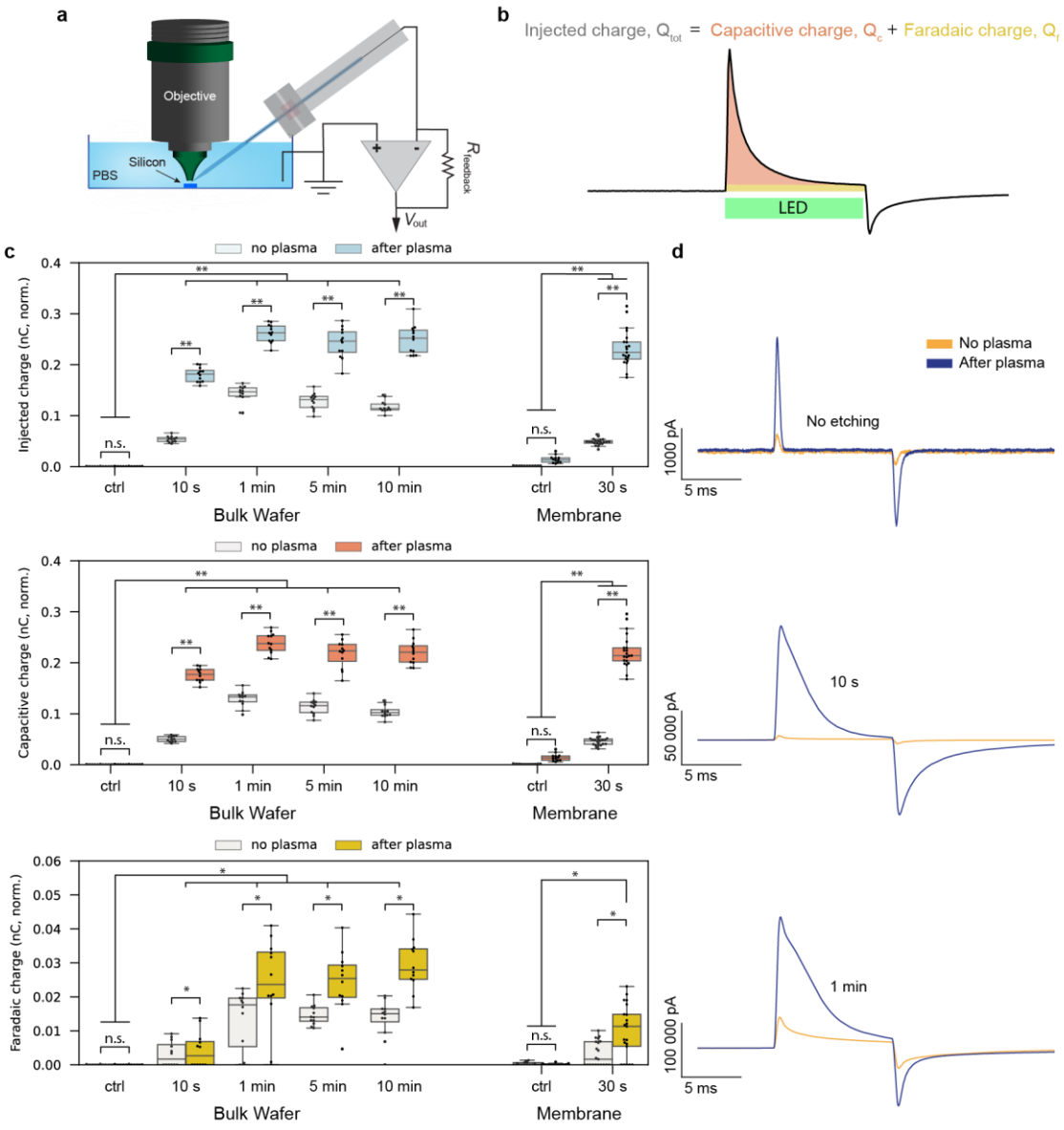

Figure 5.8 Screening of etching conditions for photocurrent generation.

(**a**) Schematic of the patch-clamp integrated photocurrent measurement setup used to study wafers and membranes. (**b**) Definition of the total injected charge, capacitive charge, and faradaic charge, used as figures of merit in optimisation of material processing parameters. (**c**) Photocurrents measured from p-type silicon materials under different etching time with 1% nitric acid. Even short etching times (10 s) are sufficient to generate strong photocurrents from the materials.

Oxygen plasma induces significant photocurrent enhancement across the entire series and recorded photocurrents show similar saturation levels. Large photocurrents are also recorded with 2 μm silicon membranes. 10 ms, ~4.3 W/cm^2, 532 nm LED pulses are used (power: 19 mW, spot size 0.75 mm). Boxes bind interquartile range (IQR) divided by the median; whiskers extend 1.5 ± IQR. All datapoints are plotted. Each box is calculated from at least three different locations on four separate samples for N ≥ 12. Experimental groups are paired, *i.e.*, photocurrents from the same sample are measured before and after oxygen plasma treatment. Statistics are calculated using Tukey HSD. p-values for comparisons are shown: * $p < 0.05$; ** $p < 0.001$, all not significant (n.s.) comparisons had a p-value > 0.8. (**d**) Representative photocurrent traces recorded from the stain etched wafers.

In the absence of the standard p-i-n or p-n doping regime, the stain etching-derived heterojunction was able to generate strong capacitive and faradaic currents upon light illumination. This fast and simple stain etching technique was performed under ambient temperature and pressure, using only wet etching solution, and without the need for any instrumentation. Notably, oxygen plasma treatment that passivated the pore surface with a thin silicon oxide layer enabled a further 4- to 10-fold enhancement of the generated photocurrents. Electron dispersive X-ray spectroscopy confirmed oxidation of the silicon surface; the oxygen content after plasma treatment increased from 4.9% to 18.8% (**Fig. 5.9**). Besides increasing the hydrophilicity of the material such that water and ions could access the nanoscale pores, we believe the oxygen plasma may have eliminated radiative surface recombinations[26], given that the characteristic orange fluorescence was completely quenched upon plasma treatment (**Fig. 5.10**).

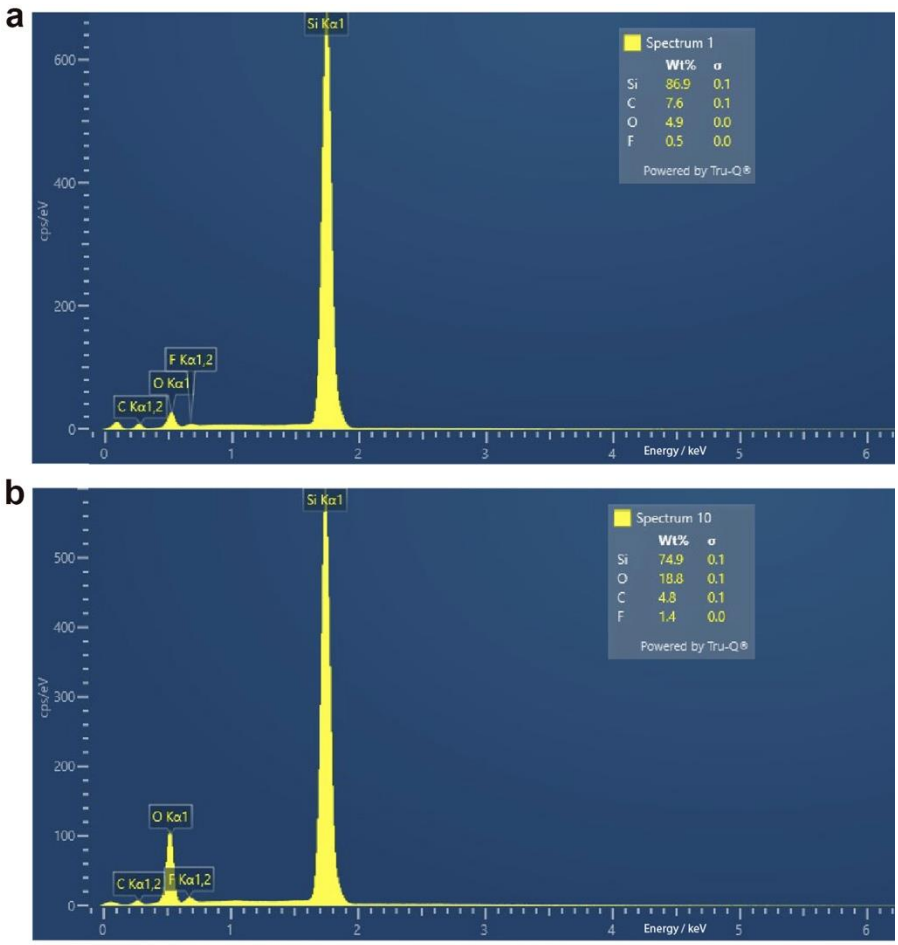

Figure 5.9 Energy dispersive X-ray spectra of the silicon wafers stain etched with 1% nitric acid before (a) and after (b) oxygen plasma treatment.

Elemental analysis reveals increase in the surface oxygen content after the treatment.

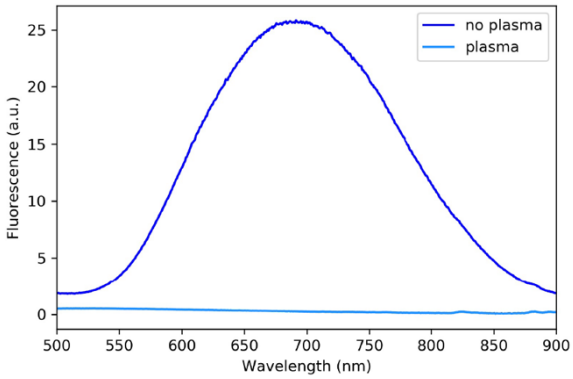

Figure 5.10 Fluorescence spectrum of silicon wafers stain etched with 1% nitric acid for 1 min before and after oxygen plasma treatment.

Oxygen plasma reduces radiative recombination and effectively quenches fluorescence in the material.

The fabrication approach is also compatible with the processing of ultrathin, soft, and flexible silicon membranes (thickness ~2 μm) fabricated from silicon-on-insulator (SOI) substrates. For silicon membranes, prolonged etching times over 40 s caused the breakdown of the heterojunction (**Fig. 5.11**). But as long as the supportive crystalline silicon layer was not completely etched (due to the vertical progression of the etching front), the heterojunction generated photocurrents sufficient for biomodulation experiments.

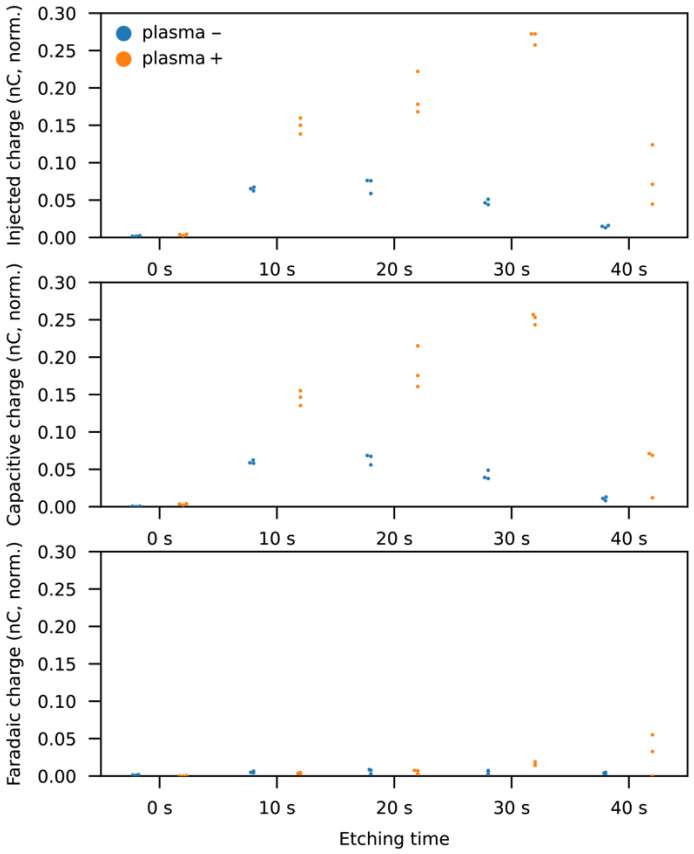

Figure 5.11 Time-dependent etching of silicon membranes in 1% HNO_3 in HF.

The optimal photocurrents are reached right before the membrane breakdown. The optimal etching time might depend on the batch of the reagents, but for the same combination of acids and SOIs it stays consistent between experiments.

We studied how varying concentrations of nitric acid in the etching solution affected photocurrent generation, and found that 1% nitric acid concentration was optimal for 10 s stain etching time (**Fig. 5.12**). Additionally, we investigated ferric ion and vanadium oxide as alternative oxidants for stain etching, but their performance was lower than that of nitric acid (**Fig. 5.13**). We attribute this lower performance to the suboptimal pore morphology, which had a more solid

structure than the spongy surface created by nitric acid (**Fig. 5.14**). Notably, we found that stain etching of n-type and intrinsic silicon wafers did not result in the creation of photoelectrochemical materials (**Fig. 5.15**). We attribute this behaviour to the dopant-dependent energy levels produced in the silicon substrate upon porosification (**Fig. 5.16**). These results support our proposed porosity-based heterojunction mechanism (**Fig. 5.1a**). Finally, we added surfactants in the etchant solution to avoid the gas bubble accumulation and the micropillars formation upon etching. Results showed dramatically reduced photoelectrochemical currents (**Fig. 5.17**), suggesting that gas bubble-templating (**Fig. 5.2c**) may be critical in forming the light-trapping structures.

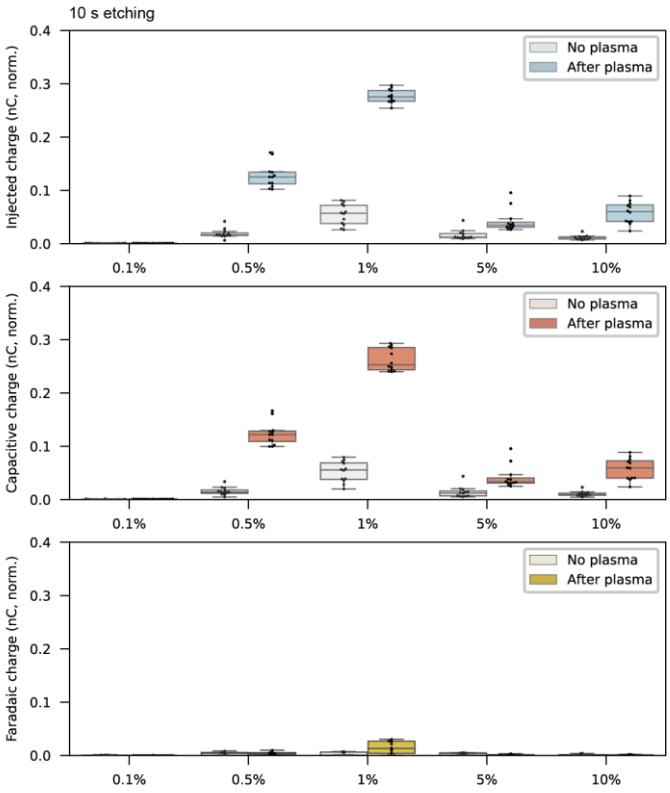

Figure 5.12 Photocurrents obtained using stain etching with different concentrations of nitric acid for 10 s.

Concentration higher than 1% significantly reduce photocurrents. The boxes bound interquartile range (IQR) divided by the median, and whiskers extend 1.5×IQR. All datapoints are plotted.

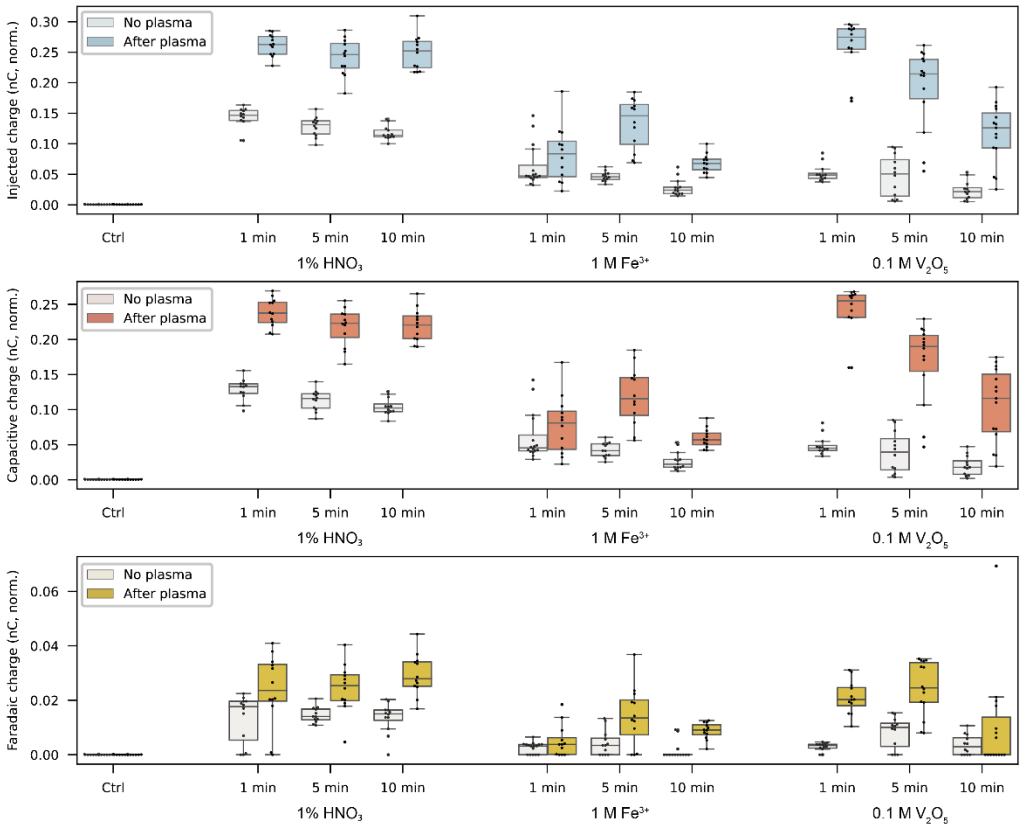

Figure 5.13 Comparison of photocurrents recorded from stain etching performed using 1% nitric acid, 1 M iron (III) cations, and 0.1 M vanadium (V) oxide as hole-injecting oxidants. Improvement in the photocurrent generation was observed for all oxidants, but only nitric acid generated photocurrents independent of the etching time (self-limiting), and achieved photocurrents were in general higher than for other oxidants. The data for nitric acid is reused from figure 5.8, and shown here for direct comparison with other oxidants. The boxes bound interquartile range (IQR) divided by the median, and whiskers extend 1.5×IQR. All datapoints are plotted.

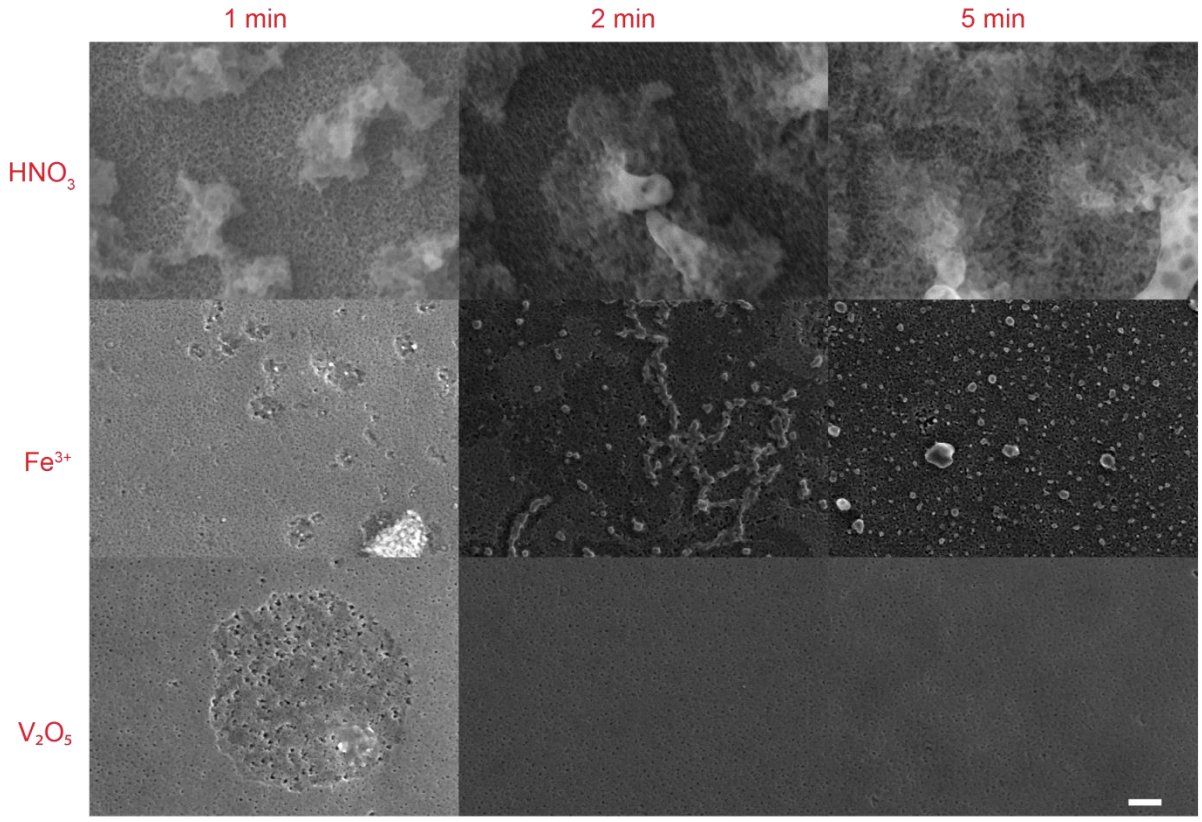

Figure 5.14 Scanning electron microscopy images of wafers' surface after stain etching using different oxidants.

Only nitric acid showed a sponge-like morphology. Concentrations: 1% nitric acid, 1 M Fe^{3+}, 0.1 M V_2O_5. Scale bar, 100 nm.

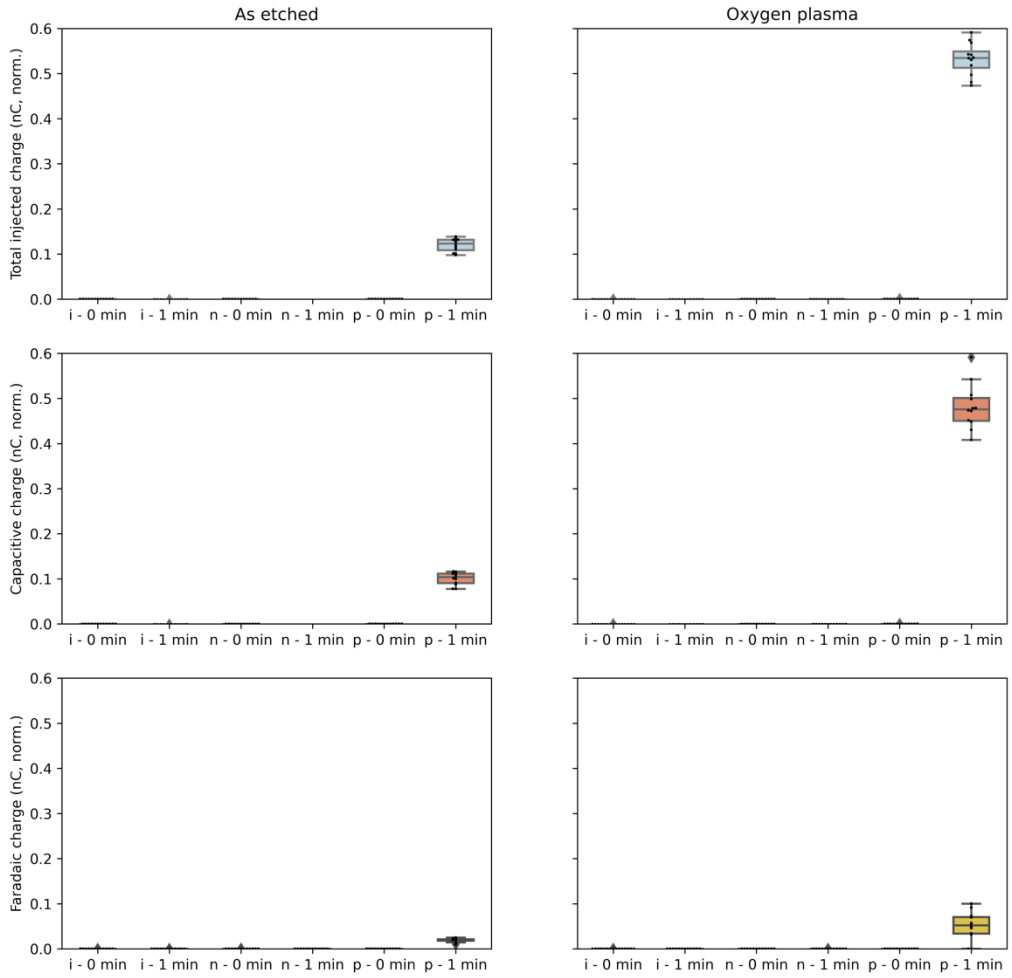

Figure 5.15 Photocurrents obtained after stain etching different types of wafers with 1% nitric acid for 1 min.

Photocurrents and their significant enhancement after oxygen plasma treatment was observed only for a p-type wafer. The boxes bound interquartile range (IQR) divided by the median, and whiskers extend 1.5×IQR. All datapoints are plotted.

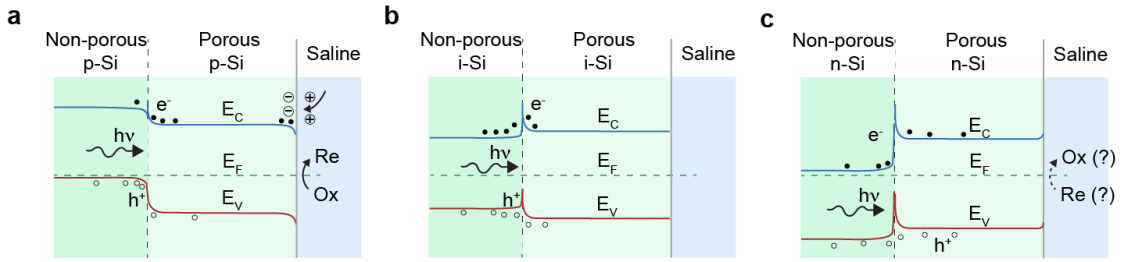

Figure 5.16 Proposed schematic band diagrams of the non-porous/porous silicon interfaces in materials obtained through self-limiting stain etching in p-type (a), intrinsic (b) and n-type (c) silicon substrates.

Only the p-type silicon substrate yields the desired light-induced charge separation.

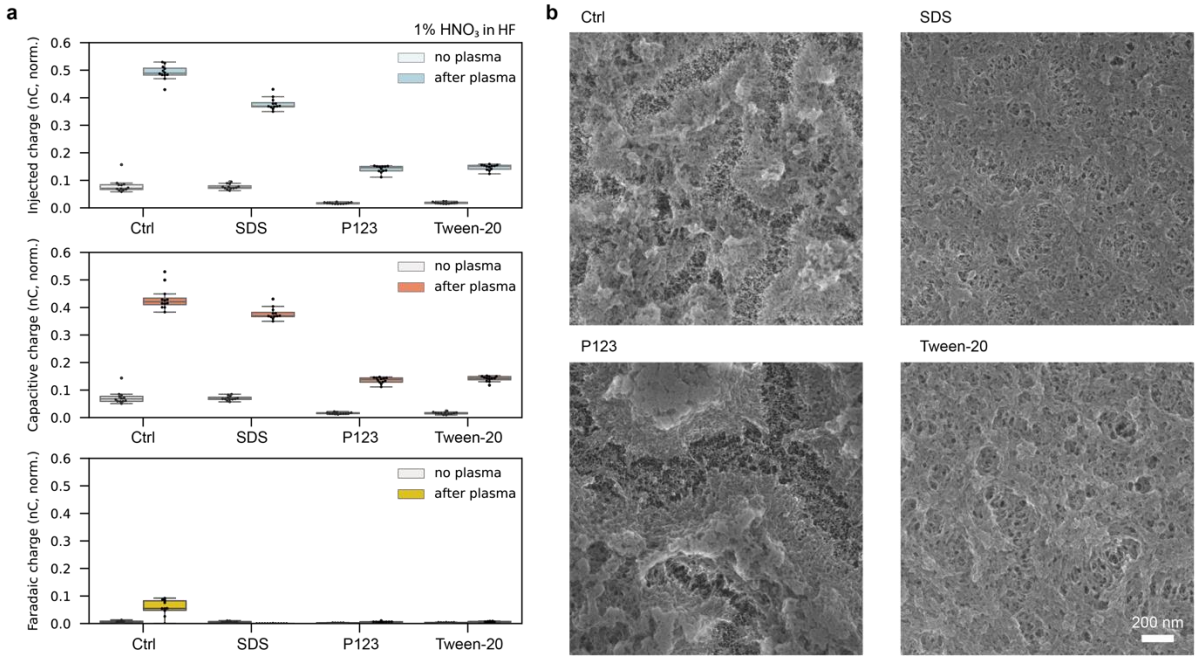

Figure 5.17 Photocurrents obtained using stain etching with 1% nitric acid for 1 min and addition of 0.1% (w/v) surfactants and the scanning electron microscopy images of the obtained porous materials.

(**a**) We tested a selection of ionic and non-ionic surfactants to investigate the effect of hydrogen bubble formation on the surface microstructure. In general, addition of surfactants was detrimental

to the recorded photocurrents and pure formulation yielded the highest currents. The boxes bound interquartile range (IQR) divided by the median, and whiskers extend 1.5×IQR. All datapoints are plotted. (**b**) While surfactants affect the microstructure formation and pore morphology, there does not seem to exist a direct correlation between the appearance of material surface and recorded photocurrents. As observed above, the addition of sodium dodecyl sulfate (SDS) eliminated the micropillars. However, the observed photocurrents were higher than when Pluronic P123 was used, in which the micropillars were preserved. The results suggest that pore morphology is a primary factor determining the photoelectrochemical performance of the materials.

5.4 Electrochemical and Photoelectrochemical Characterization

To understand the effects of stain etching and oxygen plasma treatment on the electrochemistry of the silicon, we performed standard electrochemical tests using wired electrodes. **Figure 5.18a** shows cyclic voltammetry (CV) curves of silicon electrodes with different surfaces (*i.e.* bulk silicon, stain etched p-type silicon, and p-i-n silicon with or without gold decoration). Stain etching improved the capacitance of the electrode interface over the flat wafer, and oxygen plasma treatment resulted in further enhancement. Additionally, when performing scans with 532 nm light irradiation (**Fig. 5.18b**), a pair of reversible-redox peaks were observed, which may be attributed to oxygen reduction reaction on the porous surface[27]. This photoelectrochemical process is suggested by hydrogen peroxide production as detected through the dye degradation assay (**Fig. 5.19**). This electrochemical behaviour is functionally different from our previously reported gold-decorated p-i-n junction[28], which showed strong, but irreversible redox peaks (marked on CV curve in **Fig. 5.18a-b**). Furthermore, electrochemical impedance spectroscopy showed that the combination of stain etching and oxygen plasma reduced the impedance of the electrode over the

entire range of frequencies (**Fig. 5.18c**). Impedance reduction may be attributed to the increase in surface area available for current injection and increased hydrophilicity of the surface, which reduces the barrier for ion transfer to and from the solution. Electrical impedance spectra can be described using Randles equivalent circuit with restricted diffusion element to account for ion transfer through the nanoporous material. (**Fig. 5.20**).

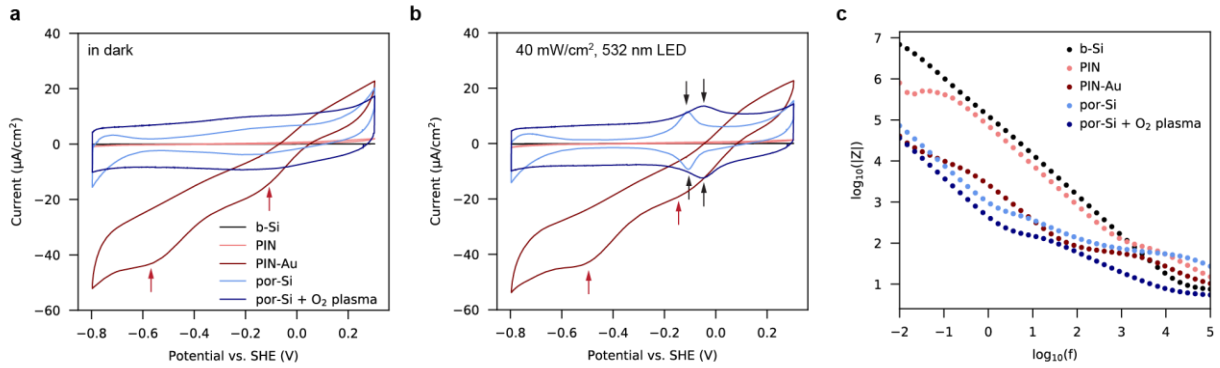

Figure 5.18 Electrochemical analysis of the nanoporous silicon.

(**a**) Cyclic voltammetry of silicon electrodes in the dark shows improved pseudocapacitive performance of the nanoporous (por-Si) and activated silicon. (**b**) Under light illumination, reversible redox peaks are identifiable in por-silicon, which can be attributed to oxygen reduction reaction on the surface of the material. Black arrows indicate reversible redox peaks in por-Si, and red arrows indicate irreversible redox peaks in a gold-decorated p-i-n junction. (**c**) Electrochemical impedance spectroscopy of silicon electrodes shows that stain etching combined with oxygen plasma treatment reduces impedance in the entire range of frequencies. Two electrodes of each type were fabricated, and representative results are shown.

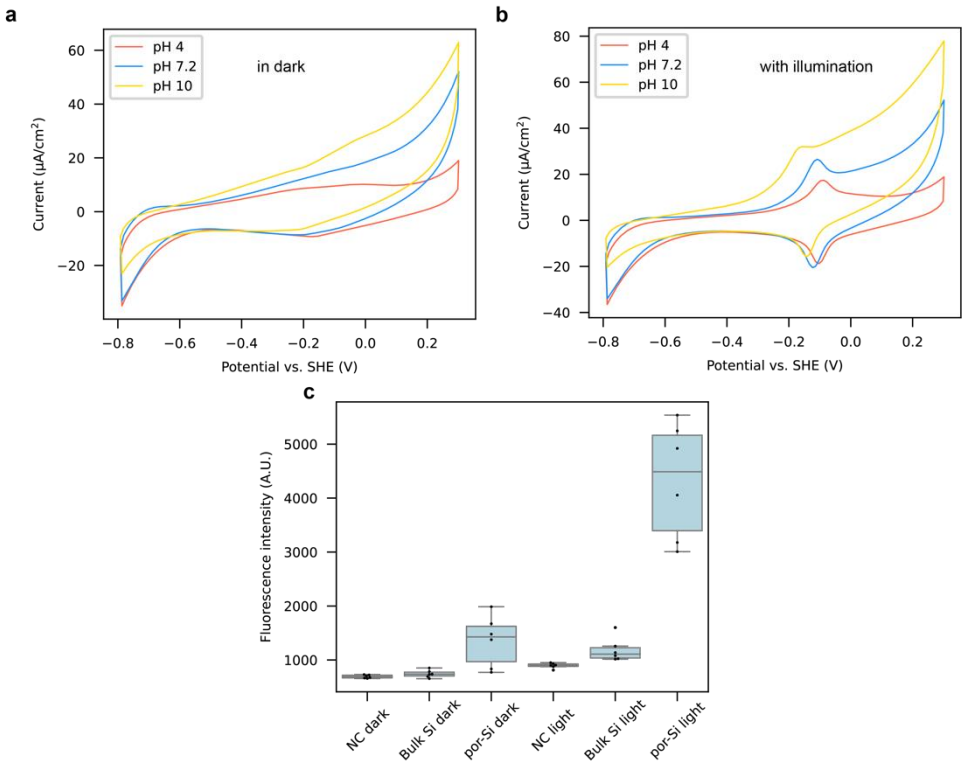

Figure 5.19 Electrochemical investigation of photoelectrochemical reactions at the nanoporous silicon interface.

(a) Cyclic voltammetry scans of porous silicon electrode in different pH in the dark. **(b)** Cyclic voltammetry scans of porous silicon electrode in different pH under illumination. As the standard potential of oxygen reduction reaction (that is related to the proton concentration, amount of dissolved oxygen, etc.) is dependent on pH, the overpotential to activate the reaction will also change hence leading to a shift in the peak position. **(c)** Dye degradation assays shows production of hydrogen peroxide under illumination at the interface with porous silicon, which is further increased upon light illumination. (NC – negative control, no material present)

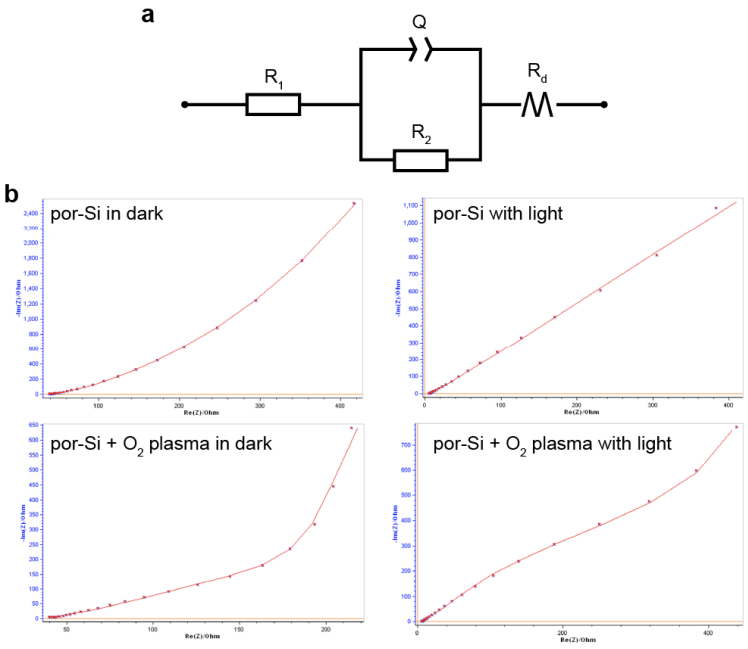

c

	Nanoporous Si		Nanoporous Si + O_2 plasma	
	Dark	Light	Dark	Light
R_1 (Ohm)	35	38	4.1	4.4
Q ($F \cdot s^{(\alpha-1)}$)	5.2E-4	4.6E-4	1.8E-4	1.6E-4
α	0.57	1	0.82	0.084
R_2 (Ohm)	1270	3900	4.8E-2	514
R_d ($Ohm \cdot s^{-1/2}$)	9.49	47	750	68
R_t (s)	5.9E-4	0.21	5.4	1.6E-2
Chi/|Z|	6E-3	1.7E-2	1.6E-2	6E-3

Figure 5.20 Electrochemical impedance equivalent circuit.

(a) Equivalent circuit used for modelling impedance spectra. R_1 is the contact resistance, R_2 is the charge transfer resistance, Q is constant phase element (with parameter α), R_d is restricted diffusion (with parameter t_d). **(b)** Fitting results for porous silicon in the dark and under 532 nm LED illumination. (**c**) Parameters obtained from model fitting.

We studied the stability of the silicon heterojunction in phosphate buffered saline (PBS) under illumination. We found no significant degradation in photocurrent between samples that underwent pulsed illumination of 14,000 pulses and samples stored in the dark for the same time period (**Fig. 5.21**). This observation is in sharp contrast to our previously reported gold-decorated

p-i-n junction[28], where a degradation of 30% in generated photocurrents was observed after only 1,000 pulses. The improved device performance supports our CV findings that the photoelectrochemical processes occurring on the nanoporous silicon surface may be more reversible, as opposed to the irreversible redox reaction on the gold-decorated p-i-n junction. Although the nanoporous layer is prone to dissolution in PBS when stored for more than 48 hr (**Fig. 5.21**), chemical surface modification or deposition of passivation layers can further improve its stability, similar to stabilisation of photovoltaic cells[29]. We found that atomic layer deposition can improve the material stability and increase the lifespan of the photoelectrochemical effects (**Fig. 5.21**).

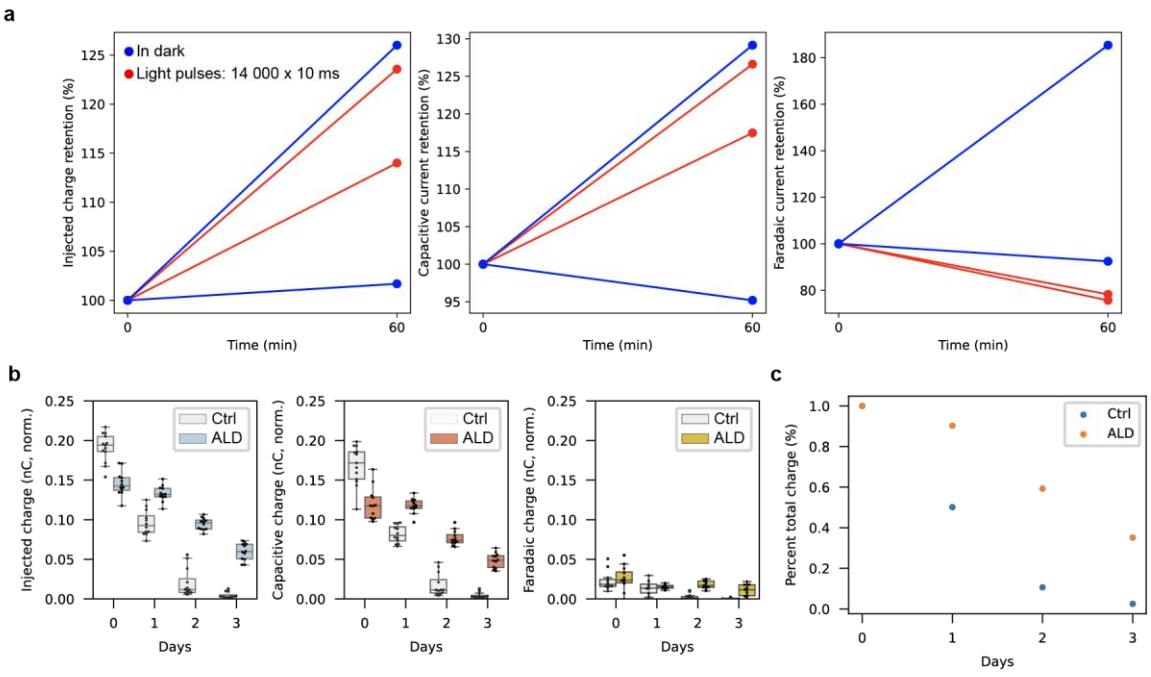

Figure 5.21 Analysis of the stability of photocurrents in the silicon membrane.

(**a**) Short-term stability shows that capacitive currents decrease during the first hour, but faradaic currents can significantly increase leading to the increase in total injected charge. No significant difference in the trends was observed whether the membrane was stored in the dark or under

repeating 4 Hz illumination suggesting photostability of the observed photoelectric effects. Each datapoint represents mean of 3 measurements on the single membrane. Lines do not represent real data and are used to visualize the trend. (**b**) Long-term static stability analysis shows that total injected charge decreases approximately by 50% during the first 24 hours in 1 × PBS at 37 °C, and to the insignificant values over the 3 days for the regular nanoporous Si samples (Ctrl). Deposition of titianium/aluminum oxide dielectric layers through atomic layer deposition (ALD) increased material's stability. The boxes bound interquartile range (IQR) divided by the median, and whiskers extend 1.5×IQR. All datapoints are plotted. (**c**) ALD allowed to preserve 60% of photocurrent intensity of the time of 48 hours. Mean normalized photocurrents are shown.

We investigated the dependence of the photoelectrochemical currents on the power and wavelength of the illumination light. While the materials generated large photoelectrochemical currents under visible and near-infrared light (NIR) (**Fig. 5.22**), ultraviolet (UV) light illumination did not elicit a photoresponse. We attribute this absence of photoresponse to the increased scattering and absorption of UV wavelengths in the nanoporous layer, such that the UV photons cannot reach the buried heterojunction (~1 μm below the surface) and generate photocarriers. This observation highlights the dominant role of the nanoporous/non-porous heterojunction (that UV photons cannot reach) over that of the nanoporous/saline junction (that UV photons can reach) in producing the observed photoelectrochemical effect. Moreover, although NIR light, which is more attractive for clinical biomodulation applications, was found less effective, it is important to note that the entire stain etching protocol was optimized for 530 nm green light illumination. Thus, it is reasonable to assume that different etching protocol that will be optimized for 808 nm light will yield a better photoresponse for 808 nm tissue penetrating NIR light. To connect the optical

properties of the material with photoelectrochemical performance, we performed microspectrometry of the silicon membranes before and after processing (**Fig. 5.23**). We found that stain etching and oxygen plasma treatment increased transmittance of the silicon membrane, due to removal of part of the material, but reduced reflectance of the membrane. Overall light absorption of the membrane was only slightly increased after complete processing. Given that the recorded photocurrent level is improved by orders-of-magnitude upon stain etching, we believe that the charge separating diode-like heterojunction (**Fig. 5.1a**), as opposed to the nanoporous antireflective layer, is responsible for the enhanced photoelectrochemical properties.

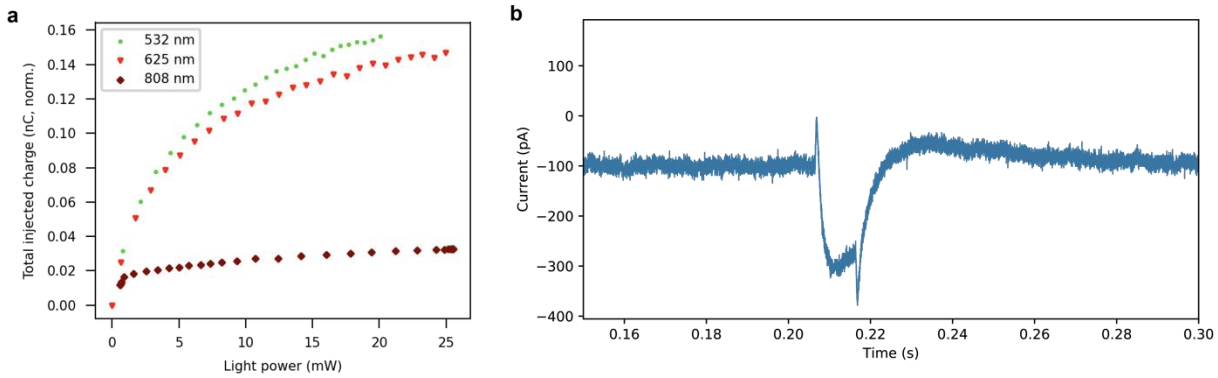

Figure 5.22 Analysis of the power- and wavelength-dependent photoresponse in a silicon wafer stain etched with 1% nitric acid for 1 min.

(**a**) 532 nm and 625 nm light generated comparable photocurrents. Significantly less photocurrents were observed for 808 nm light. (**b**) No significant photocurrents were recorded with 365 nm light, and low-level compound signal of capacitive and thermal photocurrents was observed. The dataset is a series of measurements for single sample.

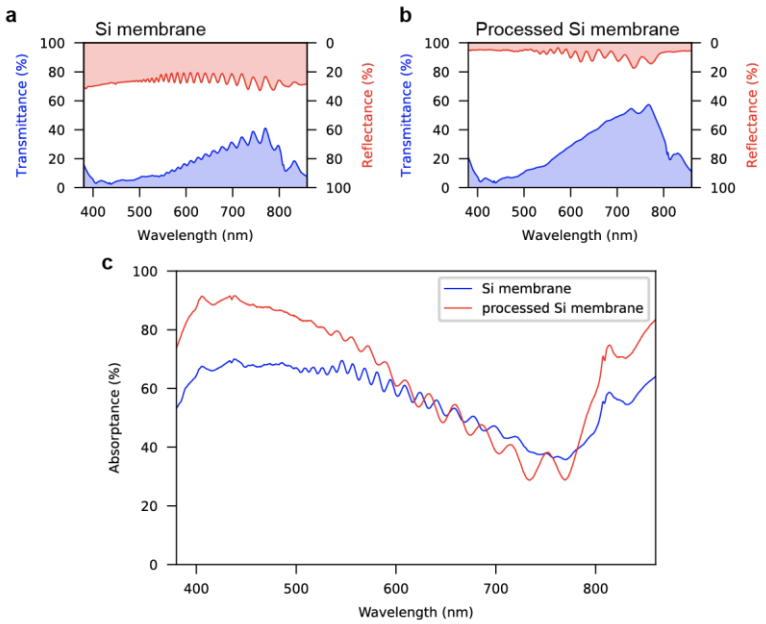

Figure 5.23 Microspectrometry of silicon membranes.

Transmittance and reflectance spectra of as etched Si membrane (**a**) and Si membrane after stain etching and plasma treatment (**b**). The white area on the plot represents absorbance. **(c)** Comparison of membranes absorptance before and after processing.

5.5 Summary

In this chapter, I have presented morphological and electrochemical characterization of stain etching-derived heterojunctions. I have shown how the pores preserve the single-crystal structure with no sign of amorphization. I also described how surface microstructure could contribute to the enhanced light absorptance in the material. I have studied the mechanical properties of the material's surface using nanoindentation and the uniformity of the nanoporous layers with spectroscopic ellipsometry. I have thoroughly explored stain etching conditions to achieve optimal

photocurrents and shown that increased photocurrent might come primarily from suppressing radiative recombination in the porous silicon. I have also successfully applied the stain etching procedure to generate photoelectrochemical materials in 2 μm thin single crystals. I have studied the electrochemistry of nanoporous/non-porous heterojunctions and detected the formation of hydrogen peroxide under illumination, suggesting the presence of an oxygen reduction reaction. Finally, I have studied the stability of the porous heterojunctions in vitro and described how atomic layer deposition of thin dielectric layers could improve material stability. In a subsequent chapter, thin silicon membranes with strong photoelectrochemical effects will be used to optoelectronically pace isolated hearts and stimulate sciatic nerves in a rat model.

5.6 Methods

Stain etching of wafers and membranes

Silicon wafers (P <100> 0.001-0.005 ohm·cm, N <100> 0.001-0.005 ohm·cm, I <100> >10,000 ohm·cm) were obtained from Nova Electronic Materials (Flower Mound, TX, USA). The wafers were diced using the Disco DAD3240 Dicing Saw. 5 mm × 5 mm squared pieces were used in photocurrent evaluation experiments and 10 mm × 10 mm squared pieces were used for fabrication of electrodes used in photoelectrochemical measurements and fluorescence measurements. PTFE tweezers were used for all sample manipulation, from initial to final washing steps. Directly before etching, wafers were washed in an ultrasonic bath for 5 min in acetone (Histological grade, A16P-4, Fisher) followed by 5 min in isopropanol (Certified ACS Plus, A416P-4, Fisher), and then stored in deionized water (DI water, 18.2 MOhm, Micropure UV/UF, ThermoFisher). All stain etching experiments were performed in concentrated hydrofluoric acid (HF, TraceMetal grade, A513-500, Fisher). Concentrated nitric acid (HNO_3, TraceMetal grade, A509-P500, Fisher), iron(III) chloride

hexahydrate ($FeCl_3$, ACS reagent, 97%, 236489-500G, Sigma Aldrich), and vanadium(V) oxide (V_2O_5, 99.6+%, 206422500, Acros Organics) were used as porous silicon-forming oxidizers. Sodium dodecyl sulfate (SDS, BioReagent, ≥98.5% (GC), L3771-25G, Sigma Aldrich), Pluronic® P123 (435465-250ML, Sigma Aldrich) and Tween® 20 (P2887-100ML, Sigma Aldrich) were used as a surfactant additives. Solutions and chemicals were used as received without additional processing and all experiments were performed at room temperature (24-26°C). Directly before etching, HNO_3 was mixed with HF in specified v/v ratios, or $FeCl_3$, V_2O_5 and surfactants were dissolved at specified concentrations and solution was deoxygenated for 30 min by bubbling with argon. Each etching series (a set of samples using the same etchant composition and time) used approximately 10 mL of freshly prepared etchant and was performed in a fresh polypropylene dish. Silicon wafer samples were transferred from water bath to etching solution, moved along the bottom of the dish with the tweezers for the first 10 seconds, and left undisturbed for the specified amount of time. After etching, samples were soaked twice for 1 min in separate DI water baths to remove the HF, once for 1 min in IPA, and dried using compressed nitrogen. 5 mm × 5 mm samples were mounted on reclaimed grade silicon wafers using double sided tape to ease further handling, and silicon membranes were transferred and attached to PDMS substrate using fresh wet oxide silicon wafers. PDMS casting solution was prepared by mixing PDMS base (Sylgard™ 184, Dow), PDMS cure (Sylgard™ 184, Dow) and hexane (anhydrous, 95%, 296090-1L, Sigma-Aldrich) in a 10:1:10 (w/w) ratio. The solution was then degassed under vacuum, spin coated at 4,000 rpm onto the PMMA covered microscope slide and cured at 65°C for 45 min. All samples were stored in a desiccator under vacuum for prolonged periods between experiments (>2 h). **5.24** shows optical microscopy photographs demonstrating formation of colorful stains on the surface of the wafers and silicon membranes. Porous bulk wafer appears mostly black under the reflected light and the

silicon membrane shows iridescent stains due to thin-film interference. It is important to note that the difference in optical appearance is due to different substrate thicknesses and not different etching conditions.

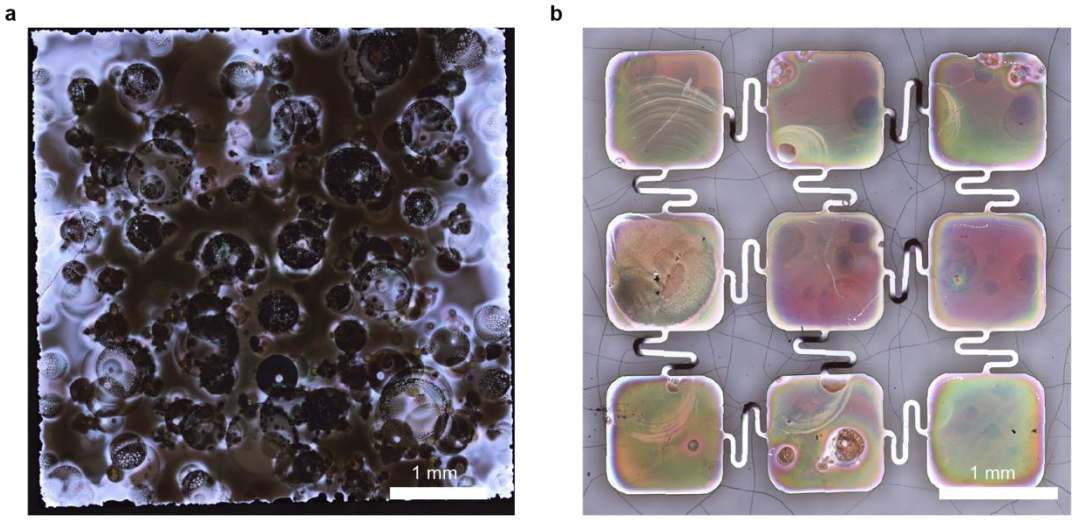

Figure 5.24 Macroscopic optical photographs of stain etched silicon.

(**a**) Stain etched silicon wafer showing black-colored porous silicon. (**b**) Stain etched silicon membrane showing opalescent stains due to thin-film interference. Both samples were etched for 10 s in 1% HNO_3 in HF (v/v).

Silicon membrane fabrication

Silicon-on-insulator (SOI) wafers (p++, device 2 μm, 0.001-0.002 ohm·cm, handle 10-100 ohm·cm, BOX 1 μm) were obtained from Ultrasil (Hayward, USA). Photomask was designed using AutoCAD software and is shown in **Figure 5.25** Fabrication followed standard lithography procedures. A thick positive resist AZ40XT-11D (MicroChemicals) was used as a mask for reactive ion etching (RIE). Patterns were exposed using the Heidelberg MLA150 direct writer and uncovered SOI was removed using SF_6/CHF_3 (20 sccm/50 sccm) RIE (ICP 600 W, RF 60 W) in a

Plasma-Therm ICP Fluoride etcher with an etching rate of about 600 nm/min. Photoresist was stripped using AZ NMP (MicroChemicals) and wafers were washed in an ultrasonic bath for 5 min in acetone followed by 5 min IPA and dried using compressed nitrogen. Samples were submerged in concentrated HF (analytical grade, 48 to 51% in water, 223335000, Acros Organics) for 4 h to remove buried oxide layers. The membranes, together with the handle wafer, were subsequently soaked twice for 1 min in separate DI water baths to wash off the HF. The wafers were soaked in IPA bath for 1 min and moved to an acetone bath to ease interactions between membranes and handle wafer. Finally, the free-floating membranes were transferred to a fresh IPA bath using separate wet oxide silicon wafers and stored at 4°C before further processing.

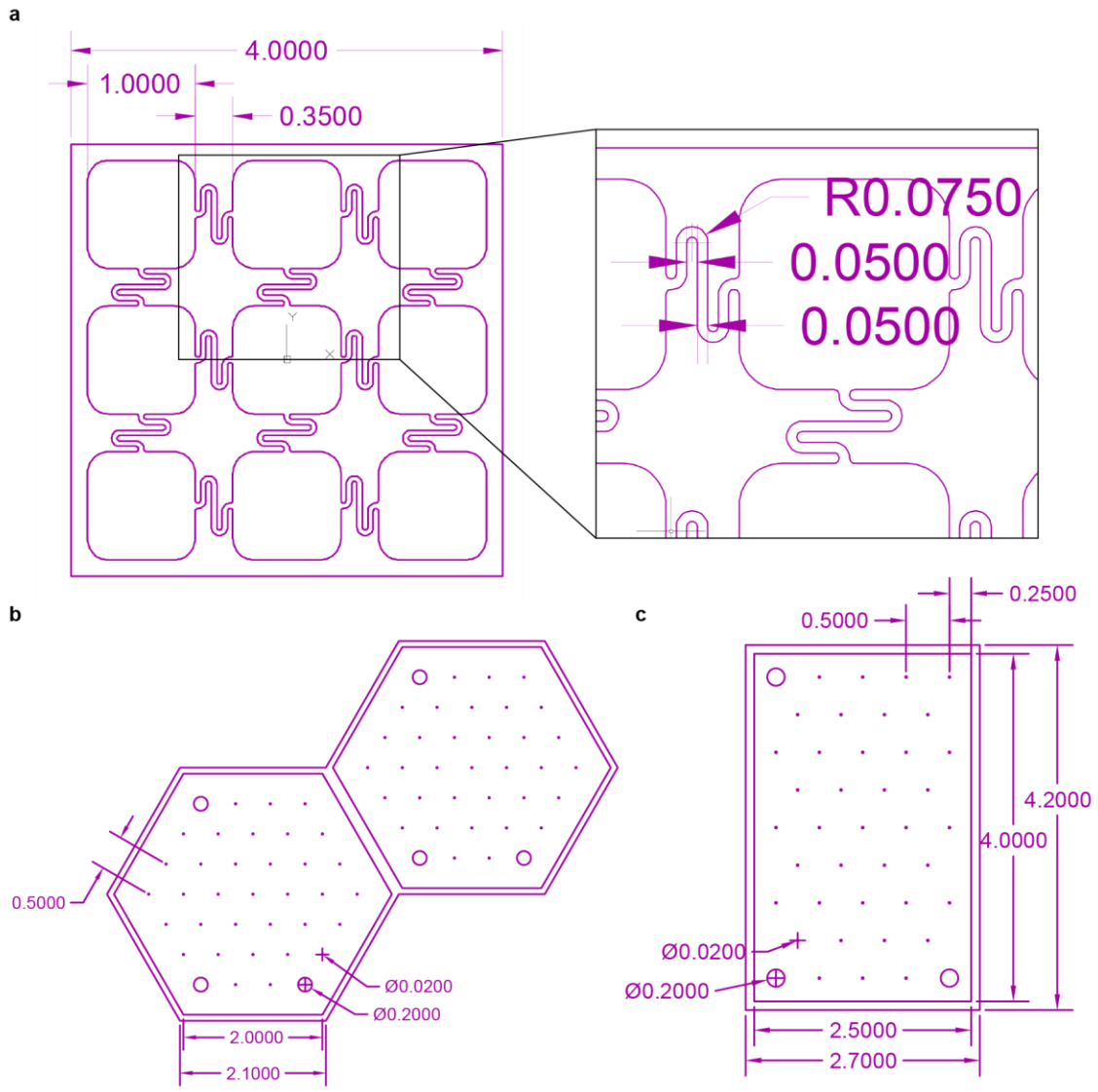

Figure 5.25 Schematics of the designs of the positive photomasks used for fabrication of silicon membranes.

(a) Partially stretchable 9-pad design. View of the entire mask (left) and the detail of the meandering interconnect (right). Shapes were loaded for direct writing in XOR mode. Units are in millimeters. Continues area (~ 10 mm^2) designs: **(b)** hexagon design and **(c)** rectangular design. Hexagonal array of holes was used in designs (b) and (c) to ease etching and lift-off of large flat surface area membranes.

Oxygen plasma processing

Stain etched silicon samples were treated with 800 W oxygen plasma at 50 sccm without RF bias for 10 min in a Plasma-Therm ICP Fluoride etcher. Free samples of silicon wafers were directly attached to the carrier wafers using vacuum mounting oil, and mounted samples and silicon membranes were attached to their respective carrier substrates.

P-type/intrinsic/N-type (PIN) diode junction synthesis

PIN junctions were synthesized through chemical vapor deposition (CVD) growth of intrinsic and n-type layers on p-type silicon wafers as previously described[30]. Gold-decoration was performed for 1 min at room temperature in a solution of 1 mL 10 mM chloroauric acid (16583, Electron Microscopy Sciences), 9 mL DIW, and 0.2 mL concentrated HF (Acros Organics).

Photocurrent measurement

Photocurrent measurements generally followed previously described methods[25]. Patch clamp-setup integrated with an upright microscope (Olympus, BX61WI) with a 20x/0.5 numerical aperture water-immersion objective was used for photocurrent measurements. Light pulses were delivered using episcopic illumination with a dichroic mirror (for 365 nm, 532 nm, and 625 nm LEDs, FF660-Di02-25x36, Semrock) or Thorlabs protected silver mirrors (for 808 nm laser, PF10-03-P01, PFR10-P01). Applied light sources and their validation is described in a separate subsection. Clamp voltage and current were measured using silver chloride electrodes and amplified using an AxoPatch 200B amplifier (Molecular Devices). Voltage-clamp levels and light pulsing were digitally controlled using transistor-transistor logic (TTL) or analog signals delivered from a Digidata 1550 digitizer (Molecular Devices) controlled with Clampex software (Molecular Devices). Glass pipettes were pulled in a P-97 micropipette puller (Sutter Instrument) usually to a resistance of 1-4 MΩ and filled with 1 × PBS. In a typical measurement, the material was placed

in a petri dish filled with 1 × PBS and positioned in the center of the field-of-view. The pipette tip was lowered close to the surface of the material (<10 μm) and the measurement sequence was executed. The measurement sequence spans 400 ms, with a first voltage level of −0.5 mV between 100-300 ms. At 200 ms, a 10 ms light pulse was delivered to elicit a photoresponse from the material. The holding current was adjusted so that the current in the first voltage level was close to 0 pA (usually under 2000 pA). Following the measurements, all samples were soaked in DI water for 1 min, washed with DI water, washed with IPA, dried using compressed nitrogen, and stored under vacuum or immediately used for further experiments.

Photocurrent analysis

Photocurrents were analysed with Python script working directly on the raw data files using pyABF library. Total injected charge Q_{tot} was calculated through the integration of the area under the current transient during light illumination. Due to high capacitive photocurrents in the material, the faradaic charge was calculated through fitting the last 20% of the current transient to the exponential decay equation: $I(t) = A\exp^{kt} + I_f$, where *I(t)* is current, *t* is time, I_f is the faradaic current, and *A* and *k* are constants. Poor quality fits were obtained if more of the transient was used for calculations due to supercapacitive behavior of the material in early charging stages that does not follow exponential trend. Non-linear solver using Trust Region Reflective algorithm implemented in Scipy python package was used for fitting. Faradaic current is assumed to stay constant during the illumination and was used to calculate faradaic charge $Q_f = I_f \Delta t$. Finally, the capacitive charge was calculated by subtracting faradaic charge from total injected charge $Q_c = Q_{tot} - Q_f$. All recorded values are normalized to measurement performed with 1 MΩ pipettes according to Ohm's law. The detected photocurrents were exported into the delimited text files for

further analysis and plotting. Analysis script used for calculations is shown in **Appendix A1**. Only measurements that failed due to technical reasons (such as broken pipette, or light pulse not fired) were excluded from analysis. An unsatisfactory photoresponse was not considered a valid reason for a datapoint rejection. Photothermal currents in wafer and membrane samples were not detected (**Fig. 5.26**), and therefore they are ignored in the general analysis. Additional validation of the photocurrent analytical methods is described in **Figure 5.27**.

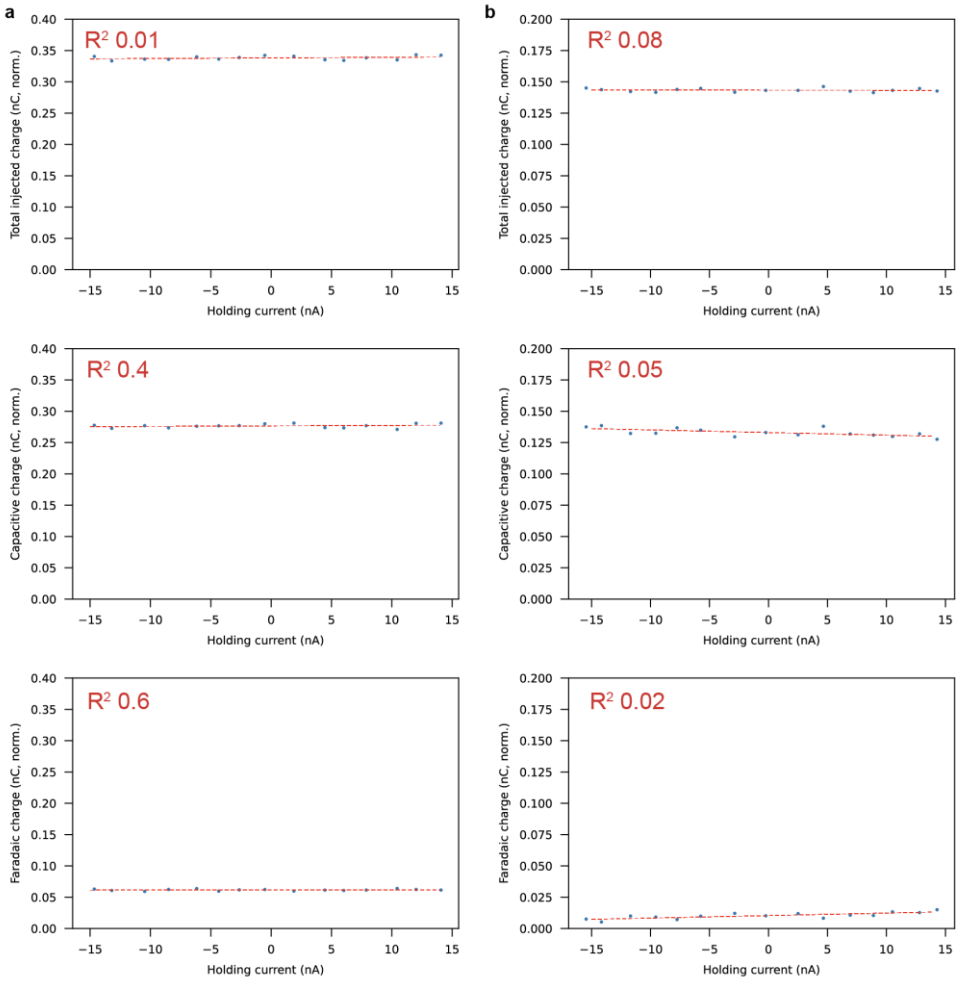

Figure 5.26 Analysis of the photothermal effects.

(**a**) Holding current dependent photocurrents in a wafer stain etched with 1% nitric acid for 20 min and after oxygen plasma treatment. (**b**) Holding current dependent photocurrents in a silicon membrane stain etched with 1% nitric acid for 10 s and after oxygen plasma treatment. Linear regression showing little correlation between the holding current and recorded photocurrents with negligible slope suggests lack of photothermal currents in the measurements. Dashed line is a fitted linear function and R^2 denotes the coefficient of determination calculated using residual sum of squares.

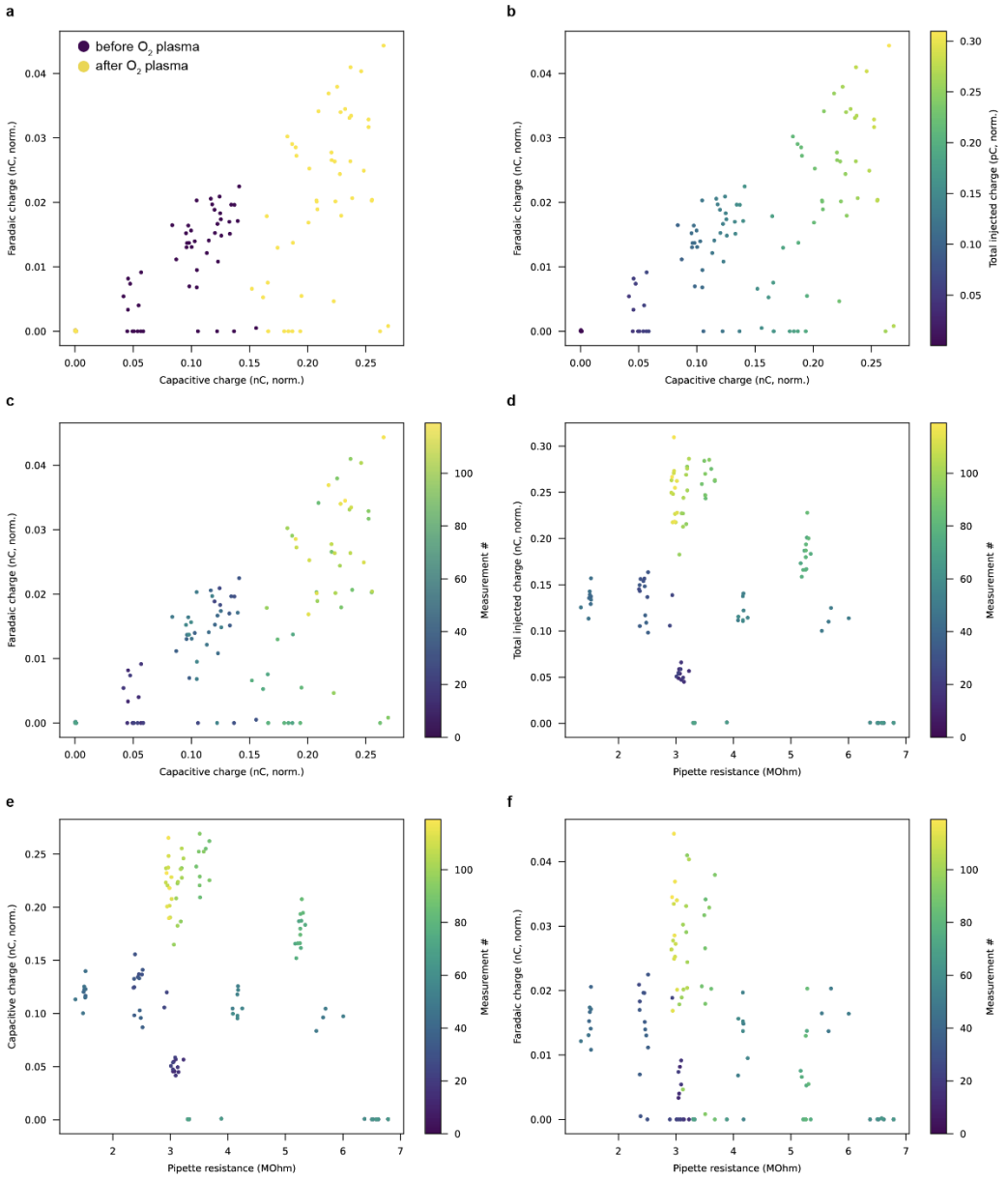

Figure 5.27 Validation of the photocurrent data analysis framework.

Data for silicon wafers etched with 1% nitric acid for different amounts of time is used. (**a**) Clustering of datapoints for pre- and post-oxygen plasma measurements demonstrate significant effect of this treatment on the photocurrents. (**b**) Plot of capacitive vs. faradaic vs. injected charge, expected linear relationship. (**c**) Plots shows no apparent clustering in capacitive and faradaic currents depending on the order of measurements. (**d-f**) Plots show no relationship

between pipettes resistance and recorded photocurrents, e.g., some range of resistance recording only high or only low values. Clustering around measurement number is expected, because samples in the same series were measured together until finished or pipette was completely broken. Values recorded with < 1 MΩ correspond to partially damaged pipettes. Pipettes were not pulled to this resistance.

Electrode fabrication

10 × 10 mm wafers were used for electrode fabrication. To achieve Ohmic contact with the back side of the wafer, samples were dip-etched in 5% HF, and 50 nm Al and 25 nm Au metal layers were deposited using an Angstrom Engineering EvoVac e-beam evaporator. Copper wires were then connected to the Au layer using silver paste (PECLO®, 16062, Ted Pella). The paste was pre-dried at room temperature for 30 min and fully dried for 30 min at 65°C. The resistance of the interconnects was under 3 Ω. Wiring and sides of the wafer were insulated, and the glass tube was attached to the electrode using electrical epoxy (8332, MG Chemicals) to improve mechanical stability. The epoxy was cured for 30 min at 65°C before measurements. Schematics and representative pictures of the electrodes are shown in **Figure 5.28**.

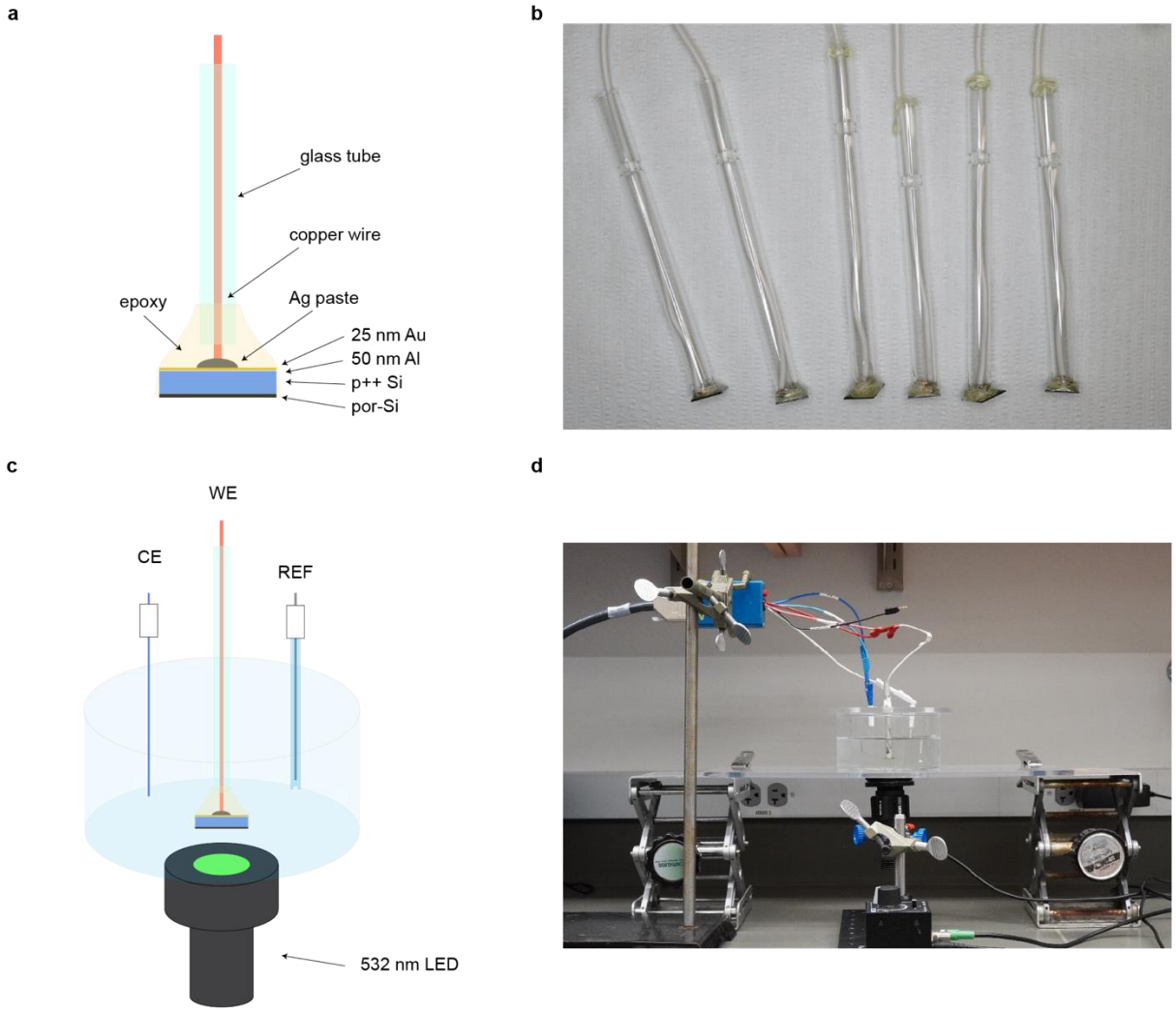

Figure 5.28 Additional information on the photoelectrochemistry measurements.

(**a**) Schematic of the silicon electrode assembly and (**b**) photograph of representative electrodes. (**c**) Schematic of the photoelectrochemical cell (WE - working electrode, CE – counter electrode, REF – reference electrode), and (**d**) photograph of the experimental setup.

Electrochemical tests

Cyclic voltammetry (CV) and electrochemical impedance spectroscopy (EIS) were performed using a potentiostat (SP-200, BioLogic) controlled with EC-Lab software. A platinum wire was

used as the counter electrode, an Ag/AgCl electrode (saturated KCl) as the reference electrode, and a silicon wafer as the working electrode. The potentials were corrected to standard hydrogen electrode potential using $E_{Ag/Cl(3.5\ M)} = -0.2037\ V$[31]. Light was delivered from the bottom of the setup using a 532 nm Thorlabs LED. 0.5 M K_2SO_4 (ReagentPlus®, >99%, P0772-250G) with pH 6.3 was used as an electrolyte. A pyrex glass dish was used as a cell container. Cell temperature was not controlled and was measured to be within 24-26°C which was unaffected by the LED illumination. EIS was performed in potentiostatic mode at the open circuit voltage with a sinusoidal voltage amplitude of 25 mV. CV was measured at 20 mV/s and the second CV cycle was plotted. Schematic and pictures of the photoelectrochemistry measurement setup are shown in **Figure 5.28**. EIS data was fitted to electrical circuit models using ZFit solver included in EC-Lab software (V11.43) in the range of 1 Hz-10 kHz.

Hydrogen peroxide production assays under ambient conditions

Sample pieces (5 mm × 5 mm) were placed in plastic cuvettes with a frontside facing up. The aqueous solution was freshly prepared right before the experiment and contained horseradish peroxidase (HRP; 4250 units/L, Sigma) and (p-hydroxyphenyl) acetic acid (p-HPA, 1×10^{-3} M, Sigma) in Tris buffer (0.25 M). Samples submerged in 0.5 mL of PBS solution was placed in the cuvettes for 20 min. Xe arc lamp at the power intensity of 150 mW/cm^2 was used for sample irradiation. After the exposure, 0.1 mL of the solution was transferred to the black-walled 96-well plate, 0.1 mL of enzyme solution was added, and was incubated for 10 min. Fluorescence intensity was evaluated using a plate read (Synergy Neo HTS). Fluorescence signals were measured by an excitation wavelength of 320 nm and an emission wavelength of 405 nm.

Silicon membrane photocurrent stability

For long term stability, silicon membranes were stored in 1× PBS at 37 °C in a tissue culture incubator and removed only for measurements in the patch-clamp setup. For short term photostability tests, the membranes were stored in 1× PBS at room temperature in the dark or in the patch-clamp setup under pulsed illumination at 4 Hz.

Atomic layer deposition

Atomic layer deposition (ALD) of TiO_2/Al_2O_3 superlattice was performed on the 5 mm × 5 mm stain-etched silicon wafers using Savannah G2 Thermal ALD System. Prior to the ALD process the samples were mounted on the carrier wafer using copper tapes. The chamber has been stabilized at 150 °C for 10 mins before deposition. The flow rate was set to 90 sccm. The TiO_2 deposition cycle comprised alternative pulses of O_3/H_2O (0.1 s, wait 10 s) and TDMAT (Ti precursor) (0.015 s, wait 10 s) for expected deposition rate of 0.6 Å/cycle. The Al_2O_3 deposition cycle comprised alternative pulses of O_3/H_2O (0.015 s, wait 5 s) and TMA (Al precursor) (0.015 s, wait 5 s) for the expected deposition of 1 Å/cycle. To achieve a total deposition profile of 20-cycle TiO_2/4-cycle Al_2O_3, every 1-cycle Al_2O_3 was deposited following every 4-cycle TiO_2 where the process was repeated 5 times.

Light sources and light analysis

Light sources used in this study are: 1) 532 nm LED (M530L3 mounted on SM1P25-A, Thorlabs), 2) 365 nm LED (M365L3-C1, Thorlabs), 3) 625 nm LED (M625L4-C1, Thorlabs), 4) diode-pulsed solid-state 532 nm laser (500 mW, LRS-0532-PFM-00300-05, Laserglow) coupled into P1-460AR-2 fiber (Thorlabs), 5) 808 nm diode laser (10 W, LRD-0808-PFI-10000-01, Laserglow) coupled into MHP365L02 fiber (Thorlabs). LEDs were mounted into the microscope and

electrochemical setup as received. The 532 nm laser was focused using a CFC-2X-A collimator (Thorlabs) for biostimulation experiments. The 808 nm laser was focused using a F220SMA-850 or F230SMA-850 collimator (Thorlabs) for biostimulation experiments and a F220SMA-85 for microscope setup. Laser power was controlled using front-panel analog knob adjustments and modulated with TTL or analog input signals. Light power was measured using Thorlabs S120C and S310C sensors connected to the PM100D console. Spot sizes for LEDs and lasers were measured using the knife-edge technique (5/95 width). Output spectra of the light sources were measured using a Fergie spectrometer (Princeton Instruments) and are displayed in **Figure 5.29**.

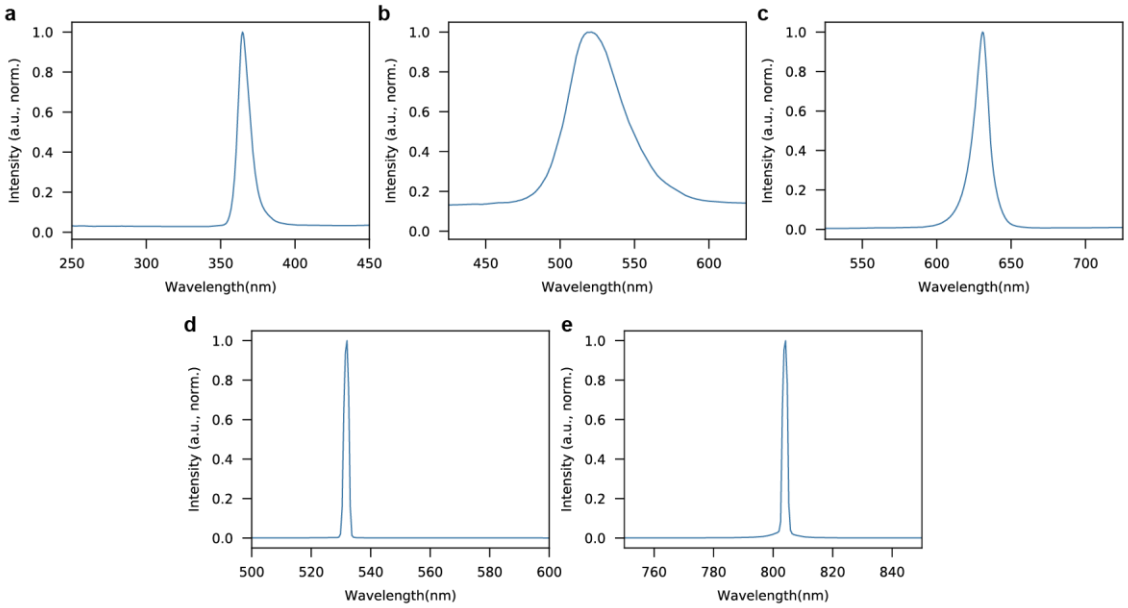

Figure 5.29 Spectra of light sources used in the study of silicon membranes.

(**a**) 365 nm LED. (**b**) 532 nm LED. (**c**) 625 nm LED. (**d**) 532 nm laser. (**e**) 808 nm laser.

Scanning electron microscopy

Scanning electron microscopy was performed using a Merlin scope (Carl Zeiss). Samples were mounted on aluminum sample holders using copper tape. Cross sections were prepared by scratching the back side of the wafer using diamond scribe, breaking the sample in half and mounting on a 90° sample holder using copper tape. EDS was performed on the same scope using an Oxford Ultim Max 100 EDS system and data were analyzed using AZTEC software (Oxford Instruments).

Focused ion beam milling

Samples for scanning transmission electron microscopy (STEM) were prepared using the Tescan LYRA3 FIB-SEM system equipped with a gallium ion gun. The lamella was lifted *in situ* with a tungsten manipulator and transferred to the post on the copper TEM half-circle grid. A platinum layer (~1 μm) was deposited onto the sample to protect its surface during milling to the thickness of ~ 200 nm. SEM images of the lamella are shown in **Figure 5.30**.

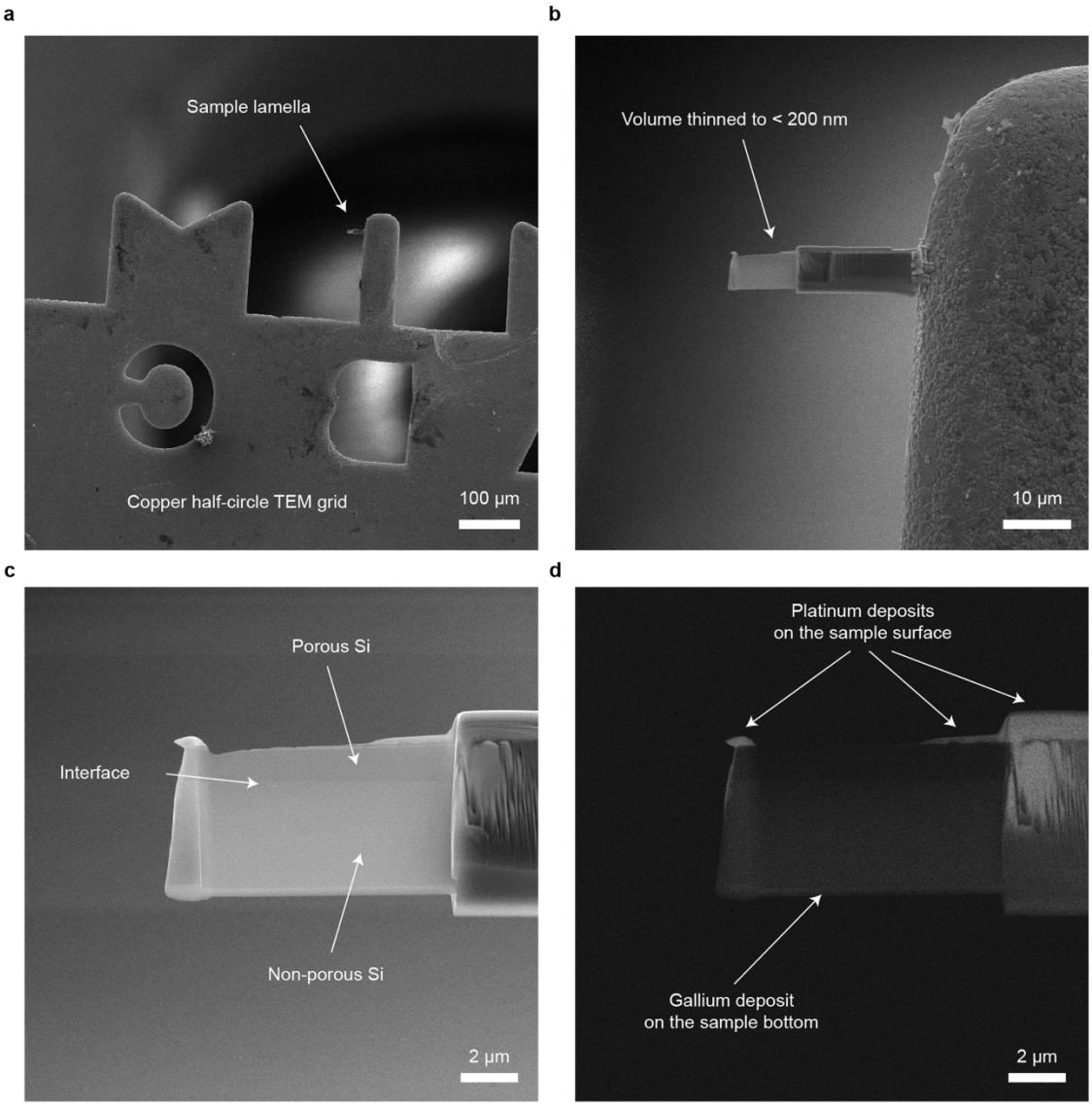

Figure 5.30 Scanning electron microscopy images of a sample lamella used for scanning transmission electron microscopy imaging.

(**a**) Low magnification image showing sample on the copper half-circle grid. (**b**) Only part of the lamella was thinned to < 200 nm. (**c**) Thinned region with visible porous and non-porous material domains. (**d**) Backscattered electron image showing platinum and gallium deposits on the lamella.

Scanning transmission electron microscopy

STEM was carried out using a 200 kV aberration-corrected JEOL ARM200F with a cold field emission source, which gives spatial resolution ~ 0.8 Å. High-angle annular dark-field (HAADF) detector angle was set to 90-270 mrad to give Z contrast images. Diffraction patterns were taken under TEM mode. Images were processed using ImageJ software.

Atomic force microscopy

Atomic force microscopy (AFM) was performed with a Bruker Dimension Icon microscope using a ScanAsyst probe in automated Peak Force Tapping™ mode. Gwyddion software was used to remove scars from the scans, crop the scan area, and plot the 3D model of the material surface.

Spectroscopic ellipsometry

Spectroscopic ellipsometry was performed using Horiba UVISEL 2.

Indentation

Modulus and hardness measurements were carried out using a TI950 Triboindenter (Bruker-Hysitron) with a Berkovich tip at Scanned Probe Imaging and Development facility at NUANCE center, Northwestern University. The loading-holding-unloading cycles were used for the nanoindentations test. Standard quartz substrate was used to calibrate the system before measurement on silicon samples. Indentation results obtained were analysed based on the method suggested by Oliver and Pharr[32].

Silicon membrane microspectrometry

Microspectrometry of silicon membranes was performed on an inverted microscope (Olympus IX71) using a 20x/0.45 Ph1 (Olympus) lens. A fluorescent X-Cite lamp (120PC Q, Lumen

Dynamics) was used as a light source in both transmission and reflectance mode. The spot size was reduced to <1 mm using the input aperture. An 80/20 beamsplitter (21001, Chroma) was used for reflectance measurements. Spectra were recorded using a Fergie spectrometer and LightField software (Princeton Instruments). A dielectric mirror (BB1-E02, Thorlabs) was used as a reflectance standard. The presented spectra are an average of at least six measurements from different membranes to average the effects of thin-film interference on the measurements. For transmittance, PDMS absorption was subtracted. Schematic of the experimental setup is shown in **Figure 5.31**.

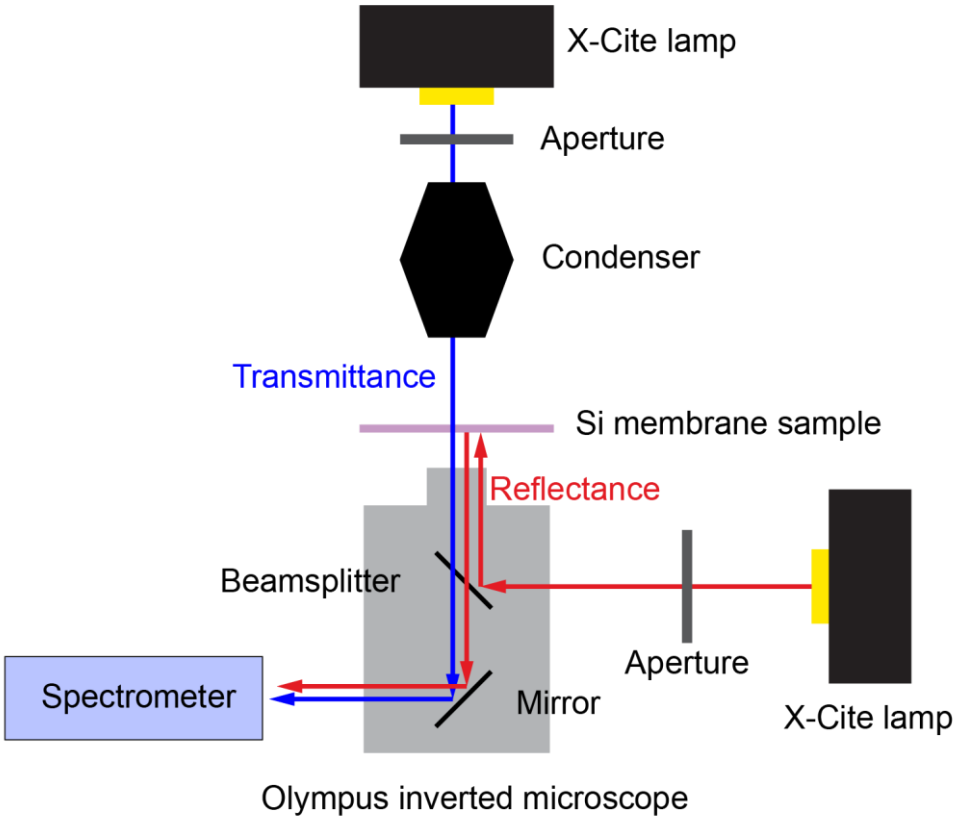

Figure 5.31 Schematic of the optical setup used for microspectrometry of silicon membranes.

Optical materials microscopy

Color optical microscopy was performed on the Olympus OLS5000 LEXT system.

Fluorescence measurements

Fluorescence measurements were performed on a HORIBA Fluorolog-3 Spectrofluorometer using 320 nm excitation light and a Synapse OE-CCD detector.

Numerical data processing

Analysis of numerical data and plotting was performed with Python scripts using NumPy, Matplotlib, Scipy, and Seaborn libraries. Statistics were calculated using statmodels library by applying Tukey's honestly significant difference (HSD) multiple comparison test.

5.7 Bibliography

1 Feiner, R. & Dvir, T. Tissue–electronics interfaces: from implantable devices to engineered tissues. *Nature Reviews Materials* **3**, 1-16 (2017).

2 Yang, X. *et al.* Bioinspired neuron-like electronics. *Nature Materials* **18**, 510-517, doi:10.1038/s41563-019-0292-9 (2019).

3 Liu, Y. *et al.* Morphing electronics enable neuromodulation in growing tissue. *Nature Biotechnology* **38**, 1097-1097, doi:10.1038/s41587-020-0533-0 (2020).

4 Murphy, J. J. Current practice and complications of temporary transvenous cardiac pacing. *BMJ* **312**, 1134, doi:10.1136/bmj.312.7039.1134 (1996).

5 Austin, J. L., Preis, L. K., Crampton, R. S., Beller, G. A. & Martin, R. P. Analysis of pacemaker malfunction and complications of temporary pacing in the coronary care unit. *The American journal of cardiology* **49**, 301-306, doi:10.1016/0002-9149(82)90505-7 (1982).

6 Betts, T. R. Regional survey of temporary transvenous pacing procedures and complications. *Postgraduate medical journal* **79**, 463-465, doi:10.1136/pmj.79.934.463 (2003).

7 Nolewajka, A. J., Goddard, M. D. & Brown, T. C. Temporary transvenous pacing and femoral vein thrombosis. *Circulation* **62**, 646-650, doi:10.1161/01.cir.62.3.646 (1980).

8 Koo, J. *et al.* Wireless bioresorbable electronic system enables sustained nonpharmacological neuroregenerative therapy. *Nature medicine* **24**, 1830-1836 (2018).

9 Choi, Y. S. *et al.* Fully implantable and bioresorbable cardiac pacemakers without leads or batteries. *Nat Biotechnol* **39**, 1228-1238, doi:10.1038/s41587-021-00948-x (2021).

10 Jiang, Y. & Tian, B. Inorganic semiconductor biointerfaces. *Nat Rev Mater* **3**, 473-490, doi:10.1038/s41578-018-0062-3 (2018).

11 Rotenberg, M. Y. & Tian, B. Talking to cells: semiconductor nanomaterials at the cellular interface. *Advanced Biosystems* **2**, 1700242 (2018).

12 Silvera Ejneby, M. *et al.* Chronic electrical stimulation of peripheral nerves via deep-red light transduced by an implanted organic photocapacitor. *Nat Biomed Eng*, doi:10.1038/s41551-021-00817-7 (2021).

13 McCall, J. G. *et al.* Preparation and implementation of optofluidic neural probes for in vivo wireless pharmacology and optogenetics. *Nature protocols* **12**, 219 (2017).

14 Montgomery, K. L. *et al.* Wirelessly powered, fully internal optogenetics for brain, spinal and peripheral circuits in mice. *Nature methods* **12**, 969-974 (2015).

15 Nussinovitch, U. & Gepstein, L. Optogenetics for in vivo cardiac pacing and resynchronization therapies. *Nature Biotechnology* **33**, 750-754, doi:10.1038/nbt.3268 (2015).

16 Yan, F., Bao, X.-M. & Gao, T. Photovoltage spectra of silicon/porous silicon heterojunction. *Solid State Communications* **91**, 341-343, doi:10.1016/0038-1098(94)90630-0 (1994).

17 Palsule, C. *et al.* Electrical and optical characterization of crystalline silicon/porous silicon heterojunctions. *Solar Energy Materials and Solar Cells* **46**, 261-269, doi:10.1016/s0927-0248(97)00004-4 (1997).

18 Suntao, W., Yanhua, W. & Qihua, S. Measurement and analysis of the characteristic parameters for the porous silicon/silicon using photovoltage spectra. *Applied Surface Science* **158**, 268-274, doi:10.1016/s0169-4332(00)00008-8 (2000).

19 Fang, Y. *et al.* Micelle-enabled self-assembly of porous and monolithic carbon membranes for bioelectronic interfaces. *Nature Nanotechnology* **16**, 206-+, doi:10.1038/s41565-020-00805-z (2021).

20 Jiang, Y. W. *et al.* Heterogeneous silicon rnesostructures for lipid-supported bioelectric interfaces. *Nature Materials* **15**, 1023-1030, doi:10.1038/nmat4673 (2016).

21 Kolasinski, K. W. in *Handbook of Porous Silicon* Ch. Chapter 4, 39-59 (2018).

22 Yerokhov, V. Y. & Melnyk, I. I. Porous silicon in solar cell structures: a review of achievements and modern directions of further use. *Renewable and Sustainable Energy Reviews* **3**, 291-322, doi:10.1016/s1364-0321(99)00005-2 (1999).

23 Alhmoud, H., Brodoceanu, D., Elnathan, R., Kraus, T. & Voelcker, N. H. A MACEing silicon: Towards single-step etching of defined porous nanostructures for biomedicine. *Progress in Materials Science* **116**, 100636, doi:10.1016/j.pmatsci.2019.100636 (2021).

24 Hopcroft, M. A., Nix, W. D. & Kenny, T. W. What is the Young's Modulus of Silicon? *Journal of Microelectromechanical Systems* **19**, 229-238, doi:10.1109/jmems.2009.2039697 (2010).

25 Jiang, Y. *et al.* Nongenetic optical neuromodulation with silicon-based materials. *Nat Protoc* **14**, 1339-1376, doi:10.1038/s41596-019-0135-9 (2019).

26 Glunz, S. W. & Feldmann, F. SiO2 surface passivation layers – a key technology for silicon solar cells. *Solar Energy Materials and Solar Cells* **185**, 260-269, doi:10.1016/j.solmat.2018.04.029 (2018).

27 Nosaka, Y. & Nosaka, A. Y. Generation and Detection of Reactive Oxygen Species in Photocatalysis. *Chemical Reviews* **117**, 11302-11336, doi:10.1021/acs.chemrev.7b00161 (2017).

28 Jiang, Y. *et al.* Rational design of silicon structures for optically controlled multiscale biointerfaces. *Nature biomedical engineering* **2**, 508 (2018).

29 Tampo, H., Kim, S., Nagai, T., Shibata, H. & Niki, S. Improving the Open Circuit Voltage through Surface Oxygen Plasma Treatment and 11.7% Efficient Cu2ZnSnSe4 Solar Cell. *ACS Appl Mater Interfaces* **11**, 13319-13325, doi:10.1021/acsami.9b01756 (2019).

30 Jiang, Y. *et al.* Rational design of silicon structures for optically controlled multiscale biointerfaces. *Nat Biomed Eng* **2**, 508-521, doi:10.1038/s41551-018-0230-1 (2018).

31 Kahlert, H. in *Electroanalytical Methods* (eds Fritz Scholz *et al.*) Ch. Chapter 15, 291-308 (Springer Berlin Heidelberg, 2010).

32 Oliver, W. C. & Pharr, G. M. An improved technique for determining hardness and elastic modulus using load and displacement sensing indentation experiments. *Journal of Materials Research* **7**, 1564-1583, doi:10.1557/jmr.1992.1564 (1992).

Chapter 6

Nongenetic Optical Stimulation of Hearts and Nerves Using Porous Silicon Membranes

Research study presented in this chapter is expected for publication in Prominski, A., Shi, J., Li, P., Yue, J., Lin, Y., Park, J., Tian, B. & Rotenberg, M. Y. "Porosity-based heterojunctions enable leadless optoelectronic modulation of tissues." Nature Materials (2022).

6.1 Introduction

Lead-free electroceuticals represent an important segment of future bioelectronic medical therapies. Elimination of electric wires generates the potential for minimally invasive implantation surgeries and improves the biocompatibility of the entire device. Especially, affordable solutions to the epicardial heart stimulation can enable support of contractions post-surgery, improving patients' survival rate and peripheral nerve stimulation brings the promise of a drug-free pain management solution and an essential tool for fighting the opioid epidemic. Therefore, I have explored proof of concept applications of my photoelectrochemical materials in clinically relevant bioelectronic stimulations.

In this chapter, I will show how silicon membranes with nanoporous/non-porous heterojunctions can be applied to the optical stimulation of isolated hearts and sciatic nerves in a rat model. (**Fig. 6.1)** I will first demonstrate heart pacing using visible and near-infrared light pulses and study the activation threshold for heart contraction. I will also investigate the action potential waves in the myocardium during proof of concept dual-chamber stimulation.

Subsequently, I will show acute sciatic nerve stimulation *in vivo* and quantify the selectivity of muscle activation from the membranes using multichannel electromyography recording. Finally, I will demonstrate partial implantation of membranes and stimulation of sciatic nerves through an optical fiber in a closed wound.

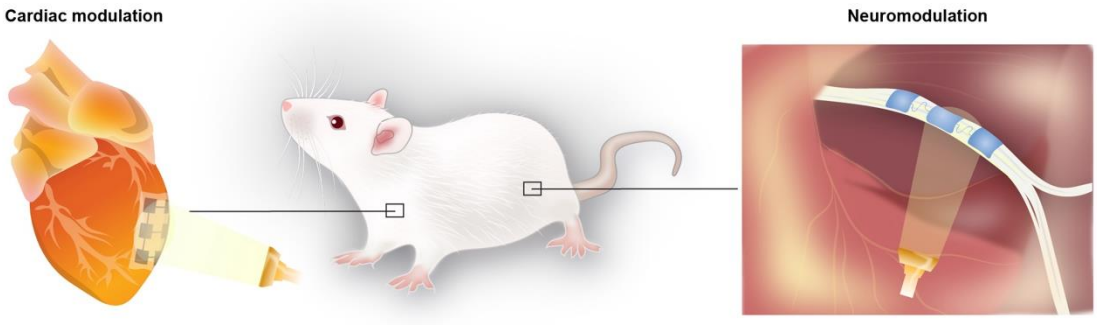

Figure 6.1 Nanoporous/non-porous silicon membranes can be used for nongenetic optomodulation of biointerfaces.

Thin and flexible nanoporous/non-porous silicon membranes allow stimulation of rat hearts *ex vivo* and sciatic nerves *in vivo* using low energy light pulses.

6.2 *Ex Vivo* Cardiac Modulation

To demonstrate the utility of our free-standing device in converting low optical power into bioelectrical stimulation, we interfaced the device with isolated cardiac tissue in a Langendorff apparatus (**Fig. 6.2a**). Figure 5b shows an image of the device conforming to the soft curvilinear cardiac surface and interfacing with the left ventricle (LV). Capillary forces between the flexible membrane and the heart were enough to hold the device in place without any surface glues or physical modifications, despite the wet surface and buffer perfusion. An electrocardiogram (ECG)

recording of the electrical activity of the heart showed an extremely slow atrioventricular node rhythm (due to removal of the atriums). Upon application of light pulses (**Fig. 6.2c**), the heart immediately synchronized to the frequency of the light pulses (**Fig 6.2d, Fig. 6.3**) due to effective depolarization of myocardium through injected photoelectrochemical currents. To determine the optical density required for overdrive pacing, we stimulated a heart with 532 nm and 808 nm lasers, as shown in Figures 5d and 5e, respectively. We found that 532 nm light had a lower stimulation threshold than 808 nm light (**Figure 6.2f**). We achieved a significantly improved stimulation efficiency over previously reported nanowire-based materials[1]; as little as 4 mW/mm^2 of light (532 nm) was sufficient to stimulate the heart compared to the previously used power of 3.5 kW/mm^2[1]. The radiant exposure (532 nm) is now on the same order of magnitude as that required for heart stimulation using optogenetics (0.3-2 mJ/cm^2)[2]. A notable quality of our device is the ability to utilize NIR wavelengths (808 nm) for optical biomodulation which can penetrate into deep tissues[3]. This is another meaningful advantage over optogenetics, in which opsins have a distinct light absorption band limited to visible light with low tissue penetration capabilities. Moreover, the radiant exposure necessary to stimulate the heart with NIR light (~2 mJ/cm^2) was also significantly lower than that required for the unaided IR stimulation of embryonic hearts (800 mJ/cm^2)[4].

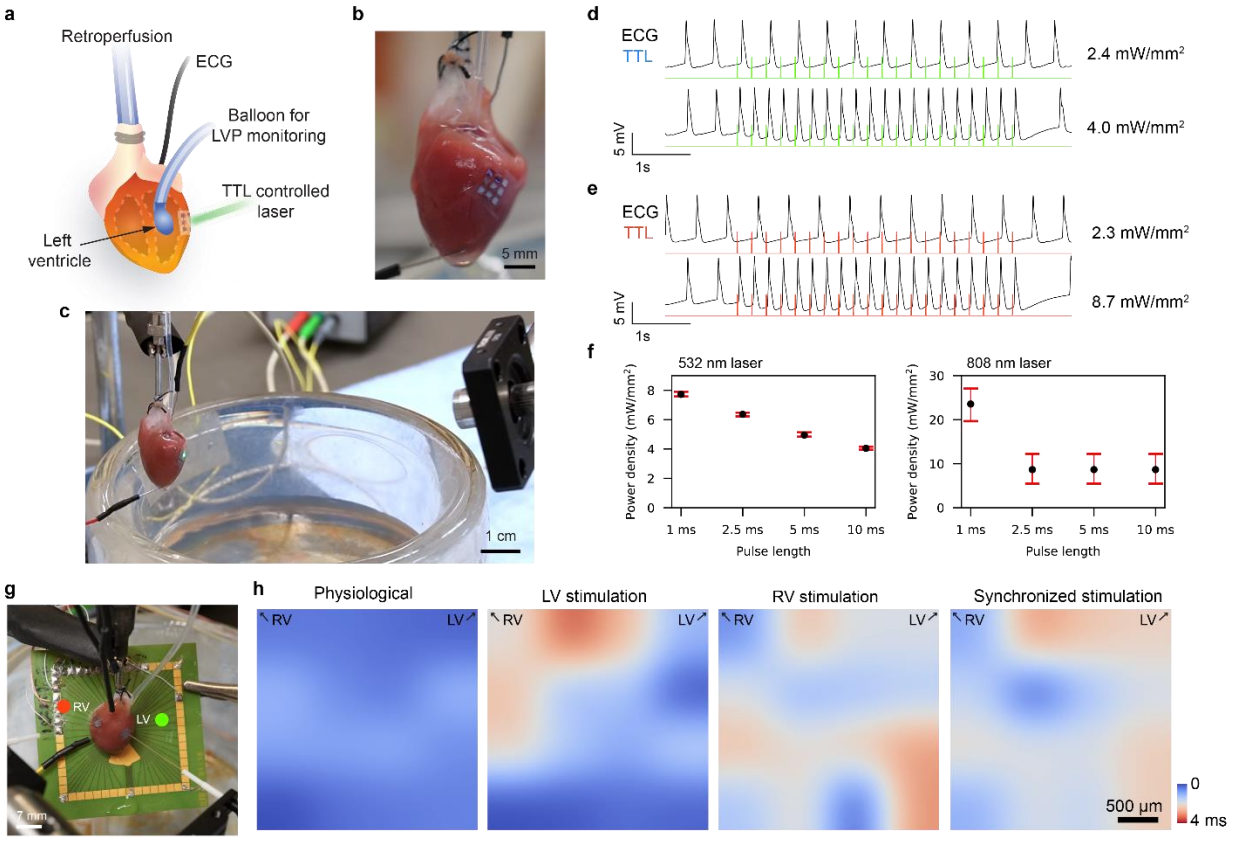

Figure 6.2 Pacing of isolated hearts *ex vivo*.

(**a**) Schematic of experimental setup used for isolated heart in the Langendorff apparatus. (**b**) Photograph of the membrane attached to the heart on the left ventricular wall. (**c**) Photograph of 532 nm laser illuminating membrane attached to the isolated heart. (**d**) Synchronized electrocardiogram (ECG) and transistor-transistor (TTL) signals showing heart stimulation at 4 Hz using 532 nm laser with sub- (2.4 mW/mm^2) and supra-threshold (4.0 mW/mm^2) optical power densities. Subthreshold stimulation results in only small artifacts in the ECG trace; suprathreshold illumination demonstrates overdrive pacing. (**e**) When the heart is stimulated using 808 nm lasers at 4Hz, the threshold is higher, as only 8.7 mW/mm^2 is able to achieve overdrive pacing. Results in (d) and (e) are representative of over four independent experiments performed with different membranes and hearts. (**f**) Optical power threshold for stimulation of heart tissue with 532 and 808

nm lasers. Central point represents the lowest power setting for which uninterrupted pacing was observed. Error bars represent half of the distance to the nearest laser power setting to estimate power readout limitations. (**g**) Photography of fiber setup and microelectrode array used in the dual chamber pacing experiments. 532 nm laser (4 mW/mm^2) was used to stimulate LV and 808 nm laser (60 mW/mm^2) was used to stimulate RV. (**h**) Isochrone maps of the electrical propagation in the ex vivo heart show different patterns of electrical propagation for spontaneous, single chamber (LV or RV), or dual chamber optical pacing.

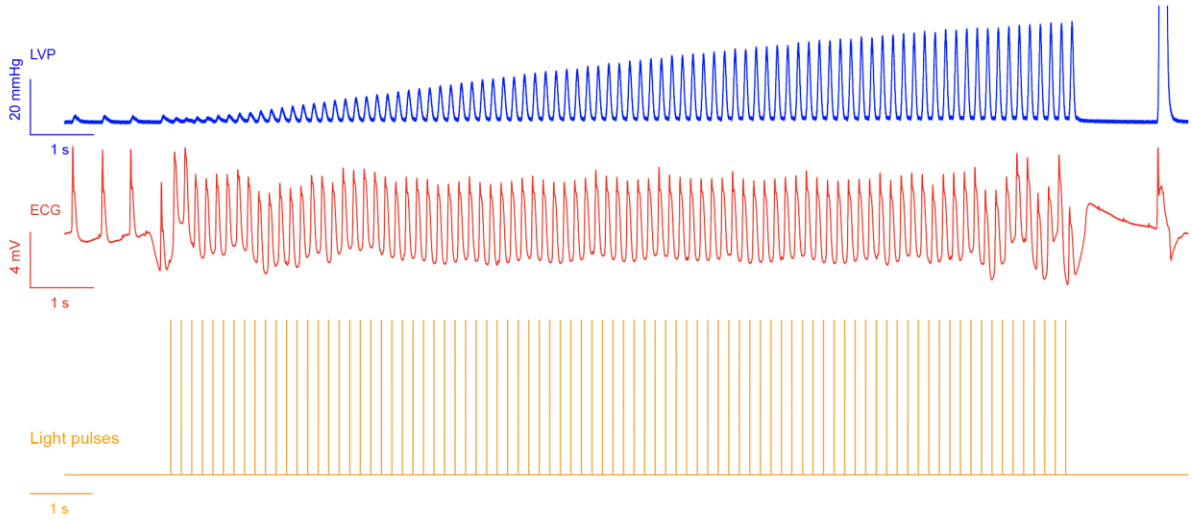

Figure 6.3 Physiology measurements of the isolated heart paced at 6 Hz with 1.7 ms 532 nm laser pulses.

Electrocardiography (ECG) recording shows efficient pacing during the period of the light pulsing. The heart contractions adjust mechanically to the new pacing conditions which is indicated by the increasing left ventricular pressure (LVP) signal. The stimulation using these conditions can be maintained for more than 1 hour in the isolated heart setting.

As our device is completely free-standing, it can be positioned at any location on the heart, free of lead-associated limitations. This suggests that the device can be used for simultaneous stimulation at multiple sites for cardiac resynchronisation therapy, similar to previously reported work[5], but without the need for genetic modifications. To demonstrate the applicability of dual chamber pacing, we have performed experiments using two devices, one placed on the LV wall and the other on the right ventricular (RV) wall (**Fig. 6.2g**). Additionally, we used microelectrode array to map the field potential propagation throughout the myocardium, and observed different propagation waves under different stimulation conditions (**Fig. 6.2h)**. Two separate contractions were observed only when sufficient time delay between the two pulses was used (**Fig. 6.4**), which also depends on which pulse is leading in the stimulation. We believe that this preliminary result shows potential for application of the device in heart stimulations from different positions, which increases its versatility and therapeutic potential.

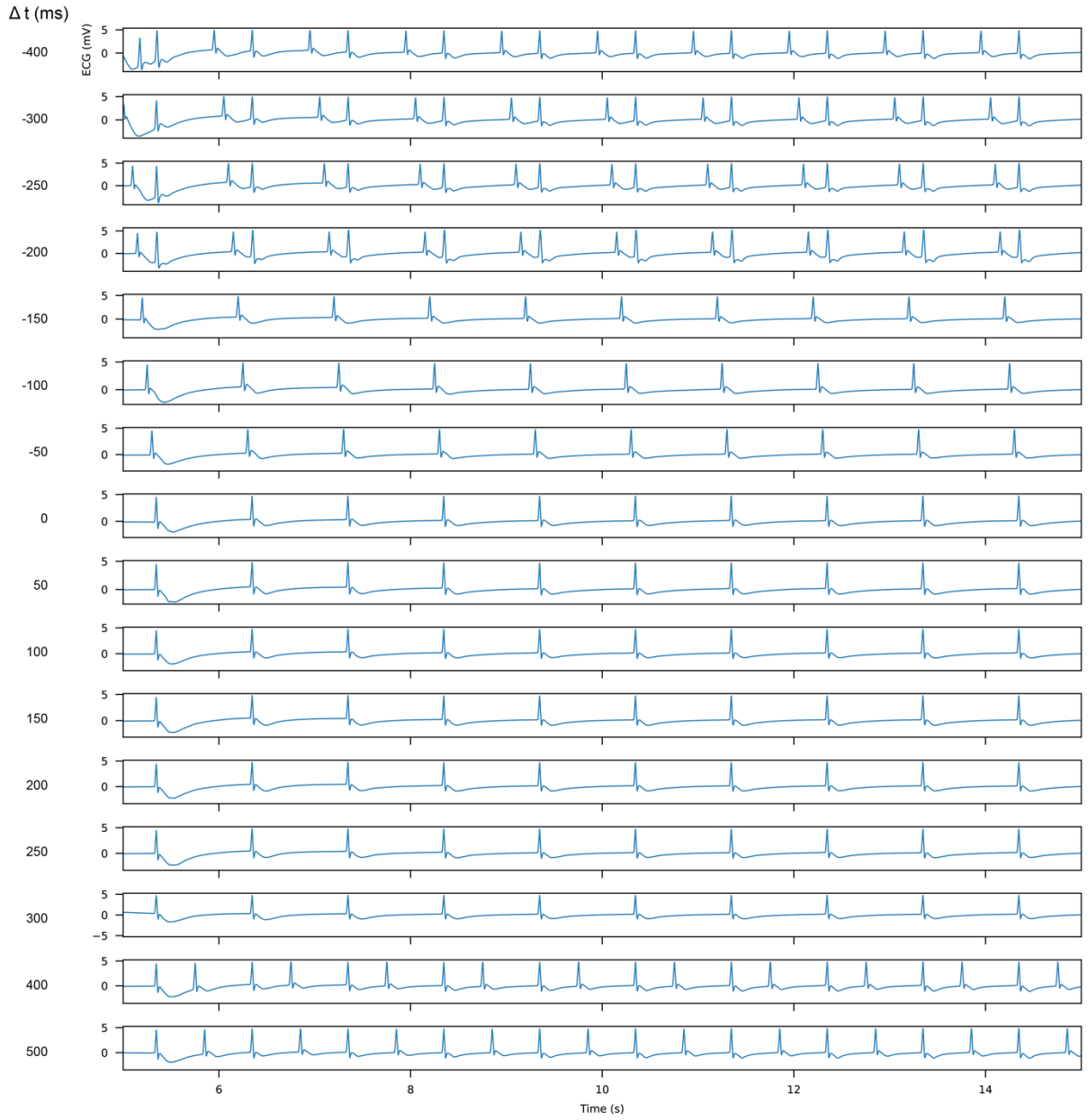

Figure 6.4 Pacing of the isolated heart using dual chamber stimulation and different spacing between light pulses.

Δt describes the time difference between LV and RV stimulation. Negative values are used when RV pulse precedes LV pulse. When RV pulse is leading two compound action potentials and two contractions were observed up to the 200 ms spacing between stimulation pulses, but when the

order of pulses is reversed, the spacing between pulses must be at least 400 ms apart to observe two contractions.

6.3 *In Vivo* Sciatic Nerve Modulation

Finally, we demonstrated the utility of the device in neuroregenerative applications and studied acute *in vivo* sciatic nerve biomodulation in rats (**Fig. 6.5a**). **Figure 6.5b** shows that the flexible device can wrap around the exposed sciatic nerve without any apparent breakage and can adhere to it without need for glue or suture. Illuminating the device with pulsed light resulted in an action potential (AP) that propagated through the nerve and moved the associated lower limb (**Fig. 6.5c**). In contrast to heart stimulation, where we observed binary, sub- or supra-threshold pacing effects, the sciatic nerve showed an intensity-dependent effect. We investigated stimulation of the nerve using 532 and 808 nm lasers and measured compound action potential (CAP) amplitude and maximal leg displacement. **Figures 6.5d-e** and **Fig. 6.5f** show a correlation between the optical power densities and the pulse duration to the CAP amplitude and leg displacement, respectively.

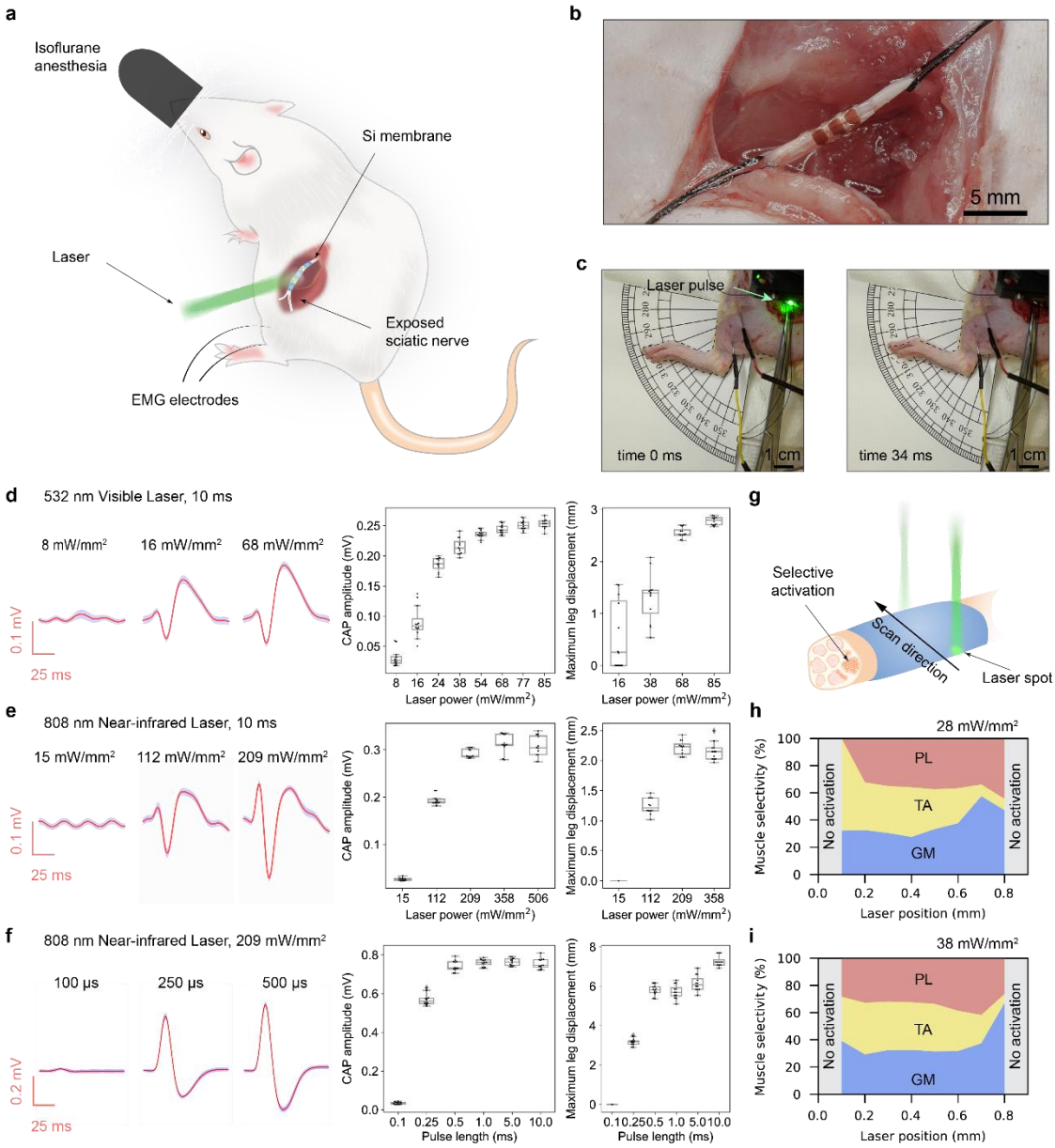

Figure 6.5 *In vivo* sciatic nerve stimulation.

(**a**) Schematic diagram of sciatic nerve stimulation in an acute *in vivo* rat model. (**b**) Photograph of silicon membrane wrapped around the sciatic nerve. (**c**) Still images from the video before (left) and after (right) photo-stimulation showing limb movement. (**d**) Analysis of nerve stimulation with 10 ms visible 532 nm laser pulses. (**e**) Analysis of nerve stimulation with 10 ms near-infrared (NIR) laser pulses. (**f**) Analysis of nerve stimulation with different NIR laser pulse lengths.

Functional analysis of nerve stimulation in (d-f) is achieved through analysis of the electromyography (EMG) signal (left), maximum amplitude of the compound action potential (CAP, center), and maximum leg displacement distance (right) for the same 12 subsequent stimulation events at a frequency of 1 Hz. EMG signals at selected conditions are presented as an average; shaded area encompasses ± SD. For CAP amplitude and maximum leg displacement, the boxes bind IQR divided by the median, and whiskers extend 1.5 ± IQR. All datapoints are plotted, unless not detected (N.D.). Data in panels (d) and (e) were recorded in the same experimental setup with only a change of the applied laser, and data in panel (f) was acquired in a separate experiment. All results are representative of at least four independent experiments using different membranes and rats. (**g**) Schematic diagram of a laser scanning and selective nerve activation. (**h-i**) Selectivity index for a muscle stimulation with different laser positions and power. GM - gastrocnemius medialis, TA - tibialis anterior, PL - plantar interossei.

In this context, it is important to realize that the sciatic nerve is a bundle of nerves[6]; consequently, the different nerves within the sciatic bundle may have different stimulation thresholds and/or different distances from the interfacing silicon membrane. Thus, the intensity dependence of the optical stimulation may be attributed to the ability of higher electrical intensity to stimulate nerves with higher thresholds and penetrate deeper into the bundle. We used multichannel electromyography (EMG) recording from muscles controlled by the sciatic nerve to study the activation selectivity (**Fig. 6.5g, Fig. 6.6**). By adjusting power and position of the laser beam (**Fig. 6.5h-i**) we were able to activate different muscles (*i.e.*, gastrocnemius medialis, tibialis anterior, plantar interossei) to a varying extent. In clinical application, controlling the intensity and selectivity allows tuning the stimulation to yield a therapeutic output while minimizing pain and

discomfort. Additionally, the selectivity reduces inverse recruitment of muscle groups, which delays the onset of muscle fatigue[7]. While silicon membranes are not as selective as multipolar cuff and intrafascicular implants[8,9], the improvement in membrane pattern design and application of beams with smaller diameters may further increase selectivity. Finally, we were able to stimulate the limb with a pulse as short as 500 μs for NIR laser which corresponds to a radiant exposure of 10 mJ/cm^2, an exposure that is energetically efficient and safe for most tissues.

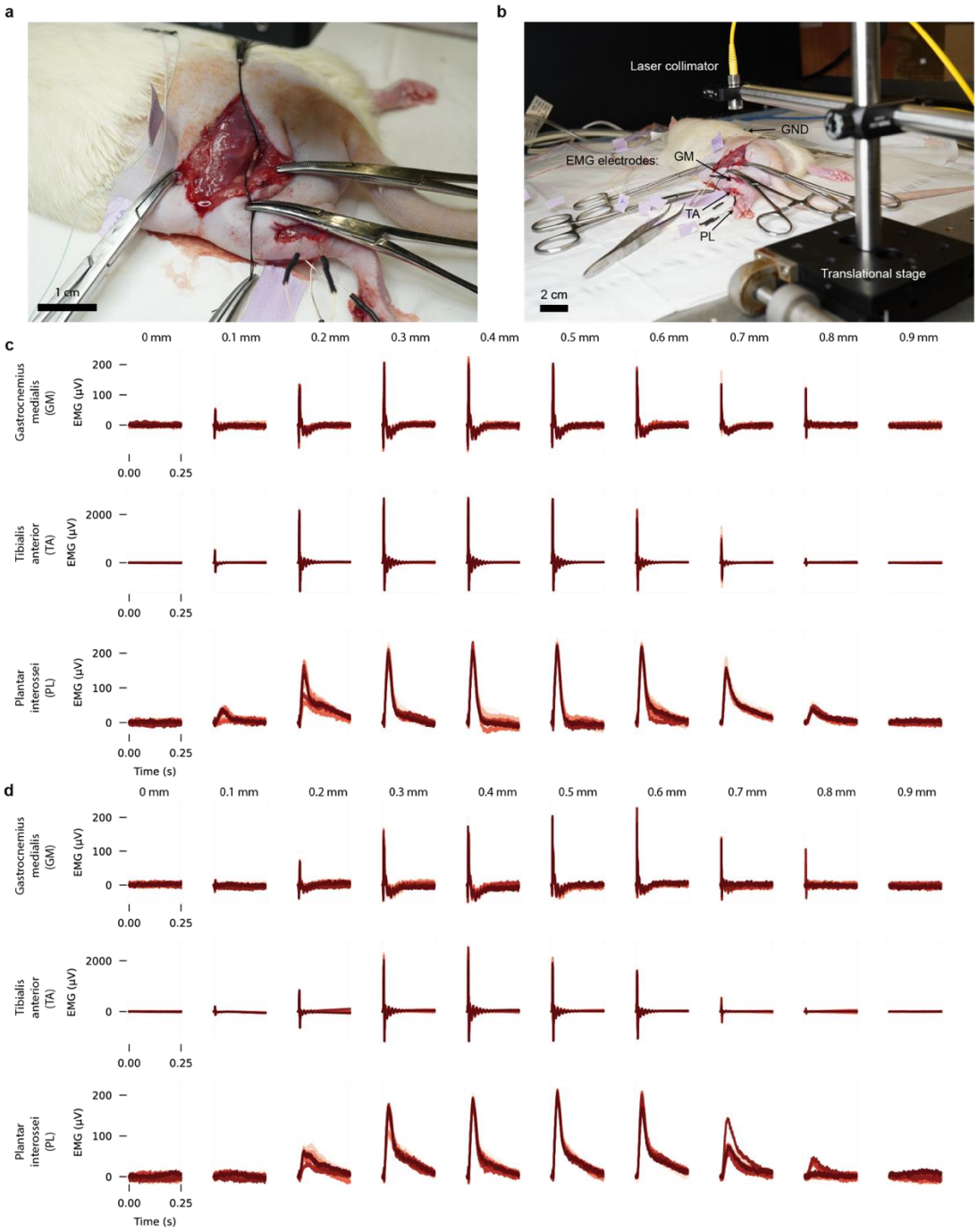

Figure 6.6 The measurement setup and multichannel EMG recordings.

(a) Top view of the rectangular silicon membrane wrapped around the sciatic nerve. **(b)** Overview of the measurement and laser irradiation setup. **(c)** Plot of 12 overlapping EMG signals recorded in gastrocnemius medialis (GM), plantar interossei (PL) and tibialis anterior (TA) muscles for each

laser position using 38 mW/mm^2 laser power. **(d)** Plot of 12 overlapping EMG signals for each muscle and laser position using 28 mW/mm^2 laser power. For the measurement at position 0.5 mm, the sixth signal was excluded from analysis due to surge in an amplifier circuit and only 11 curves are shown.

While our experiments operate on the exposed nerve, the method is easily translatable to standard post-operative stimulation methods that employ implanted optical fiber cannulas (**Fig. 6.7**). Although in this proof of concept we used a standard optical fiber cannula, soft and flexible hydrogel-based optical fibers[10] can be used to lead light to the interfacing nerve *in vivo*. Additionally, deep red- and NIR-induced photocurrent generation may enable fully remote transdermal stimulation using an NIR transmission window[3]. Moreover, the thin PDMS used here as a support layer for the silicon membrane can be avoided or replaced with clinically available hydrogel-based conduits to improve adhesion and retention of the electrode after wound closure.

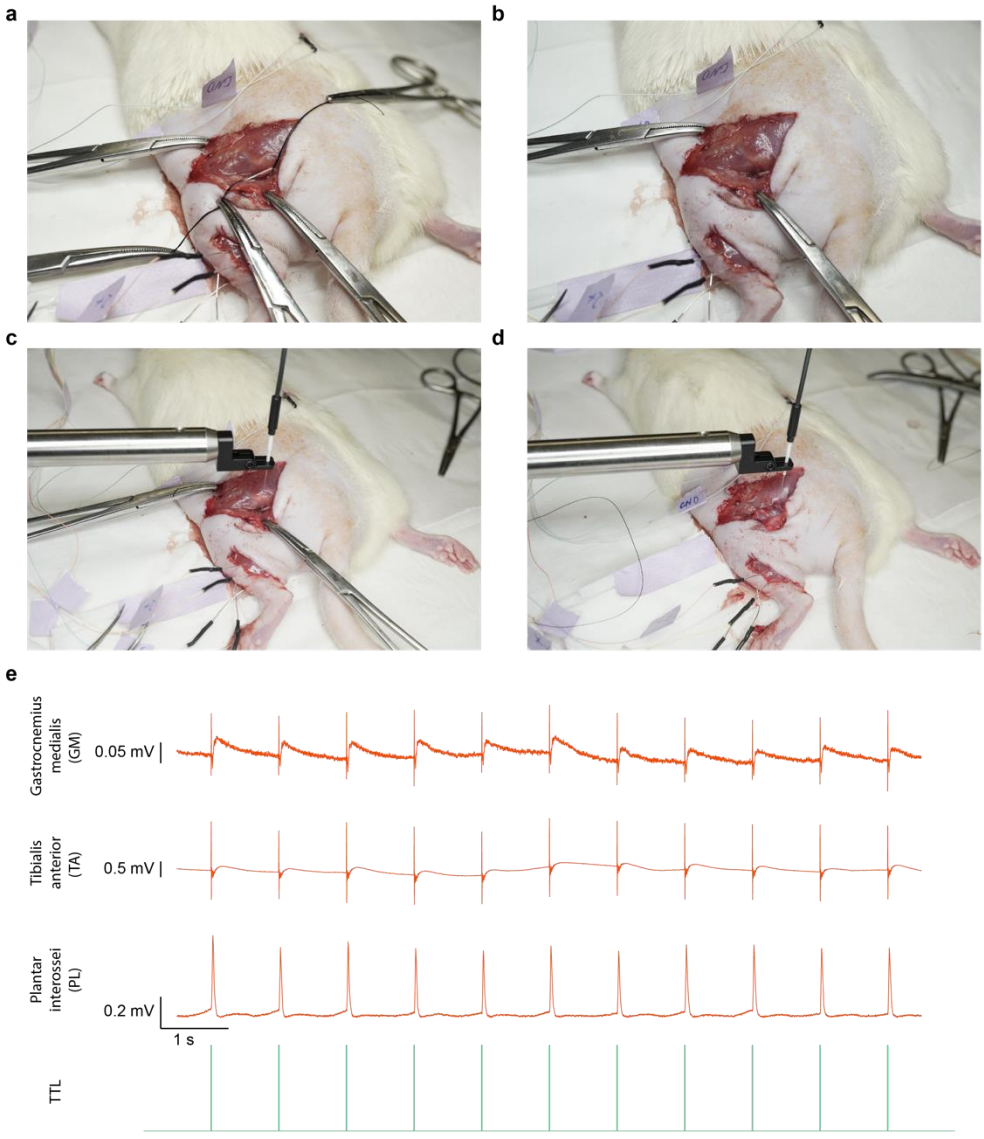

Figure 6.7 Proof of concept implantation of the silicon membrane and fiber cannula in the rat limb and electromyography (EMG) recording upon light stimulation.

Overview of the implantation procedure: **(a)** Membrane wrapped around a sciatic nerve. **(b)** Nerve repositioned between the muscles. **(c)** Fiber positioned over the membrane. **(d)** Muscle closed using Nylon sutures. **(e)** Multichannel EMG recordings of the compound action potential in the muscle during stimulation (532 nm laser, 20 mW/mm^2).

6.4 Summary

I have described in this chapter how silicon membranes achieved using simple fabrication strategy can show high functional efficiency and demonstrated effective stimulation in clinically relevant animal model. Combination of simple material design and processing opens the door to clinical translation through reducing cost of materials and simplifying regulatory burden since only pristine p-type silicon is used as a substrate for which the biocompatibility data is well known. While instability might limit some early applications, the preliminary results from surface modifications suggest that the material stability can be easily tuned to meet the desired therapeutic time scale. Therefore, the material presented herein forms a basis of a promising platform for the development of leadless electroceuticals.

6.5 Methods

Ex vivo heart stimulation

Isolated heart preparation followed methods described previously[11]. In short, an adult male rat (300-400 g body weight) was heparinized and anaesthetized using open-drop exposure of isoflurane in a bell jar configuration. The heart was removed and placed in ice cold HBSS buffer, and the aorta was cannulated in preparation for use in a Langendorff setup. Oxygenated HEPES-buffered Tyrode's solution was perfused through the cannulated aorta after passing through a heating coil and bubble trap (Radnoti). The heart was placed in a water-jacketed beaker (Fisher Scientific) to maintain a temperature of 37 °C. The perfusion pressure was maintained at 80-100 mmHg. The sinoatrial node along with the atria were removed to lower atrioventricular node pace. The perfusion and left ventricular pressure (LVP) were monitored using a BP-100 probe (iWorx) connected to the perfusion line and a water-filled balloon (Radnoti) inserted into the left

ventricle, respectively. For ECG recordings, needle electrodes were positioned on the left ventricular wall and aorta, ground on the cannula, and connected to a C-ISO-256 preamplifier (iWorx). All signals (perfusion, LVP, and ECG) were amplified using an IA-400D amplifier (iWorx) and interfaced with a computer using a Digidata 1550 digitizer with Clampex software (Molecular Devices). The silicon membrane was placed on the left ventricular wall and adhered stably to the heart. The lasers were pointed at the membranes and stimulation and recording were controlled using the Digidata 1550 digitizer. When only light pulses, or only membranes were used in the experiment, no stimulation was observed. Heart could be paced only when both membranes and light pulses were present (**Figure 6.8**). For dual chamber pacing experiments, hexagon shaped membranes were placed on left and right ventricular wall and light was delivered from 532 nm and 808 nm laser through 200 µm core glass fiber cannulas (CFMC22L20, Thorlabs) coupled to a 200 µm multimode fiber (M86L01 and M84L01, Thorlabs) using ceramic mating sleeve. Electrical mapping was performed using 4 × 4 micro electrode array (0.7 mm spacing between electrodes) and recorded using Intantech RHD USB interface board and RHD 16-channel input recording headstage. The signals were recorded at 10 kS/s in the 0.1-100 Hz bandwidth. Isochrone maps of the electrical propagation were calculated using Python script shown in **Appendix A4**. Timestamp of peak positive signal deflection for each contraction was determined and average was calculated for multiple signals. Gaussian interpolation was used for map rendering to improve readability.

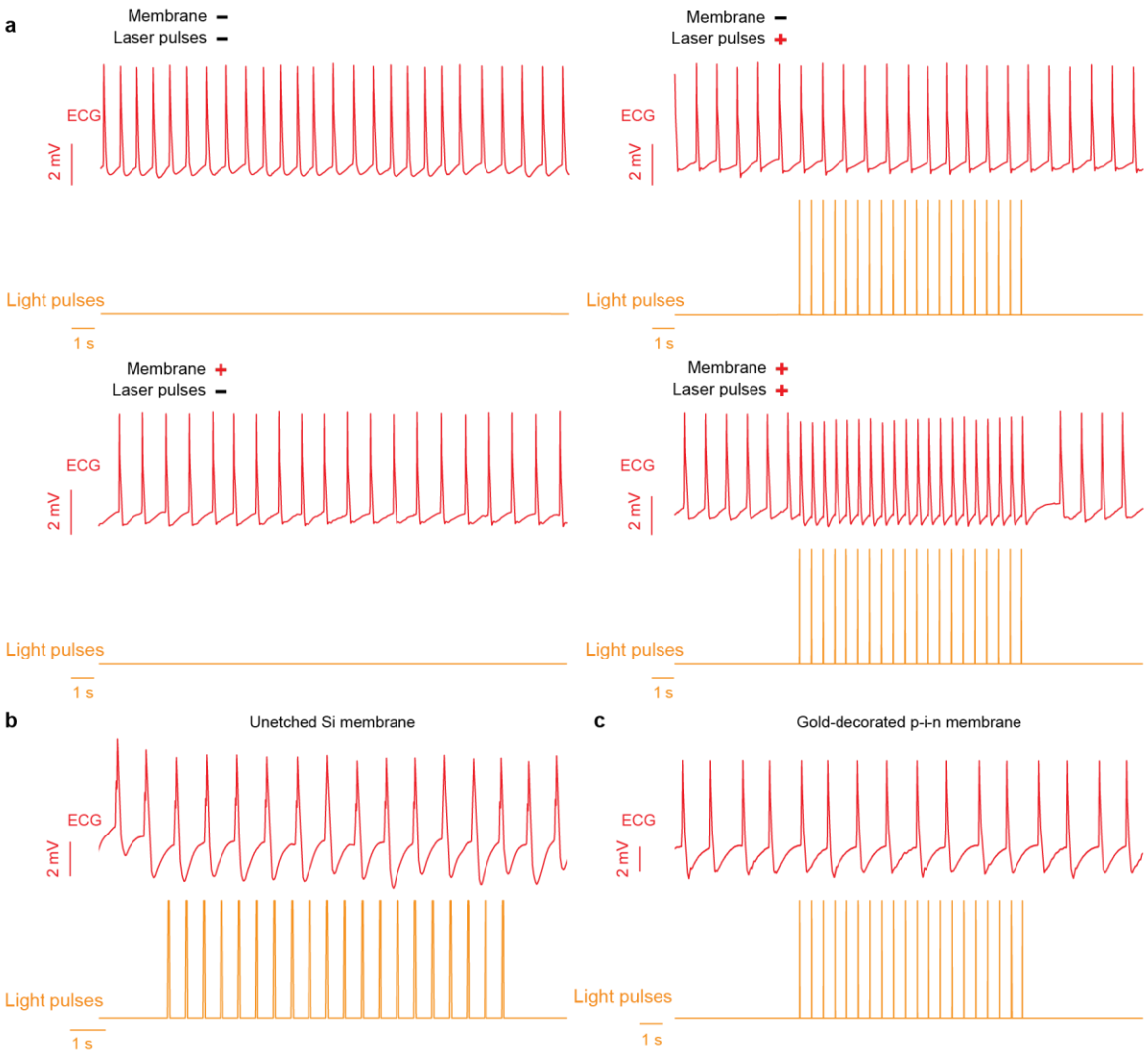

Figure 6.8 Control experiments for the photoelectrochemical heart pacing.

(a) Membranes or laser pulses alone have no effect on the heart contractions. Successful stimulation was observed only when both devices and light pulses were present. Similarly, unetched Si membranes (**b**) and gold-decorated p-i-n membranes (**c**) were not able to stimulate the heart.

Acute sciatic nerve stimulation

Sciatic nerve surgery followed methods described previously[11]. In short, adult rats (10-24 weeks, males and females) were deeply anaesthetized with isoflurane (3-4%). The fur was removed from the hindquarters using a surgical clippers and hair removal cream. An incision across the midline was made in the skin, and the fascial plane was opened between the gluteus maximus and the anterior head of the biceps femoris exposing the sciatic nerve. The nerve was extruded using sutures and the silicon membrane was wrapped around the nerve. For electromyography (EMG) recordings, stainless steel needle electrodes in an ungrounded configuration were inserted into the soleus and connected to a C-ISO-256 preamplifier (iWorx). The EMG signal was amplified using an IA-400D amplifier (iWorx) and interfaced with a computer using a Digidata 1550 digitizer with Clampex software (Molecular Devices). The lasers were pointed at the membranes and stimulation and recording were controlled using the Digidata 1550 digitizer. Note that the data in **Fig. 6.4d and e** was collected from the same experiment (by only changing the laser source), while the data in f was collected from a different experiment which accounts for the difference in recorded amplitudes. For analysis of leg displacement, a protractor was placed under the leg for a distance reference. Videos of limb movement were recorded using a Sony α6100 camera with a 30 mm macro lens (E 3.5/30, Sony) at 60 frames per second. The videos were cropped and sliced using Adobe Premiere Pro, exported as an image sequence, and imported into ImageJ for processing. The image sequence was set as an 8-bit greyscale stack. A Gaussian filter with 4 px radius was applied to the entire stack and the intensity of the first frame was subtracted. A binary threshold was used to isolate the displacement distance and the maximum displacement was measured under the first nail. If no movement was detected, a value of 0 was assigned to the pulse. Intantech RHD USB interface board and RHD 16-channel bipolar-input recording headstage were used for

multichannel EMG recording. The signals were recorded at 10 kS/s in the 0.1-200 Hz bandwidth. Parts of the skin were removed to expose the muscles and silver wires were inserted into gastrocnemius medialis (GM), plantar interossei (PL) and tibialis anterior (TA) muscles following the anatomical cues. Ground silver electrode was placed under the skin on the upper right body side of the animal, opposite of the recording side. Rectangular silicon membrane was placed on the exposed sciatic nerve and was illuminated from above using 532 nm laser light pulses with a spot size of 0.5 mm. The laser collimator was installed on the manual linear translational stage, and the nerve was scanned along the diameter at the steps of 0.1 mm. 12 light pulses were delivered at each position and EMG signals were recorded. Analysis of the recording was performed using Python analysis scripts shown in **Appendix A2** and **Appendix A3**. In short, for each laser pulse maximum positive deflection of EMG signal was calculated. The selectivity index for each laser position was calculated as suggested in the literature[8] using equation $SI_n = \frac{EMG_{n,norm}}{\sum_i EMG_{i,norm}}$, where SI_n is a selectivity index for a muscle n, $EMG_{n,norm}$ is a normalized maximum positive signal deflection for muscle n, and $\sum_i EMG_{i,norm}$ is the sum of normalized maximum positive deflections for all muscles included in the analysis. Signal from PL muscle was background corrected using iterative polynomial smoothing algorithm implemented in pybaselines package to remove large drift coming from the limb movement. No activation was defined where no signals were observed. For acute stimulation with a closed muscle, 532 nm laser pulses were delivered using 200 µm core glass fiber cannulas (CFMC22L20, Thorlabs) coupled to a 200 µm multimode fiber (M86L01, Thorlabs) using ceramic mating sleeve. The muscle was closed using Nylon sutures.

Animal subjects

CD/SD rats were originally obtained from Charles River and were housed and bred in the animal facility at the University of Chicago. The animal room was maintained at a humidity of 40-60%

and a temperature of 18-23°C under a 12-h-light/12-h-dark cycle. The animals were allowed free access to food and water. All animal procedures were approved by the Institutional Animal Care and Use Committees of the University of Chicago.

Numerical data processing

Analysis of numerical data and plotting was performed with Python scripts using NumPy, Matplotlib, Scipy, and Seaborn libraries. Statistics were calculated using statmodels library by applying Tukey's honestly significant difference (HSD) multiple comparison test.

6.6 Bibliography

1 Parameswaran, R. *et al.* Optical stimulation of cardiac cells with a polymer-supported silicon nanowire matrix. *Proc Natl Acad Sci U S A* **116**, 413-421, doi:10.1073/pnas.1816428115 (2019).

2 Bruegmann, T. *et al.* Optogenetic control of heart muscle in vitro and in vivo. *Nat Methods* **7**, 897-900, doi:10.1038/nmeth.1512 (2010).

3 Jacques, S. L. Optical properties of biological tissues: a review. *Phys Med Biol* **58**, R37-61, doi:10.1088/0031-9155/58/11/R37 (2013).

4 Jenkins, M. W. *et al.* Optical pacing of the embryonic heart. *Nature photonics* **4**, 623 (2010).

5 Nussinovitch, U. & Gepstein, L. Optogenetics for in vivo cardiac pacing and resynchronization therapies. *Nature Biotechnology* **33**, 750-754, doi:10.1038/nbt.3268 (2015).

6 Ushiki, T. & Ide, C. Three-dimensional organization of the collagen fibrils in the rat sciatic nerve as revealed by transmission-and scanning electron microscopy. *Cell and tissue research* **260**, 175-184 (1990).

7 Koutsou, A. D., Moreno, J. C., del Ama, A. J., Rocon, E. & Pons, J. L. Advances in selective activation of muscles for non-invasive motor neuroprostheses. *Journal of NeuroEngineering and Rehabilitation* **13**, 56, doi:10.1186/s12984-016-0165-2 (2016).

8 Badia, J. *et al.* Comparative analysis of transverse intrafascicular multichannel, longitudinal intrafascicular and multipolar cuff electrodes for the selective stimulation of nerve fascicles. *J Neural Eng* **8**, 036023, doi:10.1088/1741-2560/8/3/036023 (2011).

9 Strauss, I. *et al.* Q-PINE: A quick to implant peripheral intraneural electrode. *J Neural Eng* **17**, 066008, doi:10.1088/1741-2552/abc52a (2020).

10 Guo, J. *et al.* Highly Stretchable, Strain Sensing Hydrogel Optical Fibers. *Adv Mater* **28**, 10244-10249, doi:10.1002/adma.201603160 (2016).

11 Fang, Y. *et al.* Micelle-enabled self-assembly of porous and monolithic carbon membranes for bioelectronic interfaces. *Nat Nanotechnol* **16**, 206-213, doi:10.1038/s41565-020-00805-z (2021).

Chapter 7

Machine Intelligence-enabled Subthreshold Training of Cell Cultures Using Nanoporous Metal Electrodes

7.1 Introduction

Research automation is a necessary direction to enable high-throughput biophysical investigation. Human experimenters have limited endurance when prolonged experiments are required, and data analysis is strenuous and labor-intensity. These constraints are even more relevant when adaptable experimental conditions are desired. Due to the significant diversity of biological specimens, it is unlikely that different batches of the same cell and tissue culture would respond optimally to the same amount of pharmacological, mechanical, or electrical stimulus. Therefore, there is a need to analyze experiments *in situ* to adjust the stimulation conditions instantaneously. The development of closed-loop stimulation systems has been identified as a relevant trend in the current literature[1,2], but experimental demonstrations of such techniques remain sparse[3].

Heart muscle cells, or cardiomyocytes, are one of the most clinically relevant cell types, and the derivation of such phenotype from pluripotent stem cells has been extensively studied4 due to the promise of applications in regeneration medicine. It has been identified that chemical, mechanical, and electrical cues are necessary for the proper cell differentiation[4,5]. However, the identification of optimal conditions for cell development remains a challenge. The application of multielectrode arrays to study their physiology has already been used to record the action potential of hundreds of cells at once[6,7]. While this straightforward approach might seem attractive, the

action potential alone is insufficient to describe the cell phenotype, as factors such as cell morphology, anisotropy, clustering, and connectivity are essential for our understanding of tissue development. Additionally, when it comes to electrical stimulation, fabricating devices that allow stimulation and recording from electrodes in close vicinity is challenging due to the cross-talk between electrical lines and the inevitable appearance of recording artifacts.

Optical microscopy must be integrated with automated experimental platforms to understand the biological systems in full capacity. Applications of fluorescent probes have been a standard for cell imaging but can present a set of disadvantages[8]. Primarily, the stability of fluorescent probes is limited, which does not allow to keep the imaging quality constant over prolonged periods (>24h). Secondly, high concentrations of fluorescent probes are toxic to cells and might disturb their natural physiology and development. It is necessary to use non-invasive modes of optical microscopy to study cell development in their natural, undisturbed conditions. While fluorescent signals coming from stained cell structures can be easily detected and segmented from microscopy images using simple algorithms, feature extraction from stain-free data is challenging, and available image-based evaluation tools are limited to investigations of single cells[9] or employ additional markers such as fluorescent beads to aid with motion detection[10].

In this chapter, I will describe my approach and preliminary results for developing a machine vision-enabled subthreshold stimulation system to train cardiomyocytes in culture. I will discuss the hypothesis of subthreshold training of cells. I will describe the development of the training system and designs of software and stimulation devices. Finally, I will discuss the preliminary results, current limitations, and future directions in the developments.

7.2 Hypothesis - Cell Training is Better Than Stimulation

The scientific problem that this study is meant to answer is ‘what are the best conditions for the electrical stimulation of cardiomyocytes?’ Especially whether intelligent application of stimulation conditions can be beneficial to the stimulation prescribed *a priori*, that is, without concern for the current state of cell culture. To illustrate the technical problem that prevents us from studying this question, we need to understand that human data analysis is a limiting factor. The cellular response cannot be observed instantaneously, so a waiting period on the scale of minutes to hours must be applied between the application of stimuli and results analysis. If we were to identify the minimal electrical stimulation parameters (potential, current) at which cells begin to adjust their phenotype to the environment, we would require a constant presence of a human at the imaging apparatus to perform analysis and evaluation of the experimental conditions, adjusting them if necessary. The timescale of such an experiment can take hours to days, and the constant presence of human experimenters becomes not practical. For this reason, most current approaches rely on parallelization of a single type of stimulation (**Fig. 7.1a**) which concludes with the intelligent analysis after the endpoint. This type of investigation allows to use of a single set of stimulation conditions or prescribed varying conditions (e.g., periodic increase in frequency) but is agnostic to the current state of the cell culture during its execution. Therefore, due to large variability between biological specimens, the prescribed conditions might be insufficient to achieve proper stimulation or be too intense and result in the loss of the expensive material. Additionally, since evaluation is not continuous, meaningful information on the cell culture developmental dynamics is also lost.

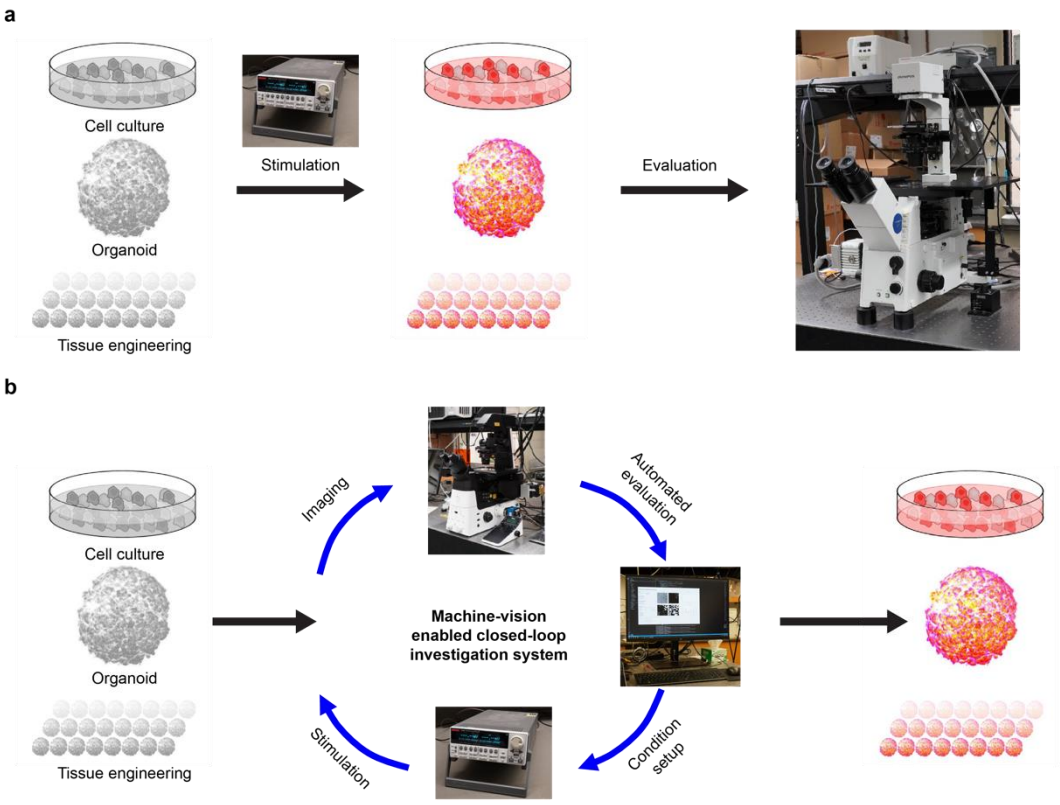

Figure 7.1 Comparison of one-way simulation experiment with automated bioelectronic training.

(a) Schematic of a one-way stimulation approach. The final step requires human input, and if the results are unsatisfactory, repeat the entire process. (**b**) Schematic of a closed-loop training system. In this approach, only mild stimulations conditions are applied at the beginning of the experiment and are adjusted as necessary to reach the threshold at which system response is observed, but the conditions are not too high to damage the cells.

I propose to develop an adaptable approach, here referred to as training, that applies only minimal stimulation necessary for the cell phenotype development (**Fig. 7.1b**). In this experiment, electrical stimulation parameters (voltage, current, frequency) will be dynamically

adjusted to adapt to the cellular state and behavior. For example, the cells will only be stimulated using a frequency similar to the present contraction rate, and the frequency will be increased or decreased as necessary. Finally, since the evaluation will be performed continually, the experiment will produce intermediate information about the cellular response to the training condition allowing us to drive future experiments and better understand cell physiology. The central thesis of this study is that training cells, that is, applying minimal stimuli necessary, will enable more gentle, safe, and efficient stimulation of cardiomyocytes *in vitro*. Machine vision-enabled software systems can allow us to realize this type of experiment.

7.3 Approach

Neonatal primary rat cardiomyocytes were chosen as a primary biological model. Such cells can be obtained at high yields with low cost (compared to the stem cell-derived cardiomyocytes) and still poses developmental potential. Despite strong regeneration capacity, these cells show significant batch-to-batch variability, making them suited for testing the stated hypothesis. The unique characteristic of cardiomyocytes is their contractility, characterized by periodic rhythmic movements of cell bodies at specific frequencies. This dynamic phenotype-specific behavior is an easier target for automated detection than shape classification, but its realization remains non-trivial.

The overview of the experimental platform is shown in **Figure 7.2**. The system consists of the cell culture device placed in a 5% CO2 microscope stage incubator to provide a stable environment for cell growth. Phase-contrast imaging is performed using an inverted microscope equipped with a sCMOS camera, and electrical stimulation is delivered using a computer-

controller source meter. The microscope and stimulator are directly connected to the workstation computer, which controls data acquisition, analysis, and stimulation.

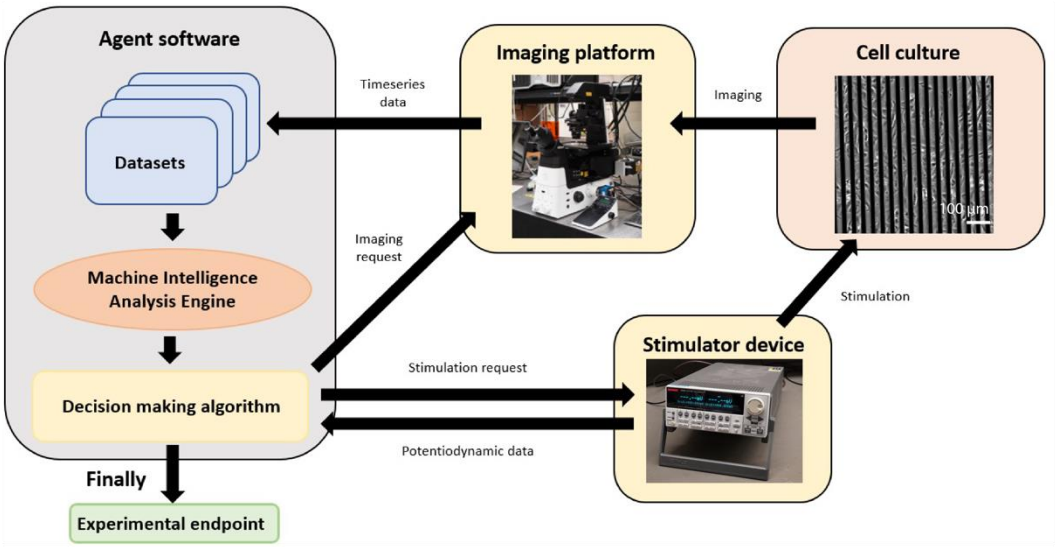

Figure 7.2 Overview of the bioelectronic cell training platform.

Integrating software and hardware components is necessary to realize the intelligent, adaptable bioelectronic system.

Monolithic custom Python code is used to control the entire platform centrally. The use of dedicated GPU allows real-time neural network computations making the system independent of the network connection. During the experiment, the control routine performs cycles of imaging-analysis-decision making-stimulation at each iteration. The analysis is driven by what I currently call ‘Machine Intelligence Analysis Engine,’ which uses combinations of classic machine vision and machine learning algorithms and novel approaches to extract data from the captured image time series, which will be described in a subsequent section. The analysis summary is then fed into the heuristic decision-making algorithm that controls the stimulation conditions. The platform will

deliver the upregulated cardiomyocytes contracting at the expected frequencies on success at the endpoint. Additionally, a summary of the experimental run will be generated to get insights into the development and behavior of the cell culture.

7.4 Algorithms and Software Design

I made two general design choices to enable uninterrupted real-time analysis with minimal latency. First, I decided that all code would be executed locally. While cloud-enabled GPUs can provide improved calculation times, they incur additional costs to the system and increase the time necessary for code development. Additionally, the computations speed-up might not necessarily offset the communication delay between client and server. However, this aspect of the system was not benchmarked. Second, I have decided to develop software in pure Python without applying existing open-source microscopy frameworks. The most prominent of the available frameworks are ImageJ[11-13]and derived from it μManager[14]. These frameworks, while powerful, have, in my opinion, expanded to encompass too large a scope to help develop new solutions. The abundance of features makes management of projects complicated, and unintuitive graphic user interface (GUI) creates a steep learning curve for new users. Additionally, too strong reliance on pre-created plugins distances scientists from understating their working principles leading to misuse. Finally, a machine learning environment is dominated by Python-based application programming interfaces. ImageJ, written in Java, is slowly becoming obsolete, and software developed for this platform might not be very relevant in the long term.

The sCMOS camera and electrical stimulator control were achieved using available Python packages and implemented without unique techniques. However, the development of the machine intelligence engine requires detailed discussion. A new algorithm had to be deployed to detect

cardiomyocytes' movement since the method based on background subtraction has performed poorly. It has been noted that rhythmic oscillations are easily distinguishable from the background noise on the scale of single pixels. I decided to apply a 3-stage convolutional neural network (**Fig. 7.3**) for time series classification to distinguish the contracting from non-contracting cells. After applying standard data augmentation approaches, the machine learning model was trained using 1000 manually annotated samples. The classification is applied to the entire phase-contrast video (**Fig. 7.4a**), which allows detecting contracting cells with high fidelity (**Fig. 7.4b**). Further processing employs segmentation of phase contrast image using contraction map with the custom algorithm based on image dilution followed by watershed segmentation (**Fig. 7.4c**). Finally, the frequencies are calculated for each pixel using fast Fourier transformation and assigned to specific regions. Overall, the algorithm detects the number of contracting cells and their contraction frequencies (**Fig. 7.4d**). The entire analysis takes 21.8 ± 0.8 s on an average-performance workstation and allows for continuous analysis and data reduction during the training experiment. In situ analysis followed by the data reduction is essential in this context as saving camera frames at 40 frames per second would use approximately 600 GB for every hour of recording, which would not be practical for experiments that span multiple days.

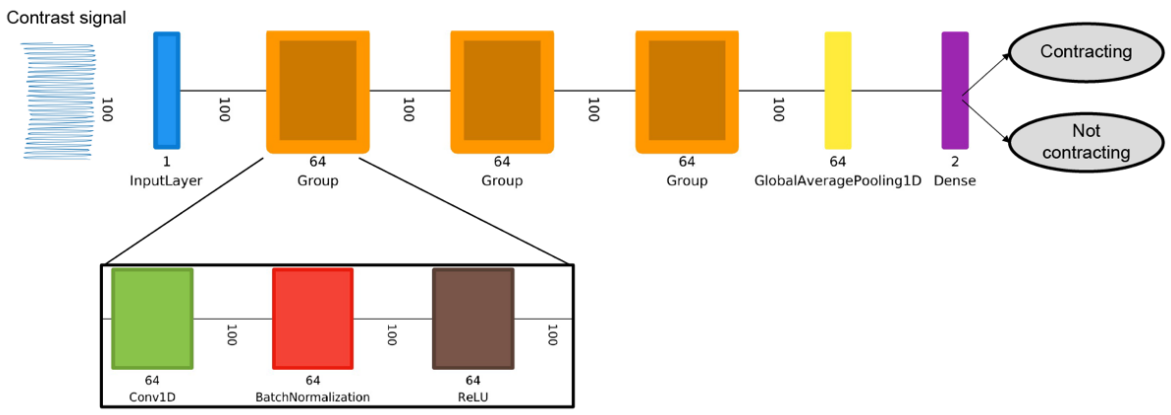

Figure 7.3 The design of a convolutional neural network used for contraction detection.

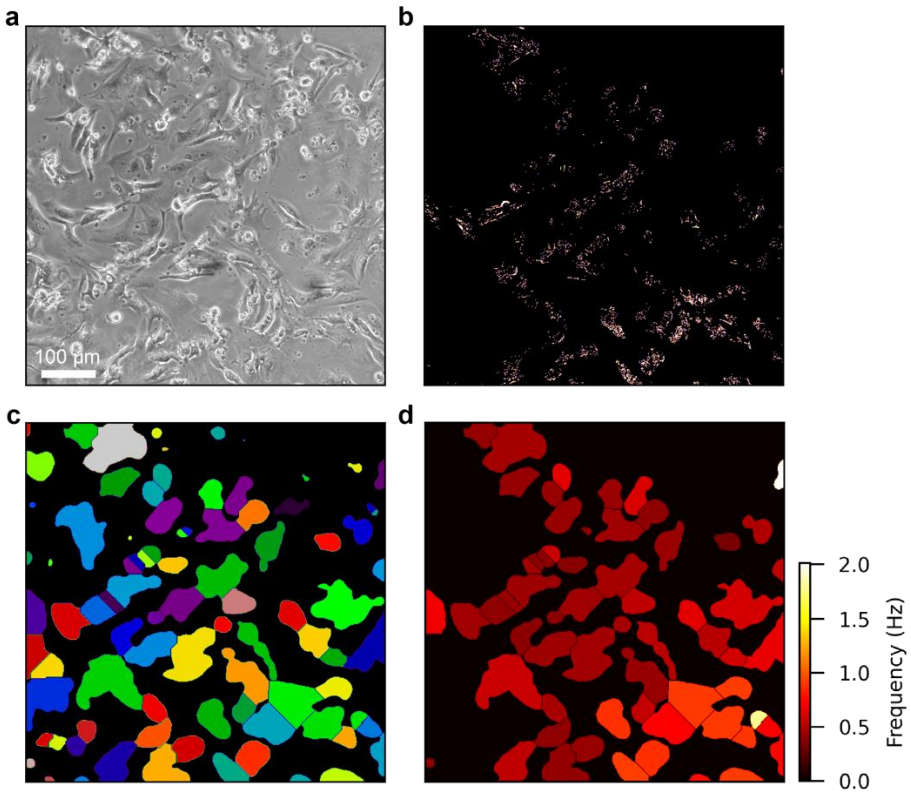

Figure 7.4 The representative results of time series analysis.

(**a**) Phase contrast image of the cell culture. (**b**) Pixels at which contraction was detected. (**c**) Segmentation of the contraction map. (**d**) Contracting cells with shading corresponding to the detected contraction frequency.

The analysis results are then fed into a simple heuristic algorithm that decides the continuation of stimulation. For example, the following conditions are tested by the decision-making program:

- Are cells contracting at the stimulation frequency?
    - YES - increase the frequency
    - NO - keep the frequency
- Are contractions detected?
    - YES - continue stimulation
    - NO - cease stimulation
- Did cells increase frequency during the last hour?
    - YES - continue with the same current
    - NO - increase stimulation current
- Etc.

The results of analysis and decision-making are being saved in a modern HDF5® format for efficient storage and making it available for big data analysis in the future. Additionally, I have developed a GUI (**Fig. 7.5**) with minimal functionality that allows to set up the training conditions by the user and displays the results of the experiment in real-time, allowing for identification of technical difficulties (for example, incorrect imaging configurations). While many improvements are necessary for the software to improve its stability and efficiency, the current version allows basic experiments for preliminary investigations.

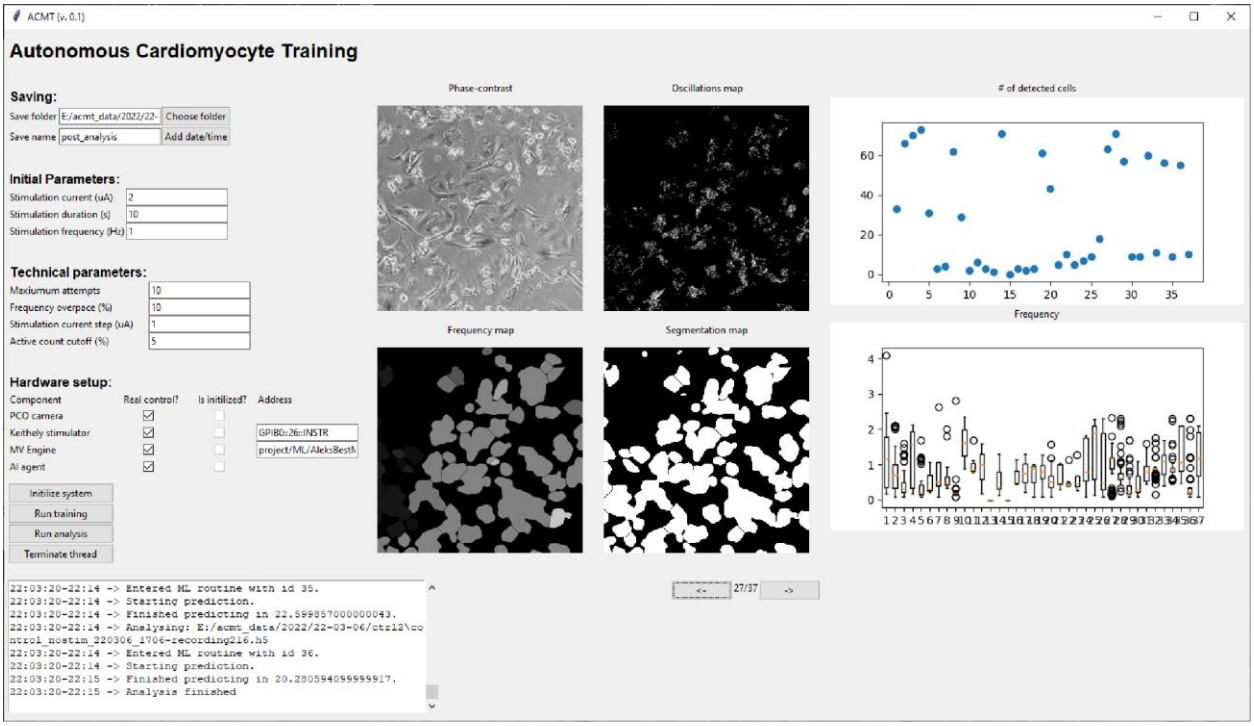

Figure 7.5 Example view of the training softwares' graphic user interface.

The software allows to decide on the location for saving data as well as setup the initial and technical parameters. Additionally, the interface displays the results of analysis and decision making in real time.

7.5 Cell Culture Stimulation Device

Specifically for this project, I designed cell culture stimulation devices for testing the training hypothesis. The presented design (**Fig. 7.6a**) solves substantial technical difficulties and allows the exploration of additional scientific questions during the training experiment. First, the device was fabricated using standard photolithography methods through e-beam metal evaporation on a glass substrate. While cell training is performed in a wide-field low-magnification view, I used 0.17 mm glass as a substrate so that the device is compatible with high-magnification optics,

allowing further investigation of subcellular structures using confocal and superresolution microscopy post-training.

Another aspect taken into consideration is biocompatibility and stability. The device must have a negligible effect on cells and must be able to be handled with ease during sterilization and cell culture. For this reason, except for metal electrodes, pure glass and highest-grade medical adhesives were used for the device construction. The small form factor enables straightforward handling and efficient cleaning, making the device very stable and reusable. Therefore, it possesses qualities not often available for research-grade devices. Additionally, the device is leadless and for the placement in the microscope and connection to the stimulator 3D-printed custom holder is used (**Fig. 7.6b**). Contact-based connection further improves device stability and allows sterilization approaches that are not available for devices utilizing regular wiring, for example, autoclaving, which is highly relevant for achieving reproducible results in the cell culture experiments.

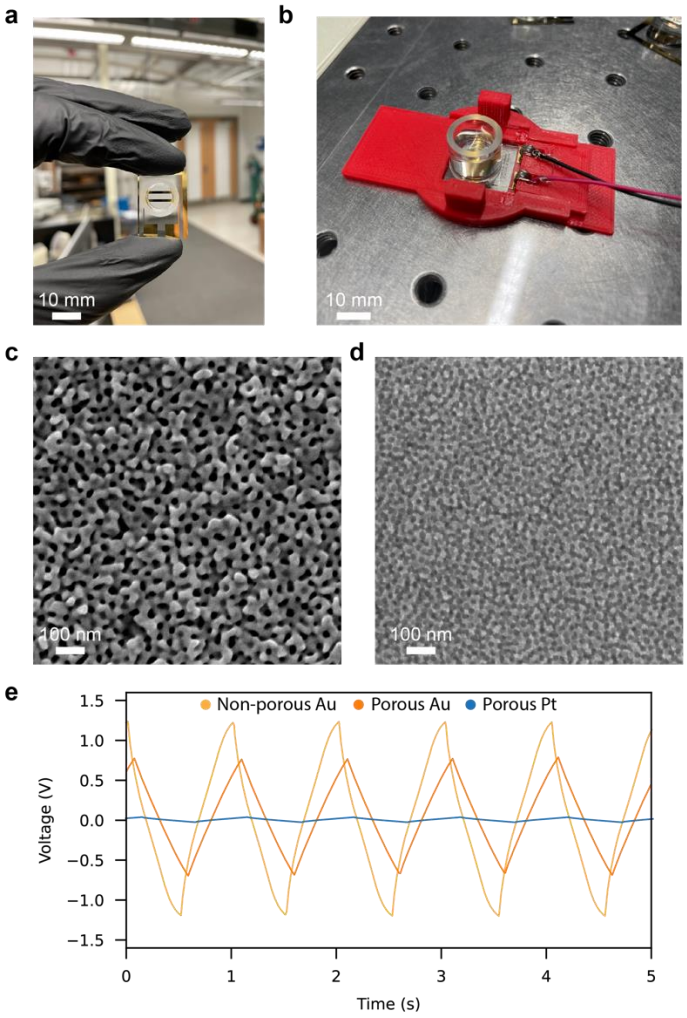

Figure 7.6 The device design, material analysis, and electrical performance overview.

(**a**) Photograph of a cell culture stimulation device. (**b**) Cell stimulation device inserted into the 3D-printed holder and electrical connector. SEM image of porous gold (**c**) and porous platinum (**d**) synthesized through electrodeposition. (**e**) Voltage waveform recorded during square wave stimulation with 50% duty cycle with ~ 1 μA/mm^2 current for different electrode materials. Porous platinum shows higher charge injection than gold and porous gold.

The second aspect of device design is the electrode material, which I chose to focus on noble metals due to their low reactivity and excellent biocompatibility. I wanted to study the effects of the solution current and overpotential on the success of cell training. Our preliminary results with carbon supercapacitor showed that high charge injection capacity is necessary for observing cell training with minimal electricity threshold[15]. However, carbon membrane fabrication is incompatible with the resistance of glass substrate, and I decided to focus on porous metal electrodes. The block copolymer template-based method was chosen to fabricate such porous electrodes[16]. The templated electrodeposition allowed to produce porous gold and platinum electrodes with varying porosity levels (**Fig. 7.6c-d**). Such electrodes require different potentials to elicit the same electrical current in the cell culture media (**Fig. 7.6e)**, with porous platinum showing the most efficient charge injection. Applying different electrode materials in this experiment will allow us to disentangle the contribution of overpotential and current to the cell training. Additionally, it would help confirm the hypothesis that the materials more efficient in charge injection have better biocompatibility in electrical stimulation.

Finally, I have fabricated devices with the macroscopic distance between the electrodes (1 mm) and microscopic distance (10-20 μm) in the interdigitated layout but with the same total electrode area. This design allows us to investigate the effect of electric field strength and distance from the cells on the bioelectronics training. Overall, the device design is versatile, allowing to study of multiple aspects of the system while stable enough to minimize resources necessary for its fabrication, also enabling reusability.

7.6 Preliminary System Operation

Preliminary data obtained using the most recent version of training software bring interesting yet challenging insights into the physiology of cardiomyocytes in cell culture. Analysis of the frequencies in the control sample (**Fig. 7.7a**) imaged over 18 hours shows large variability in the observed contraction frequencies in time under these conditions. Noteworthy are the periods of rest in which cultured cardiomyocytes are not contracting and periods where contraction is surprisingly fast (> 4 Hz). Manual inspection of selected recordings confirmed the accuracy of the machine vision-based algorithm and the correctness of summary data. Similar observations were noted in previous experiments using an earlier version of analysis algorithms.

A detailed literature review is necessary to confirm whether such behavior in cell culture has been reported previously. However, the data generated in this study and developed analytical tools have not been available in the past, and there is a possibility that this behavior was not reported due to human bias and willingness to perform experiments only on the contracting clusters in a cell culture dish and ignoring immobile cells in the short-term experiments. Another explanation for these observations is the effect of the cell culture conditions on the cardiomyocyte contraction, such as instability of microscope stage incubator or insufficient culture density. Nevertheless, more investigation is necessary to understand cell behavior *in vitro*, and this preliminary experimental run suggests the utility of the developed methods giving us an ability to perform unbiased observation of a large field of view of cardiomyocytes over long periods.

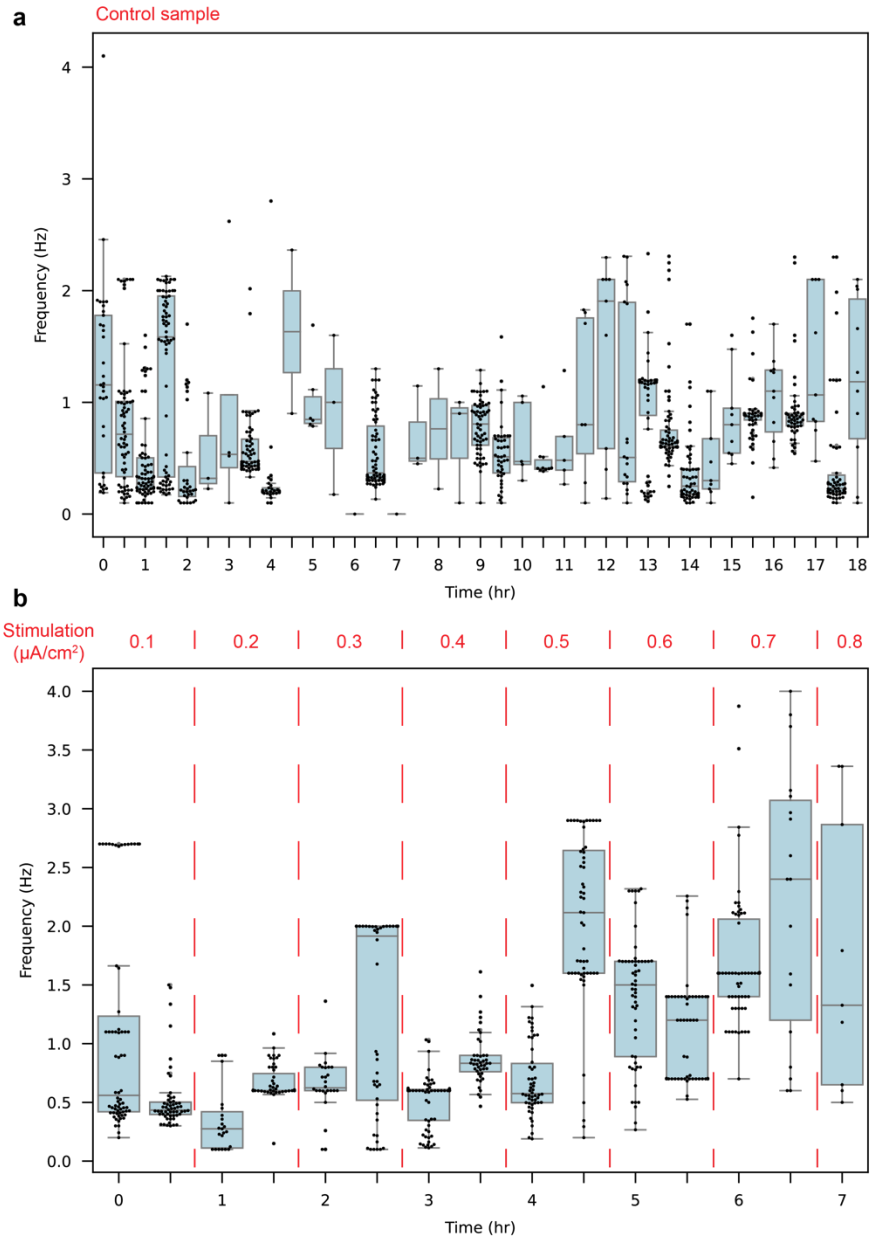

Figure 7.7 Results of the preliminary experiments using training software.

(**a**) Detection of the contraction frequency in the control sample without electrical stimulation. Variable yet consistent contractions are observed in the cell culture over 18 hours. (**b**) Detection of the contraction frequency during stimulation using a macroscopic non-porous gold electrode.

Cells underwent lysis in about 30 minutes after stimulation current reached 0.8 μA/mm^2 at the 7th hour of the experiment.

Preliminary stimulation with two non-porous, 1 mm width gold electrodes positioned 2 mm apart shows that the cells begin to increase their contraction frequency at approximately 6 hours from the beginning of the experiment when the stimulation current reached 0.7 μA/mm2. However, the stimulation control software did not properly react to the change and kept increasing the current. Cell death and lysis were observed approximately 30 minutes after stimulation with 0.8 μA/mm2 current. The voltage amplitude delivered to the cell culture at this time was about 2.4 V which is above the window of safe potential for water solutions which causes the formation of reactive oxygen species, gases, increased temperature, and can lead to cell electroporation. In future experiments, the application of electrode materials with better charge injection capacity might show higher biocompatibility towards cells at the same current range.

7.7 Discussion

The cell culture data produced in this study so far, most of which is not shown in this thesis, has come from many different iterations of analysis and control software, and cross-check of datasets obtained and analyzed using different conditions does not yield valid conclusions. For the proposed investigation, it is necessary to perform the complete dataset collection once the final software and hardware methods are finalized. I believe that the current software version would allow the generation of a valid dataset with many technical replicates. Data collection from devices

utilizing different electrode layouts and materials would bring new insights into cell-electrode interactions.

Even though the current version of the software has reached enough fidelity to perform proof of concept studies, additional improvements can be made to make the system more intelligent. First, the detection algorithm can be improved by studying different neural network designs that allow motion detection. However, such developments must consider computational cost coming from the increased fidelity, which might not qualify for low-latency decision-making. Similar improvements can be made to segmentation algorithms that can be made to utilize neural networks. Many of such approaches have been presented in the recent literature[17]. The challenge for this improvement is the generation of annotated datasets necessary to train strong models that can still perform fast segmentation. Finally, the decision-making algorithm currently uses pre-defined heuristics as guidelines for cell training. The algorithm could be modified to include additional factors enabling the introduction of reinforcement learning into the program. Such a program would partially remember previous experimental runs and learn from mistakes (for example, too high stimulations current too early) and enable better cell training.

Once the working principles of the training platform are well-validated, many additional investigations can be performed. One of the directions could be the fixation of cell post-training and superresolution imaging to unravel subcellular changes inflicted on the cells during the stimulation. Another approach could be trypsinization of cells and homogenization followed by genomic, transcriptomic, or proteomic analysis. Analysis of molecular changes in the cells undergoing different types of training can better drive the development of new strategies for stimulation.

7.8 Summary

In this chapter, I have described the concept of cardiomyocyte training using a machine vision-enabled bioelectronic platform. I have shown the status of the developed materials, methods, and devices for cell training and prospects of their improvement. I have discussed representative experimental data from the current iteration of the control system and the promise of insights coming from experiments scheduled for the future. I believe that automation and machine-enabled investigations have a great potential to improve our experimental capabilities allowing the generation of big datasets in a manner that was not possible using conventional methods. A better understanding of cell physiology and the use of alternative stimulation approaches can enable the development of new therapies for regenerative medicine employing stem cell-derived organoids.

7.9 Methods

Fabrication and design of cell culture devices

ClariTex Coverslips (No. 1.5, 50 x 64 mm, 0.17 mm thickness, CellPath, Ltd.) were used as a substrate for device fabrication. Electrode patterns were defined using standard lithography procedures using a direct writer (MLA150, Heidelberg). 5 nm Cr, 100 nm Au and 5 nm Cr layers were evaporated on the patterned surface using an e-beam evaporator (EvoVac, Angstrom Engineering). All device layouts were designed to achieve the same cell stimulation area of approximately 1 mm^2 for electrode of each polarity. Glass wells were made of borosilicate glass tube (1/2" OD, 0.38" ID, McMaster-Carr) cut the 10 mm height. Wells were attached to the electrode patterns using medical adhesive (EP42HT-2N-2MED Black, Master Bond) and cured overnight at room temperature followed by 6 hours at 65 °C. Before each cell culture, the devices

were cleaned in the ultrasonic bath in acetone for 5 min, in isopropanol for 5 min, and dried at 80 °C followed by sterilization with oxygen plasma (200 W for 10 min, Plasma Etch PE-100LF).

Synthesis of porous metal layers

The synthesis followed literature methods[16]. The electrodeposition of porous metal precursors was performed for 15 min at -0.5 V for gold and -0.2 V for platinum.

Animal subjects.

All animal procedures were approved by the Institutional Animal Care and Use Committees of the University of Chicago.CD/SD rats were originally obtained from Charles River and were housed and bred in the animal facility at the University of Chicago.

Cardiomyocyte isolation and cell culture.

Hearts were excise from P1-P3 neonatal SD/CD rats. A Pierce™ primary cardiomyocyte isolation kit (Thermo Fisher Scientific) was used for digesting the tissue. After digestion, the cells were pre-plated for 1-2 h in the plastic petri dishes to allow fibroblasts to adhere to the surface and increase the culture purity. The enriched cardiomyocyte population was seeded onto the devices pre-treated with fibronectin (Sigma) at the density of 1 mln/mL.

Imaging conditions.

Nikon Ti2-E microscope was used for phase-contrast optical imaging (20x lens, Nikon CFI Plan Fluor NA 0.5) and timeseries were recorded at 40 frames per second using sCMOS camera (PCO panda 4.2) with 4x binning to the resolution of 512x512 pixels. Nikon's perfect focus system (PFS) was used to stabilize the imaging plane over long periods. 5% CO_2 microscope stage incubator heated to 37 °C was used provide a stable environment for cell growth.

Stimulation conditions.

Stimulation waveforms were delivered using a source meter (Keithley 2636A) in a two-electrode configuration.

Computer code.

Software for training was developed for Python 3.8 using publicly available packages and was run in the Conda environment. The versions of used packages and developed computer code is shown in **Appendix B.** Software was run on a HP Z4 workstation (CPU Intel Xeon W-2123, 4 cores @ 3.6 GHz, 32 GB RAM, GPU Nvidia Quadro P4000).

7.10 Bibliography

1 Datta-Chaudhuri, T. Closed-loop neuromodulation will increase the utility of mouse models in Bioelectronic Medicine. *Bioelectron Med* **7**, 10, doi:10.1186/s42234-021-00071-x (2021).

2 Guemes Gonzalez, A., Etienne-Cummings, R. & Georgiou, P. Closed-loop bioelectronic medicine for diabetes management. *Bioelectron Med* **6**, 11, doi:10.1186/s42234-020-00046-4 (2020).

3 Selberg, J. *et al.* Machine Learning-Driven Bioelectronics for Closed-Loop Control of Cells. *Advanced Intelligent Systems* **2**, 2000140, doi:10.1002/aisy.202000140 (2020).

4 Zhang, J. *et al.* Functional cardiomyocytes derived from human induced pluripotent stem cells. *Circ Res* **104**, e30-41, doi:10.1161/CIRCRESAHA.108.192237 (2009).

5 Ronaldson-Bouchard, K. *et al.* Engineering of human cardiac muscle electromechanically matured to an adult-like phenotype. *Nat Protoc* **14**, 2781-2817, doi:10.1038/s41596-019-0189-8 (2019).

6 Spira, M. E. & Hai, A. in *Nano-Enabled Medical Applications* 567-602 (Jenny Stanford Publishing, 2020).

7 Asakura, K. *et al.* Improvement of acquisition and analysis methods in multi-electrode array experiments with iPS cell-derived cardiomyocytes. *J Pharmacol Toxicol Methods* **75**, 17-26, doi:10.1016/j.vascn.2015.04.002 (2015).

8 Jensen, E. C. Use of fluorescent probes: their effect on cell biology and limitations. *Anat Rec (Hoboken)* **295**, 2031-2036, doi:10.1002/ar.22602 (2012).

9 Sala, L. *et al.* MUSCLEMOTION: A Versatile Open Software Tool to Quantify Cardiomyocyte and Cardiac Muscle Contraction In Vitro and In Vivo. *Circ Res* **122**, e5-e16, doi:10.1161/CIRCRESAHA.117.312067 (2018).

10 Tseng, Q. *et al.* Spatial organization of the extracellular matrix regulates cell-cell junction positioning. *Proc Natl Acad Sci U S A* **109**, 1506-1511, doi:10.1073/pnas.1106377109 (2012).

11 Schneider, C. A., Rasband, W. S. & Eliceiri, K. W. NIH Image to ImageJ: 25 years of image analysis. *Nat Methods* **9**, 671-675, doi:10.1038/nmeth.2089 (2012).

12 Rueden, C. T. *et al.* ImageJ2: ImageJ for the next generation of scientific image data. *BMC Bioinformatics* **18**, 529-529, doi:10.1186/s12859-017-1934-z (2017).

13 Schindelin, J. *et al.* Fiji: an open-source platform for biological-image analysis. *Nat Methods* **9**, 676-682, doi:10.1038/nmeth.2019 (2012).

14 Edelstein, A. D. *et al.* Advanced methods of microscope control using μManager software. *J Biol Methods* **1**, e10, doi:10.14440/jbm.2014.36 (2014).

15 Fang, Y. *et al.* Micelle-enabled self-assembly of porous and monolithic carbon membranes for bioelectronic interfaces. *Nat Nanotechnol* **16**, 206-213, doi:10.1038/s41565-020-00805-z (2021).

16 Lim, H. *et al.* A universal approach for the synthesis of mesoporous gold, palladium and platinum films for applications in electrocatalysis. *Nat Protoc* **15**, 2980-3008, doi:10.1038/s41596-020-0359-8 (2020).

17 von Chamier, L. *et al.* Democratising deep learning for microscopy with ZeroCostDL4Mic. *Nature Communications* **12**, 2276, doi:10.1038/s41467-021-22518-0 (2021).

Chapter 8

Conclusions and Outlook

8.1 Conclusions

The realization of electroceutical therapies requires advances in materials design and device fabrication and our improvements in understanding of junctions between artificial devices and biological structure. In this thesis, I have described the principles of operating at biointerfaces and concepts for designing materials with improved efficiency and biocompatibility. I have shown studies of two materials systems: mesoporous carbon membranes and nanoporous/non-porous silicon membranes. The materials systems demonstrate two approaches to electrical stimulation: wired and lead-free utilizing photoelectrochemical effect. Such approaches were shown to successfully modulate the activity of a range of biological targets such as cardiomyocytes, retina slices, isolated hearts, and nerve bundles. Finally, I have presented the concept of applying bioelectronic systems, optical microscopy, and machine vision-based image processing for cell culture studies and subthreshold training. I believe that all these developments firmly demonstrate the promise for the development of future medical therapies based on principles of bioelectronics.

8.2 Outlook[2]

Many important directions can be plotted for future research in bioelectronics. First and foremost, the efficiency of bioelectronic stimulation must be improved to minimize the energy required for stimulation and make such applications more resilient to sources of biological variability. Application of new material systems such as low-dimensional carbon-based composite,[1,2] can potentially improve the modulation efficiency. Advances in nanostructure synthesis and further modification on the nanoscale and atomic-scale are promising to yield more robust signal transduction interfaces, where biomechanical sensing by the cellular machinery[3] or biocatalysis[4] may play additional roles. I believe that many paradigms previously successfully applied in energy science and catalysis can be adapted to improve bioelectronic devices. One recent example is *in situ* electrochemical generation of nitric oxide for neuronal signaling.[5] I speculate that a similar approach should be achievable using photoelectrochemical effects. Moreover, utilization of non-conventional nano-enabled photonic processes such as upconversion[6] and mechanoluminescence[7] can enable new approaches to energy transduction in biomodulation.

Living bioelectronics is another direction that deserves particular attention due to significant benefits coming from seamless integration of natural and artificial elements. While this direction will benefit from improved nanostructure efficiency, there are concerns that require scientific insight. One of the most critical concerns is the stability of such hybrid cells and tissue. When pertaining to internalization of nanostructures, it must be determined how long the nanostructures will be active in the cells and how to control their persistence. One unanswered question is what happens to nanostructures when cells undergo mitosis. Keeping a large number of active hybrids in the cell population would be critical for long-term and chronic stimulation.

[2] Adapted from: Prominski, A., Li, P., Miao, B. A., & Tian, B. Nanoenabled Bioelectrical Modulation. *Accounts of Materials Research* **2021** *2* (10), 895-906.

Optimization of size, shape, and composition of nanostructures can enable control over their organization and location within the cytosol. The possibility of synthesis of bioelectronic structures *in situ* in living cells and tissues is a noteworthy idea. Recently, the conductive polymer polyaniline was synthesized directly onto cell membranes, which affected the conductivity of specific neuronal cells *in vivo*.[8] While challenging, it would be extremely valuable to demonstrate assembly of photoresponsive materials or nanostructures within living cells. This approach has the potential to challenge optogenetic modulation approaches in terms of efficiency and safety.

While targeting single cells and subcellular regions with bioelectronics has been demonstrated, the next natural goal is to increase specificity of interrogation and study effects of stimulation on subcellular targets. Examples of such targets can include the cell membrane, organelles, cytoskeleton, liquid condensates, and extracellular vesicles. Such studies will bring important biophysical insight to the internal functionality of cellular machinery and enable new bioelectronic solutions. Modulating cells through triggered release of extracellular vesicles or through mechanical changes to the nucleolus may be important in future stimulation approaches. Subcellular insight will be used to further the design of nanostructures for internalization and creation of living bioelectronics as well.

Another frontier that I would like to highlight is creation of adaptable bioelectronics. Living systems are, in general, highly active environments undergoing constant change. We should think about designing or programing our materials to respond to presented conditions. Computer-assisted or intrinsically enabled closed-loop response systems are critical for realization of such adaptable materials. With increased complexity of autonomous behavior of nanostructured materials, we will be moving closer to achieving truly nanorobotic bioelectronic systems.

Finally, much as genomics and proteomics redefined how we study molecular and cellular biology, I envision that "*bioelectromics"*, if established through a suite of complementary characterizations and nano-enabled probing, can redefine our approach to electrophysiology, synthetic biology, and biomedical science. While efforts using traditional electrophysiology tools, combined with molecular biology and quantitative biophysical tools, have elucidated how single cells and tissues behave electrically, a systems-level understanding of bioelectrical activities and their heterogeneities at the subcellular level is lacking. Additionally, new synthetic biology or cellular engineering principles, especially those from non-genetic perspectives, would help establish autonomous, auto-regulatory, cell-like materials. *Bioelectromics* may serve as a powerful bioengineering "blueprint" for completely new efforts in synthetic biology. Alongside chemical and transcriptional modules currently explored in the synthetic biology community, nano-enabled understanding of bioelectrical driving forces in cells and tissues may allow us to expand the diversity and application domains of cellular engineering.

8.3 Closing remarks

This thesis has described investigations of the basic science of materials design and applications of electroceuticals. With every new technology come new challenges and dangers, and here I would like to mention the ethical considerations of bioelectronic therapies. The first medical devices that will reach the market will most likely rely on simple circuits with uncomplicated feedback loops. However, one day, we will surely establish high-fidelity machine-brain interfaces that would be able to interact with human cognition seamlessly. Setting appropriate safety and transparency standards is crucial when developing such technologies. With ever-increasing connectivity between electronic devices and our social life through mesh networks

and internet of things-like approaches, prospects of surrendering cognitive autonomy to such technologies would be very distressing. Therefore, ethical discussions, like the ones currently surrounding gene modification technologies, are necessary for the bioelectronics community.

8.4 Bibliography

1 Dipalo, M. *et al.* Intracellular action potential recordings from cardiomyocytes by ultrafast pulsed laser irradiation of fuzzy graphene microelectrodes. *Sci Adv* **7**, eabd5175, doi:10.1126/sciadv.abd5175 (2021).

2 San Roman, D., Garg, R. & Cohen-Karni, T. Bioelectronics with graphene nanostructures. *APL Materials* **8**, 100906, doi:10.1063/5.0020455 (2020).

3 Zhao, W. *et al.* Nanoscale manipulation of membrane curvature for probing endocytosis in live cells. *Nat Nanotechnol* **12**, 750-756, doi:10.1038/nnano.2017.98 (2017).

4 Phillips, A. W. *et al.* Gold-Decorated Silicon Nanowire Photocatalysts for Intracellular Production of Hydrogen Peroxide. *ACS Appl Mater Interfaces* **13**, 15490-15500, doi:10.1021/acsami.0c23164 (2021).

5 Park, J. *et al.* In situ electrochemical generation of nitric oxide for neuronal modulation. *Nat Nanotechnol* **15**, 690-697, doi:10.1038/s41565-020-0701-x (2020).

6 Li, H., Wang, X., Huang, D. & Chen, G. Recent advances of lanthanide-doped upconversion nanoparticles for biological applications. *Nanotechnology* **31**, 072001, doi:10.1088/1361-6528/ab4f36 (2020).

7 Wu, X. *et al.* Sono-optogenetics facilitated by a circulation-delivered rechargeable light source for minimally invasive optogenetics. *Proc Natl Acad Sci U S A*, 26332–26342, doi:10.1073/pnas.1914387116 (2019).

8 Liu, J. *et al.* Genetically targeted chemical assembly of functional materials in living cells, tissues, and animals. *Science* **367**, 1372-1376, doi:10.1126/science.aay4866 (2020).

Appendix A

Python Code Used for Data Analysis in Silicon Membrane Study

A1 Photocurrent Analysis

```
import pyabf
import os
import glob
import numpy as np
import matplotlib.pyplot as plt
from scipy.optimize import curve_fit
from scipy.integrate import trapezoid

## Fetches data from ABF files from all the sweeps available
def get_data(filename):
    abf = pyabf.ABF(filename)
    x = []
    I = []
    V = []
    analog =[]
    for sweepNumber in abf.sweepList:
        abf.setSweep(sweepNumber, channel=0)
        x.append(abf.sweepX)
        I.append(abf.sweepY)
        abf.setSweep(sweepNumber, channel=1)
        V.append(abf.sweepY)
        abf.setSweep(sweepNumber, channel=2)
        analog.append(abf.sweepY)
    if len (x) == 1:
        return x[0], I[0], V[0], analog[0]

    return x, I, V, analog

## Finds indices of analog/TTL and voltage pulses in a clamp setup:
##
## TTL_up - analog/TTL pulse up
## TTL_down - analog/TTL pulse down
## TTL_level - maximum pulse level
## V_up - voltage pulse up
```

```
## V_down - voltage pulse down

def find_all_pulses(analog,V):
    TTL_up = []
    TTL_down = []
    TTL_level = []
    V_up = []
    V_down = []

    ### FLAGS do not change
    tmp = 0
    UP = 1
    DOWN = 0
    direction = UP
    ###

    for n,_ in enumerate(analog):
        if direction == UP and analog[n] - analog[tmp] > 0.1:
            TTL_up.append(n)
            TTL_level.append(analog[n])

            tmp = n
            direction = DOWN

        elif direction == DOWN and analog[n] - analog[tmp] > 0.1:
            tmp = n
            TTL_level.pop()
            TTL_level.append(analog[n])

        elif direction == DOWN and analog[n] - analog[tmp] < -0.1:
            TTL_down.append(n)

            tmp = n
            direction = UP

        elif direction == UP and analog[n] - analog[tmp] < -0.1:
            tmp = n

    ### FLAGS do not change
    tmp = 0
    UP = 1
    DOWN = 0
    direction = DOWN
    ###

    for n,_ in enumerate(V[:-10]):
```

```
            tmpval = np.mean(V[tmp:tmp+10])
            currentval = np.mean(V[n:n+10])
            if direction == UP and currentval - tmpval > 0.4:
                V_up.append(n)

                tmp = n
                direction = DOWN

            elif direction == DOWN and currentval - tmpval > 0.4:
                tmp = n

            elif direction == DOWN and currentval - tmpval < -0.4:
                V_down.append(n)
                tmp = n
                direction = UP

            elif direction == UP and currentval - tmpval < -0.4:
                tmp = n

        ### Error handling
        if len(TTL_up) > 1:
            print('TTL_up too long')
            plt.plot(np.arange(0,len(analog),1), analog)
            plt.show()
        if len(V_up) > 1:
            print('V_up too long')
            plt.plot(np.arange(0,len(V),1), V)
            plt.show()

        if len(TTL_up)<1:
            return -1, -1, -1, V_up[0], V_down[0]

        if len(TTL_up) == 1:
            return TTL_up[0], TTL_down[0], TTL_level[0], V_up[0], V_down[0]

        return TTL_up, TTL_down, TTL_level, V_up, V_down

    ## For calculating pipette resistance
    def getR(I,V,V_down):

        ### raise error if voltage down step is not where expected
        if abs(V_down - 10626) > 10:
            print('R calc error, V down step not where expected. Inspect the data.')
            print(V_down)
            plt.plot(np.arange(0,len(V),1),V)
            plt.show()
```

```
    start = V_down - 1000
    end = V_down + 1000
    N=500

    I1 = np.sum(I[start:start+N])
    I2 = np.sum(I[end:end+N])
    V1 = np.sum(V[start:start+N])
    V2 = np.sum(V[end:end+N])

    Ip = abs(I2 - I1)*1e-12 ## mV
    Vp = abs(V2 - V1)*1e-3 ## pA

    R = Vp/Ip/1e6 ## MOhm

    return R

###
# Function fitting currents:
# If - faradaic current, i.e. exponential decay y-axis offset
# A - pre-exponential constant
# k - rate constant
# t - time variable
###
def photoresponse(t, If, A, k):
    return A*np.exp(k*t)+If

def fit_currents(x, I, TTL_up, TTL_down, output = None):

    t_d = int(10/0.01) ### time before TTL for avg init calculation - 10 ms
    avg_init = np.mean(I[TTL_up-2*t_d:TTL_up-t_d])

    current_shifted = I[TTL_up:TTL_down] - avg_init ### holding current offset
subtraction
    current_shifted = current_shifted/1000 ### pA to nA

    time = x[TTL_up:TTL_down] ### time axis for the pulse position
    time = time - time[0] ### first timepoint subtracted

    n = int(len(current_shifted)*4/5) ### use only last 20% of the transient for
calculations
    y_data = current_shifted[n:]
    x_data = time[n:]

    ### Intial guesses, magic numbers, but work well in practice
```

```
    If_guess = 0
    A_guess = np.amax(y_data)
    k_guess = -0.693/0.01
    p0 = [If_guess, A_guess, k_guess]

    b = ([0, 0, -np.inf],[np.inf, np.inf, np.inf] )

    ### Try fitting function
    try:
        popt, pcov = curve_fit(photoresponse, x_data, y_data, p0 = p0, method = 'trf',
jac='3-point', bounds=b)
    except:
        print(f'No solution.')
        popt = [0,0,0]

    I_fit = popt[0]

    ### Plot data, initial guess and model for visual inspection of the fitting
    y_init = [photoresponse(t, *p0) for t in x_data]
    y_model = [photoresponse(t, *popt) for t in x_data]
    plt.scatter(x_data, y_data, s = 2)
    plt.plot(x_data, y_model, c='red')
    plt.plot(x_data, y_init, c = 'black')
    plt.show()


    ### Calculate charges, through integration and subtraction
    If_final = I_fit
    faradaic = np.full_like(time, If_final)

    Q_tot = trapezoid(current_shifted, time)
    Qf_final = trapezoid(faradaic, time)
    Qc_final = Q_tot - Qf_final

    return Q_tot, Qc_final, Qf_final

### Fit currents in file and calculate charge contribution
def fitting(abf):
    print(f'Analyzing: {abf}')
    file = abf
    x, I, V, analog = get_data(file)
    TTL_up, TTL_down, TTL_level, V_up, V_down = find_all_pulses(analog, V)
    tot, c, f = fit_currents(x, I, TTL_up, TTL_down)
    R = getR(I,V,V_down)

    return tot*R, c*R, f*R, R
```

```
if __name__ == '__main__':
    ### Find directory names
    dirs = sorted(glob.glob('*/'))
    ### Get abfs filenames in each directory
    abfs = [sorted(glob.glob(d + '*abf')) for d in dirs]
    ### generate sample names from directory names and print
    names = [x[:-1] for x in dirs]
    print(names)
    ### Calculate delivered charges for each measurement
    results = [[fitting(file) for file in a] for a in abfs]
    ### Reshape the array for better handling
    data = [np.array([[a[0],a[1],a[2],a[3]] for a in b]) for b in results]
    ### Export to csv, no header
    for d,n in zip(data,names):
        np.savetxt(f'analysis_out_{n}-.csv', d, delimiter = ',')
```

A2 Heart Surface Potential Mapping

```
### Load the background Python functions for reading RHD files
### Available from https://github.com/Intan-Technologies/load-rhd-notebook-python
### Distributed under GPL 3.0 license
import importrhdutilities.py
### importrhdutilities.py was modified to include the following function:
#
# def get_tV(channel_name, result):
#     channel_found, signal_type, signal_index =
find_channel_in_header(channel_name, result)
#     if channel_found:
#         if signal_type == 'amplifier_channels':
#             ylabel = 'Voltage (microVolts)'
#             signal_data_name = 'amplifier_data'
#             time = result['t_amplifier']
#
#
#         elif signal_type == 'aux_input_channels':
#             ylabel = 'Voltage (Volts)'
#             signal_data_name = 'aux_input_data'
#             time = result['t_aux_input']
#
#         elif signal_type == 'supply_voltage_channels':
#             ylabel = 'Voltage (Volts)'
#             signal_data_name = 'supply_voltage_data'
#             time = result['t_supply_voltage']
#
#
#         elif signal_type == 'board_adc_channels':
#             ylabel = 'Voltage (Volts)'
#             signal_data_name = 'board_adc_data'
#             time = result['t_board_adc']
#
#         elif signal_type == 'board_dig_in_channels':
#             ylabel = 'Digital In Events (High or Low)'
#             signal_data_name = 'board_dig_in_data'
#             time = result['t_dig']
#
#         elif signal_type == 'board_dig_out_channels':
#             ylabel = 'Digital Out Events (High or Low)'
#             signal_data_name = 'board_dig_out_data'
#             time = result['t_dig']
#         else:
#             print('channel is not amplifier')
#         voltage = result[signal_data_name][signal_index,:]
```

```
#     else:
#         print('channel not foud')
#     return time, voltage

from glob2 import glob
import matplotlib.pyplot as plt
import pyabf
import numpy as np
import re

def natural_sort(l):
    con = lambda text: int(text) if text.isdigit() else text.lower()
    sort_key = lambda key: [con(c) for c in re.split('([0-9]+)', key)]
    return sorted(l, key=sort_key)

import pybaselines
from scipy.signal import find_peaks
from matplotlib import cm

### get filenames
abfs = sorted(glob('03*/*.abf'))
rhds = glob('RHD/**/*.rhd')

## read ABFs times
abfs_time = []
for a in abfs:
    f = pyabf.ABF(a)
    head = f.headerText
    a = re.search('abfDateTime.*$', head, re.MULTILINE)
    b = re.search('..:..:..', a[0])
    c = b[0].replace(':','')
    abfs_time.append(c)

## read RHDs times
rhds_time = []
for r in rhds:
    rhds_time.append(r[-10:-4])


def to_secs(s):
    a = int(s[0:2])
    b = int(s[2:4])
    c = int(s[4:6])
    return a*3600 + b*60 + c

matched_rhd = []
```

```
for a in abfs_time:
    a_s = to_secs(a)
    for e,n in enumerate(rhds_time):
        flag = False
        n_s = to_secs(n)
        if abs(n_s-a_s) < 10:
            print('Found!')
            flag = True
            matched_rhd.append(e)
            break
    if flag == False:
        matched_rhd.append(None)
        print(f'Match not found for {a}')

## Fetches data from ABF file
def get_data(filename):
    abf = pyabf.ABF(filename)

    abf.setSweep(0, channel=0)
    t_vector = abf.sweepX
    TTL = abf.sweepY

    abf.setSweep(0, channel=1)
    TTL2 = abf.sweepY

    abf.setSweep(0, channel=2)
    LVP = abf.sweepY

    abf.setSweep(0, channel=3)
    ECG = abf.sweepY

    abf.setSweep(0, channel=4)
    PP = abf.sweepY

    return t_vector, PP, ECG, LVP, TTL, TTL2

def isochrone_map(r, beats, offset = 0, name = 'map'):
    result, data_present = load_file(r)

    ### electrode connection on MEA, was confirmed using laser irradiation

    ch_n = ['13','22','10','23','08','09','14','19','12', '17','18','15','20', '21', '16', '11']
    chnnls = [f'A-0{c}' for c in ch_n]

    T = []
    V = []
```

```
    fig, axs = plt.subplots(16,1)
    fig.set_size_inches(11, 8.5)
    for ch,ax in zip(chnnls,axs):


        t, v = get_tV(ch, result)
        T.append(t)
        V.append(v)
        ax.plot(t,v)
        ax.set_xlim(-2,4)


    plt.savefig(f'{r[-21:-4]}-signals.png', dpi=600)
    plt.show()
    plt.close()
    Tstack = np.stack(T)
    print(f'tstack shape: {Tstack.shape}')
    Vstack = np.stack(V)

    reT = np.reshape(Tstack, (4,4,Tstack.shape[-1]))
    reV = np.reshape(Vstack, (4,4,Vstack.shape[-1]))
    print(f'reT shape: {reT.shape}')

    ### max plot
    zero = np.argwhere(reT[0,0,:] == 0)[0][0]

    mean = np.zeros((4,4))

    max_N = beats
    spacing = 10*10000//beats

    ### ignores first peak due to possible
    for N in range(1,max_N):
        print(f'Signal: {N}')
        #print(f'map {N}')
        Vs = reV[:,:,zero+offset+spacing*N:zero+offset+spacing+spacing*N]
        ts = reT[:,:,zero+offset+spacing*N:zero+offset+spacing+spacing*N]*1000 ## to
ms
        #plt.plot(ts[0,0,:],Vs[0,0,:])
        #plt.show()
        #print(np.amax(Vs, axis=-1))
        maxarg = np.argmax(Vs, axis = -1)

        out = np.empty((4,4))
        for n in range(4):
            for k in range(4):
```

```
            #tharg = np.argwhere(Vs[n,k,:] > 4000)[0]
            #out[k,n] = ts[k,n,tharg]
            out[k,n] = ts[k,n,maxarg[k,n]]

        img = out-ts[:,:,0]
        #print(reT[:,:,zero+offset+spacing*N])
        mean += img

        #img = img.round(4)

        fig, ax = plt.subplots()
        im = ax.imshow(img, interpolation='bicubic')

        for i in range(4):
            for j in range(4):
                text = ax.text(j, i, img[i, j], ha="center", va="center", color="w")

        plt.show()
        plt.close()



    plt.rcParams.update({'font.size': 5})
    plt.rcParams['axes.linewidth'] = 0.5
    plt.rcParams['lines.linewidth'] = 0.5
    plt.rcParams['xtick.major.width'] = 0.5
    plt.rcParams['ytick.major.width'] = 0.5
    print('Mean map')
    mean = mean/(max_N-1)
    img = mean-np.amin(mean)
    img = img.round(1)

    fig, ax = plt.subplots(figsize=(1.75,1.75))
    im = ax.imshow(img, cmap='coolwarm', interpolation = 'gaussian', vmin=0, vmax=4)

#     for i in range(4):
#         for j in range(4):
#             text = ax.text(j, i, img[i, j], ha="center", va="center", color="w")
    ax.axis('off')
    #plt.colorbar(im, fraction = 0.2)
    plt.savefig(f'{name}-map.png', dpi = 600)
    plt.show()

### Data calculation and ploting for an example map
name='LVonly'
n = 0
```

```
r = rhds[matched_rhd[n]]
print(r[-21:-4])
offset = 0
beats = 10
isochrone_map(r, beats, offset, name)
```

A3 Single-Channel Electromyography Analysis

```
import pyabf
import glob
import numpy as np
from matplotlib import pyplot as plt

### get data, single EMG sweep
def get_data(filename):
    abf = pyabf.ABF(filename)

    abf.setSweep(sweepNumber=0, channel=0)
    x = abf.sweepX
    TTL = abf.sweepY
    abf.setSweep(sweepNumber=0, channel=1)
    EMG = abf.sweepY

    data = x,EMG,TTL

    return data

### detect all light pulses in the file
def find_all_pulses(a):
    pulse_up = []
    pulse_down = []
    tmp = 0
    UP = 1
    DOWN = 0
    direction = UP

    for n in range(1, len(a)):

        if direction == UP and a[n] - a[tmp] > 0.1:
            pulse_up.append(n)
            tmp = n
            direction = DOWN
            #print('switch down')
        elif direction == DOWN and a[n] - a[tmp] > 0.1:
            pass
        elif direction == DOWN and a[n] - a[tmp] < -0.1:
            pulse_down.append(n)
            tmp = n
            direction = UP
            #print('switch up')
        elif direction == UP and a[n] - a[tmp] < -0.1:
            pass
```

```
    return pulse_up,pulse_down

### find and analyze pulses
def extract_pulses(abf,n):
    print('{}'.format(n))

    ## get data
    x, EMG, TTL = get_data(abf)

    ## find where ligth pulses are
    pulse_up, pulse_down = find_all_pulses(TTL)

    ## extract pulses into the separate arrays
    time_base = 0.025 # 10 us
    length = pulse_down[0] - pulse_up[0]
    max_len = length*time_base

    t_extent =100 # datapoints ms
    extent = int(t_extent/time_base)

    x = np.arange(0,max_len+t_extent,time_base)

    data = None
    for up,down in zip(pulse_up,pulse_down):
        new_data = EMG[up:down+extent]
        data = np.vstack((data, new_data)) if data is not None else new_data
    subsets = data


    # calculate the and standard deviation of all the pulses
    mean = np.mean(subsets, axis=0)
    stdev = np.std(subsets, axis=0)

    ## plot the pulse +/- standard deviation
    fig = plt.figure(figsize=(4,4))
    plt.fill_between(x, mean+stdev, mean-stdev, facecolor='blue', alpha=0.25)
    plt.plot(x,mean, c = 'red')
    plt.ylim(-0.3,0.7)
    plt.savefig('{}.svg'.format(n), dpi=300)
    plt.show()


    ## amplitude is defined as a miximum difference in the recorded signal
    amplitudes = []
    for x in subsets:
```

```
        amplitudes.append(np.amax(x) - np.amin(x))
    amplitudes = np.array(amplitudes)

    return amplitudes

if __name__ == '__main__':
    abfs = glob.glob('*abf')

    names = [x[:-4] for x in abfs]

    for e,n, in enumerate(names):
        print('{}: {}'.format(e,n))

    ### collect amplitudes from all recordings in the folder
    amplitudes = []
    for abf,n in zip(abfs,names):
        amplitudes.append(extract_pulses(abf,n))
```

A4 Multi-Channel Electromyography Analysis

```
### Load the background Python functions for reading RHD files
### Available from https://github.com/Intan-Technologies/load-rhd-notebook-python
### Distributed under GPL 3.0 license
import importrhdutilities.py
### importrhdutilities.py was modified to include the following function:
#
# def get_tV(channel_name, result):
#     channel_found, signal_type, signal_index =
find_channel_in_header(channel_name, result)
#     if channel_found:
#         if signal_type == 'amplifier_channels':
#             ylabel = 'Voltage (microVolts)'
#             signal_data_name = 'amplifier_data'
#             time = result['t_amplifier']
#
#
#         elif signal_type == 'aux_input_channels':
#             ylabel = 'Voltage (Volts)'
#             signal_data_name = 'aux_input_data'
#             time = result['t_aux_input']
#
#         elif signal_type == 'supply_voltage_channels':
#             ylabel = 'Voltage (Volts)'
#             signal_data_name = 'supply_voltage_data'
#             time = result['t_supply_voltage']
#
#
#         elif signal_type == 'board_adc_channels':
#             ylabel = 'Voltage (Volts)'
#             signal_data_name = 'board_adc_data'
#             time = result['t_board_adc']
#
#         elif signal_type == 'board_dig_in_channels':
#             ylabel = 'Digital In Events (High or Low)'
#             signal_data_name = 'board_dig_in_data'
#             time = result['t_dig']
#
#         elif signal_type == 'board_dig_out_channels':
#             ylabel = 'Digital Out Events (High or Low)'
#             signal_data_name = 'board_dig_out_data'
#             time = result['t_dig']
#         else:
#             print('channel is not amplifier')
#         voltage = result[signal_data_name][signal_index,:]
```

```
#     else:
#         print('channel not foud')
#     return time, voltage

from glob2 import glob
import matplotlib.pyplot as plt
import pyabf
import numpy as np
import re

def natural_sort(l):
    con = lambda text: int(text) if text.isdigit() else text.lower()
    sort_key = lambda key: [con(c) for c in re.split('([0-9]+)', key)]
    return sorted(l, key=sort_key)

import pybaselines
from scipy.signal import find_peaks
from matplotlib import cm

plt.rcParams.update({'font.size': 5})
plt.rcParams['axes.linewidth'] = 0.5
plt.rcParams['lines.linewidth'] = 0.5
plt.rcParams['xtick.major.width'] = 0.5
plt.rcParams['ytick.major.width'] = 0.5

abfs = sorted(glob('*.abf'))
rhds = sorted(glob('*.rhd'))

for e,a in enumerate(abfs):
    print(f'{e}: {a}')

abfs_time = []
for a in abfs:
    f = pyabf.ABF(a)
    head = f.headerText
    a = re.search('abfDateTime.*$', head, re.MULTILINE)
    b = re.search('..:..:..', a[0])
    c = b[0].replace(':','')
    abfs_time.append(c)

rhds_time = []
for r in rhds:
    rhds_time.append(r[-10:-4])

def to_secs(s):
    a = int(s[0:2])
```

```
    b = int(s[2:4])
    c = int(s[4:6])
    return a*3600 + b*60 + c

match = []
for a in abfs_time:
    a_s = to_secs(a)
    for e,n in enumerate(rhds_time):
        flag = False
        n_s = to_secs(n)
        if abs(n_s-a_s) < 5:
            print('Found!')
            flag = True
            match.append(e)
            break
    if flag == False:
        print(f'Match not found for {a}')

chs = ['A-002','A-003','A-004','ANALOG-IN-07']

def get_peaks(n):

    fig,axs = plt.subplots(11,3)

    result, data_present = load_file(rhds[match[n]], verbose = False)
    a002,a003,a004,ain = [get_tV(c, result) for c in chs]
    start = np.argwhere(a002[0] == 0)[0][0]

    for d in (a002,a003,a004):
        for n in range(0,12):
            x = (d[0][start+10000*n:start+250+10000*n]-n,
d[1][start+10000*n:start+250+10000*n]-d[1][start+10000*n])

            plt.plot(*x)
        plt.show()

def plot_scan(l : list):
    N = len(l)

    length = 2500
    fig, axs = plt.subplots(3,N, figsize=(6,3))

    limits = [[0,0],[0,0],[0,0]]

    output_array = []
    for e,N in enumerate(l):
```

```
        scan_array = []

        result, data_present = load_file(rhds[match[N]], verbose = False)
        a002,a003,a004,ain = [get_tV(c, result) for c in chs]
        start = np.argwhere(a002[0] == 0)[0][0]

        x,y = a004
        bkg_1 = pybaselines.smooth.ipsa(y)[0]
        a004 = (x, y-bkg_1)

        if N ==1:
            x,y = a002
            bkg_1 = pybaselines.smooth.ipsa(y)[0]
            a002 = (x, y-bkg_1)
            x,y = a003
            bkg_1 = pybaselines.smooth.ipsa(y)[0]
            a003 = (x, y-bkg_1)


        window = 10000 ### in us, 25 ms

        for d,ax,lim in zip((a002,a003,a004),axs[:,e], limits):
            channel_array = []
            color = cm.Reds(np.linspace(0, 1, 12))
            for n,c in zip(range(0,12),color):
                if N == 1 and n == 5:
                    channel_array.append(0)
                    continue
                x = (d[0][start+window*n:start+length+window*n]-n,
d[1][start+window*n:start+length+window*n]-d[1][start+window*n])

                max_v = np.amax(x[1])
                min_v = np.amin(x[1])
                channel_array.append(max_v)

                if lim[0] > min_v:
                    lim[0] = min_v
                if lim[1] < max_v:
                    lim[1] = max_v

                ax.plot(*x, c=c, linewidth=1)
            scan_array.append(channel_array)
        output_array.append(scan_array)

    print(limits)
    for ax,lim in zip(axs,limits):
```

```
        ylim = lim
        for sax in ax:
            sax.set_ylim(ylim[0]*1.1,ylim[1]*1.1)

            for axis in ['top','bottom','left','right']:
                sax.spines[axis].set_linewidth(0)


    for ax in axs:
        for sax in ax[1:]:

            sax.set_xticks([])
            sax.set_yticks([])


    axs[2][0].set_xlabel('Time (s)')

    axs[0][0].set_ylabel('EMG (μV)')
    axs[1][0].set_ylabel('EMG (μV)')
    axs[2][0].set_ylabel('EMG (μV)')
    plt.tight_layout()
    plt.savefig(f'EMG{str(l)}.svg', dpi= 600)
    plt.show()
    return output_array

### Plots an output array of the entire set of muscles and distances
l = range(0,10)
output_array = plot_scan(l)


### Calculations of selectivity index

EMG_amp = np.asarray(output_array)
print(EMG_amp.shape)
max_amp = np.amax(EMG_amp,axis = (0,2))
print(max_amp)
norm_amp = EMG_amp/max_amp[None,:,None]
print(norm_amp.shape)

###selectivity index
norm_amp_sum = np.sum(norm_amp, axis=1)

selectivity_idx = norm_amp/norm_amp_sum[:,None,:]


x = [0.1,0.2,0.3,0.4,0.5,0.6,0.7,0.8]
```

```
gm = np.nanmean(selectivity_idx[:,0,:], axis=-1)
ta = np.nanmean(selectivity_idx[:,1,:], axis=-1)
pi = np.nanmean(selectivity_idx[:,2,:], axis=-1)

gm[0] = 0
pi[0] = 0
pi[1] = 0
gm[-1] = 0
pi[-1] = 0

#### Plots the selectivity plot
fig,ax = plt.subplots(figsize=(1.5,1))
#ax.scatter(x, gm[1:-1]*100,c='blue', s=1)
ax.fill_between(x, gm[1:-1]*100,0, facecolor='blue', alpha=0.25)
ax2=ax.twinx()
#ax2.scatter(x, (pi[1:-1])*100, c = 'red',s = 1)
ax2.fill_between(x, (pi[1:-1])*100, 0, facecolor='red', alpha=0.25)
ax2.invert_yaxis()
ax.set_ylabel('Muscle selectivity (%)')
ax.set_ylim(0,100)
ax2.set_ylim(100,0)

ax.set_xlabel('Laser position (mm)')
plt.tick_params(right = False, labelright = False)
plt.xlim(0,0.9)
plt.savefig('power7activation.png', dpi=600)
plt.savefig('power7activation.svg', dpi=600, transparent=True)
plt.show()
```

Appendix B

Python Code Developed for the Autonomous Cardiomyocyte Training

B1 Main Control Program for Training Software

```
from tkinter import *
from tkinter import ttk
from tkinter import filedialog
from tkinter.scrolledtext import ScrolledText
from tkinter import messagebox

from PIL import Image, ImageTk

from matplotlib.backends.backend_tkagg import FigureCanvasTkAgg

import matplotlib.pyplot as plt

from threading import Thread, Event
import queue
import os
from glob import glob
import h5py as h5
import re

from ElecStim import stim_control
from agent import Agent
from MicroscopeControl import PCO_direct
from Analysis.MVengine import MVengine

from datetime import datetime

import numpy as np

import multiprocessing as mp

class ACMT(Tk):

    def __init__(self):
        super().__init__()
```

```
        self.title("ACMT (v. 0.1)")

        self.current_view = 0
        self.max_views = 0

        #### View collectors lists
        self.results_collector = ResultsCollector()
        self.stop_event = Event()

        self.phase_images = []
        self.freq_images = []
        self.oscillations_images = []
        self.segmentation_images = []

        self.active_count_list = []
        self.freq_list = []

        self.init_variables()
        self.init_widgets()

    def init_variables(self):
        ##################
        ### VARIABLES ###
        ##################

        self.savefolder = StringVar()
        self.savename = StringVar()

        self.openfolder = StringVar()

        ## init parameters
        self.stim_current_uA = IntVar()
        self.stim_duration = IntVar()
        self.stim_freq = IntVar()

        ### stop parameters
        self.target_freq = IntVar()
        self.timeout = IntVar()
        self.max_dV =IntVar()

        ### technical parameters
        self.max_attempts =IntVar()
        self.freq_overpace =IntVar()
        self.stim_current_step_uA =IntVar()
        self.active_count_cutoff = IntVar()
```

```
### hardware setup
self.k26k_addrs = StringVar()

self.MLmodelpath = StringVar()

self.HOME_DIR= os.path.expanduser("~")

if not os.path.isdir(self.HOME_DIR):
    self.HOME_DIR = ""

##DEFAULTS
self.savefolder.set(f'{self.HOME_DIR}\\')
self.savename.set('training')

self.openfolder.set('\\')

## init parameters
self.stim_current_uA.set(2)
self.stim_duration.set(10)
self.stim_freq.set(1)

### stop parameters
self.target_freq.set(5)
self.timeout.set(24)
self.max_dV.set(2)

### technical parameters
self.max_attempts.set(10)
self.freq_overpace.set(10)
self.stim_current_step_uA.set(1)
self.active_count_cutoff.set(5)

### Hardware address
self.k26k_addrs.set('GPIB0::26::INSTR')

self.MLmodelpath.set('project/ML/AleksBestModel.h5')

### State variables
self.camera_ctrl = BooleanVar()
self.stim_ctrl = BooleanVar()
self.mv_engine_ctrl = BooleanVar()
self.agent_ctrl = BooleanVar()
self.camera_init_state = BooleanVar()
self.stim_init_state = BooleanVar()
self.mv_engine_init_state = BooleanVar()
self.agent_init_state = BooleanVar()
```

```
        self.camera_ctrl.set(True)
        self.stim_ctrl.set(True)
        self.mv_engine_ctrl.set(True)
        self.agent_ctrl.set(True)
        self.camera_init_state.set(False)
        self.stim_init_state.set(False)
        self.mv_engine_init_state.set(False)
        self.agent_init_state.set(False)

        ### View
        self.viewnumber = StringVar()
        self.viewnumber.set(f'{self.current_view}/{self.max_views}')

    def init_widgets(self):
        ### Title frame
        Frame1  = ttk.Frame(self, padding="5 10 5 10")
        Frame1.grid(column=0,row=0, sticky=(N, W, E))
        main_title =ttk.Label(Frame1, text='Autonomous Cardiomyocyte Training',
font=('Helvetica', 18,'bold'))
        main_title.pack()


        ### FRAME WITH SAVING PARAMETERS
        Frame2  = ttk.Frame(self, padding="5 10 5 10")
        Frame2.grid(column=0, row=1, sticky=(W, E, S))

        title2_1 = ttk.Label(Frame2, text='Saving:', font=('Helvetica', 12,'bold'))
        title2_1.grid(column=0, row=0, sticky=(W, E))

        label2_1 = ttk.Label(Frame2, text="Save folder")
        label2_1.grid(column=0, row=1, sticky=(W, E))
        label2_2 = ttk.Label(Frame2, text="Save name")
        label2_2.grid(column=0, row=2, sticky=(W, E))

        entry2_1 = ttk.Entry(Frame2, textvariable=self.savefolder)
        entry2_1.grid(column=1, row=1, sticky=(W, E))
        entry2_2 = ttk.Entry(Frame2, textvariable=self.savename)
        entry2_2.grid(column=1, row=2, sticky=(W, E))

        button2_1 = ttk.Button(Frame2, text = 'Choose folder', command =
self.askforfolder)
        button2_1.grid(column=2, row=1, sticky=(W, E))
        button2_2 = ttk.Button(Frame2, text='Add date/time', command =
self.addtdatetime)
        button2_2.grid(column=2, row=2, sticky=(W, E))
```

```
        ### FRAME WITH INITIAL PARAMTERES
        Frame3  = ttk.Frame(self, padding="5 10 5 10")
        Frame3.grid(column=0, row=2, sticky=(W, E, S))

        subtitle3 = ttk.Label(Frame3, text='Initial Parameters:', font=('Helvetica',
12,'bold'))
        subtitle3.grid(column=0, row=0, sticky=(W, E))

        lab3_1 = ttk.Label(Frame3, text="Stimulation current (uA)")
        lab3_1.grid(column=0, row=1, sticky=W)
        lab3_2 = ttk.Label(Frame3, text="Stimulation duration (s)")
        lab3_2.grid(column=0, row=2, sticky=W)
        lab3_3 = ttk.Label(Frame3, text="Stimulation frequency (Hz)")
        lab3_3.grid(column=0, row=3, sticky=W)

        entry3_1 = ttk.Entry(Frame3, textvariable= self.stim_current_uA)
        entry3_1.grid(column=1, row=1, sticky=W)
        entry3_2 = ttk.Entry(Frame3, textvariable= self.stim_duration)
        entry3_2.grid(column=1, row=2, sticky=W)
        entry3_3 = ttk.Entry(Frame3, textvariable= self.stim_freq)
        entry3_3.grid(column=1, row=3, sticky=W)

        ### FRAME WITH INITIAL PARAMTERES
        Frame4  = ttk.Frame(self, padding="5 10 5 10")
        Frame4.grid(column=0, row=3, sticky=(W, E, S))

        subtitle4 = ttk.Label(Frame4, text='Technical parameters:', font=('Helvetica',
12,'bold'))
        subtitle4.grid(column=0, row=0, sticky=(W, E))

        lab4_1 = ttk.Label(Frame4, text="Maxiumum attempts")
        lab4_1.grid(column=0, row=1, sticky=W)
        lab4_2 = ttk.Label(Frame4, text="Frequency overpace (%)")
        lab4_2.grid(column=0, row=2, sticky=W)
        lab4_3 = ttk.Label(Frame4, text="Stimulation current step (uA)")
        lab4_3.grid(column=0, row=3, sticky=W)
        lab4_4 = ttk.Label(Frame4, text="Active count cutoff (%)")
        lab4_4.grid(column=0, row=4, sticky=W)

        entry4_1 = ttk.Entry(Frame4, textvariable=self.max_attempts)
        entry4_1.grid(column=1, row=1, sticky=W)
        entry4_2 = ttk.Entry(Frame4, textvariable=self.freq_overpace)
        entry4_2.grid(column=1, row=2, sticky=W)
        entry4_3 = ttk.Entry(Frame4, textvariable=self.stim_current_step_uA)
        entry4_3.grid(column=1, row=3, sticky=W)
```

```
        entry4_4 = ttk.Entry(Frame4, textvariable=self.active_count_cutoff)
        entry4_4.grid(column=1, row=4, sticky=W)

        ### FRAME WITH INITIAL PARAMTERES
        Frame5  = ttk.Frame(self, padding="5 10 5 10")
        Frame5.grid(column=0, row=4, sticky=(W, E, S))

        subtitle4 = ttk.Label(Frame5, text='Hardware setup:', font=('Helvetica', 12,'bold'))
        subtitle4.grid(column=0, row=0, sticky=(W, E))

        ### Table

        ### Header
        head1 = ttk.Label(Frame5, text="Component")
        head1.grid(column=0, row=1, sticky=(W, E))
        head1 = ttk.Label(Frame5, text="Real control?")
        head1.grid(column=1, row=1, sticky=(W, E), padx=10,)
        head1 = ttk.Label(Frame5, text="Is initilized?")
        head1.grid(column=2, row=1, sticky=(W, E),padx=10)
        head1 = ttk.Label(Frame5, text="Address")
        head1.grid(column=3, row=1, sticky=(W, E))

        col0 = ttk.Label(Frame5, text="PCO camera")
        col0.grid(column=0, row=2, sticky=(W, E))
        col0 = ttk.Label(Frame5, text="Keithely stimulator")
        col0.grid(column=0, row=3, sticky=(W, E))
        col0 = ttk.Label(Frame5, text="MV Engine")
        col0.grid(column=0, row=4, sticky=(W, E))
        col0 = ttk.Label(Frame5, text="AI agent")
        col0.grid(column=0, row=5, sticky=(W, E))

        col1 = ttk.Checkbutton(Frame5, variable=self.camera_ctrl, onvalue=True,
offvalue=False)
        col1.grid(column=1, row=2)
        col1 = ttk.Checkbutton(Frame5, variable=self.stim_ctrl, onvalue=True,
offvalue=False)
        col1.grid(column=1, row=3)
        col1 = ttk.Checkbutton(Frame5, variable=self.mv_engine_ctrl, onvalue=True,
offvalue=False)
        col1.grid(column=1, row=4)
        col1 = ttk.Checkbutton(Frame5, variable=self.agent_ctrl, onvalue=True,
offvalue=False)
        col1.grid(column=1, row=5)

        col2 = ttk.Checkbutton(Frame5, variable=self.camera_init_state, onvalue=True,
offvalue=False, state=DISABLED)
```

```
        col2.grid(column=2, row=2)
        col2 = ttk.Checkbutton(Frame5, variable=self.stim_init_state, onvalue=True,
offvalue=False, state=DISABLED)
        col2.grid(column=2, row=3)
        col2 = ttk.Checkbutton(Frame5, variable=self.mv_engine_init_state,
onvalue=True, offvalue=False, state=DISABLED)
        col2.grid(column=2, row=4)
        col2 = ttk.Checkbutton(Frame5, variable=self.agent_init_state, onvalue=True,
offvalue=False, state=DISABLED)
        col2.grid(column=2, row=5)

        col3 = ttk.Entry(Frame5, textvariable=self.k26k_addrs)
        col3.grid(column=3, row=3, sticky=(W, E))
        col3 = ttk.Entry(Frame5, textvariable=self.MLmodelpath)
        col3.grid(column=3, row=4, sticky=(W, E))

        initButton1 = ttk.Button(Frame5, text = 'Initilize system', command =
self.initializeSystem)
        initButton1.grid(column=0, row=6, sticky=(W, E),pady=(10,0))

        runButton2 = ttk.Button(Frame5, text = 'Run training', command =
self.runTraining)
        runButton2.grid(column=0, row=7, sticky=(W, E))

        runButton3 = ttk.Button(Frame5, text = 'Run analysis', command =
self.runAnalysis)
        runButton3.grid(column=0, row=9, sticky=(W, E))

        runButton4 = ttk.Button(Frame5, text = 'Terminate thread', command = lambda :
self.stop_event.set())
        runButton4.grid(column=0, row=10, sticky=(W, E))

        #### CANVAS FOR VIEW
        Frame6  = ttk.Frame(self, padding="5 10 5 10", width = 256)
        Frame6.grid(column=1, row=1, rowspan=4, sticky=(N, W))

        subtitle = ttk.Label(Frame6, text = 'Phase-contrast')
        subtitle.grid(column=0, row=0)
        subtitle = ttk.Label(Frame6, text = 'Frequency map')
        subtitle.grid(column=0, row=2)
        subtitle = ttk.Label(Frame6, text = 'Oscillations map')
        subtitle.grid(column=1, row=0)
        subtitle = ttk.Label(Frame6, text = 'Segmentation map')
        subtitle.grid(column=1, row=2)

        empty = np.zeros((256,256), dtype=np.uint8)
```

```
        self.black = ImageTk.PhotoImage(Image.fromarray(empty))

        self.phaseView = Canvas(Frame6, width=256, height=256)
        self.phaseViewItem = self.phaseView.create_image(0,0,
image=self.black,anchor=NW)
        self.phaseView.grid(column = 0, row = 1, padx=10,pady=10)
        self.frequencyView = Canvas(Frame6, width=256, height=256)
        self.frequencyViewItem = self.frequencyView.create_image(0,0,
image=self.black,anchor=NW)
        self.frequencyView.grid(column = 0, row = 3, padx=10,pady=10)
        self.oscillationView = Canvas(Frame6, width=256, height=256)
        self.oscillationViewItem = self.oscillationView.create_image(0,0,
image=self.black,anchor=NW)
        self.oscillationView.grid(column = 1, row = 1, padx=10,pady=10)
        self.segmentationView = Canvas(Frame6, width=256, height=256)
        self.segmentationViewItem = self.segmentationView.create_image(0,0,
image=self.black,anchor=NW)
        self.segmentationView.grid(column = 1, row = 3, padx=10,pady=10)

        Frame7 = ttk.Frame(self, padding="5 10 5 10")
        Frame7.grid(column=1, row=5,  sticky=(N, E))

        swtichleft = ttk.Button(Frame7, text = '<-', command = self.viewshowPrevious)
        swtichleft.grid(column=0, row=0, sticky=(N, E))
        numberInd = ttk.Label(Frame7, textvariable = self.viewnumber)
        numberInd.grid(column=1, row=0, sticky=(N, E))
        switchright = ttk.Button(Frame7, text = '->', command = self.viewshowNext)
        switchright.grid(column=2, row=0, sticky=(N, E))

        ##########################
        ### Frame with plots ###
        ##########################

        self.Frame8plots  = ttk.Frame(self, padding="5 10 5 10")
        self.Frame8plots.grid(column=2, row=1, rowspan= 10, sticky=(N, W))

        subtitle = ttk.Label(self.Frame8plots, text = '# of detected cells')
        subtitle.grid(column=0, row=0)
        subtitle = ttk.Label(self.Frame8plots, text = 'Frequency')
        subtitle.grid(column=0, row=2)

        self.placeholder1 = Canvas(self.Frame8plots, width=512, height=256)
        self.placeholder1.grid(column = 0, row = 1)
        self.placeholder2 = Canvas(self.Frame8plots, width=512, height=256)
        self.placeholder2.grid(column = 0, row = 3)
```

```
    ##############################
    ### Frame with text output ###
    ##############################
    Frame9  = ttk.Frame(self, padding="5 10 5 10")

    Frame9.grid(column=0, row=5, columnspan=2, sticky=(N, W))
    self.scrolledtext = ScrolledText(Frame9, height=10, width= 64)
    self.scrolledtext.pack()
    self.scrolledtext.configure(state='disabled')

def askforfolder(self):
    dirname = filedialog.askdirectory()
    if dirname != '':
        self.savefolder.set(f'{dirname}/')

def askforfolder_open(self):
    dirname = filedialog.askdirectory()
    if dirname != '':
        self.openfolder.set(f'{dirname}/')

def addtdatetime(self):
    today = datetime.today()
    suffix = today.strftime('_%y%m%d_%H%M')
    self.savename.set(f'{self.savename.get()}{suffix}')

def initializeSystem(self):
    ### PARAMETERS DICTIONARY FOR AGENT
    params = {
## init parameters
'stim_current_uA' : self.stim_current_uA.get(),
'duration' : self.stim_duration.get(),
'stim_freq' : self.stim_freq.get(),

### stop parameters
'target_freq' : self.target_freq.get(),
'timeout' : self.timeout.get(),
'max_dV' : self.max_dV.get(),

### technical parameters
'max_attempts' : self.max_attempts.get(),
'freq_overpace' : self.freq_overpace.get(),
'stim_current_step_uA' : self.stim_current_step_uA.get(),
'active_count_cutoff' : self.active_count_cutoff.get()

}
```

```
    ### initialize subcomponents
    try:
        self.stimulator = stim_control.Stimulator(
                        control = self.stim_ctrl.get(),
                        addrs = self.k26k_addrs.get(),
                        savefolder = self.savefolder.get(),
                        savename=self.savename.get())
        self.stim_init_state.set(True)
    except Exception as e:
        print(e)

    try:
        self.mv_engine = MVengine(
                        control = self.mv_engine_ctrl.get(),
                        savefolder=self.savefolder.get(),
                        savename=self.savename.get(),
                        MLmodelpath=self.MLmodelpath.get() )
        self.mv_engine_init_state.set(True)
    except Exception as e:
        print(e)

    try:
        self.camera = PCO_direct.Camera(
                        control = self.camera_ctrl.get(),
                        savefolder=self.savefolder.get(),
                        savename=self.savename.get(),
                        data_instance=self.mv_engine)
        self.camera_init_state.set(True)
    except Exception as e:
        print(e)

    try:
        self.agent = Agent(control = self.agent_ctrl.get(),
                        stim_device = self.stimulator,
                        savefolder=self.savefolder.get(),
                        savename=self.savename.get(),
                        params=params)
        self.agent_init_state.set(True)
    except Exception as e:
        print(e)

    self.mv_engine.add_agent(self.agent)
    self.stimulator.add_agent(self.agent)
    self.camera.add_agent(self.agent)

def runTraining(self):
```

```
        try:
            self.training_thread
        except:
            self.training_thread = AsyncTraining(
                                    self.stimulator,
                                    self.mv_engine,
                                    self.camera,
                                    self.agent,
                                    self.results_collector,
                                    self.stop_event,
                                    self.savefolder.get(),
                                    self.savename.get())

            self.training_thread.start()
            self.after(500, self.monitor, self.training_thread)

    def monitor(self, thread):
        if not thread.is_alive() and self.results_collector.is_empty():
            return


        while not self.results_collector.text_queue.empty():
            textupdate = self.results_collector.text_queue.get()
            today = datetime.today()
            timestamp = today.strftime('%y:%m:%d-%H:%M -> ')

            self.scrolledtext.configure(state='normal')
            self.scrolledtext.insert(INSERT, f'{timestamp}{textupdate}\n')
            self.scrolledtext.configure(state='disabled')
            self.scrolledtext.see('end')

        update_views = False
        update_plots = False

        while not self.results_collector.phase_queue.empty():
            self.phase_images.append(self.results_collector.phase_queue.get())
            update_views = True

        while not self.results_collector.freq_queue.empty():
            self.freq_images.append(self.results_collector.freq_queue.get())
            update_views = True

        while not self.results_collector.oscillations_queue.empty():
            self.oscillations_images.append(self.results_collector.oscillations_queue.get())
            update_views = True
```

```
        while not self.results_collector.segmentation_queue.empty():

self.segmentation_images.append(self.results_collector.segmentation_queue.get())
            update_views = True

        while not self.results_collector.cellnumber_queue.empty():
            self.active_count_list.append(self.results_collector.cellnumber_queue.get())
            update_plots = True

        while not self.results_collector.cellfreq_queue.empty():
            self.freq_list.append(self.results_collector.cellfreq_queue.get())
            update_plots = True

        if update_views:
            self.update_views()

        if update_plots:
            self.update_plots()

        self.after(500, self.monitor, thread)

    def runAnalysis(self):
        self.mv_engine = MVengine(control = True,
                                  savefolder=self.savefolder.get(),
                                  savename=self.savename.get(),
                                  MLmodelpath=self.MLmodelpath.get())

        self.analysis_thread = AsyncAnalysis(mv_engine = self.mv_engine,
                                             results_collector = self.results_collector,
                                             stop_event = self.stop_event,
                                             savefolder = self.savefolder.get(),
                                             savename = self.savename.get())
        self.analysis_thread.start()

        self.after(500, self.monitor, self.analysis_thread)

    def viewshowPrevious(self):
        if self.current_view - 1 > 0:
            self.current_view -= 1
            self.update_views()

    def viewshowNext(self):
        if self.current_view + 1 <= self.max_views:
            self.current_view += 1
            self.update_views()
```

```
    def update_max_views(self):
        count = [
            len(self.phase_images),
            len(self.freq_images),
            len(self.oscillations_images),
            len(self.segmentation_images)
            ]

        self.max_views = max(count)
        self.update_view_number()

    def update_view_number(self):
        self.viewnumber.set(f'{self.current_view}/{self.max_views}')

    def update_views(self):
        self.update_max_views()
        if self.current_view == 0 and self.max_views > 0:
            self.current_view = self.max_views

        idx = self.current_view - 1

        try:
            self.phase_img =
ImageTk.PhotoImage(Image.fromarray(self.phase_images[idx]).resize((256,256)))
        except:
            self.phase_img = self.black
        try:
            self.freq_img =
ImageTk.PhotoImage(Image.fromarray(self.freq_images[idx]).resize((256,256)))
        except:
            self.freq_img = self.black
        try:
            self.osc_img =
ImageTk.PhotoImage(Image.fromarray(self.oscillations_images[idx]).resize((256,256)
))
        except:
            self.osc_img = self.black
        try:
            self.seg_img =
ImageTk.PhotoImage(Image.fromarray(self.segmentation_images[idx],
mode='P').resize((256,256)))
        except:
            self.seg_img = self.black

        images = [self.phase_img, self.freq_img, self.osc_img, self.seg_img]
```

```
        canvases = [
            self.phaseView,
            self.frequencyView,
            self.oscillationView,
            self.segmentationView
            ]

        containers = [
            self.phaseViewItem,
            self.frequencyViewItem,
            self.oscillationViewItem,
            self.segmentationViewItem
            ]

        for canvas, container, image in zip(canvases, containers, images):
            canvas.itemconfig(container,image=image)

        self.update_view_number()

    def update_plots(self):
        px = 1/plt.rcParams['figure.dpi']  # pixel in inches
        ### cell number scatterplot
        fig = plt.Figure(figsize=(512*px,256*px))

        x = np.arange(1, len(self.active_count_list)+1)
        y = self.active_count_list

        plot1 = fig.add_subplot(111)
        plot1.scatter(x,y)
        canvas = FigureCanvasTkAgg(fig, master=self.Frame8plots)
        canvas.draw()
        canvas.get_tk_widget().grid(column=0, row=1)

        ### frequency boxplot
        fig = plt.Figure(figsize=(512*px,256*px))

        x = np.arange(1, len(self.freq_list)+1)
        y = self.freq_list
        try:
            plot1 = fig.add_subplot(111)
            plot1.boxplot(y, labels=x)
            canvas2 = FigureCanvasTkAgg(fig, master=self.Frame8plots)
            canvas2.draw()
            canvas2.get_tk_widget().grid(column=0, row=3)
        except:
            pass
```

```
class AsyncTraining(Thread):
    def __init__(self, stimulator, mv_engine, camera, agent, results_collector,
stop_event, savefolder, savename):
        super().__init__()
        self.daemon = True
        self.stop_event = stop_event

        self.stimulator = stimulator
        self.mv_engine = mv_engine
        self.camera = camera
        self.agent = agent
        self.results_collector= results_collector

        self.results_collector.init_h5(f'{savefolder}{savename}')

    def run(self):

        self.results_collector.log('Analysis started')

        self.agent.init_log()

        self.camera.image(self.results_collector)

        self.mv_engine.analyze_dynamic(self.results_collector)

        self.agent.make_decision(self.results_collector)
        self.agent.set_stimulator(self.results_collector)

        if self.agent.state == 'stop':
            self.results_collector.log('First decision is to stop, no stimulation performed.')
            return

        self.results_collector.increment_id()

        while True:

            self.stimulator.run(self.results_collector)

            self.camera.image(self.results_collector)

            #input("Copy image file and press Enter to continue...")
            self.mv_engine.analyze_dynamic(self.results_collector)

            self.agent.make_decision(self.results_collector)
            self.agent.set_stimulator(self.results_collector)
```

```
            if self.agent.state == 'stop':
                self.results_collector.log('Program has finished.')
                break
            self.results_collector.increment_id()

            if self.stop_event.is_set():
                self.results_collector.log('Training interrupted.')
                self.stop_event.clear()
                return

        self.agent.close_logfile()

class AsyncAnalysis(Thread):
    def __init__(self, mv_engine, results_collector, stop_event, savefolder, savename):
        super().__init__()

        self.daemon = True
        self.stop_event = stop_event
        self.datafolder = savefolder
        self.mv_engine = mv_engine
        self.results_collector = results_collector

        self.results_collector.init_h5(f'{savefolder}{savename}')

    def run(self):

        self.results_collector.log('Analysis started')

        ### sorting of names into natural order
        convert = lambda text: int(text) if text.isdigit() else text.lower()
        alphanum_key = lambda key: [convert(c) for c in re.split('([0-9]+)', key)]

        filelist = sorted(glob(f'{self.datafolder}*recording*.h5'), key=alphanum_key)
        if not filelist:
            filelist = sorted(glob(f'{self.datafolder}*.nd2'))
        if not filelist:
            messagebox.showerror('Error!', 'No useful files found in the folder.')
            return

        for fh in filelist:
            self.results_collector.log(f'Analysing: {fh}')
            self.mv_engine.load_data(fh)
            self.mv_engine.analyze_static(self.results_collector)

            if self.stop_event.is_set():
```

```
                self.results_collector.log('Analysis interrupted')
                self.stop_event.clear()
                return
            self.results_collector.increment_id()
        self.results_collector.log('Analysis finished')

class ResultsCollector:
    def __init__(self):
        ### async queues
        self.text_queue = queue.Queue()
        self.phase_queue = queue.Queue()
        self.freq_queue = queue.Queue()
        self.oscillations_queue = queue.Queue()
        self.segmentation_queue = queue.Queue()
        self.cellnumber_queue = queue.Queue()
        self.cellfreq_queue = queue.Queue()

        self.id = 0
        self.logid = 0

    def is_empty(self):
        status = [
            self.text_queue.empty(),
            self.phase_queue.empty(),
            self.freq_queue.empty(),
            self.oscillations_queue.empty(),
            self.segmentation_queue.empty(),
            self.cellnumber_queue.empty(),
            self.cellfreq_queue.empty()
            ]

        if False in status:
            return False
        else:
            return True

    def log(self, s):
        self.text_queue.put(s)
        self.save(s,'log',logid = self.logid)
        self.logid += 1

    def add_phase(self, img):
        self.phase_queue.put((img/256).astype(np.uint8))
        self.save((img/256).astype(np.uint8),'phase')

    def add_freq(self, img):
```

```
        self.save(img.astype(np.float16),'freq')
        img = img/np.amax(img)
        img = img*256
        self.freq_queue.put((img).astype(np.uint8))

    def add_osc(self, img):
        self.save(img.astype(np.float16),'osc')
        img = img*256
        self.oscillations_queue.put((img).astype(np.uint8))

    def add_segmentation(self, img):
        self.save(img.astype(np.uint16),'seg')
        tmp = img.copy()
        tmp[tmp>0] = 255
        self.segmentation_queue.put((tmp).astype(np.uint8))

    def init_h5(self, savepath):
        self.savepath = savepath

        with h5.File(f'{self.savepath}.h5', "w-") as f:
            f.create_group('log')
            f.create_group('phase')
            f.create_group('freq')
            f.create_group('osc')
            f.create_group('seg')
            f.create_group('cell_num')
            f.create_group('cell_freq')

    def add_number_active_cells(self, number_of_active_regions):
        self.cellnumber_queue.put(number_of_active_regions)
        #can be derived from frequencies array, no need to save
        #self.save(number_of_active_regions,'cell_num')

    def add_frequencies(self, avg_freqs):
        #print(avg_freqs)
        self.cellfreq_queue.put(avg_freqs)
        self.save(np.asarray(avg_freqs), 'cell_freq')

    def save(self, data, data_type, logid = None):
        with h5.File(f'{self.savepath}.h5', "a") as f:
            if logid is not None:
                dset = f[data_type].create_dataset(f'{data_type}_{self.id}_{logid}',
data=data)
            else:
                dset = f[data_type].create_dataset(f'{data_type}_{self.id}', data=data)
```

```
    def increment_id(self):
        self.id += 1

if __name__ == "__main__":
    try:
        root = ACMT()
        root.mainloop()
    except Exception as e:
        print(f'Exception: {e}')
```

B2 Machine Vision Analysis Class

```
import warnings
import h5py as h5
import numpy as np
import matplotlib.pyplot as plt
import keras
import scipy.ndimage as sndi

from skimage.filters import gaussian

from skimage.segmentation import watershed
from skimage.morphology import disk, dilation

from skimage.feature import peak_local_max

from scipy.stats import mode
import time

from nd2reader import ND2Reader

class MVengine:

    def __init__(self, control = False, savefolder=None, savename = None,
MLmodelpath=None):

        self.control = control

        self.savepath = f'{savefolder}/{savename}'

        self.model = keras.models.load_model(MLmodelpath)

        self.agent = None
        self.data = None
        self.id = 0

        self.sampling_interval = 0.025

    def add_agent(self, agent):
        self.agent = agent

    def send_data(self, frames):
        self.data = frames

    def load_data(self, fh):
        if fh[-2:] == 'h5':
```

```
            with h5.File(fh) as data:
                self.data = data['recording'][:,:,:]
        elif fh[-2:] == 'd2':
            warnings.filterwarnings('ignore', message="Z-levels details missing in
metadata. Using Z-coordinates instead.")

            try:
                with ND2Reader(fh) as nd2:
                    try:
                        nd2.iter_axes = "z"
                    except:
                        nd2.iter_axes = "t"

                    #turn nd2 iterator into python list
                    frames = [x for x in nd2]

                    #turn into a 3D numpy array
                    arr=np.dstack(frames)

                    self.data = arr
            except IOError:
                pass

    def analyze_static(self, results_collector):
        self.runML(results_collector)

        self.freq_with_segmentation(results_collector)
        self.id += 1

    def analyze_dynamic(self, results_collector = None):

        if self.control == True:
            self.runML(results_collector)

            self.freq_with_segmentation(results_collector)

            ### send results to the agent
            self.agent.add_results(self.freq_stats)
            self.id += 1
        else:
            results_collector.log('Fake analysis.')
            self.id += 1
            return 0

    ### Machine Learning ###
```

```
def runML(self,results_collector):
    results_collector.log(f'Entered ML routine with id {self.id}.')

    results_collector.add_phase(np.mean(self.data, axis=2))

    arr = self.data.astype(np.float32)

    xshape, yshape, zshape = arr[:,:,:].shape

    #Normalize Signals
    arr =  arr - np.amin(arr, axis=2)[:,:,None]
    max_val = np.amax(arr,axis=2)[:,:,None]
    arr = np.divide(arr, max_val, out=np.zeros_like(arr), where = (max_val != 0))

    sig_list = np.reshape(arr, (xshape*yshape,zshape))

    #Perform Predictions
    sig_stack = sig_list[:,:100]
    results_collector.log(f'Starting prediction.')
    start = time.perf_counter()
    prediction = self.model.predict(sig_stack)
    end = time.perf_counter()
    elapsed = end-start
    results_collector.log(f'Finished predicting in {elapsed}.')

    #Reshape Confidence Values into 2D Array
    prediction = prediction[:,1]
    prediction = prediction.reshape(xshape,yshape)
    self.confidence_mask = prediction
    out_confidence_mask = np.copy(prediction)
    out_confidence_mask[out_confidence_mask < 0.9] = 0

    #####
    results_collector.add_osc(out_confidence_mask)
    #####

def freq_with_segmentation(self, results_collector):
    arr = self.data

    xshape, yshape = arr[:,:,0].shape
    xr = range(xshape)
    yr = range(yshape)

    fourier = np.fft.fft(arr, axis=2)
    fourier = np.abs(fourier)
```

```
        sampling= 1/40

        freqs = np.fft.fftfreq(len(arr[0,0,:]), d=sampling)

        ### new vectorized calculation
        freqs_red = freqs[1:int(len(freqs)/2)]
        fourier_real = fourier[:,:,1:int(len(arr[0,0,:])/2)]
        max_power = np.argmax(fourier_real, axis=2)
        freq_map = freqs_red[max_power]

        segmented = self.segment_image(self.confidence_mask)
        detected_regions = np.amax(segmented) + 1

        labels = np.arange(1,detected_regions)

        rand_lab = np.random.choice(labels, detected_regions-1, replace=False)
        rand_lab = np.hstack(([0],rand_lab))

        assert len(rand_lab) == detected_regions

        out_segmentation = rand_lab[segmented]

        ###
        results_collector.add_segmentation(out_segmentation)
        ###

        freq_of_contracting_pixels = freq_map[self.confidence_mask > 0.9]
        labels_of_contracting_pixels = segmented[self.confidence_mask > 0.9]

        assert len(freq_of_contracting_pixels) == len(labels_of_contracting_pixels),
'different length of arrays'

        region_list = [[] for _ in range(detected_regions)]

        for f,l in zip(freq_of_contracting_pixels, labels_of_contracting_pixels):
            region_list[l].append(f)

        for region in region_list:
            if len(region) < 2:
                region.clear()

        region_list_no_background = region_list[1:]

        region_list_no_background_len = [len(r) for r in region_list_no_background]
        number_of_active_regions = np.count_nonzero(region_list_no_background_len)
```

```
        ###
        results_collector.add_number_active_cells(number_of_active_regions)

        ###

        avg_freqs = np.asarray([np.mean(r) for r in region_list_no_background])

        avg_freqs_copy = np.asarray([np.mean(r) for r in region_list])
        avg_freqs = avg_freqs[~np.isnan(avg_freqs)]

        if len(avg_freqs) <= 1:
            avg_freqs = [0]
            number_of_active_regions = 1

        assert len(avg_freqs) == number_of_active_regions, 'different number of active
regions and frquencies'

        ###
        results_collector.add_frequencies(avg_freqs)
        ###

        avg_freqs_copy[0] = 0
        out_freq_map = avg_freqs_copy[segmented]
        out_freq_map[np.isnan(out_freq_map)] = 0

        ###
        results_collector.add_freq(out_freq_map)
        ###

        try:
            freq_mode = float(mode(avg_freqs)[0][0])
            num_mode = int(mode(avg_freqs)[1][0])
        except:
            freq_mode = 0
            num_mode = 0

        self.freq_stats = {
            "freq_num" : number_of_active_regions,
            "freq_mean" : np.mean(avg_freqs),
            "freq_std" : np.std(avg_freqs),
            "freq_mode" : freq_mode,
            "num_mode" : num_mode,
            "freq_list": avg_freqs
        }

    def segment_image(self, image):
```

```
    gauss = gaussian(image,5)
    img = dilation(gauss,disk(5))

    img = img/np.amax(img)
    markers = np.zeros_like(img)
    markers[gauss > 0.05] = 2
    markers[gauss < 0.05] = 1

    ws = watershed(img, markers)

    image = ws == 2

    distance = sndi.distance_transform_edt(image)
    coords = peak_local_max(distance, footprint=disk(20), labels=image)
    mask = np.zeros(distance.shape, dtype=bool)
    mask[tuple(coords.T)] = True
    markers, _ = sndi.label(mask)
    labels = watershed(-distance, markers, mask=image, watershed_line = True)

    return labels

 ### Frequency Data ###

def freq_statistics(self, results_collector):
    indices = np.argwhere(self.confidence_mask > 0.90).T

    num_frames = 400
    active_pixels = self.data[indices[0], indices[1], :num_frames]

    fourier = np.fft.fft(active_pixels, axis=-1)
    fourier = np.abs(fourier)

    freqs = np.fft.fftfreq(num_frames, d=self.sampling_interval)

    freq_arr = np.zeros(active_pixels.shape[0])

    for i in range(freq_arr.shape[0]):
        idx = np.argmax(fourier[i,1:num_frames//2])
        # indexing of sliced array start from 0 causing off-by-one bug
        #### FIX FOR OFF-BY-ONE ERROR:
        freq_arr[i] = freqs[idx+1] # using idx+1

    self.freq_num = freq_arr.shape[0]

    self.freq_mean = np.mean(freq_arr)
```

```
        self.freq_std = np.std(freq_arr)

        try:
            freq_mode = float(mode(freq_arr)[0][0])
            num_mode = int(mode(freq_arr)[1][0])
        except:
            freq_mode = 0
            num_mode = 0

        results_collector.cellnumber_queue.put(self.freq_num)

        results_collector.cellfreq_queue.put(freq_arr.tolist())

        self.freq_stats = {
            "freq_num" : self.freq_num,
            "freq_mean" : self.freq_mean,
            "freq_std" : self.freq_std,
            "freq_mode" : freq_mode,
            "num_mode" : num_mode,
            "freq_list": freq_arr.tolist()
        }

        hf = h5.File(f'{self.savepath+str(self.id)}-signals.h5', 'w')

        ds1 = hf.create_dataset('activepixels', data=active_pixels, dtype=np.float16)
        ds2 = hf.create_dataset('self.confidence_mask > 0.90',
    data=self.confidence_mask > 0.90, dtype=np.uint8)
        ds3 = hf.create_dataset('indices', data = indices, dtype=np.uint16)
        ds4 = hf.create_dataset('freq_array', data = freq_arr, dtype=np.float16)
        hf.close()

        try:
            self.agent
        except Exception as e:
            self.id += 1
```

B3 Microscope Control Class

```
import pco
import numpy as np
import h5py as h5
import multiprocessing as mp
from multiprocessing import shared_memory

class Camera():
    def __init__(self, control = False, savefolder=None, savename=None,
data_instance = None):
        self.control = control
        self.savefolder = savefolder
        self.savename = savename
        self.data = data_instance
        self.agent = None

        img_array = np.empty((400,512,512), dtype=np.uint16)
        self.shm = shared_memory.SharedMemory(create=True,
size=img_array.nbytes)

    def add_agent(self, agent):
        self.agent = agent

    def image(self, results_collector = None):
        if self.control == True:
            results_collector.log("Imaging from PCO:")

            proc = mp.Process(target=get_img, args=(self.shm,))
            proc.daemon = True
            proc.start()
            proc.join()
            frames = np.ndarray((512,512,400), dtype=np.uint16, buffer=self.shm.buf)
            self.data.send_data(frames[1:,:,:])

            if self.agent.current_id % 6 == 0:
                print('saving')
                hf = h5.File(f'{self.savefolder + self.savename}-
recording{self.agent.current_id}.h5', 'w')
                ds1 = hf.create_dataset('recording', data=frames, dtype=np.uint16)
                hf.close()

        else:
            results_collector.log('Fake imaging.')
            return 0
```

```
    def getsingleview(self):
        view = self.cam.record()
        return view [1:,:]

def get_img(shm):
    img = np.ndarray((512,512,400), dtype=np.uint16, buffer=shm.buf)
    configuration = {'exposure time': 0.025,
            'roi': (1, 1, 512, 512),
            'timestamp': 'binary',

            'trigger': 'auto sequence',

            'binning': (4, 4)}

    with pco.Camera(timestamp='on') as cam:
        cam.configuration = configuration
        cam.record(400, mode = 'sequence')
        array,meta = cam.images()

    img[:,:,:] = np.swapaxes(np.asarray(array),0,-1)

if __name__ == "__main__":
    print('PCO module')
```

B4 Stimulator Control Class

```
from time import sleep, time
import threading
from keithley2600 import Keithley2600 as k26k
import numpy as np
import os

class Stimulator():

    def __init__(self, control = False, savefolder= None, savename = None,
addrs=None):

        self.control = control

        self.savepath = f'{savefolder}stim/'

        isExist = os.path.exists(self.savepath)

        if not isExist:
            print('Creating directory.')
            os.makedirs(self.savepath)

        self.agent = None
        self.active = False

        #default frequencies
        self.freq = 1
        self.duration = 300
        self.current = 1e-6

        if self.control == True:
            self.k = k26k(addrs, visa_library='C:\\WINDOWS\\system32\\visa64.dll')
            self.k.smua.source.output = self.k.smua.OUTPUT_OFF
            self.k.smua.source.output = self.k.smua.OUTPUT_OFF
            self.k.smua.source.levelv= 0
            self.k.smua.source.leveli= 0
            self.k.set_integration_time(self.k.smua, 0.001)

    def add_agent(self, agent):
        self.agent = agent

    def run(self,results_collector = None):
        if self.control == True:

            if self.active == True:
```

```
                results_collector.log('Stimulating.')
                v,i = self.run_and_save(self.agent.current_id)
                v_min, v_max = np.amin(v[:,1]), np.amax(v[:,1])
                self.agent.add_new_ecdata(v_min, v_max)
            else:
                results_collector.log('Waiting.')
                sleep(self.duration)

        else:
            results_collector.log('Stimulator is off.')
            sleep(self.duration)
            self.agent.add_new_ecdata(0.5, -0.5)
            return 0

    def run_and_save(self, id):

        v,i = self.stimulate_sq_cw(self.duration,self.freq,self.current)

        np.savetxt(f'{self.savepath}voltage_{id}.csv', v, delimiter=',' )
        np.savetxt(f'{self.savepath}current_{id}.csv', i, delimiter=',' )

        return v,i

    def stimulate_sq_cw(self, duration, freq, current):

        Stop = threading.Event()

        v_table = []
        i_table = []

        t1 = threading.Thread(target = self.collect_V, args = (v_table,Stop))
        t2 = threading.Thread(target = self.control_I, args = (i_table,current, duration,
freq, Stop))

        starttime = time()

        t1.start()
        t2.start()

        t1.join(timeout=duration+1)
        t2.join()

        v = np.array(v_table)
        i = np.array(i_table)

        v[:,0] = v[:,0] - starttime
```

```
    i[:,0] = i[:,0] - starttime

    return v,i

def collect_V(self, table, event):

    while 1:
        v = self.k.smua.measure.v()
        a = [time(), v]
        table.append(a)
        if event.isSet():
            break

    return None


def control_I(self, table,i_level, duration, freq, event):

    period = 1/freq
    phase = period/2
    N = int(duration/period)
    set_I = i_level
    self.k.smua.source.leveli = set_I
    self.k.smua.source.func = self.k.smua.OUTPUT_DCAMPS
    self.k.smua.source.output = self.k.smua.OUTPUT_ON
    for n in range(2*N):
        t1 = time()
        self.k.smua.source.leveli= set_I
        a = [time(), set_I]
        table.append(a)
        while 1:
            t2 = time()
            delta = t2-t1
            if delta > phase:
                break
            else:
                sleep(0.001)
        a = [time(), set_I]
        table.append(a)
        set_I = -set_I


    self.k.smua.source.output = self.k.smua.OUTPUT_OFF
    event.set()

    return None
```

```
def set_freq(self, f):
        self.freq = f

def set_duration(self, t):
        self.duration = t

def set_curr_uA(self, I):
        self.current = I*1e-6
```

B5 Decision Making Class

```
import json

from time import time

class Agent():
    def __init__(self, control = False,  stim_device = None, savefolder=None,
savename=None, params=None):
        ## init parameters
        self.stim_current_uA = None
        self.duration = None
        self.stim_freq = None
        ## stop parameters
        self.target_freq = None
        self.timeout = None
        self.max_dV = None
        ## technical parameters
        self.max_attempts = None
        self.freq_overpace = None
        self.active_count_cutoff = None
        self.stim_current_step_uA = None

        for k,l in params.items():
            setattr(self, k, l)

        self.savepath = f'{savefolder}{savename}'

        self.state_table = []
        self.stats = []
        self.ec_table = []
        self.stimulator = stim_device
        self.current_id = 0
        self.state = 'train'
        self.attempts = 0

        self.default_freq = self.stim_freq
        self.control = control
        self.panic = False
        self.timeout_date = time() + 3600*self.timeout

    def make_decision(self, results_collector = None):
        ### This implementation is possibly unstable
        ### Would be better if actual decision tree
        if self.panic:
```

```
    self.state = 'stop'
    results_collector.log('Agent Panic!')
    return 0

if self.control == False:

    self.state = 'train'
    results_collector.log(f'training: {self.current_id}')
    self.state_table.append(self.state)
    self.current_id += 1

    if self.current_id > 9:
        self.state = 'stop'

    return 0

### informations for decision making
goal_freq = self.target_freq
culture_freq = self.stats[-1]['freq_mean']

min_active_count = 0

new_active_count = self.stats[-1]['freq_num']

max_delivered_voltage = self.read_last_max_dV()
results_collector.log(f'Last dV was: {max_delivered_voltage}')

## TRAIN CONDITIONS

## set train if everything ok
if new_active_count >= min_active_count:
    if self.state =='train':
        ## check if frequency must be increased
        if culture_freq > 2*self.stim_freq:
            tmp = self.stim_freq
            self.stim_freq = culture_freq*(0.5*(1+self.freq_overpace*0.01))
            print(f'stim freq set to: {self.stim_freq}')
            self.attempts = 0

        ## check if current should be increased
        if self.attempts > self.max_attempts:
            self.attempts = 0
            tmp = self.stim_current_uA
            self.stim_current_uA += self.stim_current_step_uA

        self.state = 'train'
```

```
        self.attempts +=1

    elif self.state == 'wait':
        self.state = 'train'
        self.attempts = 0


        self.stim_freq = culture_freq*(0.5*1.1)

### WAIT CONDITIONS

## if cells partially stop contracting
elif new_active_count < min_active_count:
    if self.state == 'train':
        self.attempts = 0
        self.state = 'wait'

    elif self.state == 'wait':
        self.attempts += 1

### STOP CONDITIONS

# frequency reached
if culture_freq > goal_freq:
    print('goal freq reached')
    self.state = 'stop'

# timeout reached
if time() > self.timeout_date:
    print('timeout stop')
    self.state = 'stop'
# 90% loss of active cells
if new_active_count < min_active_count & self.attempts > self.max_attempts:
    print('no enough active cells')
    self.state = 'stop'
# too much voltage required for stimulation
if max_delivered_voltage > self.max_dV:
    print('Too high voltage')
    self.state = 'stop'

#if self.state == 'stop':
 #   self.close_logfile()

self.state_table.append(self.state)
```

```
        self.write_to_log(self.current_id, self.state, self.stim_freq, self.stim_current_uA,
max_delivered_voltage, self.stats[-1])

        self.current_id += 1

    def set_stimulator(self, results_collector = None):
        if self.state == 'train':
            self.stimulator.active = True
            self.stimulator.set_freq(self.stim_freq)
            self.stimulator.set_duration(self.duration)
            self.stimulator.set_curr_uA(self.stim_current_uA)
        elif self.state == 'wait':
            self.stimulator.active = False

        results_collector.log(f'Stimulator set to {self.state}. {self.stim_freq} Hz,
{self.stim_current_uA} uA.')

    def add_new_ecdata(self, v_min, v_max):
        self.ec_table.append([v_min, v_max])

    def read_last_max_dV(self):
        if self.ec_table == []:
            return 0
        vmin, vmax = self.ec_table[-1]
        vmin = abs(vmin)
        vmax = abs(vmax)

        return vmin if vmin > vmax else vmax

    def add_results(self, freq_stats):
        self.stats.append(freq_stats)

    def signal_panic(self):
        self.panic = True

    def init_log(self):
        self.logfile = open(f'{self.savepath}agent-logfile.json', 'w', encoding='utf-8')
        self.logfile.write('[\n')

    def write_to_log(self, id, decision, freq, current, prev_voltage, data):
        if data is not list:
            data = list(data)

        if id > 0:
            self.logfile.write(',\n')
```

```
        chunk = {id : {'decision': decision, 'freq': freq, 'current_uA': current, 'prev_V':
prev_voltage, 'data': data}}

        json.dump(chunk, self.logfile, ensure_ascii=False, indent=4)

        self.logfile.flush()

    def close_logfile(self):
        self.logfile.write('\n]')

        self.logfile.close()

    def __del__(self):
        try:
            print('Agent exit.')
            self.close_logfile()
        except:
            print('Logfile already closed.')
```

B6 Script Used for Training Convolutional Neural Network

```
### Based on:
### https://keras.io/examples/timeseries/timeseries_classification_from_scratch/
### Distributed under Apache License 2.0

"""
## Setup
"""

from tensorflow import keras
import numpy as np
import matplotlib.pyplot as plt

## data_load
x_train = np.load('project/ML/x_train.npy')
y_train = np.load('project/ML/y_train.npy')

### reshape the data
x_train = x_train.reshape((x_train.shape[0], x_train.shape[1], 1))

### identify number of classes
num_classes = len(np.unique(y_train))

### data shuffle for improved randomness in validation split
idx = np.random.permutation(len(x_train))
x_train = x_train[idx]
y_train = y_train[idx]

### CNN setup

def make_model(input_shape):
    input_layer = keras.layers.Input(input_shape)

    conv1 = keras.layers.Conv1D(filters=64, kernel_size=3,
padding="same")(input_layer)
    conv1 = keras.layers.BatchNormalization()(conv1)
    conv1 = keras.layers.ReLU()(conv1)

    conv2 = keras.layers.Conv1D(filters=64, kernel_size=3, padding="same")(conv1)
    conv2 = keras.layers.BatchNormalization()(conv2)
    conv2 = keras.layers.ReLU()(conv2)

    conv3 = keras.layers.Conv1D(filters=64, kernel_size=3, padding="same")(conv2)
    conv3 = keras.layers.BatchNormalization()(conv3)
    conv3 = keras.layers.ReLU()(conv3)
```

```
    gap = keras.layers.GlobalAveragePooling1D()(conv3)

    output_layer = keras.layers.Dense(num_classes, activation="softmax")(gap)

    return keras.models.Model(inputs=input_layer, outputs=output_layer)

model = make_model(input_shape=x_train.shape[1:])
model.summary()

epochs = 100
batch_size = 12

## setup callbacks
callbacks = [
    keras.callbacks.ModelCheckpoint(
        "project/ML/best_model.h5", save_best_only=True, monitor="val_loss"
    ),
    keras.callbacks.ReduceLROnPlateau(
        monitor="val_loss", factor=0.5, patience=20, min_lr=0.0001
    ),
    keras.callbacks.EarlyStopping(monitor="val_loss", patience=50, verbose=1),
]

### compile model
model.compile(
    optimizer="adam",
    loss="sparse_categorical_crossentropy",
    metrics=["sparse_categorical_accuracy"],
)

### train model
history = model.fit(
    x_train,
    y_train,
    batch_size=batch_size,
    epochs=epochs,
    callbacks=callbacks,
    validation_split=0.2,
    verbose=1,
)
```

B7 List of Packages in the Conda Environment Used for Cell Training

# Name	Version	Build	Channel
absl-py	1.0.0	pypi_0	pypi
anyio	3.3.4	pypi_0	pypi
apscheduler	3.6.3	pypi_0	pypi
argon2-cffi	21.1.0	pypi_0	pypi
astunparse	1.6.3	pypi_0	pypi
attrs	21.2.0	pypi_0	pypi
babel	2.9.1	pypi_0	pypi
backcall	0.2.0	pypi_0	pypi
backports-zoneinfo	0.2.1	pypi_0	pypi
bleach	4.1.0	pypi_0	pypi
ca-certificates	2021.5.30	h5b45459_0	conda-forge
cachetools	5.0.0	pypi_0	pypi
certifi	2021.10.8	pypi_0	pypi
cffi	1.15.0	pypi_0	pypi
charset-normalizer	2.0.12	pypi_0	pypi
clang	5.0	pypi_0	pypi
colorama	0.4.4	pypi_0	pypi
cuda-command-line-tools	11.4.2	hffd2907_0	nvidia
cuda-compiler	11.4.2	hffd2907_0	nvidia
cuda-cudart	11.4.108	h5994f8e_0	nvidia
cuda-cuobjdump	11.4.120	hce9bfb8_0	nvidia
cuda-cupti	11.4.120	h70d5594_0	nvidia
cuda-cuxxfilt	11.4.120	h88c04fa_0	nvidia
cuda-libraries	11.4.2	hffd2907_0	nvidia
cuda-libraries-dev	11.4.2	hffd2907_0	nvidia
cuda-memcheck	11.4.120	h591275e_0	nvidia
cuda-nvcc	11.4.120	hcbd42c9_0	nvidia
cuda-nvdisasm	11.4.120	h9f38c02_0	nvidia
cuda-nvml-dev	11.4.120	h895c486_0	nvidia
cuda-nvprof	11.4.120	h4335513_0	nvidia
cuda-nvprune	11.4.120	h54f66f3_0	nvidia
cuda-nvrtc	11.4.120	hc4fc4c7_0	nvidia
cuda-nvtx	11.4.120	hb0af1ca_0	nvidia
cuda-nvvp	11.4.120	hddbf988_0	nvidia
cuda-samples	11.4.120	h6c0c819_0	nvidia
cuda-sanitizer-api	11.4.120	h8040cef_0	nvidia
cuda-thrust	11.4.122	hed1706c_0	nvidia
cuda-toolkit	11.4.2	hffd2907_0	nvidia
cuda-tools	11.4.2	hffd2907_0	nvidia
cuda-visual-tools	11.4.2	hffd2907_0	nvidia
cycler	0.10.0	pypi_0	pypi
debugpy	1.5.1	pypi_0	pypi
decorator	5.1.0	pypi_0	pypi

defusedxml	0.7.1	pypi_0	pypi
entrypoints	0.3	pypi_0	pypi
flatbuffers	2.0	pypi_0	pypi
gast	0.5.3	pypi_0	pypi
glob2	0.7	pypi_0	pypi
google-auth	2.6.0	pypi_0	pypi
google-auth-oauthlib	0.4.6	pypi_0	pypi
google-pasta	0.2.0	pypi_0	pypi
grpcio	1.44.0	pypi_0	pypi
h5py	3.6.0	pypi_0	pypi
idna	3.3	pypi_0	pypi
imageio	2.9.0	pypi_0	pypi
importlib-metadata	4.11.2	pypi_0	pypi
ipykernel	6.4.2	pypi_0	pypi
ipython	7.27.0	pypi_0	pypi
ipython-genutils	0.2.0	pypi_0	pypi
jedi	0.18.0	pypi_0	pypi
jinja2	3.0.2	pypi_0	pypi
json5	0.9.6	pypi_0	pypi
jsonschema	4.1.2	pypi_0	pypi
jupyter-client	7.0.6	pypi_0	pypi
jupyter-core	4.8.1	pypi_0	pypi
jupyter-server	1.11.1	pypi_0	pypi
jupyterlab	3.2.1	pypi_0	pypi
jupyterlab-pygments	0.1.2	pypi_0	pypi
jupyterlab-server	2.8.2	pypi_0	pypi
keithley2600	2.0.1	pypi_0	pypi
keras	2.8.0	pypi_0	pypi
keras-preprocessing	1.1.2	pypi_0	pypi
kiwisolver	1.3.2	pypi_0	pypi
libclang	13.0.0	pypi_0	pypi
libcublas	11.6.1.51	h9c62911_0	nvidia
libcufft	10.5.2.100	hd1d076d_0	nvidia
libcurand	10.2.5.120	h8703a95_0	nvidia
libcusolver	11.2.0.120	h0a70368_0	nvidia
libcusparse	11.6.0.120	h6a5001c_0	nvidia
libnpp	11.4.0.110	heb7a92d_0	nvidia
libnvjpeg	11.5.2.120	h95a0c2f_0	nvidia
markdown	3.3.6	pypi_0	pypi
markupsafe	2.0.1	pypi_0	pypi
matplotlib	3.4.3	pypi_0	pypi
matplotlib-inline	0.1.3	pypi_0	pypi
memory-profiler	0.60.0	pypi_0	pypi
mistune	0.8.4	pypi_0	pypi
nbclassic	0.3.2	pypi_0	pypi
nbclient	0.5.4	pypi_0	pypi

nbconvert	6.2.0	pypi_0	pypi
nbformat	5.1.3	pypi_0	pypi
nd2reader	3.3.0	pypi_0	pypi
nest-asyncio	1.5.1	pypi_0	pypi
networkx	2.6.3	pypi_0	pypi
nidaqmx	0.5.7	pypi_0	pypi
notebook	6.4.5	pypi_0	pypi
numpy	1.22.2	pypi_0	pypi
oauthlib	3.2.0	pypi_0	pypi
openssl	1.1.1l	h8ffe710_0	conda-forge
opt-einsum	3.3.0	pypi_0	pypi
packaging	21.0	pypi_0	pypi
pandocfilters	1.5.0	pypi_0	pypi
parso	0.8.2	pypi_0	pypi
pco	0.1.3	pypi_0	pypi
pickleshare	0.7.5	pypi_0	pypi
pillow	8.3.2	pypi_0	pypi
pims	0.5	pypi_0	pypi
pip	21.0.1	py38haa95532_0	
prometheus-client	0.11.0	pypi_0	pypi
prompt-toolkit	3.0.20	pypi_0	pypi
protobuf	3.19.4	pypi_0	pypi
psutil	5.9.0	pypi_0	pypi
pyasn1	0.4.8	pypi_0	pypi
pyasn1-modules	0.2.8	pypi_0	pypi
pycparser	2.20	pypi_0	pypi
pygments	2.10.0	pypi_0	pypi
pyparsing	2.4.7	pypi_0	pypi
pyrsistent	0.18.0	pypi_0	pypi
python	3.8.11	h6244533_1	
python-dateutil	2.8.2	pypi_0	pypi
python_abi	3.8	2_cp38	conda-forge
pytz	2021.1	pypi_0	pypi
pyvisa	1.11.3	pypi_0	pypi
pyvisa-py	0.5.2	pypi_0	pypi
pywavelets	1.1.1	pypi_0	pypi
pywin32	302	pypi_0	pypi
pywinpty	1.1.4	pypi_0	pypi
pyzmq	22.3.0	pypi_0	pypi
requests	2.27.1	pypi_0	pypi
requests-oauthlib	1.3.1	pypi_0	pypi
requests-unixsocket	0.2.0	pypi_0	pypi
retrying	1.3.3	pypi_0	pypi
rsa	4.8	pypi_0	pypi
scikit-image	0.18.3	pypi_0	pypi
scipy	1.7.1	pypi_0	pypi

send2trash 1.8.0 pypi_0 pypi
setuptools 60.9.3 pypi_0 pypi
six 1.16.0 pypi_0 pypi
slicerator 1.0.0 pypi_0 pypi
sniffio 1.2.0 pypi_0 pypi
sqlite 3.36.0 h2bbff1b_0
tenacity 8.0.1 pypi_0 pypi
tensorboard 2.8.0 pypi_0 pypi
tensorboard-data-server 0.6.1 pypi_0 pypi
tensorboard-plugin-wit 1.8.1 pypi_0 pypi
tensorflow 2.8.0 pypi_0 pypi
tensorflow-estimator 2.6.0 pypi_0 pypi
tensorflow-io-gcs-filesystem 0.24.0 pypi_0 pypi
termcolor 1.1.0 pypi_0 pypi
terminado 0.12.1 pypi_0 pypi
testpath 0.5.0 pypi_0 pypi
tf-estimator-nightly 2.8.0.dev2021122109 pypi_0 pypi
tifffile 2021.8.30 pypi_0 pypi
tornado 6.1 pypi_0 pypi
tqdm 4.62.3 pypi_0 pypi
traitlets 5.1.0 pypi_0 pypi
typing-extensions 4.1.1 pypi_0 pypi
tzdata 2021.1 pypi_0 pypi
tzlocal 3.0 pypi_0 pypi
urllib3 1.26.8 pypi_0 pypi
vc 14.2 h21ff451_1
vs2015_runtime 14.27.29016 h5e58377_2
wcwidth 0.2.5 pypi_0 pypi
webencodings 0.5.1 pypi_0 pypi
websocket-client 1.2.1 pypi_0 pypi
werkzeug 2.0.3 pypi_0 pypi
wheel 0.37.1 pypi_0 pypi
wincertstore 0.2 py38_0
wrapt 1.13.3 pypi_0 pypi
xmltodict 0.12.0 pypi_0 pypi
zipp 3.7.0 pypi_0 pypi